The University of Sheffield
Department of Mechanical Engineering

3D CAFE modelling of ductile fracture in gas pipeline steel

Sabino Ayvar Soberanis

A thesis submitted for the degree of Doctor of Philosophy

November 2007

Dedicated to my Family.....

SUMMARY

This thesis describes a series of experimental and computational studies carried out on X100 pipeline steel with the objective to characterise the tearing resistance of the material. A Cellular Automata – Finite Element (CAFE) technique was used in this work to develop a 3D numerical model to provide a more realistic description of the ductile damage mechanisms of the pipeline steel. In this model, the Rousselier micro-mechanisms damage theory and an appropriate cell size in a CA array represent the material behaviour.

The experimental work consisted of laboratory tensile specimens in four different orientations of the material to determine the properties of the pipeline steel. Two novel designs were conducted to measure the deformation behaviour when loaded in the through wall direction. Compact C(T) and tear specimens were also tested to capture the crack growth, and the flat and shear fracture characteristics. The experimental data of laboratory samples were used to calibrate the continuum damage models.

SEM (Scanning Electron Microscope) micrograph observations were carried out in tensile tests, standard C(T), slant notch C(T) and tear specimens. These observations revealed that spacing between large dimples of flat fracture are of the order of five times larger than shear fracture. It is important since the transfer of the material model parameters is made by modifying the cell size according to the average spacing between large voids in the material, *d*. Therefore 3D CAFE models for flat and shear fracture were created according to the micro-structural characteristics to interpret the experimental findings.

The main aim of the research reported here is to investigate transferability of the damage model parameters to gas pipelines steels from laboratory scale samples, and then to predict the fracture response of real structures. The CAFE technique has been shown to be a powerful tool in reducing simulation time whilst maintaining good predictions of shear damage and material resistance in terms of CTOA criterion. This was not achieved by classical FE methods where a very fine mesh is required to represent the characteristic dimension of ductile fracture. Similar reasonable results were obtained when anisotropic flat fracture was predicted but transferability of the damage parameters to CT specimens needs still further investigation.

ACKNOWLEDGEMENTS

Special acknowledgments to my academic advisors Professor John R. Yates and Professor Ian C. Howard for being of inspiration and support in this research project in all experimental and modelling aspects.

I would like to acknowledge to Dr. Anton Shterenlikht and Dr. Hashemi Sayyed for their constructive suggestions and advices of this subject area that were of great importance in the realisation of my research project.

I would like to thank CONACYT for the financial support and having made all this possible.

I appreciate the assistance to the technicians of the Mechanical Engineering Department who help me in different stages of the experimental work: Mr. K A. Rotchell, Mr. P G. Downs, Mr. J. V. Goodliffe, Mr. R. Kay, Mr. J N. Bradley, Mr. R Mills, Mr. M. Jackson and Mr. P. Blackbourn (Civil Engineering Department). I would also acknowledge them for being available and professionals.

I would like to acknowledge to my friends, academic staff, department staff and PhD research students who share with me these years in Sheffield. I would also acknowledge them for their advices and help that I received.

Finally the author would like to acknowledge sincerely the support and patient of my family during the realisation of my PhD studies.

NOMENCLATURE

β damage variable (Rousselier model)

$\bar{\beta}_F$ mean critical value of the damage variable

σ_{rr} radial stresses

$\bar{\varepsilon}_{(c)}$ evolution of the deformation of coalescence

ε_{eq} equivalent strain

$\dot{\varepsilon}_{ij}^{p}$ plastic strain rate

ε_T true strain

σ_{eq} equivalent stress

σ_H Hill equivalent stress

σ_m mean stress $\sigma_m = (\sigma_{11} + \sigma_{22} + \sigma_{33})/3$

σ_T true stress

σ_Y material yield strength

f void volume fraction

f_0 initial volume fraction

f_c critical value of void volume fraction,

f_F void volume fraction at final fracture

$\dot{f}$ void volume fraction rate

$\dot{f}_g$ rate of growth of existing voids

$\dot{f}_n$ void nucleation rate

I_{ij} second order unit tensor

ρ dimensionless density

γ yield shear strains

Φ Yield function of the GTN model

$\Delta\Phi_{(c)}$ diametral contraction at the point in the curve where there is a quick change of plastic deformation due to the macroscopic coalescence

Φ_0 initial diameter of the gauge section

ν Poisson's ratio

a crack length

a_0 initial crack length

Δa crack growth extension

A_T true value of cross section area

c_D concentration factor for ductile CA array

CTOA Crack Tip Opening Angle

CMOD Crack Tip Opening Displacement

D, σ_1 material constants (Rousselier model)

d_x, d_y and d_z average dimensions of the inclusions

E Young's modulus

F the load

K strength coefficient

l_0 original gauge length of the tensile specimen

l_i instantaneous length of the tensile specimen

L_D ductile damage cell size

L_{FE} value of the element size

n hardening exponent

$\sqrt[3]{M_D}$ number of cells per linear finite element

q_1, q_2, q_3 adjustable parameters (GTN model)

$R_L, R_T, R_S, R_{LT}, R_{TS}\ R_{SL}$ coefficient of Lankford

$\underline{s}$ stress deviator

U electric potential signal

U_0 potential signal at crack initiation

$STD\beta_F$ standard deviation of the critical value of the damage variable

W specimen width

$2y$ initial spacing of the potential probes

Z reduction in areas at rupture

LIST OF FIGURES

LIST OF TABLES

CONTENTS

CHAPTER 1

1.1 PROBLEM AND POTENTIAL SOLUTION

Recent failure information from modern gas line pipe steels has revealed that experimental models to assess material resistance to ductile rupture tuned to lower grades of steel may result in significant errors when they are extrapolated to high strength high toughness steels. A possible solution to the difficulties in the use of current arrest/propagation models is to refine them by using micro-mechanism damage model of failure.

The main aim of this research is to put forward the application of micro-mechanical computer modelling of the combination of cellular automata (CA) and finite element (FE) techniques (CAFE method), together with a ductile damage theory to provide a description that is more realistic of the process that leads to failure of pipeline steel. The use of CAFE modelling offers advantages in time of simulation compared with the conventional FE analysis and in the development of finite element models with appropriate sized mesh to represent the microstructure scale of the material which is not achieved in conventional FE analyses.

The main advantage of using a damage model is that a unique set of micromechanical damage parameters can be found as material constants for the steel which are transferable to large structures. It is assumed that the same fracture micro-mechanisms govern the failure of ductile material independently of structure size (constraint) and loading conditions.

1.2 SCOPE OF THE PROJECT

A summary of the project plan is set out in Table 1.1. The project was realised as following: first, macro and micro flat and shear fracture features of the pipeline steel were captured using appropriated specimens with different flat and slant fracture characteristics. Second, 3D CAFE modelling was carried out for all specimens according to the micro-structural characteristics to interpret the experimental findings and validate the micromechanical damage models for ductile flat and shear fracture. There is also a discussion of classic FE modelling compared with the more recent CAFE technique, as a potential tool to reduce the time of simulations,

whilst maintaining a good prediction of damage. Finally the CAFE technique was applied to the CTOA criterion for modelling stable crack propagation for predicting the failure characteristics of large-scale gas pipes.

Table 1.1 Experimental and computer modelling of the project

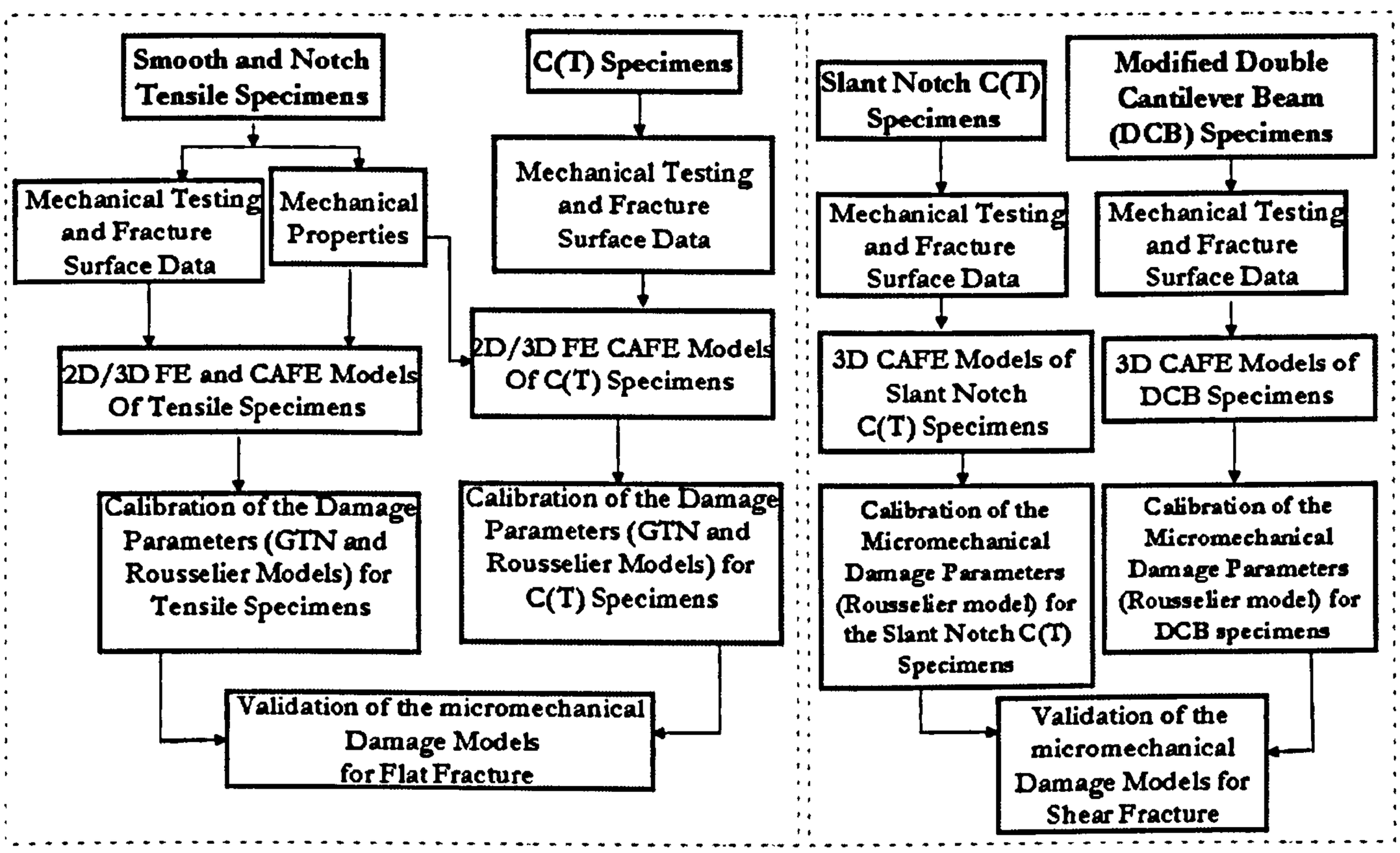

CHAPTER 2

2.1 INDUSTRIAL CONTEXT

For the safe and economical transportation of natural gas, pipelines play a vital role in gas field development. Gas companies have shown an increasing interest in the use of higher grade steel pipe for the construction of long distance gas pipelines. The use of a high strength grade offers potential benefits in terms of using a higher service pressure without increasing the pipe wall thickness. This in turn offers financial benefits arising from lower material, transportation and fabrication costs. Recent progress in the technology for controlled-rolling (CR) and thermo-mechanical control (TMC) processes has allowed high grade line pipes, such as API 5L (Kawaguchi et al., 2004) X80, X100 and X120 to be produced. These new specifications can be used to design pipelines to sustain an operational pressure of the order of 15MPa equivalent to hoop stress up to 80% of specified minimum yield stress (SMYS) of the material (Rothwell, 2000). But, due to the severe loading conditions the structural integrity of the pipeline demands closer attention.

The major concern for the designers and operators of high pressure gas transmission pipelines is the control of long running ductile fractures. The line pipe design should assure that the pipe steel is tough enough to suppress the propagation of any potential fracture. In the worst case when the crack starts to propagate, the pipe rupture resistance should be sufficient to rapidly arrest the fracture within the minimum number of segments of the pipeline. This will guarantee gas pipeline safety and minimise the loss of line pipe asset in the unlikely event of failure.

As the hoop stress in a gas pipe is the maximum stress, axial crack propagation is the most important defects from the engineering point of view. There have been several recorded instances of this mode of fracture, particularly in steel transmissions pipelines. Long running axial cracks propagate of several kilometres per second, and the consequent catastrophic results have been observed (Cabral and Kimber, 1997).

2.2 CONTROL OF FRACTURE PROPAGATION IN GAS PIPE LINES

2.2.1 Charpy energy fracture criterion

To prevent long running ductile fracture, a reliable fracture control plan and related material properties are necessary. Fracture propagation and arrest in gas pipeline has been the subject of study since a number of spectacular brittle fractures in the 1950s and 1960s. For older line-pipe steels a descriptive model was developed, based on the correlation between full scale burst tests and Charpy V-notch (CVN) or dynamic drop weight tear test (DWTT) absorbed energy. This was done on the basis that propagation could be described by the critical strain energy release rate, G_c. It was shown that G_c correlated directly with Charpy energy per area, provided that the Charpy energy used was a Charpy shear area that agreed with the shear area exhibited in full scale tests. To deal with the brittle fracture problem pipeline companies began to specify minimum required toughness levels and this problem subsequently disappeared for new pipeline steels.

In the late sixties it became noticeable that pipelines could also fail by ductile fracture. Key work describing ductile propagation and arrest was by Maxey (1974), and became known as the Battelle two curve method. This method was used to determine a required minimum Charpy upper plateau energy for arrest.

Further developments in steel making practice meant that the upper shelf Charpy energy did not correlate well with full scale fracture. New techniques for predicting ductile fracture arrest were needed. By the late 1970s, researches were examining DWTT energy as a means of predicting the toughness of controlled rolled steels. The Battelle two curve method was adapted to DWTT by use of a simple correlation of DWTT to Charpy energy (Wilkowski et al., 1978). Although this relationship is straightforward to use for a specific material, its empirical nature limits its extrapolation to other materials. Other empirical equations for minimum toughness are also used by different groups as listed by Hashemi (2003). Those equations predict the necessary Charpy energy for a propagating crack to be arrested and they are normally the result of statistical correlation between toughness of materials measured experimentally and design parameters such as hoop stress, diameter and thickness of the pipe. The main problem in using these semi-empirical relationships is that in the past most of them were calibrated on lower grades of gas pipe steels (grade 70 or lower). For modern high-

strength high toughness steels, they are under question for their ability to properly characterize ductile fracture propagation resistance. A possible solution to the difficulties in the use of current arrest/propagation models is to refine the correction factor. The main source of the discrepancy is that the Charpy energy in high-strength pipeline materials is dominated by failure process other than slant fracture. For instance, the high initiation energy occupies a considerable portion of the overall fracture energy in high grade X100 pipeline steel.

Recently, it has been suggested by Leis et al. (1998), Andrews et al. (2002) and others that the fracture energy in Charpy impact test for modern steels associated with fracture propagation can be split in two parts. One is related to the flat fracture at the centre of the typical Charpy fracture surface and the other to slant fracture at the edges. As the dominant failure mechanism in gas line pipes is fast propagating ductile shear, the latter is the most important portion of the fracture energy which can be reasonably attributed to the real failure mode of the pipe. Accordingly, specimens with different flat and slant fracture characteristics are needed for a comprehensive failure analysis of the Charpy specimen. Furthermore, finite element simulation techniques using ductile damage mechanics can be used as a tool for separating the Charpy energy into parts associated with shear and flat fracture.

2.2.2 CTOA fracture criterion

As alternatives to the Charpy energy fracture criterion, other methodologies for a safe design against stable crack growth have been proposed: crack-tip strain (Orowan, 1949), energy release rate (Broberg, 1975), the J-integral (Rice, 1968), crack-tip opening displacement (CTOD) (Wells, 1961a) and crack tip opening angle (CTOA) (Anderson, 1973). Among them, the critical CTOA criterion has been shown to be most suitable for modelling stable crack propagation and for predicting the failure characteristics of large-scale structures. This criterion was developed from the critical crack tip opening displacement (CTOD) concept proposed by Wells (Wells, 1961a; Wells, 1961b; Wells, 1963) for large scale plasticity and large amounts of stable tearing. The CTOD has a limiting value of zero at the crack tip, thus from a practical standpoint the slope of the CTOA was later suggested by Anderson (1973) and Koning (1977) to characterize the fracture behaviour. The measurement of the CTOA profile is made between a point, at a fixed distance behind the crack-tip, on the upper surface of a crack, the crack tip and a third point, again at a fixed distance behind the crack-tip, on the lower surface

(Fig. 2.1). In practice the material resistance to ductile rupture in terms of CTOA is expressed as:

$$CTOA_{applied} < CTOA_{critical} \tag{2.1}$$

where $CTOA_{applied}$ is the crack driving force acting at the crack-tip due to the kinetic energy of escaping gas in case of a pipeline. The $CTOA_{critical}$ is the fracture toughness of the material, which is assumed to be constant. Whenever this inequality is satisfied, any potential fracture should be arrested.

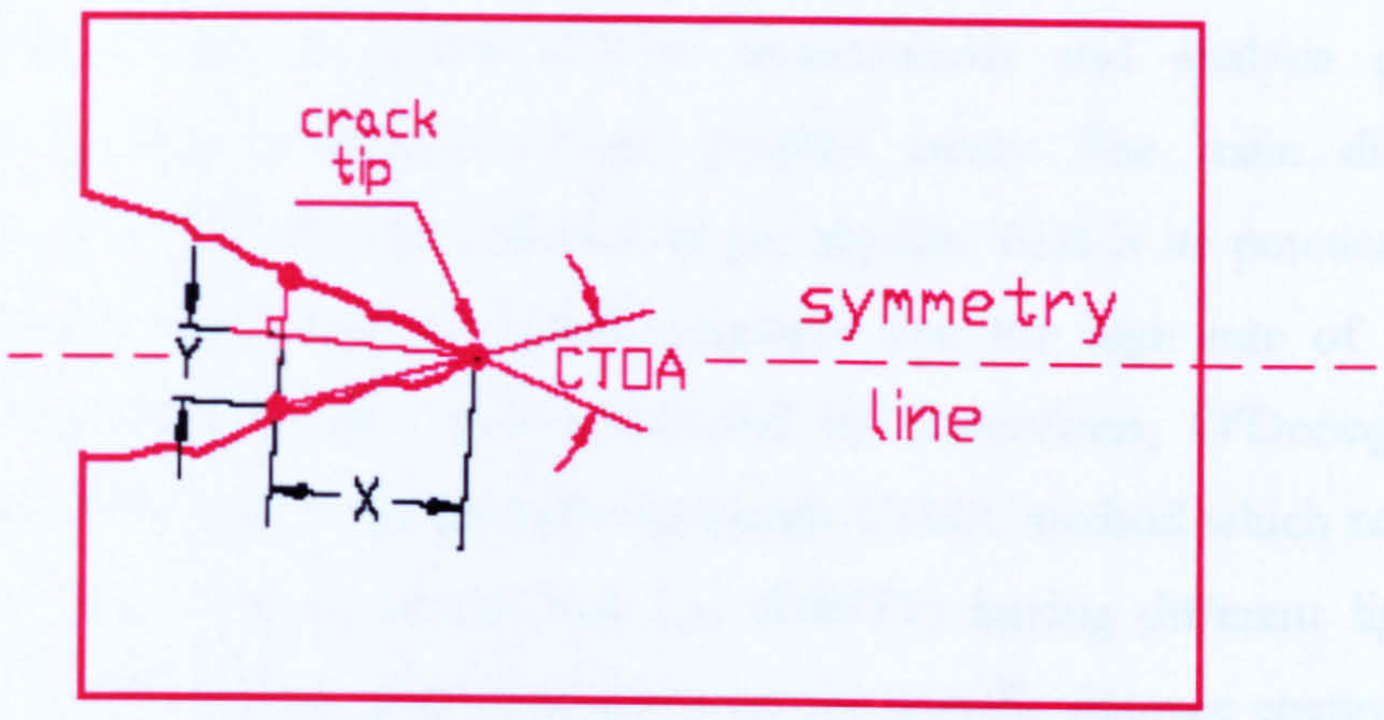

Fig. 2.1 CTOA measuring scheme

Since the early 1980's many researchers have studied, both experimentally and numerically, the use of the CTOA criterion. Extensive studies of CTOA fracture parameters in aerospace aluminium materials (Newman et al., 2003a; Newman et al., 2003b; James and Newman, 2003; Dawicke and Newman, 1998; Dawicke et al., 1997; Dawicke et al., 1995; Sutton et al., 1995; Dawicke and Sutton 1994), gas pipeline (Mannuci et al., 2000; Wilkowski et al., 2002; Rudland et al., 2003) and high pressure vessel steels (Schindler, 1996) have revealed that it can be regarded as a material constant over the stable crack propagation phase in the presence of large scale yielding. Newman, Dawicke, Sutton and their colleagues at NASA Langley have produced exhaustive investigations of the direct evaluation of CTOA of spacecraft aluminium alloys using optical methods like photography and digital imaging correlation techniques in thick compact tension tests C(T) and middle crack tension M(T) specimens of several thickness ranging from 1 to 25.4mm to monitor and estimate the CTOA, the progression of

the crack tip, constraint effects and crack tunnelling in the specimens. Their experimental measurements of CTOA values were used to predict the fracture behaviour of large scale structure by computer modelling. This gave further credibility to the CTOA fracture criterion as a promising parameter for failure analysis of engineering materials in the case of large plastic deformations. Other researches recently have contributed to the same field of aluminium materials e.g. (Lloyd, 2003; Lloyd and McClintock, 2003) in the development of a microtopography system to provide full three dimensional CTOA distributions at any amount of crack extension or the studies of Mahmoud and Lease (2003) showing that the CTOA parameter can be successfully characterised for increasing thicknesses of a common aerospace aluminium alloy.

Several researchers have proposed CTOA measurement and analysis procedures for characterizing the high toughness of gas pipeline steels. The main difficulty in the implementation of CTOA fracture criterion in gas pipeline field is its practical measurement either in laboratory scale tests or in real structures due the high rate of fracture in the experiments. Pioneering studies were conducted by Demofonti, O'Donoghue and their colleagues. They developed a standard two-specimen CTOA method which requires dynamic fracture of two sets of drop weight tear test (DWTT) having different ligament lengths (Demofonti et al., 1995). This method is based on the specific fracture energy concept and a computer code for evaluating the material and the applied CTOA values (O'Donoghue, 1997). Other experimental techniques such as high-speed photography in dynamic drop weight tear test (Wilkowski et al., 2002; Rudland et al., 2003; Wilkowski et al., 2000), full thickness burst experiments and extensive instrumentation for measuring the strain data behind the moving crack tip for reproducing the flap opening angle (Mannucci, et al., 1999; Berardo et al., 2000) and CTOA estimation from the deformed mesh in a single CTOA test approach by Shterenlikht et al. (2004) and Hashemi et al. (2004) have been used for this purpose. This latter method has offered recent developments for direct measurement of CTOA data in a laboratory scale test providing large amounts of highly consistent CTOA data even in one experiment and stable CTOA values from both sides of the specimen. The extensive data set available allows the statistics of the scatter of measured CTOA values can be calculated. However, the CTOA measurement was based on quasi-static tests.

2.3 MICROANALYSIS OF DUCTILE FRACTURE

Extensive research on macro and micro fracture mechanisms have showed that ductile fracture in metals is a result of the growth and coalescence of microscopic voids that initiate at inclusions and second phase particles. So that, to understand and predict how larger objects like gas pipelines crack under applied load requires studying the fundamental mechanisms of how cavities and defects grow around microscopic particles and then coalesce. The commonly observed stages in ductile fracture are (Knott, 1980; Wilsforf, 1983; Garrison and Moody, 1987; Argon et al., 1975)

- Formation of a free surface at an inclusion or second phase particle by either interface decohesion or particle cracking.
- Growth of the void around the particle, by means of plastic strain and hydrostatic stress.
- Coalescence of the growing void with adjacent voids.

There is a well-documentary history of efforts aimed at developing models for these three stages in ductile fracture analysis (Van et el., 1985; Garrison and Moody 1987). The most widely used continuum model for void nucleation is due to Argon and Im (1975), who argued that the interfacial stress at a cylindrical particle is approximately equal to the sum of the mean (hydrostatic) stress and the effective (Von Mises) stress. After void formation, further plastic strain and hydrostatic stress cause the voids to grow and eventually coalescence. In this phase, a number of authors have developed mathematical models for void growth and coalescence. Some of the major models for ductile fracture are described below.

2.3.1 Argon-Im-Safoglu model

The most widely used continuum model for void nucleation is due to Argon and Im (1975) and Argon, Im and Safoglu (1975). They proposed that the criterion for separation of large particles is locally reaching a critical interfacial tensile strength. For the case of spherical inclusions they derived the following equations for the radial stresses on the inclusion matrix interface:

For non interactive inclusions:

$$\sigma_{rr} = k_0 \left[\left(\frac{\gamma}{\gamma_y} \right)^{\frac{1}{n}} + \sqrt{3} \left(\frac{\sqrt{6}(n+1)}{m} \frac{\gamma}{\gamma_y} \right)^{\frac{1}{n+1}} \right] \tag{2.2}$$

For interactive inclusions:

$$\sigma_{rr} = k_0 \left[\sqrt{3} \left(\frac{\sqrt{3}}{\frac{\lambda}{\rho}} \frac{\gamma}{\gamma_y} \right)^{\frac{1}{n}} + \frac{\sqrt{6}}{m} \frac{\lambda}{\rho} + \left(\frac{\gamma}{\gamma_y} \right)^{\frac{1}{n}} \right] \tag{2.3}$$

where k_0 is the yield stress in shear, γ and γ_y are the present and yield shear strains, n is the hardening exponent, m is the Taylor factor, generally taken as 3.1, λ is the inter-particular spacing and ρ is the particle radius. According to this approach decohesion occurs when: $\sigma_{rr} \geq \sigma_c$.

2.3.2 McClintock model

The pioneering work of McClintock (1968) and Rice and Tracey (1969) showed that the mechanical processes of ductile growth of cylindrical and spherical voids in plastic materials were the major parameters in the fracture process and suggested that a precise mechanical analysis of a carefully chosen model could serve to quantify microstructural behaviour.

McClintock proposed a model for void growth and derived a criterion for ductile fracture. He assumed a material containing a regular three-dimensional array of cylindrical voids of elliptical section. The main axes of this array are parallel to the principal stress axes. The condition for fracture was that each void touches the neighbouring one. If the voids have the cylindrical axes parallel to the z direction and two semi axes are designed as a and b, and if the voids grow in the b direction then the approximate expression for the onset of fracture takes the form:

$$\frac{d\eta_{zb}}{d\varepsilon_{eq}} = \frac{1}{\ln F_{zb}^{f}} \left[\frac{\sqrt{3}}{2(1-n)} \sinh\left(\frac{\sqrt{3}(1-n)}{2} \frac{\sigma_a + \sigma_b}{\sigma_{eq}} \right) + \frac{3}{4} \frac{\sigma_a - \sigma_b}{\sigma_{eq}} \right] \tag{2.4}$$

where $\frac{d\eta_{zb}}{d\varepsilon_{eq}}$ is a damage rate (ε_{eq} - equivalent strain, $d\eta_{zb}$ - damage increment), F_{zb}^{f} is a critical value of the relative growth factor, n is a hardening exponent, σ_a and σ_b are two of the principal stresses at infinity and σ_{eq} is the equivalent stress.

The over-simplified nature of this model leads to unrealistic results. Most important is, that according to this model, void growth is a smooth process until the final rupture.

2.3.3 Rice-Tracey model

Rice and Tracey (1969) analyzed a case of dilatational growth of a single spherical void in a material under uniform stress state applied at infinity. They derived a classical equation for void enlargement under a high triaxiality stress state:

$$D = 0.283 \cdot \exp\left(1.5\frac{\sigma_m}{\sigma_{eq}}\right) \tag{2.5}$$

where D is the ratio of the strain rate on the surface of a void to the strain rate at infinity, σ_m is the mean stress and σ_{eq} is the equivalent stress.

The simplicity of the resulting equation is the major advantage of this model. The practical use of this equation however is quite limited because the model does not address void interaction

2.3.4 Gurson-Tvergaard-Needleman (GTN) Model

Inspired by the work of Rice and Tracey (1969), Needleman (1972) and Berg (1970); Gurson (1977a) proposed a methodology for obtaining an approximate yield surface for material containing voids. He analysed plastic flow in a porous medium by assuming that the material behaves as continuum and voids appear in the model indirectly through their influence on the global flow behaviour. Unlike the Rice and Tracey model, the Gurson model contains a failure criterion.

$$\Phi = \left(\frac{\sigma_{eq}}{\sigma_y}\right)^2 + 2f \cdot \cosh\left(\frac{3\sigma_m}{2\sigma_y}\right) - 1 - f^2 = 0 \qquad (2.6)$$

where f is a void volume fraction. This condition is reduced to the classical Mises yield criterion if $f = 0$. The change in void volume fraction was described as:

$$\dot{f} = \dot{f}_g + \dot{f}_n \qquad (2.7)$$

where $\dot{f}$ is the void volume fracture rate, $\dot{f}_g$ is the rate of growth of existing voids and $\dot{f}_n$ is the void nucleation rate. For the growth of existing voids Gurson (1977a) propose only dilatation:

$$\dot{f}_g = (1-f)\dot{\varepsilon}^p_{ij} I_{ij} \qquad (2.8)$$

where $\dot{\varepsilon}^p_{ij}$ is a plastic strain rate and I_{ij} is the second order unit tensor. For the void nucleation rate, various models were proposed by Gurson (1977b). Since the Gurson model does not contain discrete voids, it is incapable of predicting void interactions that lead to failure.

Yamamoto (1978) examined the condition in which the Gurson model could lead to ductile fracture by the localization of deformation in a band of material. He found that the deformation at fracture, for realistic values of the initial volume fracture of cavities, f_0, was much too high. He concluded that an initial imperfection is necessary in order to achieve localization at reasonable strain.

Since Gurson's model greatly over-predicted failure strains in real material, Tvergaard (1981) as an attempt to correct this discrepancy, added two adjustable parameters, q_1 and q_2, resulting the following equation:

$$\Phi = \left(\frac{\sigma_{eq}}{\sigma_y}\right)^2 + 2q_1 f^* \cdot \cosh\left(\frac{3q_2\sigma_m}{2\sigma_y}\right) - \left[1 + q_1^2 (f^*)^2\right] = 0 \qquad (2.9)$$

Later on, Tvergaard and Needleman (1984) introduced the function $f^*(f)$ in an effort to account for void coalescence of cavities, since the initial Gurson model could only simulate void nucleation and dilatation. The function $f^*(f)$ was chosen as:

$$f^*(f)=\begin{cases} f & for \quad f \le f_c \\ f_c - \dfrac{f_u^* - f_c}{f_f - f_c}(f - f_c) & for \quad f > f_c \end{cases} \tag{2.10}$$

If $q_1 = q_2 = 1$ then equation (2.9) reduces to (2.6). For a moderate strain hardening material, Tvergaard (1982a) and Tvergaard (1982b) found that $q_1 = 1.5$ and $q_2 = 1.0$ brought the Gurson continuum model in close agreement with micromechanical model results. Koplin and Needleman (1988) performed similar studies paying particular attention to void growth and coalescence, and their improved agreement were for $q_1 = 1.25$ and $q_2 = 1.0$. These first analyses were carried out on moderate hardening materials and although the above q values have been widely adopted in the literature, other q values for high hardening materials have been suggested by Brocks et al. (1995), Faleskog et al. (1998), Gao et al. (1998) and Kim et al. (2004). These works demonstrated that the parameters q_1 and q_2 are critical for the correct modelling of the void growth process. A major disadvantage of the revised Gurson-Tergaard-Nedelman (GTN) model is that it contains numerous adjustable parameters. Although the GTN model (and its subsequent modifications) may adequately characterize plastic flow in the early stages of the ductile fracture process, it does not provide a good description of the events that lead to final failure.

Recently the original and the extended GTN model, as other models, has been further extended using an anisotropic effective stress, $\bar{\sigma}$, instead of the von Mises stress σ_{eq}. Various expression of $\bar{\sigma}$ can be used. Doege et al. (1995) suggested leaving equation (2.6) unaltered but defining σ_{eq} as the Hill equivalent stress model σ_H (Hill, 1950)

$$\sigma_H = \sqrt{\tfrac{3}{2}\underline{s} : \underline{\underline{H}} : \underline{s}} \tag{2.11}$$

where $\underline{s}$ is the stress deviator and $\underline{\underline{H}}$ the Hill anisotropy fourth order tensor. When writing σ_H in base of the anisotropy principal axes:

$$\sigma_H^2 = \frac{3}{2}\left(h_1 s_{11}^2 + h_2 s_{22}^2 + h_3 s_{33}^2 + 2h_4 s_{12}^2 + 2h_5 s_{23}^2 + 2h_6 s_{31}^2\right) \tag{2.12}$$

where $h_1 \ldots . h_6$ are the coefficients describing the anisotropy and s_{ij} are the components of the stress deviator expressed in the orthotropic frame. Similar to the extension of Doege, Rivalin et al. (2001) and Grange et al. (2000) used the Hill model to extend to anisotropic case the equation (2.9). These modifications of the original and the extended Gurson model only affect the contribution of deviatoric stresses on the potential definition. The role of pressure (σ_m) in the modified potential remains the same in the damage model. Damage is still assumed to be isotropic.

In order to provide a micromechanical foundation to the previous phenomenological extension, following the method used by Gurson (1977a) a yield surface for a plastically anisotropic material described by the Hill quadratic criterion has been derived by Benzerga (2000) and Benzerga and Besson (2001). Cavities are still assumed to remain spherical. The new equation for the yield surface is written as:

$$\Phi = \frac{\sigma_H^2}{\sigma_y^2} + 2f\cosh\left(\frac{1}{h}\frac{\sigma_{kk}}{\sigma_y}\right) - 1 - f^2 = 0 \tag{2.13}$$

where h is a function of $h_1 \ldots h_6$:

$$h = \left[\frac{8}{5}\frac{h_1 + h_2 + h_3}{h_1 h_2 + h_2 h_3 + h_3 h_1} + \frac{4}{5}\left(\frac{1}{h_4} + \frac{1}{h_5} + \frac{1}{h_6}\right)\right]^{1/2} \tag{2.14}$$

Recently Benzerga et al., (2004) has proposed a potential including both sources of anisotropy, that due to matrix plastic anisotropy and that corresponding to cavity shape. One outcome of

using the developed constitutive relations is a loading response that includes the transition from a pre-coalescence stage to a post-coalescence stage without using adjustable factors. Another modification for the GTN damage model to extend it to plastic anisotropy has been suggested by Luu et al. (2006). This modification is the same that the one used in Rivalin et al. (2001), only affecting the contribution of deviatoric stresses on the potential definition. The damage behaviour is still assumed to be isotropic. In this proposed extension by Luu et al. (2006), σ_{eq} is defined as the model proposed by Bron and Besson (2004), (equations 2.20-25). One result of using this modified damage model is to simulate accurately the anisotropic behaviour, which was not well represented by von Mises for a high strength pipeline steel.

2.3.5 Rousselier Model

Another consistent ductile damage theory was introduced by Rousselier (1987) following the work of Lemaitre (1985). This damage theory was developed based on thermo-dynamical considerations. The plastic potential in this model has the form:

$$\frac{\sigma_{eq}}{\rho} - H\left(\varepsilon_{eq}^{p}\right) + B(\beta) D \exp\left(\frac{\sigma_m}{\rho\sigma_1}\right) = 0 \tag{2.15}$$

Where

$$\dot{\beta} = \dot{\varepsilon}_{eq}^{p} D \exp\left(\frac{\sigma_m}{\rho\sigma_1}\right) \tag{2.16}$$

$$\rho(\beta) = \frac{1}{1 - f_0 + f_0 \exp^{\beta}} \tag{2.17}$$

$$B(\beta) = \frac{\sigma_1 f_0 \exp\beta}{1 - f_0 + f_0 \exp\beta} \tag{2.18}$$

β is a scalar damage variable. Its evolution is determined by the equation (2.16). While material is within elasticity limits $\beta = 0$. B is the damage function, ρ is a dimensionless density, D and σ_1 are material constants, f_0 is the initial void volume fraction and $H\left(\varepsilon_{eq}^{p}\right)$ is a term describing the hardening properties of material.

As in the Gurson model and its extensions, there have been some models aimed at exploring how far the Rousselier approach is capable of incorporating plastic anisotropy into the constitutive equations. Benzerga (2000) suggested extending the original Rousselier damage model (equation 2.15) to plastic anisotropy introducing the Hill model instead of the equivalent von Mises stress. In this extended model it was pointed out that there is no actual coupling between ductile damage and plasticity. The treatment of the spherical cavities of the plastic potential is then similar to the isotropic case. Benzerga considered that when plasticity is anisotropic then the scalar variable β should be associated with some weighted mean stress $\sigma_h = \underline{\underline{J}}_h : \underline{\underline{\sigma}}$ instead of σ_m. The weighting tensor takes the form $\underline{\underline{J}}_h = X_i \underline{\underline{e}}_i \otimes \underline{\underline{e}}_i$ and its components fulfil $\sum_i X_i = 1$ for any kind of plastic orthotropy.

Recently an extended Rousselier model by Tanguy and Besson (2002) has been used by Bron and Besson (2006) in order to account the plastic anisotropy of the material in thin sheets of aluminium alloy. The modification of Tanguy and Besson (2002) is similar to that already proposed in the case of extended Gurson model by Rivalin et al., (2001). In this model the damage remains isotropic; therefore a model that incorporates rupture anisotropy will be necessary.

The yield function model is given by:

$$\Phi = \frac{\sigma_a}{(1-f)\sigma_*} + \frac{2}{3} fD \exp\left(\frac{q}{2}\frac{\sigma_m}{(1-f)\sigma_*}\right) - 1 = 0 \qquad (2.19)$$

where f is the variable to account the softening and failure, σ_* is the effective stress, D and q are material parameters which need to be adjusted from the experiments, and σ_a is that of the anisotropic yield function proposed by Bron and Besson (2006), which is an extension of Karafillis and Boyce (1993) yield function. It is defined by:

$$\sigma_a = \left(\alpha \left(\Psi^1 \right)^{a/b^1} + (1-\alpha) \left(\Psi^2 \right)^{a/b^2} \right)^{1/a} \tag{2.20}$$

$$\Psi^1 = \frac{1}{2} \left(\left| S_2^1 - S_3^1 \right|^{b^1} + \left| S_3^1 - S_1^1 \right|^{b^1} + \left| S_1^1 - S_2^1 \right|^{b^1} \right) \tag{2.21}$$

$$\Psi^2 = \frac{3^{b^2}}{2^{b^2} + 2} \left(\left| S_1^2 \right|^{b^2} + \left| S_2^2 \right|^{b^2} + \left| S_3^2 \right|^{b^2} \right) \tag{2.22}$$

where $S_{1=1-3}^k$ are the principal values of a modified stress deviator $\underline{s}^k$ defined as following:

$$s_{11}^k = \frac{\left(c_2^k + c_3^k \right) \sigma_{11} - c_2^k \sigma_{22} - c_3^k \sigma_{33}}{3}, \qquad s_{12}^k = c_4^k \sigma_{12} \tag{2.23}$$

$$s_{22}^k = \frac{\left(c_3^k + c_1^k \right) \sigma_{22} - c_3^k \sigma_{33} - c_1^k \sigma_{11}}{3}, \qquad s_{13}^k = c_5^k \sigma_{13} \tag{2.24}$$

$$s_{33}^k = \frac{\left(c_1^k + c_2^k \right) \sigma_{33} - c_1^k \sigma_1 - c_2^k \sigma_{22}}{3}, \qquad s_{23}^k = c_6^k \sigma 23 \tag{2.25}$$

a, b^1, b^2 and α are four material parameters that influence the shape of the yield surface but not its anisotropy which is controlled by $c_{i=1-6}^{k=1-2}$. Thereby this yield function has 14 independent parameters.

2.4 CELL MODEL

As stated above, the ductile rupture of steels like those used in gas pipelines occurs via nucleation and void growth associated with the larger inclusions, typically MnS particles. These inclusions act as precursors for void formation and the final fracture take places via one form or other of void linkage. Thus, micro-voids and their related size characteristics are the relevant micro-structural components for the complete modelling of ductile damage analysis.

Rousselier et al., (1989) used an inter-inclusion spacing, l_c, as a critical distance in the local fracture criterion. They estimated the value $l_c = 0.55$ mm from metallographic examination for A508 forging steel. Needleman and Tvergaard (1987) introduced D_0, the initial spacing between particle centres. Later Needleman and Tvergaard (1991) reported $D_0 \sim 0.1 - 0.14$ mm for an unspecified high strength steel.

Some modern steels contain very few or no detectable larger inclusions. Some authors suggested spacing between larger precipitates as a suitable measure of a ductile fracture advance step.

Consequently the term cell model or computational cell (Xia and Shih, 1995; Faleskog and Shih, 1997) is used to introduce to damage mechanic methods the micro-structurally significant size scales into the fracture process zone. A key feature of the computational cell is the modelling of the material in front of the crack as a layer of void-containing cells. Each cell can be a 2D/3D dimensional element chosen to be representative of the mean spacing between the voids. These cells contain a single void of initial volume fraction f_0. Void growth within the cell is driven by the stress and strain averaged over the cell. The material outside the layer of voided cells can be modelled as a conventional elastic-plastic continuum. The fracture process involving the void growth mechanism and the cell model of the material is schematically shown in (Fig. 2.2).

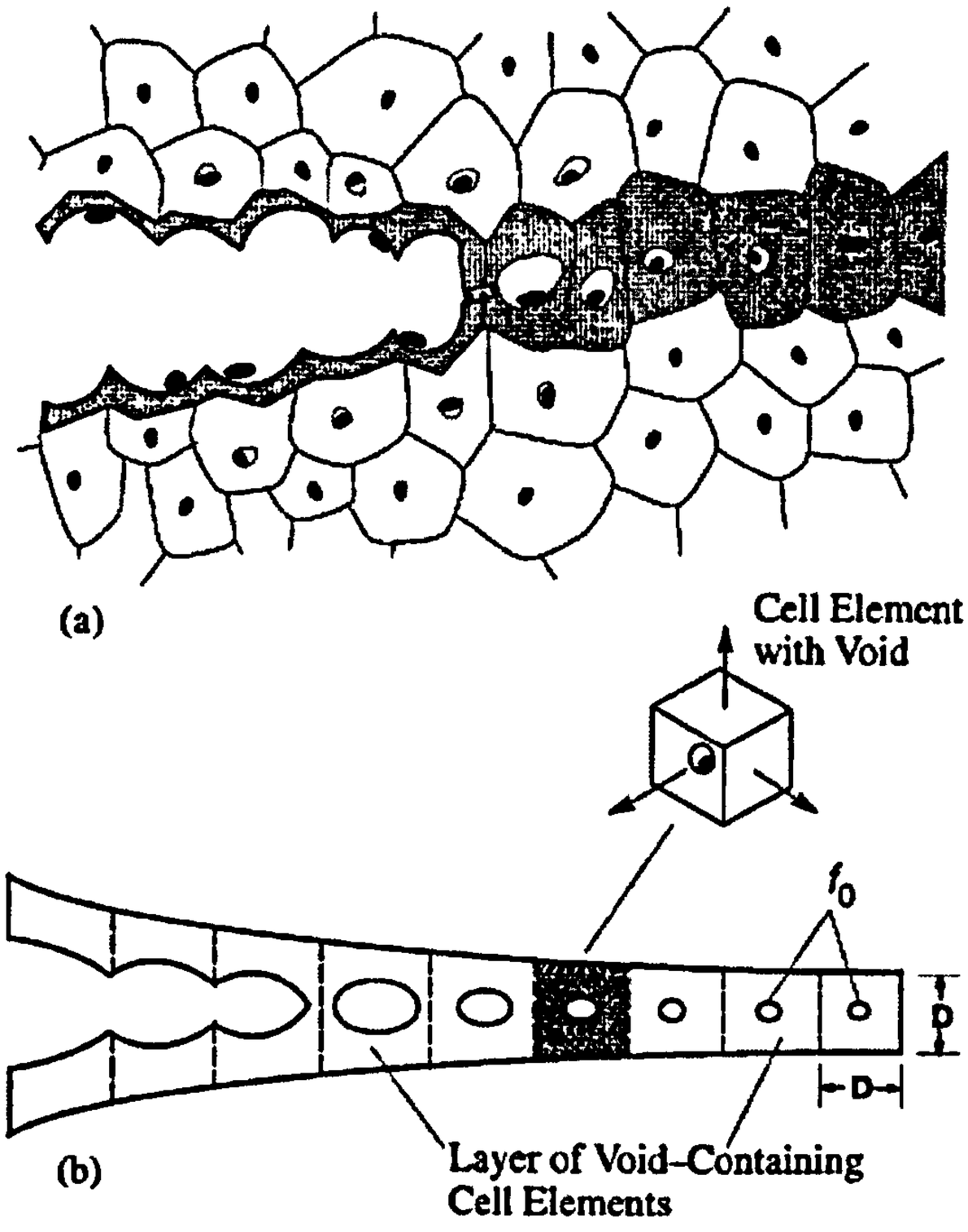

Fig. 2.2 Cell model

2.5 THE COUPLED CELLULAR AUTOMATA – FINITE ELEMENT (CAFE) METHOD

A coupled CA-FE model is an attractive method of creating a mesh independent local approach model of fracture.

In FE analysis the microstructural length scale associated with fracture has been introduced in two ways: The first approach is to associate a damage cell with a finite element in the fracture process zone. This means that finite elements that are located in or near the damage zone have the size of a damage cell. This has been called the local approach by many researches (Howard et al., 1996; Li et al., 1994; Burstow and Howard, 1996; Ruggieri and Dodds, 1996). This deals a mesh dependence of the solution and compromise the ability to model high strain gradients accurately. The other approach is not to associate the finite element size with that of a damage cell but rather introduce additional size related parameters into a fracture model. This leads to a mesh-independent analysis (Bilby et al., 1994; Howard et al. 2000).

The cell model or the local approach to fracture phenomena has been very successful in helping to transfer information derived from testing laboratory specimens to the prediction of crack growth performance of structure. The finite element models for this purpose are constructed with a ruling element size that is appropriate for the physical scale of the dominant failure mechanism. Since these are primarily of the order of the material microstructure, there is a consequential very strong mesh gradient in the area of interest. When applied to engineering structures, which can be large, the resultant finite element models become so big that they can not be run on many computers and when there is more than one material scale involved, the situation becomes impossible to resolve with conventional finite elements.

The Cellular Automata – Finite Element (CAFE) approach does not associate the finite element size with that of a damage cell; there is no mesh dependence of the solution strain analysis from the fracture process. The CAFE model offers solutions in areas where there are conflicting requirements for the mesh size and long computational times (e.g. mixed ductile-brittle fracture). Cellular automata (CA), were first introduced by von Neumann (1966), as idealizations of biological systems. The CA has been used successfully for solidification (Gandin et al., 1999), static recrystallisation (Raabe and Becker, 2000), oxide scale failure modelling (Das et al., 2001, Das, 2002; Das et al., 2003), extending the local approach to fracture (Beynon et al., 2002), transitional of ductile-brittle fracture modelling (Shterenlikht, 2003; Shterenlikht and Howard, 2004) and investigating the effect of spatial heterogeneity on failure in ductile alloys (Khvastunkov and Leggoe, 2004).

The CAFE model used in this research is that implemented by Shterenlikht (2003), which has extended the ideas described in Beynon et al. (2002), Das et al. (2001), Das (2002) and Das et al., 2003). This CAFE approach provides a more realistic description of the process of damage mechanisms than the classic local approach. This promising tool is fast and flexible for multi-scales of fracture mechanisms that can be implemented simultaneously in one computational analysis.

The main idea of the CAFE approach is to separate the structure from the material. This means that finite element analysis is constructed only to represent the macro strain gradients adequately. On the other hand CA arrays of damage mechanisms with appropriate cell size represent the appropriate material behaviour. The flow of information between the FE and CA parts of the model is shown in Fig. 2.3.

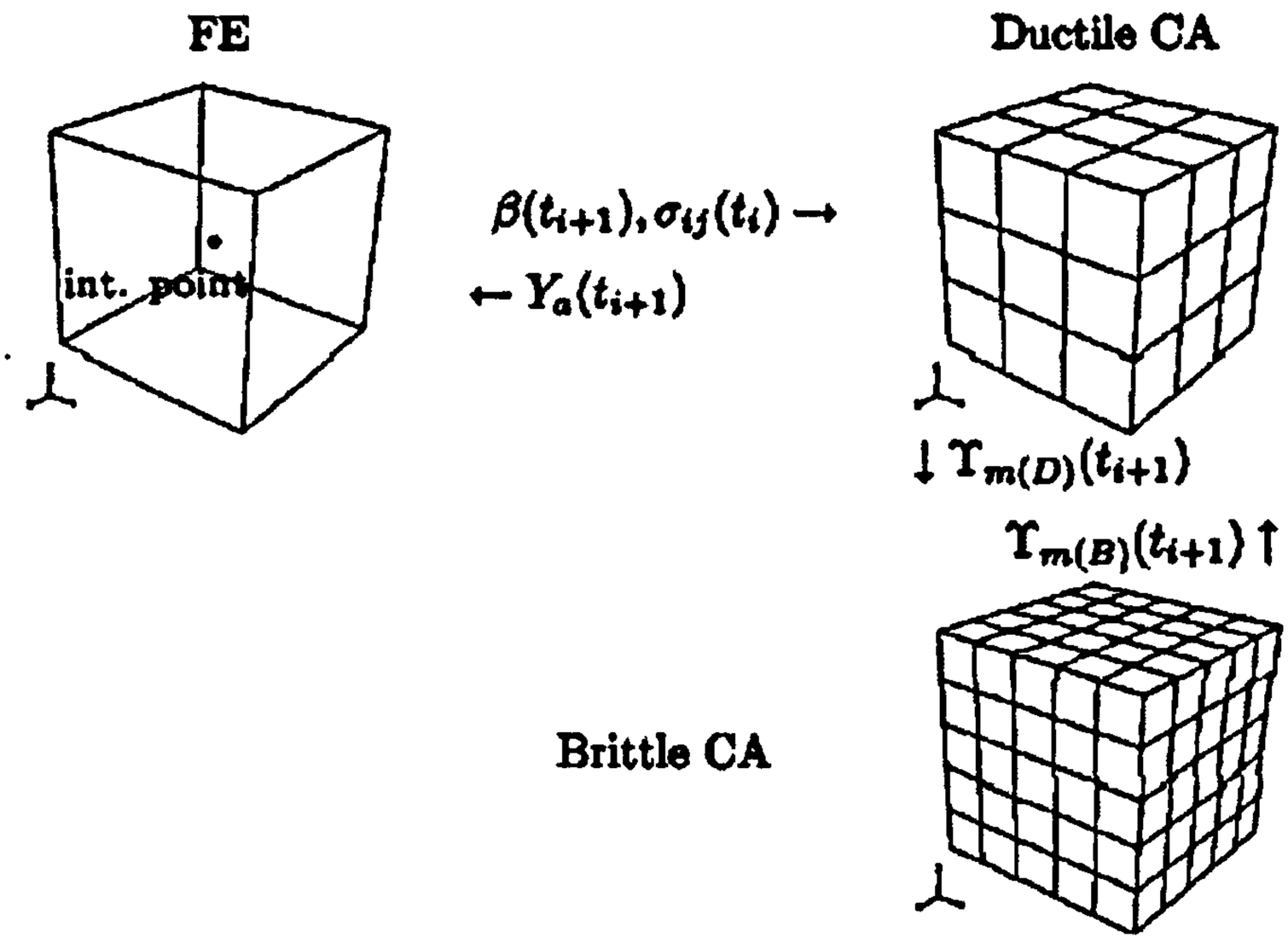

Fig. 2.3 Flow information between the finite element integration point and the ductile and the brittle CA arrays. Shterenlikht (2003).

The general strategy implemented by Shterenlikht (2003) and Shterenlikht and Howard 2004) is that two arrays of CA are connected to the FE in question. The first array is used to simulate the ductile fracture and the Rousselier continuums ductile damage model is used for this, principally because of its combination of simplicity and realism. Brittle fracture is modelled in the other array. A simple criterion is applied for assessing the state of a brittle cell; if the maximum principal stress in a cell exceeds the fracture stress from this cell then this cell is considered dead (inactive). The result of this implementation is presented at the macro (FE) and the micro (CA) scales. The macro scale shows the deformation (shape change) of a model and the macro stress. The results at the micro scale illustrate the progressive "cell by cell" fracture propagation.

In the flow information in CAFE method (Fig. 2.3), according to Shterenlikht and Howard 2004), at each time increment, t_{i+1}, the Rousselier model integration is performed at the finite element integration point producing the new stress tensor, $\sigma_{ij}(t_{i+1})$, and the new damage variable, $\beta(t_{i+1})$. The new damage variable is fed to the ductile CA array and distributed across all cells (microvoids). The FE stress tensor from the previous time increment, $\sigma_{ij}(t_i)$, is used to calculate the maximum principal stress and its direction cosines. These direction cosines define planes in which fracture propagation is most likely.

Each ductile CA cell is assigned a randomly generated critical value of the damage variable at the beginning of the simulation. Thus a simple ductile fracture criterion can be formulated. A ductile CA cell "dies" when its damage variable exceeds the critical value for this cell. The analysis of ductile CA array therefore only consists of checking all ductile CA cells against this fracture criterion. This is a very fast procedure. After all ductile CA cells have been processed, the state of the ductile CA array, $\gamma_{m(D)}$, is mapped over the brittle CA cell array because the two arrays occupy the same physical space and any change of the state in one array has to be visible in the other array.

Similarly to the ductile CA array, a brittle fracture analysis is performed by assessing all brittle CA cells against the brittle fracture criterion. After all brittle CA cells have been processed the state of the brittle CA array, $\gamma_{m(B)}$, is mapped onto the state of the ductile CA array to synchronise their states. Finally the state variables of the FE integration point, $\gamma_a(t_{i+1})$, are calculated and returned back to the FE solver. At present there are two state variables: integrity that is the fraction of alive cells; and the percentage of the brittle phase, that is the ratio of the number of dead brittle cells to the number of dead ductile cells. If integrity falls below a certain limit the FE integration points are considered to have failed and the fracture is assumed to cross the whole of the finite element.

The CAFE model used in this current investigation is suitable for modelling ductile fracture mechanisms in pipeline steel. However, CAFE models can simulate multiple scales of fracture mechanisms in other type of steels like ship steels, pressure vessel steels, nuclear reactor steels and for aluminium materials providing the appropriated material characteristics. It is important to mention that the CAFE method has some limitations for the ductile fracture analysis and it needs to be developed to take into account the following issues: a) The Rousselier continuous damage model in the CAFE structure can only account for volumetric void growth. An additional criterion has to be applied to include an appropriate shear localisation model in the ductile damage model. b) Furthermore, an appropriate anisotropic damage model into the present CAFE structure is needed for the accurate representation of the performance of steels like the X100 tested. There are some works as stated above that have been intended for this issue. The extended Rousselier model by Bron and Besson (2006) and that by Benzerga (2000) maybe could be used in order to account the plastic anisotropy of the material in the CAFE model.

CHAPTER 3

3.1 PIPE CUTTING DESIGNS

The material under investigation was an API X100 grade gas pipeline steel (36" O.D x19mm W.T). To measure the tensile properties in different orientations and the ductile fracture characteristics of the line pipe, various specimens of different geometries were made and tested. To make the specimens, the circumference of a piece of pipe was divided and then cut it into four 90^0 sections with the seam weld taken as the centre of the first segment. One of the plates was flattened by machining to 16mm and then cut up for the test specimens. Fig 3.1 shows a photograph of the plate taken from the original pipe.

Fig. 3.1 Photograph of plates taken from the original X100 pipeline steel

The chemical composition of the material is set out in Table 3.1. This information has been reported by the pipe manufacturer and will be required in the estimation of the initial void volume fraction for this steel.

Table 3.1 Chemical composition of X100 steel

Element	C	Si	Mn	P	S	Cu	Ni	Cr	Mo	Nb	Ti	Al
(wt%)	0.06	0.18	1.84	0.008	0.001	0.31	0.5	0.03	0.25	0.05	0.018	0.036

3.1.1 Pipe cutting schemes for tensile tests in transverse, longitudinal and 45 orientation.

Smooth and notched round tensile bars were taken from the original pipe along two principal directions and one off-axis 45° direction (Longitudinal or rolling "L", transverse "T" and 45° orientation respectively). Three sets of laboratory samples were made with different gauge diameter and notch acuity to achieve different constraint levels in the gauge section of the samples. The end of each specimen was machined flat for a better fit in the test machine hydraulic grips. This also made it possible to identify the orientation in the tested specimens. The orientations and the specifications of the test specimens are shown in Fig. 3.2 and listed in Table 3.2.

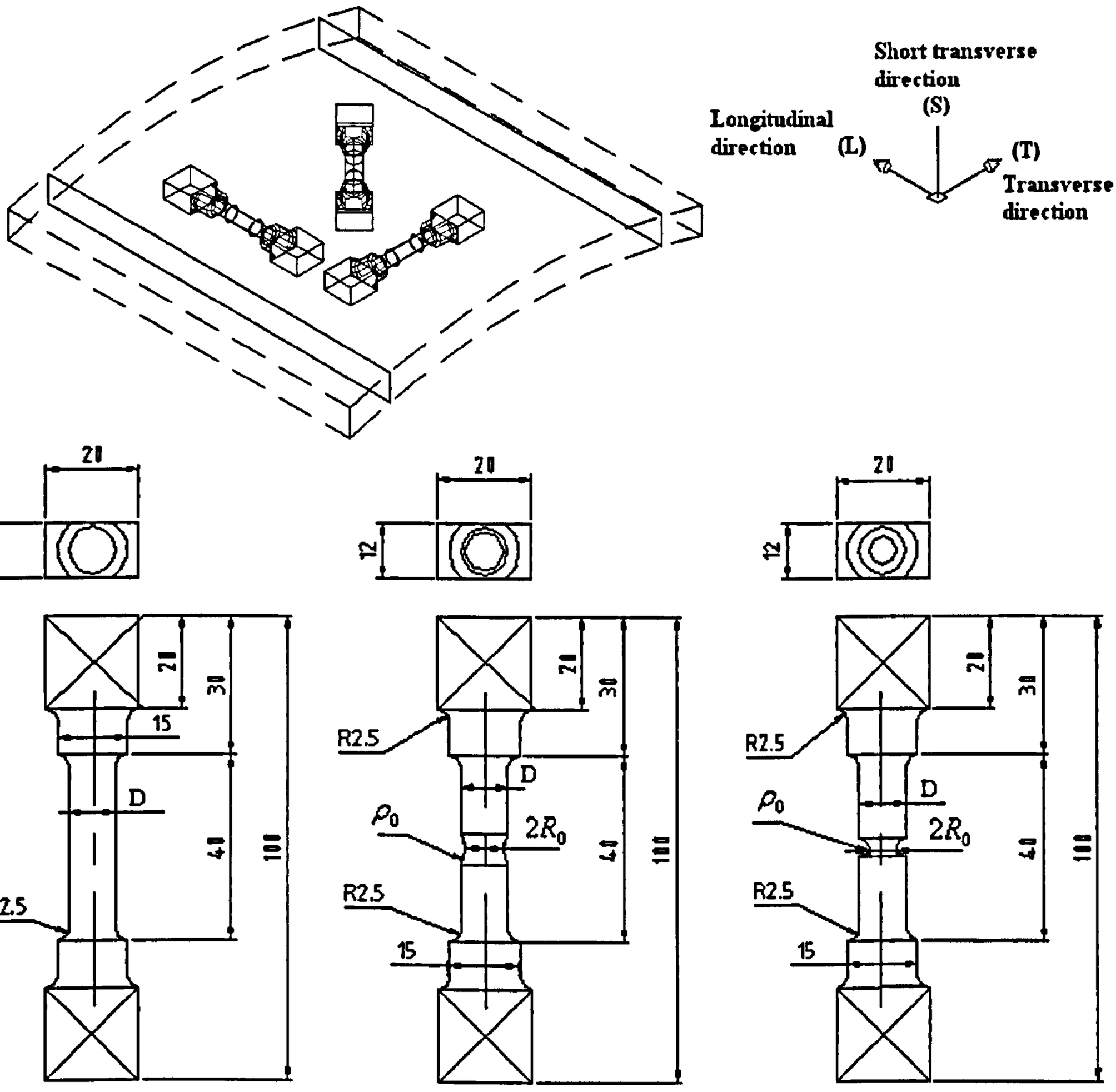

Specimen 1 plain bar
D=10mm

Specimen 2 notch bar
D=10mm, R_0=4mm

Specimen 3 notch bar
D=10mm, R_0=3mm

Fig. 3.2 Orientation and geometry of smooth and notched bar tensile specimens

Table 3.2 Specifications of plane smooth and notched tensile specimens in L, T and 45 direction

Tensile specimen	Number of specimens	Gauge length (mm)	D (mm)	R_0 (mm)	ρ_0 (mm)	R_0/ρ_0 (mm)
Longitudinal direction						
Smooth	6	40	10	-	-	0
Notched – 1st set	6	40	10	4	6	0.7
Notched 2nd set	6	40	10	3	2	1.5
Transverse direction						
Smooth	6	40	10	-	-	0
Notched – 1st set	6	40	10	4	6	0.7
Notched 2nd set	6	40	10	3	2	1.5
45 direction						
Smooth	4	40	10	-	-	0
Notched – 1st set	4	40	10	4	6	0.7
Notched 2nd set	4	40	10	3	2	1.5
Total number of specimens	48					

3.1.2 Pipe cutting schemes and friction welding for tensile tests in thickness orientation

To make the tensile specimens to test the through wall direction properties, cubic pieces (20×20×18 mm in the thickness direction) and round bars ($\phi = 20mm$ and 100mm long) were machined from the pipe. The manufacturing process consisted (Fig. 3.3) of pre-machining the above pieces, then friction welding each sample to steel grip extensions, and finally machining the tensile specimens.

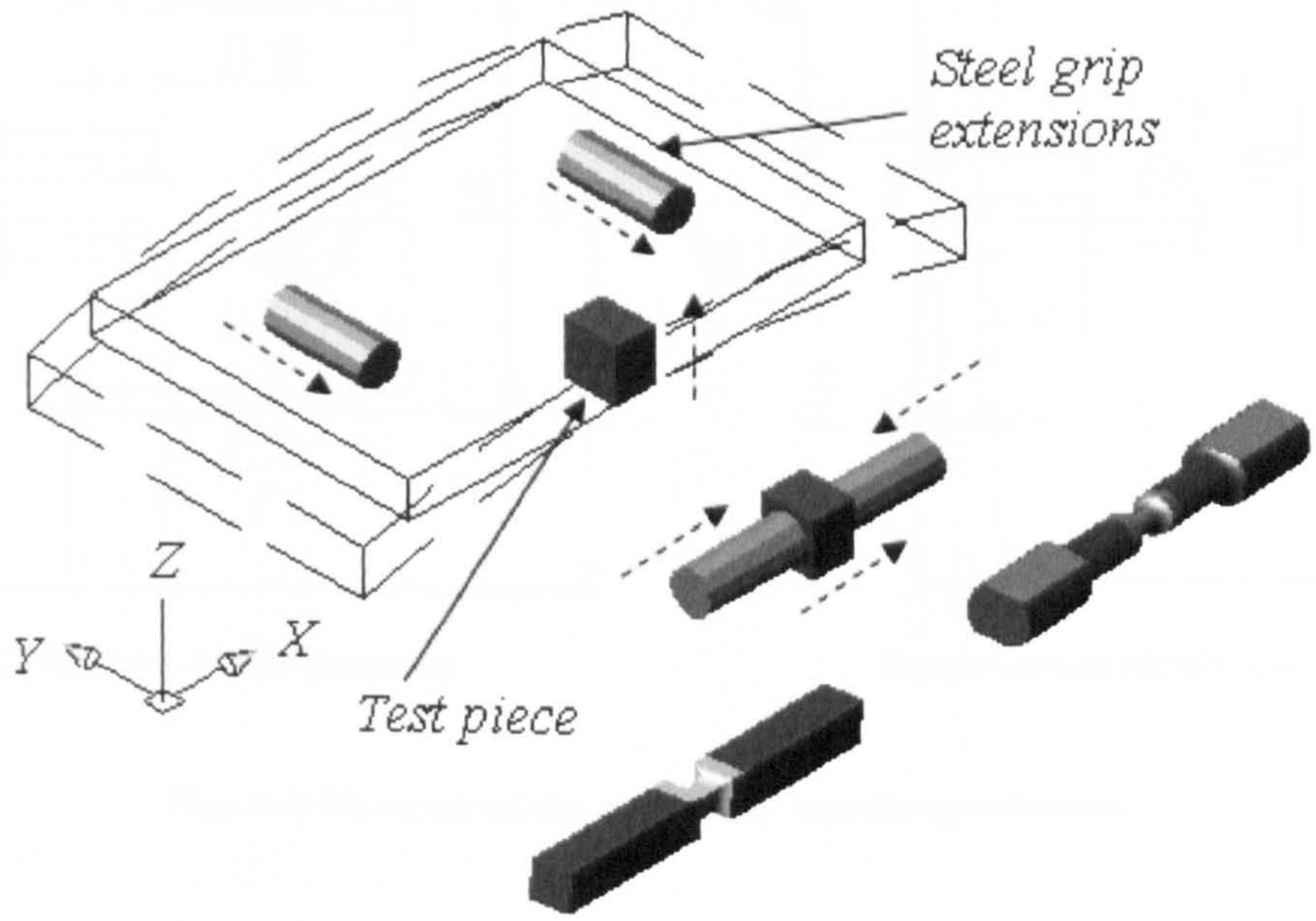

Fig. 3.3 Specimen manufacture process

In addition to the three sets of tensile samples in the L, T, and 45 directions, other two sets of laboratory specimens (cylindrical and square section tensile specimens) were specially designed in thickness orientation (short transverse) "S" to determine the mechanical properties in such direction.

According to the dimensions of the original gas pipe and the requirement of the friction welding process for these tests, the two designs were proposed as can be seen in Fig. 3.4. The cylindrical specimen was designed with a 6mm gauge length and a 5mm gauge diameter, and the square section sample was created with a gauge area of 5×5mm length. Table 3.3 lists the specification of these specimens. Note that two sets of notched tensile tests with same specifications in the gauge section as the previous designs are included.

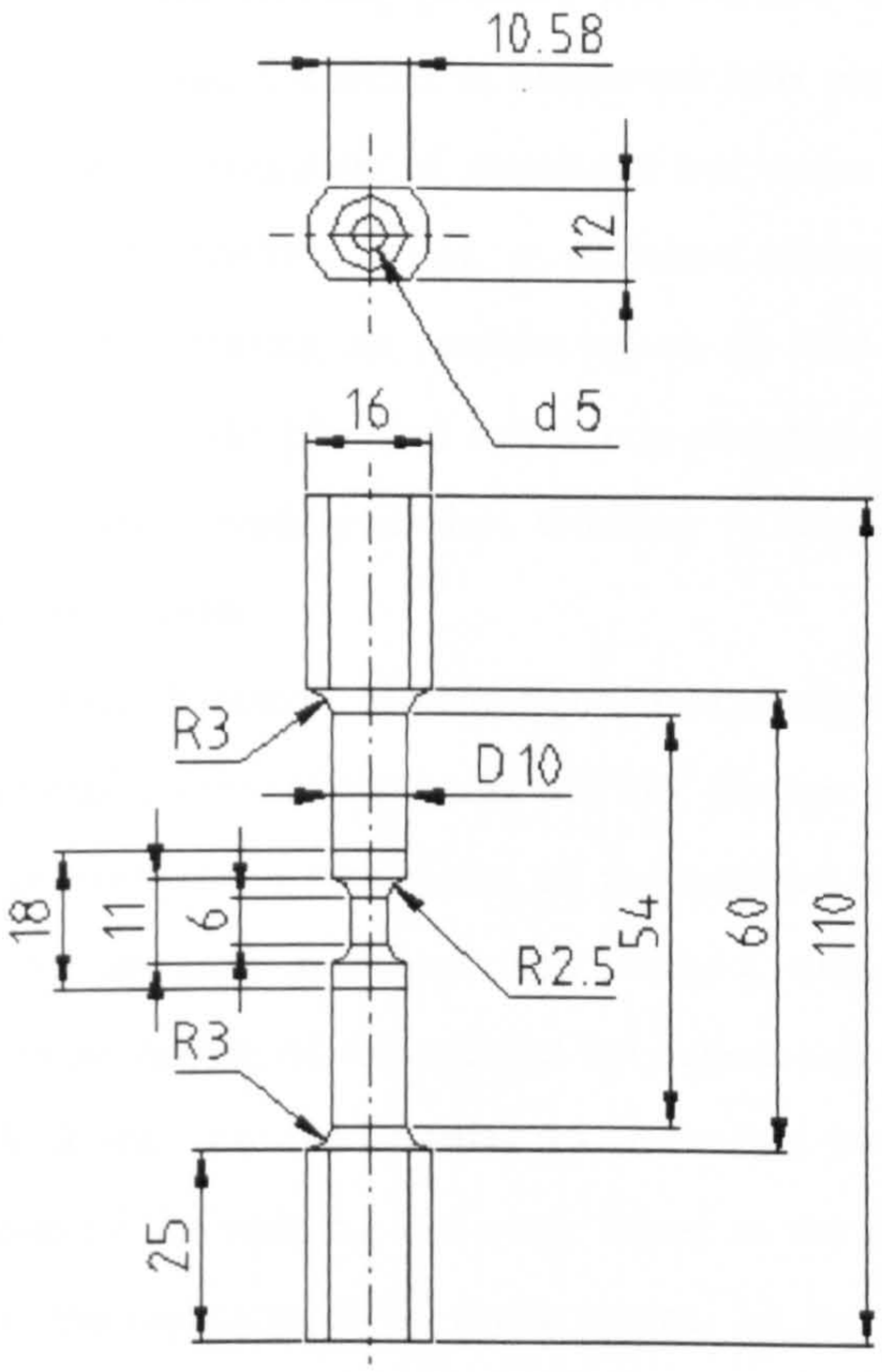

Cylindrical tensile specimen

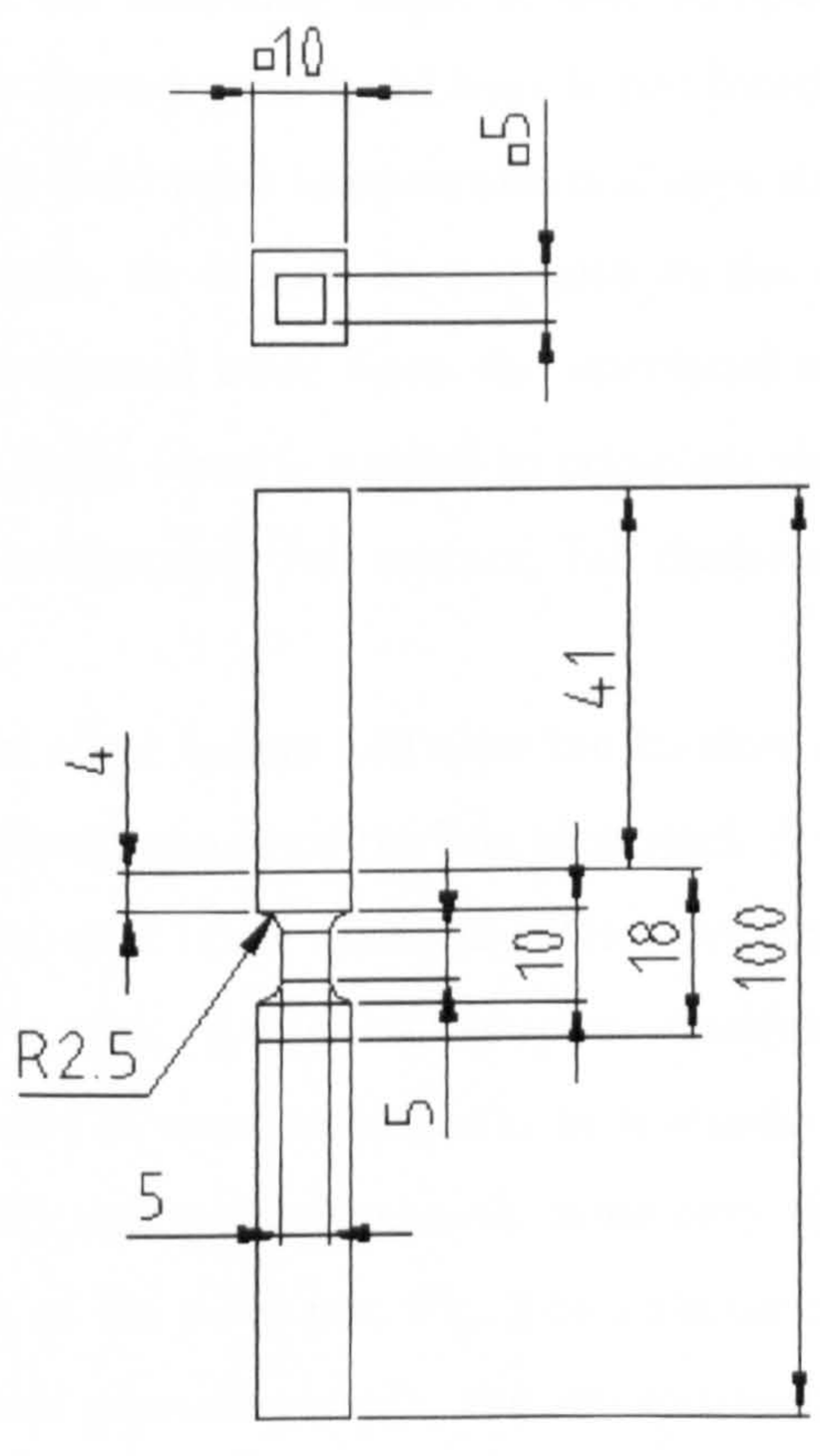

Square section tensile specimen

Fig. 3.4 Designs of the thickness tensile specimens

Table 3.3 Specifications of plane smooth, notched and square section tensile specimens in thickness direction

Tensile specimen	Number of specimens	Gauge length (mm)	D (mm)	R_0 (mm)	ρ_0 (mm)	R_0/ρ_0 (mm)
Smooth and notched specimens in thickness direction						
Smooth	4	6	D=10mm, d=5mm	-	-	0
Notched – 1st set	4	6	10	4	6	0.7
Notched 2nd set	2	6	10	3	2	1.5
Square section tensile specimens in thickness direction						
Square section	6	5	-	-	-	-
Total number of specimens	16					

The friction welding process was carried out in the following steps: a) one component is rotated while the other is advanced into pressure contact with it, b) heat is produced at the surface. Overheating of metal can not occur as the weld zone temperature is always stabilised below the melting point, c) softened material begins to extrude in response to the applied pressure, creating an annular upset, d) heat is conducted away from the interfacial area for forging to take place, e) rotation is stopped and a forge force is applied to complete the weld, f) the joint undergoes hot working to form a homogenous, full surface, full diameter, high integrity weld.

Scanning Electron Microscope (SEM) images were taken before and after the friction welding to confirm that the process did not change the microstructure of the line pipe steel. A welded specimen and a steel piece of the original pipeline were taken randomly. These two samples were ground, polished and etched using 2% nital for metallographic analysis. The microstructure of the welded specimen was revealed in three main zones as is shown in Fig. 3.5. Zone one: the annular upset created by the friction welding process, zone two: the edge close of the welding and zone three: in the centre of the piece test. Fig. 3.6a-f shows in detail the microstructures of those zones. In the original pipeline sample, the microstructure was revealed at the centre (Fig. 3.7).

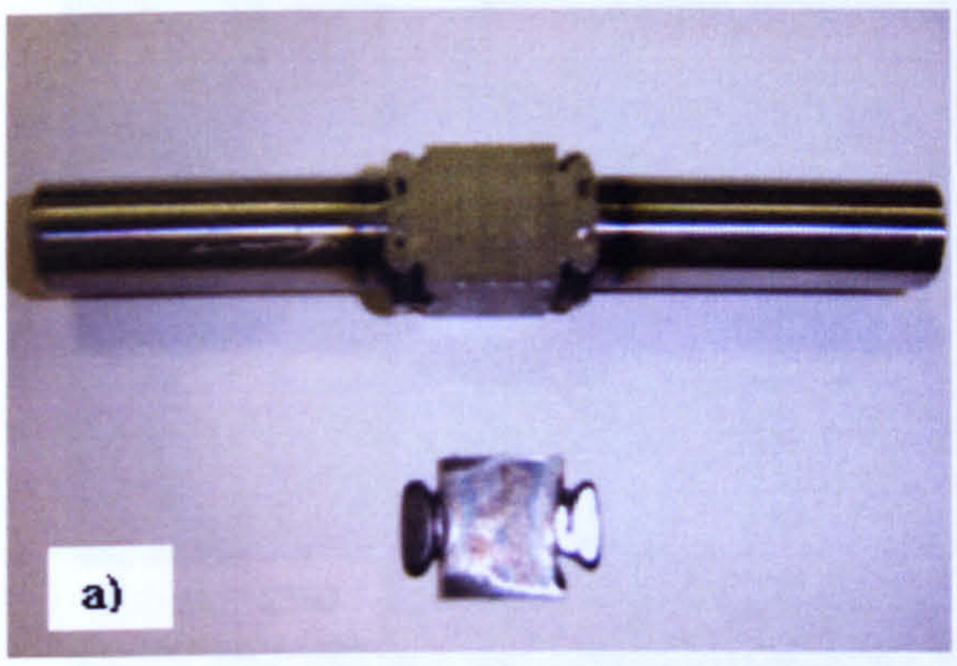

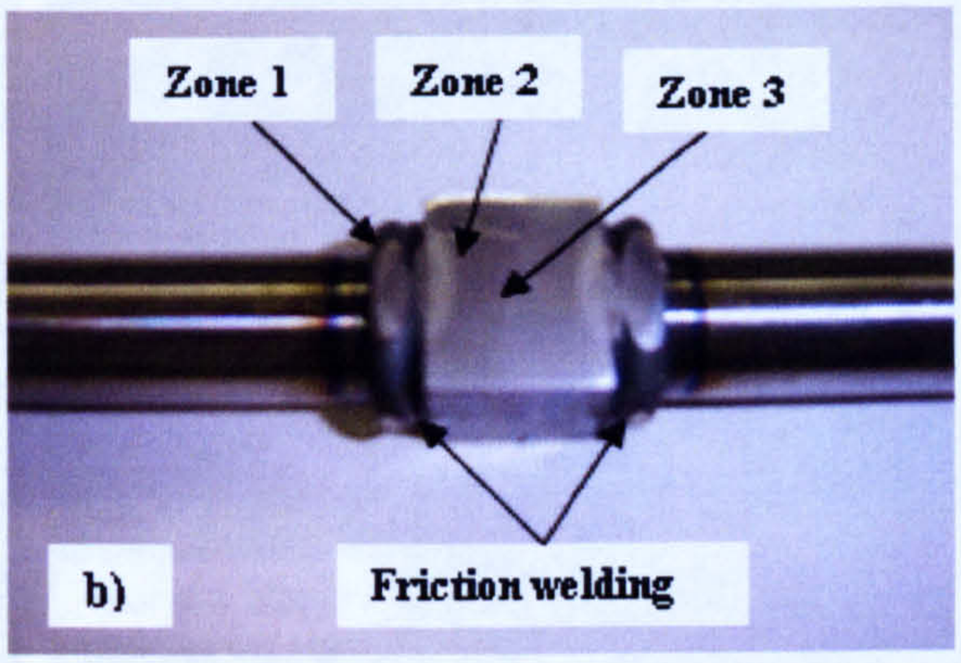

Fig. 3.5 a) Example of the welded specimen and b) the three main zones for the metallographic analysis

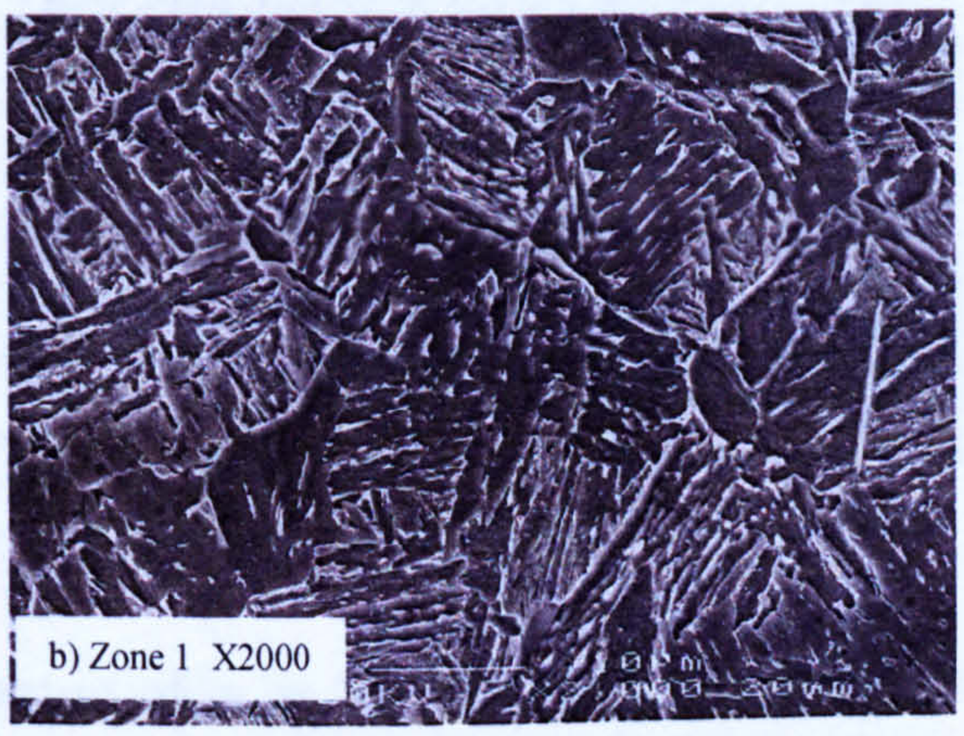

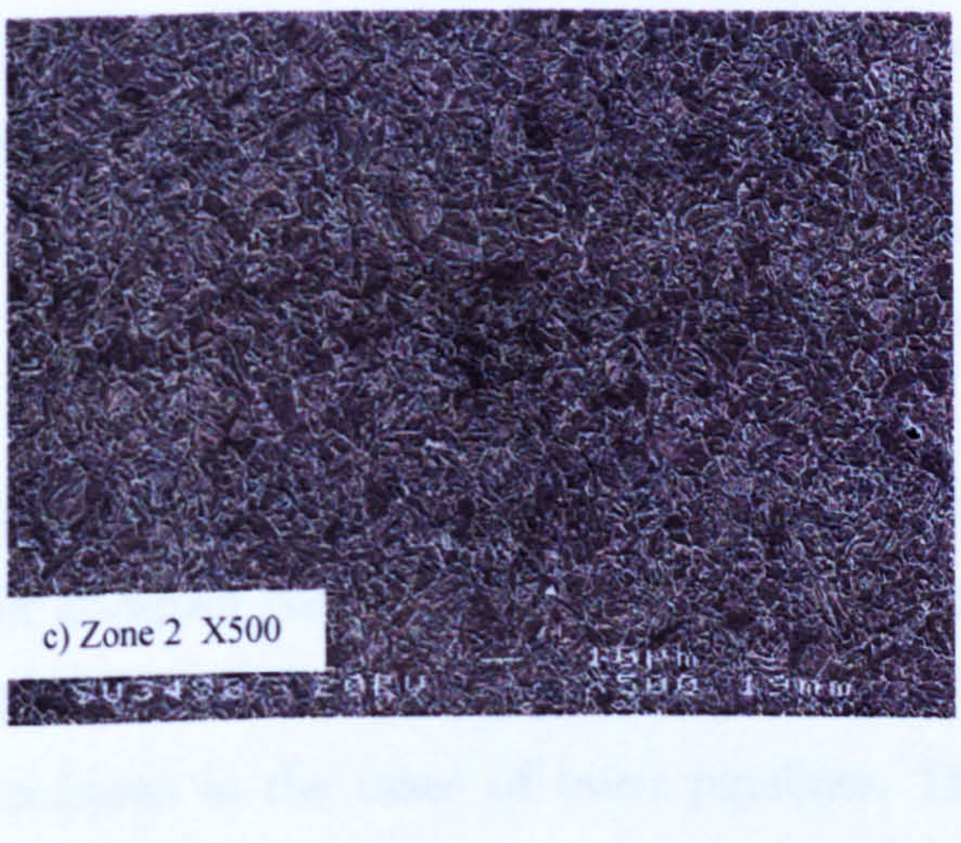

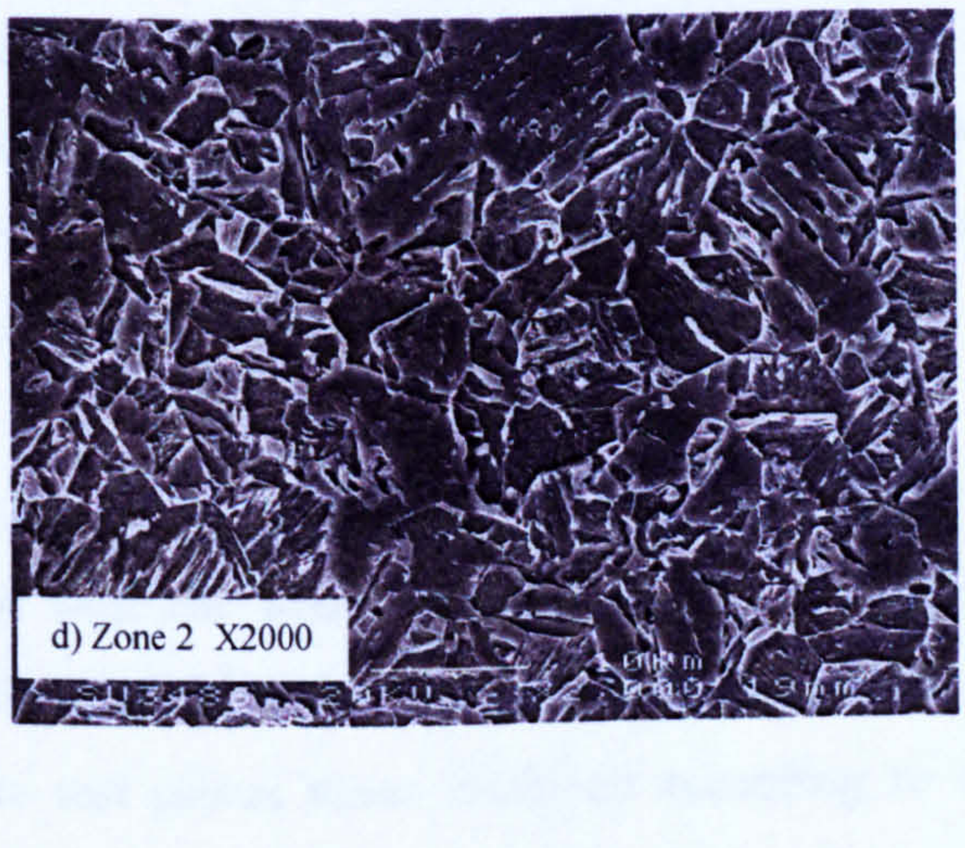

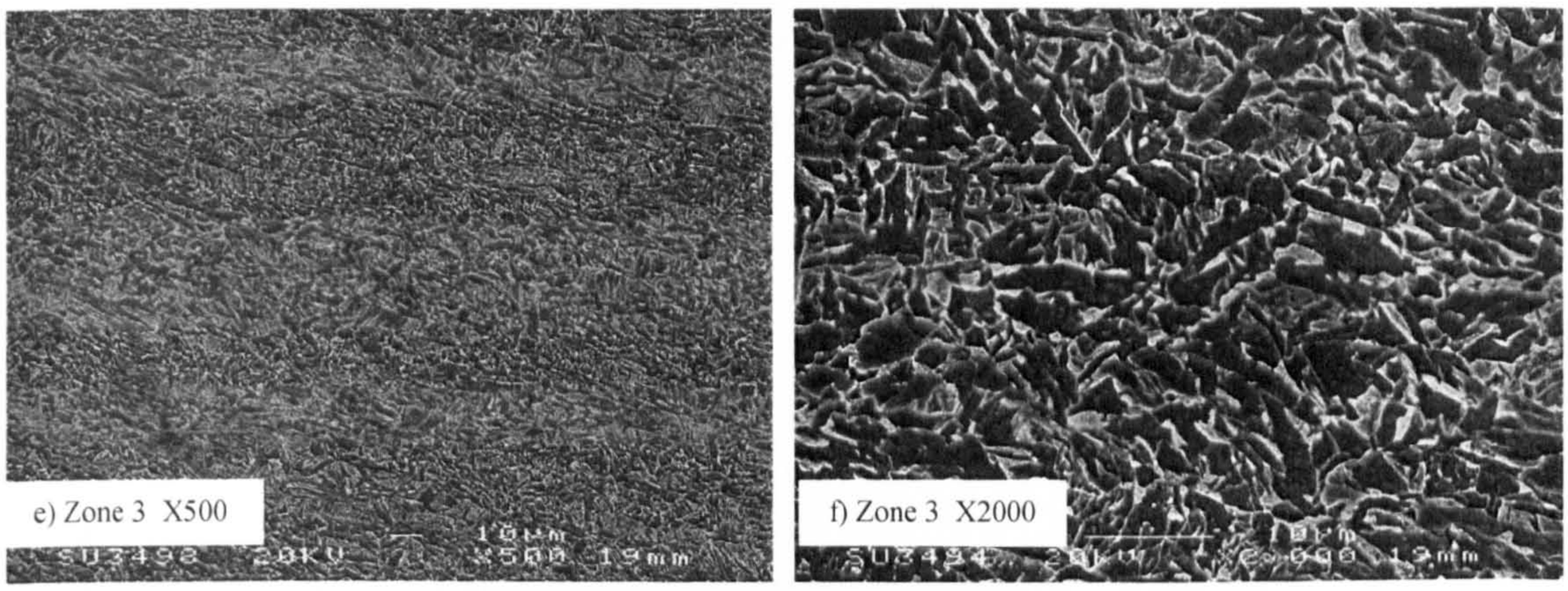

Fig. 3.6 Microstructure of three zones in the welded specimen

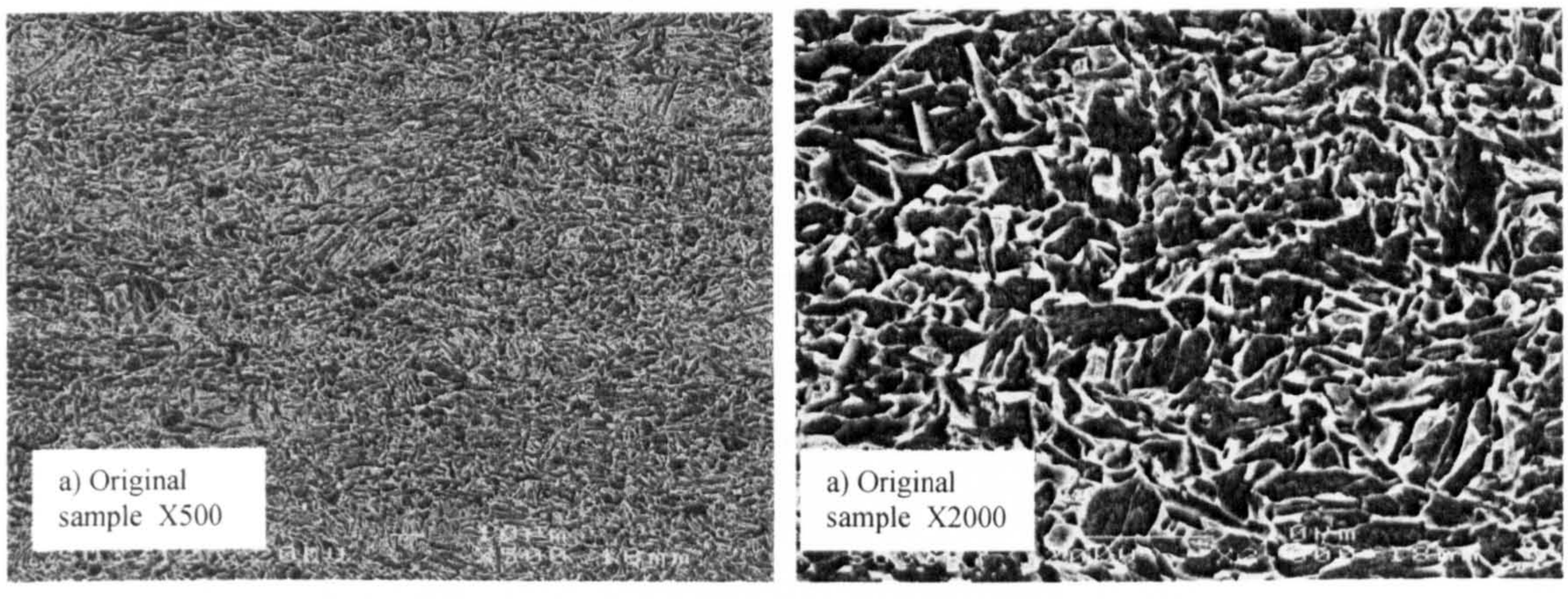

Fig. 3.7 Microstructure of the original pipeline steel sample

The SEM images showed that the microstructure of zone three is similar to the original microstructure, so that the mechanical properties were not affected by change of microstructure in that zone by the friction welding process. The microstructures of zones one and two are different from the original pipeline. However, this is not important as the test area is confined to the centre of the specimen, corresponding to zone three.

3.1.3 Pipe cutting scheme for C(T) specimen.

Six compact tensile specimens were extracted with the initial crack along the longitudinal direction "L" from the pipeline. This is the direction of a fast running shear fracture in real structures in the cases of burst pipelines. The test pieces were machined according to the recommendation of ASTM E-1820 (ASTM 2001). All test samples were side grooved on each side up to 20% of the specimen original thickness to reduce shear lip formation and ensure a

straight crack front. The specimen thickness was 15mm and the relation of initial crack length to specimen width was 0.5. The geometry of the tested specimen is shown in Fig. 3.8

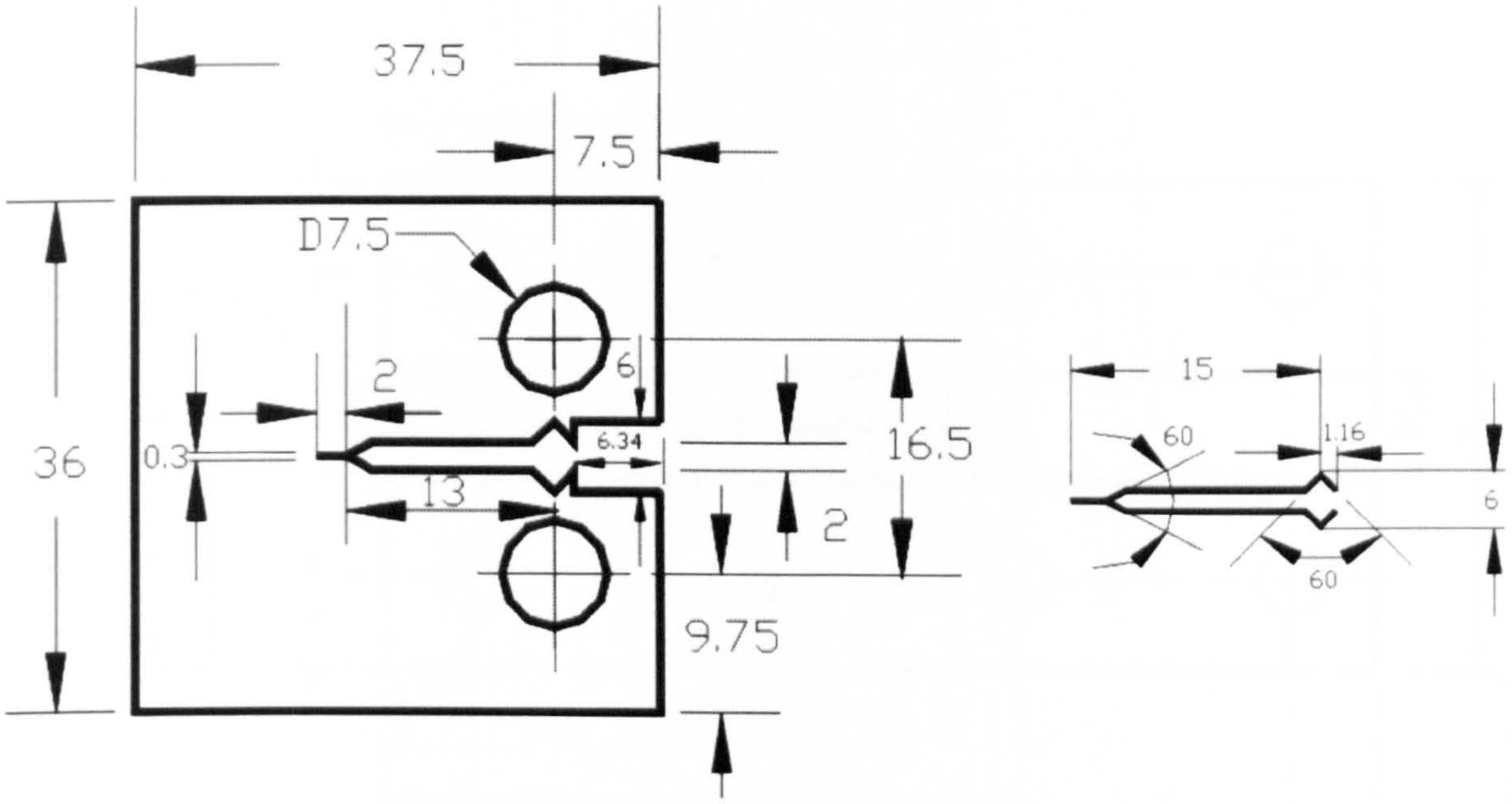

Fig. 3.8 Design specifications of C(T) specimen

3.1.4 Pipe cutting scheme for tear specimen.

Three modified double cantilever beam (DCB) specimens of 8, 10 and 12mm gauge thickness were extracted from the original pipeline with the crack propagating in the longitudinal direction. These design laboratory specimens were chosen because they offer appropriated characteristics to investigate the tearing resistance of running axial cracks in the X100 pipelines in terms of the CTOA criterion. According to previous studies by Shterenlikht et al., 2004 and Hashemi et al., 2004 the specimens have the following features: a) it can be cut directly from a pipe, without flattening, b) high constraint in the test section is introduced by two thicker loading arms, c) it provides large amounts of highly consistent CTOA data even from one experiment and therefore can be regarded as a single specimen CTOA test, d) the stable CTOA values can be estimated from both sides of the specimen, e) from the extensive data set the statistics on the scatter of measured CTOA values can be calculated, and f) an optical technique can be used to determine the CTOA values.

Fig. 3.9 shows the specimen geometry of the 8mm ligament thickness, following the recommendations of Shterenlikht et al., 2004 and Hashemi et al., 2004a.

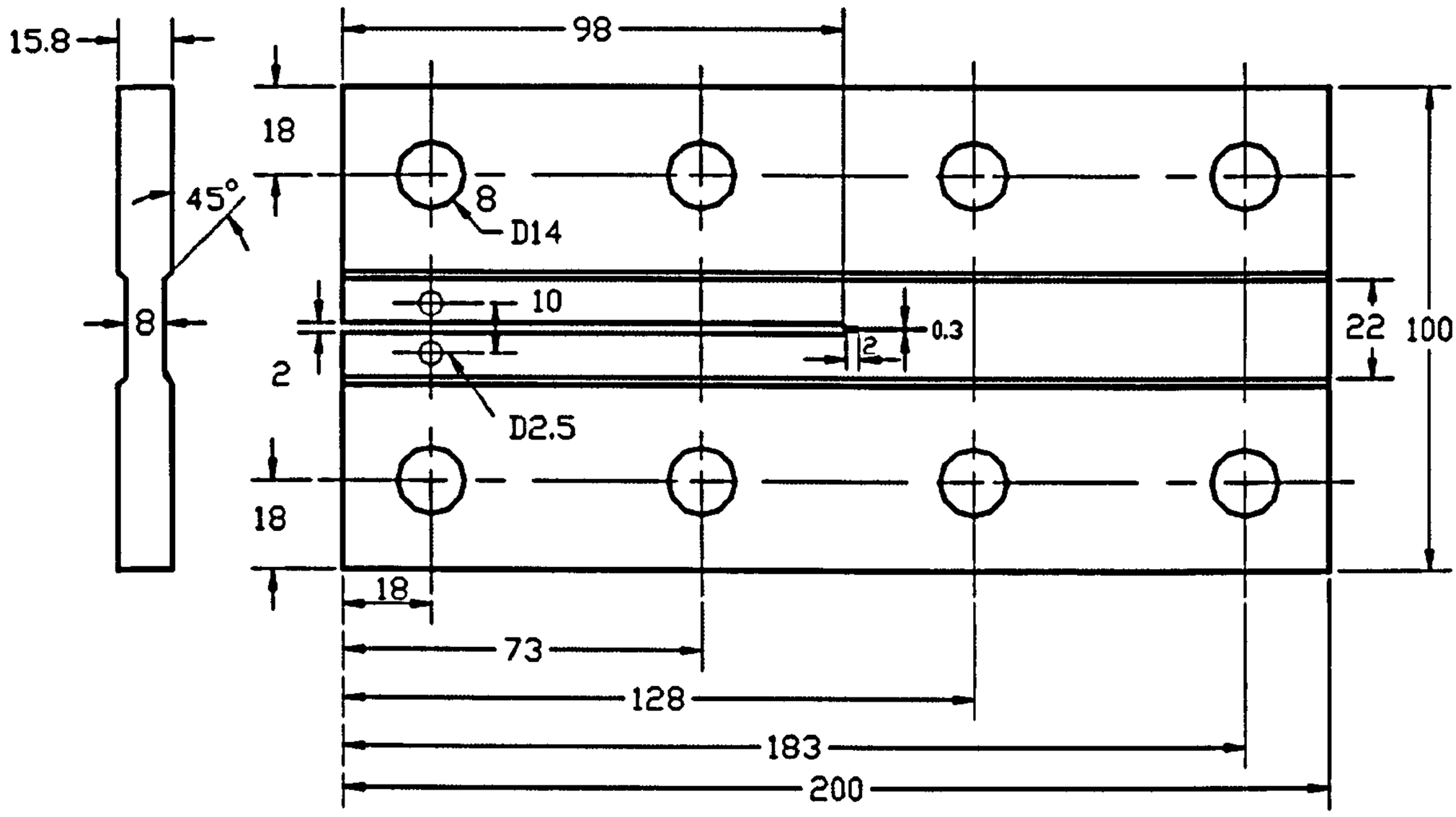

Fig. 3.9 Design specifications of tear specimen

3.2 INSTRUMENTATION SET UP FOR TENISLE AND C(T) SPECIMENS

3.2.1 Instrumentation set up for axial, longitudinal and 45 orientation tensile tests

All cylindrical specimens were loaded in uni-axial tension in a servo-hydraulic Instron 8501 machine under displacement control of 0.01 mm/s. The load, displacement, axial and transverse strains were recorded in each tests. An Instron strain gauge (model 2620-604) and an Epsilon extensometer (model 3575-100-ST) were used to capture the axial and diametral strains respectively (Fig. 3.10).

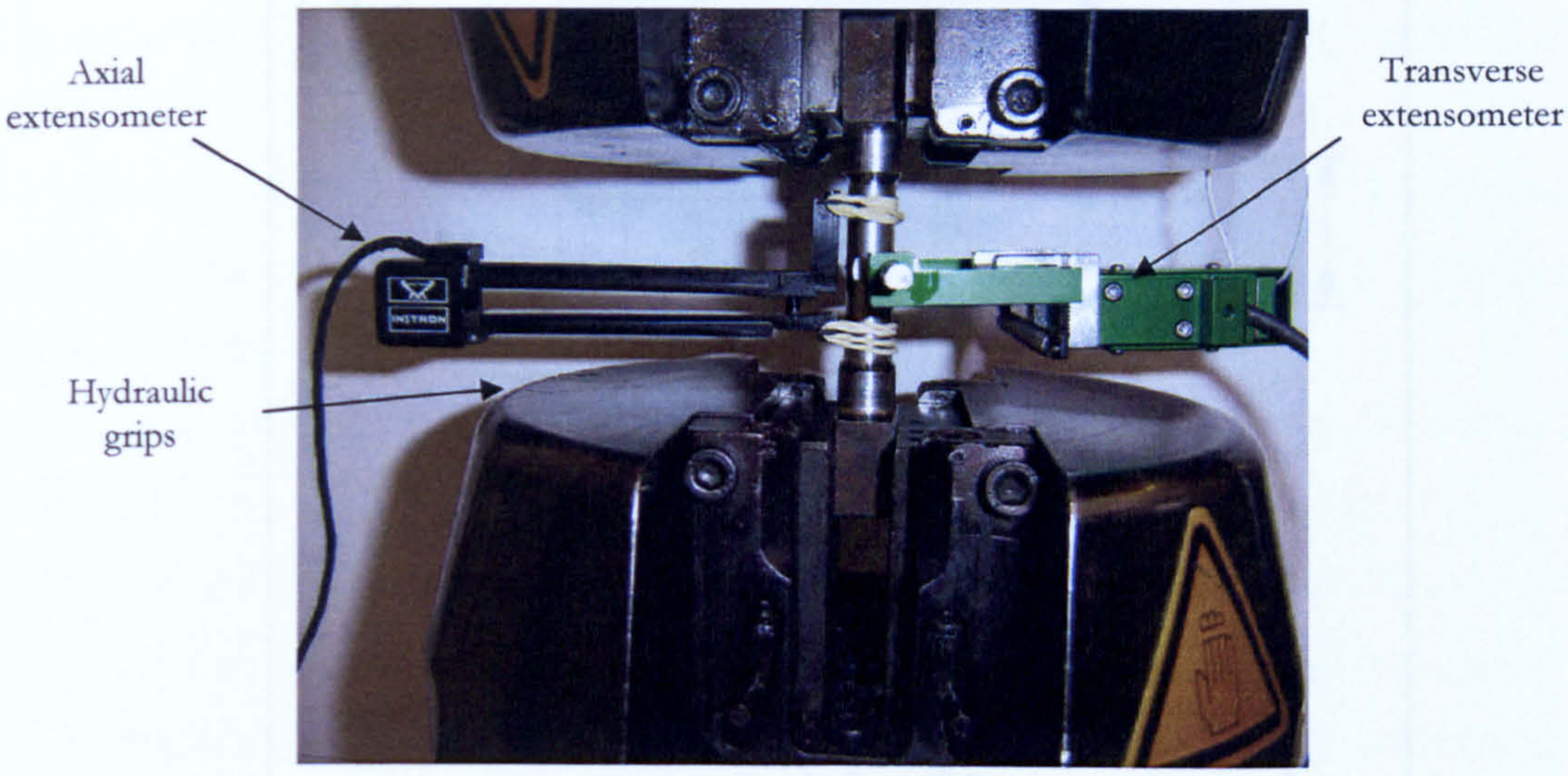

Fig. 3.10 Photograph of tensile experiment set up

3.2.2 Instrumentation set up for short transverse tensile tests

Similar as the tensile specimens tested above, a servo-hydraulic Instron machine 8501 at the same rate of displacement control was used to record the load and displacement data for the thickness tensile specimens. Two methods were used to monitor the deformation during the tensile loading.

Firstly, transverse and axial extensometers were used on cylindrical tension specimens to capture the diametral contraction and axial deformation throughout the loading process. Two grip extensions were designed (See photograph in Fig. 3.11 and design specifications in Fig. 3.12) and calibrated with a dial indicator for the Instron strain gauge (axial extensometer), due the short gauge length of the specimen.

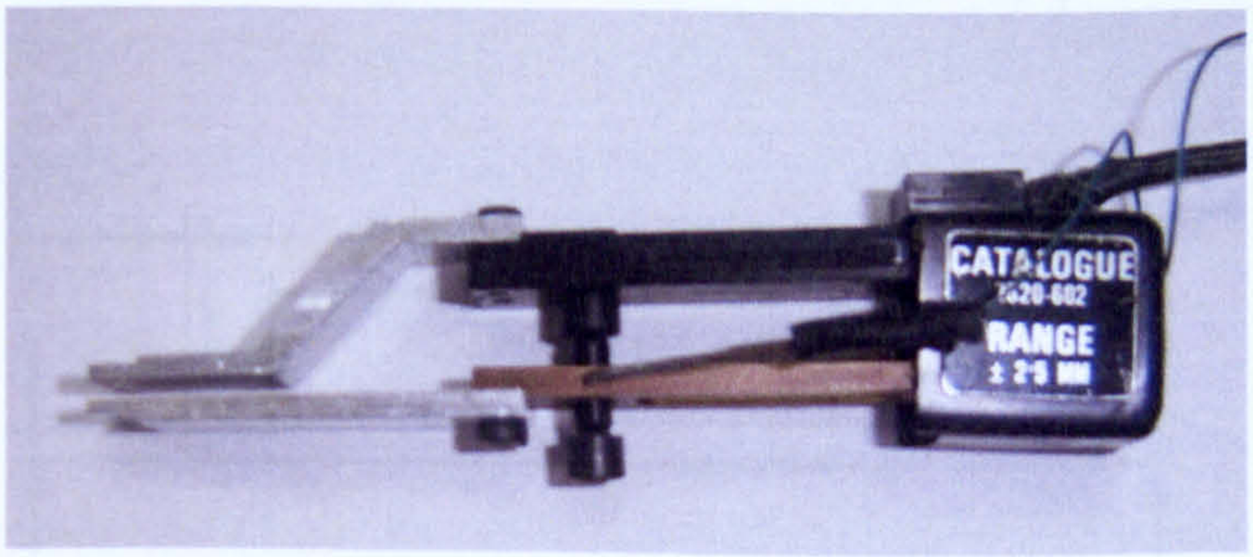

Fig. 3.11 Photograph of grip extensions fixed to the Instron strain gauge

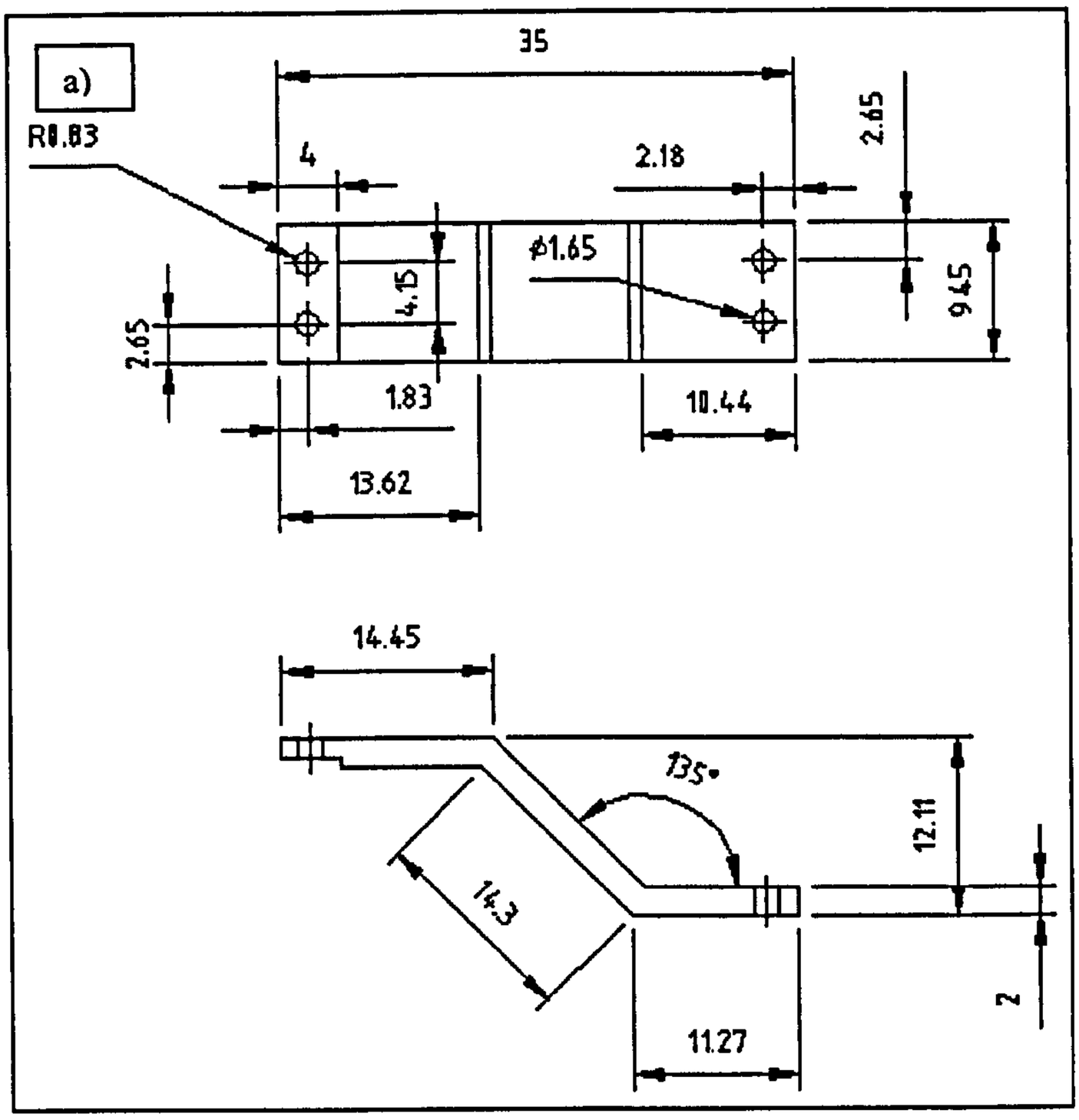

Fig. 3.12 Design specifications of the grip extensions: a) mobile grip and b) static grip for the Instron strain gauge (model 2620-604)

Secondly, the full field map of the deformation of the test material was captured by two optical methods: a fine grid scribed on faces of the square section tensile specimens; and by using digital image correlation (DIC) on a gently abraded surface.

The grid and DIC techniques can be used as non-contacting methods of capturing the longitudinal and transverse strains in a tensile test, including the important necking behavior at the end of the test.

Two gauge areas of the sample were prepared for the measurement of the deformation field (Fig 3.13). For the grid technique, blue spray-paint for metals was applied on one face and a crossed grating pattern was produced on it in a series of well-defined parallel lines of 0.5mm pitch. The fine pitch of the mesh was created carefully with a height gauge equipped with carbide tipped scriber. For the DIC technique another face of the sample was lightly scratched using abrasive paper (grade 120) to provide suitable contrast.

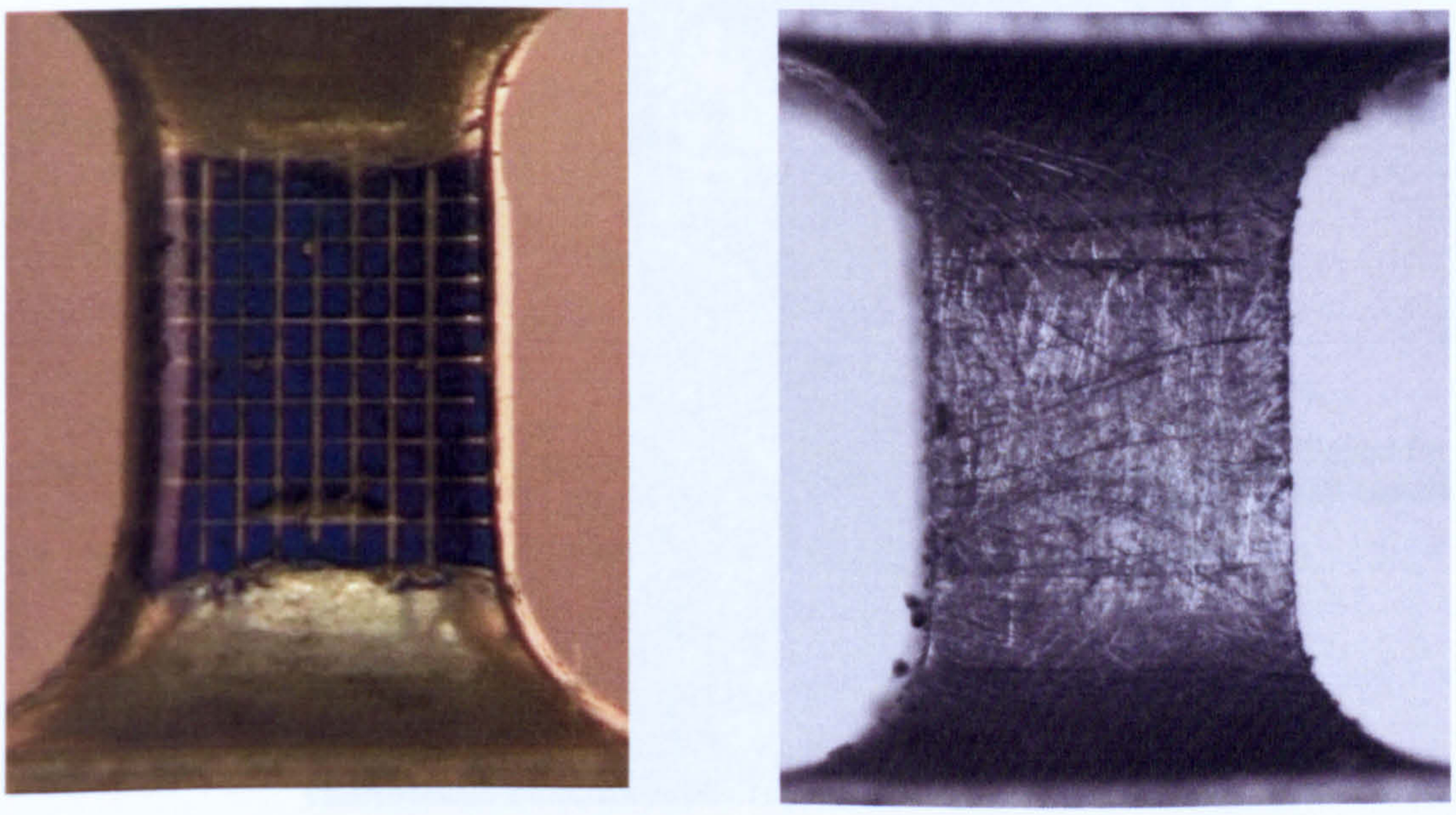

Crossed grating pattern

Scratched surface

Fig. 3.13 Photograph of the prepared gauge areas to measure the full field deformation

The experimental set-up of the grid technique (Fig. 3.14) consisted of a still camera (EOS 20D Canon) and a digital video camera (NV-GS400) fixed at the two perpendicular gauge areas to capture the full displacement field. The gauge surface with the grid pattern was lit by a lamp in order to improve the contrast and consequently the acquisition of the images.

In this laboratory test the load, displacement, and images from the still and video cameras were synchronised at the same starting time of the test. Information on load and displacement was recorded by the controlling computer every two seconds. The video frame and the photographs with a time sequence of six seconds were recorded in another computer. Thus at the end of the experiment, the two computers acquired and stored complete load-time and displacement-time curves, together with the video and photographs of the full field deformation of the specimen.

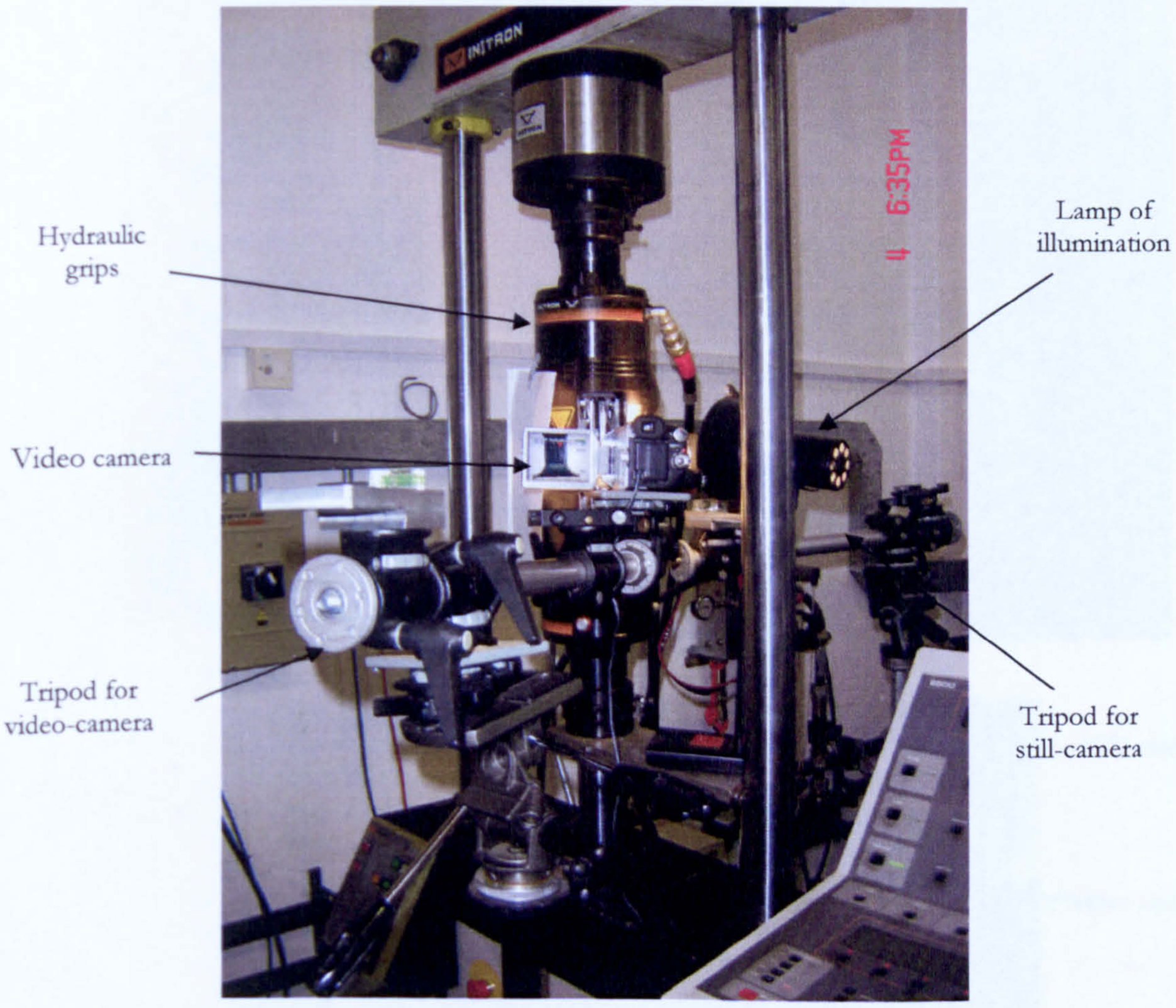

Fig. 3.14 Experimental set up of the grid technique

The acquisition of images for the DIC consisted of a CCD camera directed at the gauge face. When testing the square section tensile specimen for DIC, a digital video camera (NV-GS400) was also fixed to another perpendicular gauge area to monitor the deformation using the grid technique (Fig. 3.15). In this laboratory test the load, displacement, and images from the two video cameras were synchronised at the start of the test. At the end of each experiment, two

computers stored the complete load-time, displacement-time curves and videos of the full field deformation of the specimen.

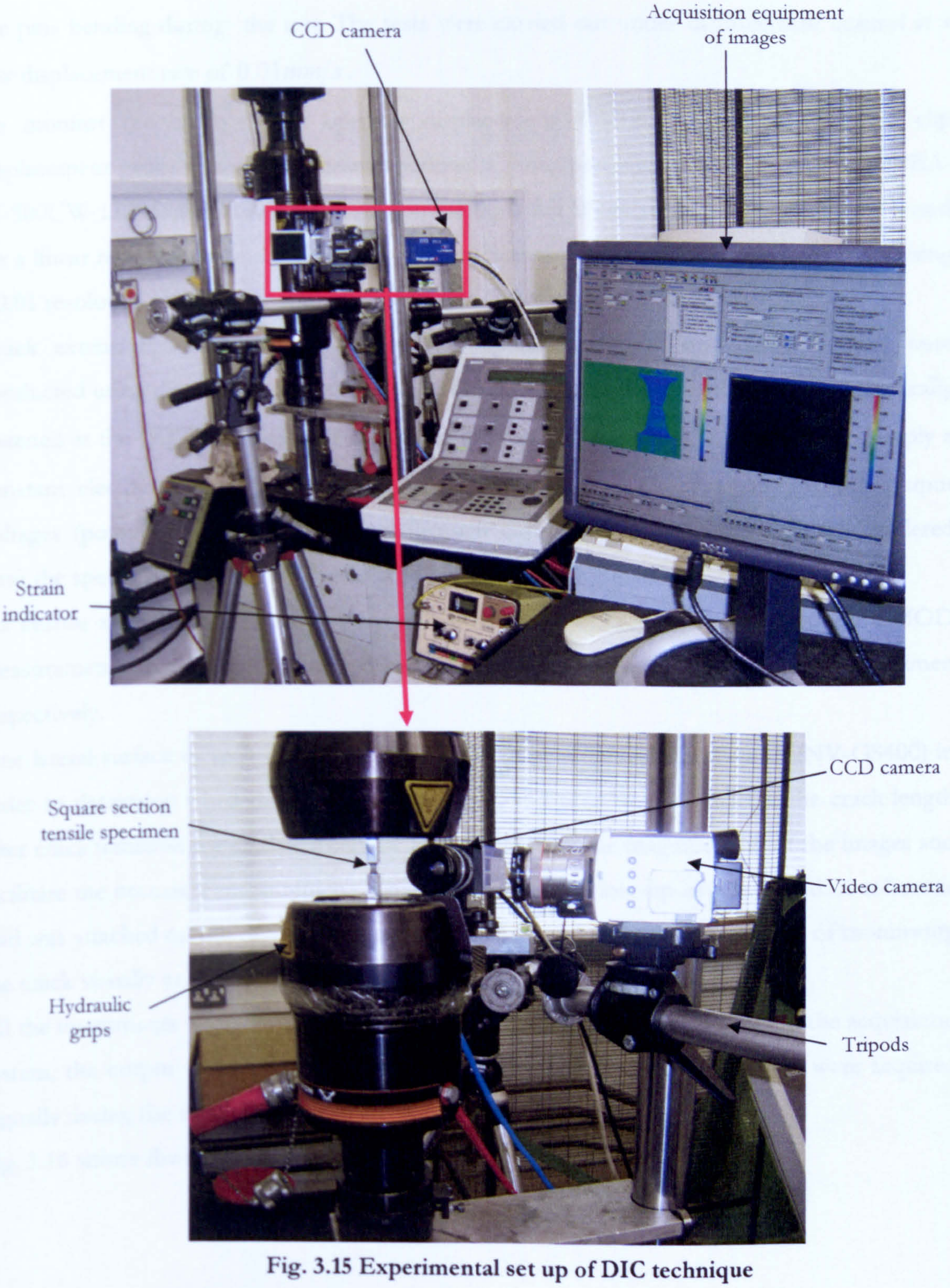

Fig. 3.15 Experimental set up of DIC technique

3.2.3 Instrumentation set up for C(T) specimens (direct current potential drop)

For the flat fracture experiments, six C(T) specimens were tested using loading fixtures on Instron 8501 test machine and loading pins with the same material of the specimens to avoid the pins bending during the test. The tests were carried out under displacement control at a low displacement rate of $0.01 mm/s$.

To monitor the crack mouth opening displacement (CMOD) a double cantilever clip displacement gauge was used in these experiments. Four precision strain gauges (model CEA-06-500UW-120) formed this clip gauge comprising a full Wheatstone bridge. It was calibrated for a linear relationship between voltage and displacement in the range of 4.5 to 14.5mm using a 0.01 resolution micrometer and strain indicator (Vishay model P-3500).

Crack extension measurements of the C(T) specimens under quasi-static loading were conducted using direct current potential drop (DCPD). Current input wires were mechanically fastened at the $W/2$ position with screws on the top and bottom of the samples to supply a constant electric current of 18A to the specimens using a DC power supply. The output voltages (potential drop) were detected through copper wires of 0.7mm diameter soldered onto the specimen mouth and measured by modules of voltmeters.

To ensure signal integrity, the grip assembly of the specimen and clip gauge for CMOD measurement were isolated from the rest of the Instron machine and from the specimen respectively.

One lateral surface of each specimen was monitored by a digital video camera (NV-GS400) in order to determine when the crack starts to grow, and therefore to calculate the crack length after crack initiation for all data using DCPD. To increase the magnification of the images and facilitate the necessary measurement, a high magnification close-up lens was used. A reference grid was attached on the perpendicular surface to the crack growth with the aim of monitoring the crack visually as well.

All the instruments were simultaneously triggered with one switch, and by using the acquisition system, the output voltages, time, load, displacement and CMOD (clip gauge) were acquired digitally during the test.

Fig. 3.16 shows the experimental set up of the CT specimen.

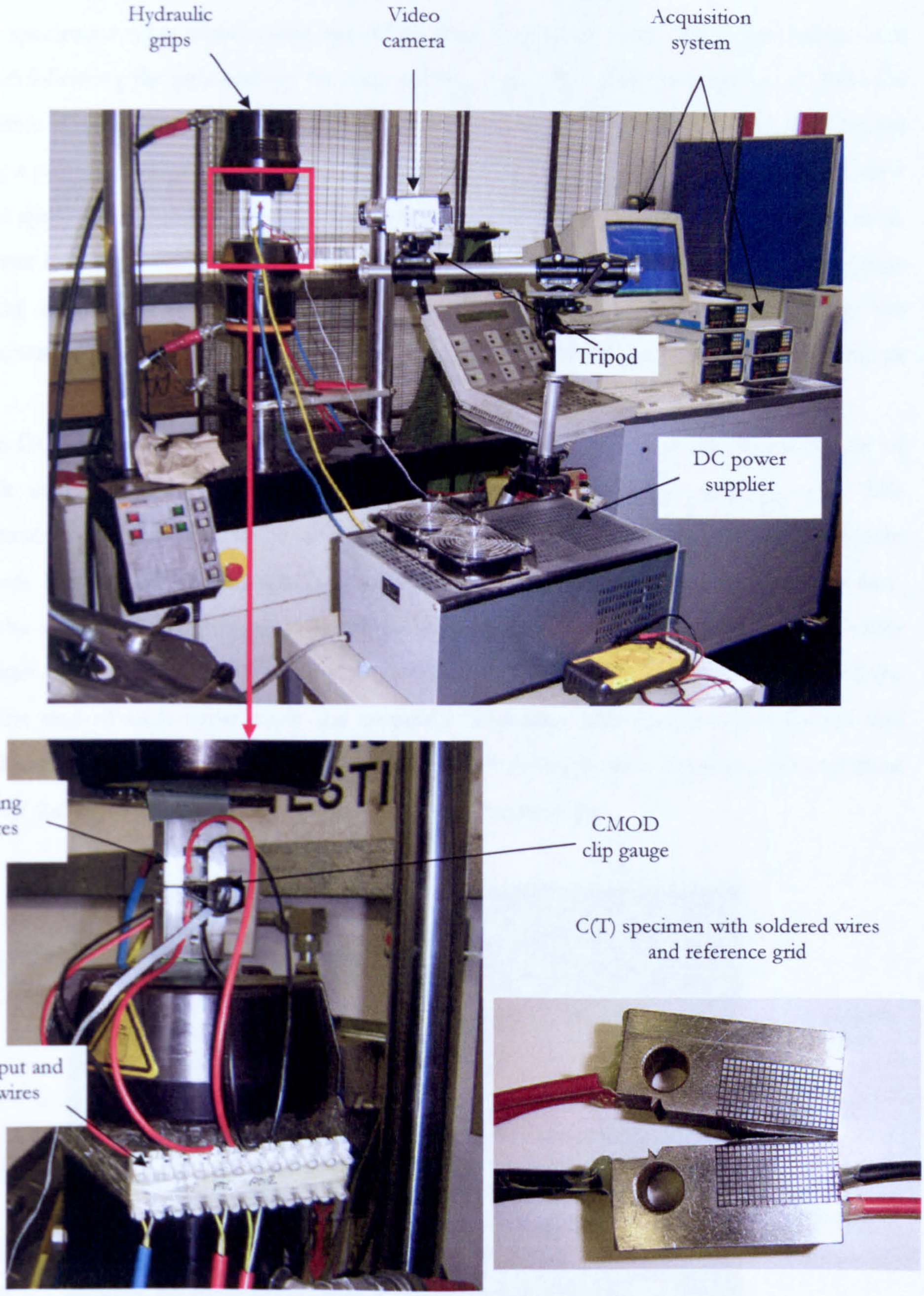

Fig. 3.16 Experimental set up of CT specimen using DCPD and optical technique to monitor the crack growth.

3.3 INSTRUMENTATION SET UP FOR TEAR SPECIMENS

The tear specimens were tested using special loading fixtures as well. All experiments were conducted following the proceedings by Shterenlikht et al., 2004 and Hashemi et al., 2004 for the modified double cantilever beam (DCB) specimens. Loading of the samples was carried out using a pair of thick plate grips on a 250kN Schenck test machine under opening mode I loading at quasi-static conditions of displacement rate of 0.05mm/s. Similar to the C(T) tests, in each tear test the crack mouth opening displacement was monitored by a large clip gauge comprising a full Wheatstone bridge. It was done with the aim of calibrating the micromechanical damage parameters for slant fracture characteristics, as discussed in chapter four.

From the DCB specimens, CTOA measurements were determined from the video history of the crack edges and the rotations of an etched grid during the crack process. The instrumentation for the acquisition of images was similar to that employed for the square tensile tests. For the DIC method a CCD camera was placed at the perpendicular gauge face, and for the etched grid technique a digital video camera (NV-GS400) was fixed to another perpendicular ligament area. In the tests, all instruments were synchronised at the start of the test. At the end of each experiment the complete load-time, displacement-time curves and images of the specimen were recorded. Figs. 3.17 and 3.18 show the complete view and close up views of the experimental set up of tear specimens, respectively.

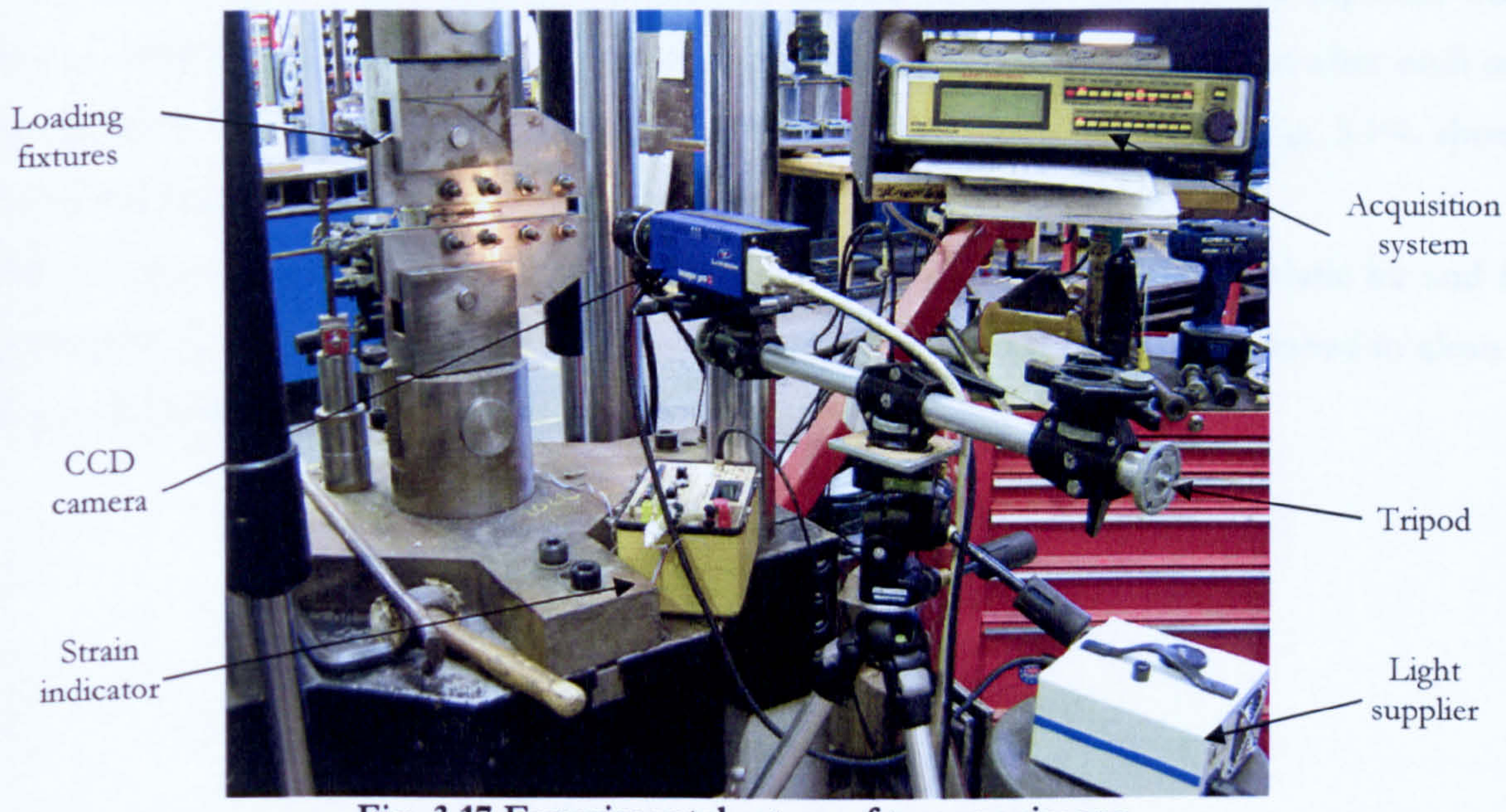

Fig. 3.17 Experimental set up of tear specimens.

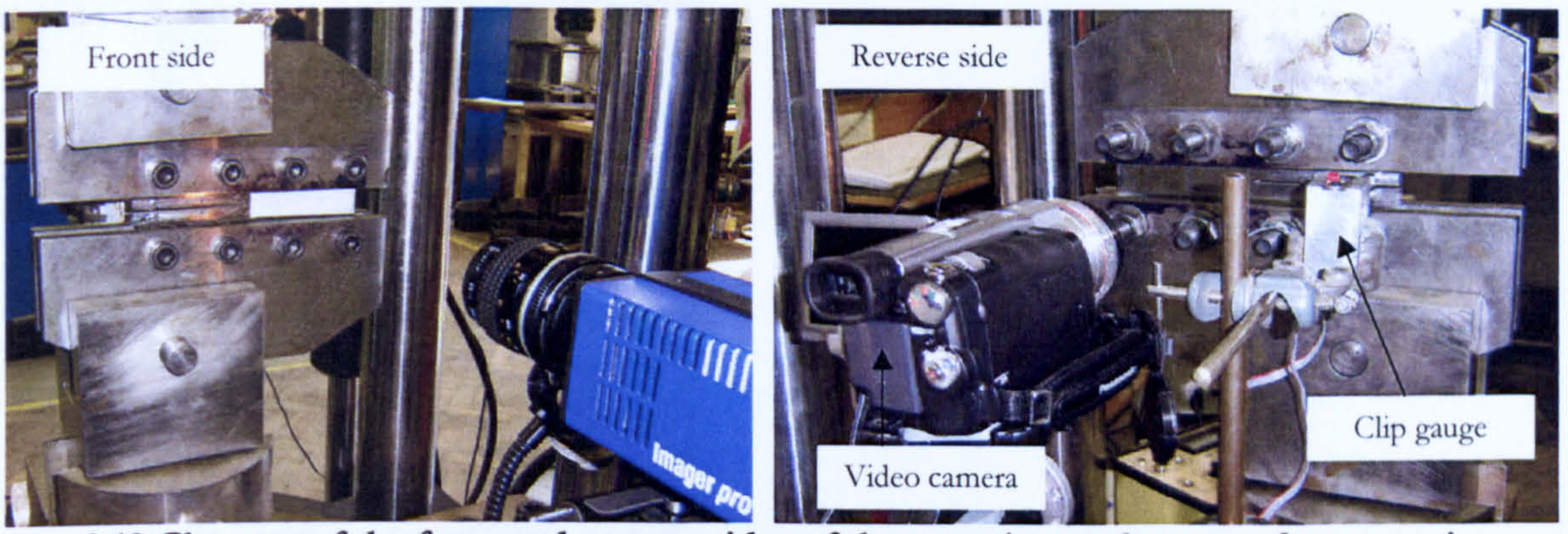

Fig. 3.18 Close up of the front and reverse sides of the experimental set up of tear specimens.

The gridlines were marked onto the gauge surface of the specimens using the photochemical etching Etch-O-Matic and the Mark 560 UV exposure kit. The etching was done in two stages; creating the grid on a stencil and etching the grids onto the gauge surface of the specimens.

The stencils were created using the Mark 560 UV kit, computer and high quality printer as follows: the first step was to create the desired grid (grid of $1x2mm$ and line thickness of 0.35mm were suitable for the analysis) using a computer with drawing software. The next step was to print the grid on a clear transparency with a good quality printer. The following step was to transfer the grid on the transparency onto the Dura-film stencil. It is best if this procedure is done in a photographic dark room or in a room with very low lighting levels. This was done by securely placing the pre-cut stencil underneath the transparency of the grid printed and exposing it in the UV exposure kit (see Fig. 3.19a). The optimum exposure time for the designed grid was 3.5 minutes. The prepared stencils can be reused but after each use the quality is deteriorated slightly so it is preferable to create various stencils. Fig. 3.19b shows the stencil developed for $1x2mm$ grid.

The etching onto the surface of the specimens was done using the Etch-O-Matic kit and its accessories (See Fig. 3.20). Before etching the ligament surface was slightly polished to clean it of any dirt and oxidation to provide a better contrast against the black grids.

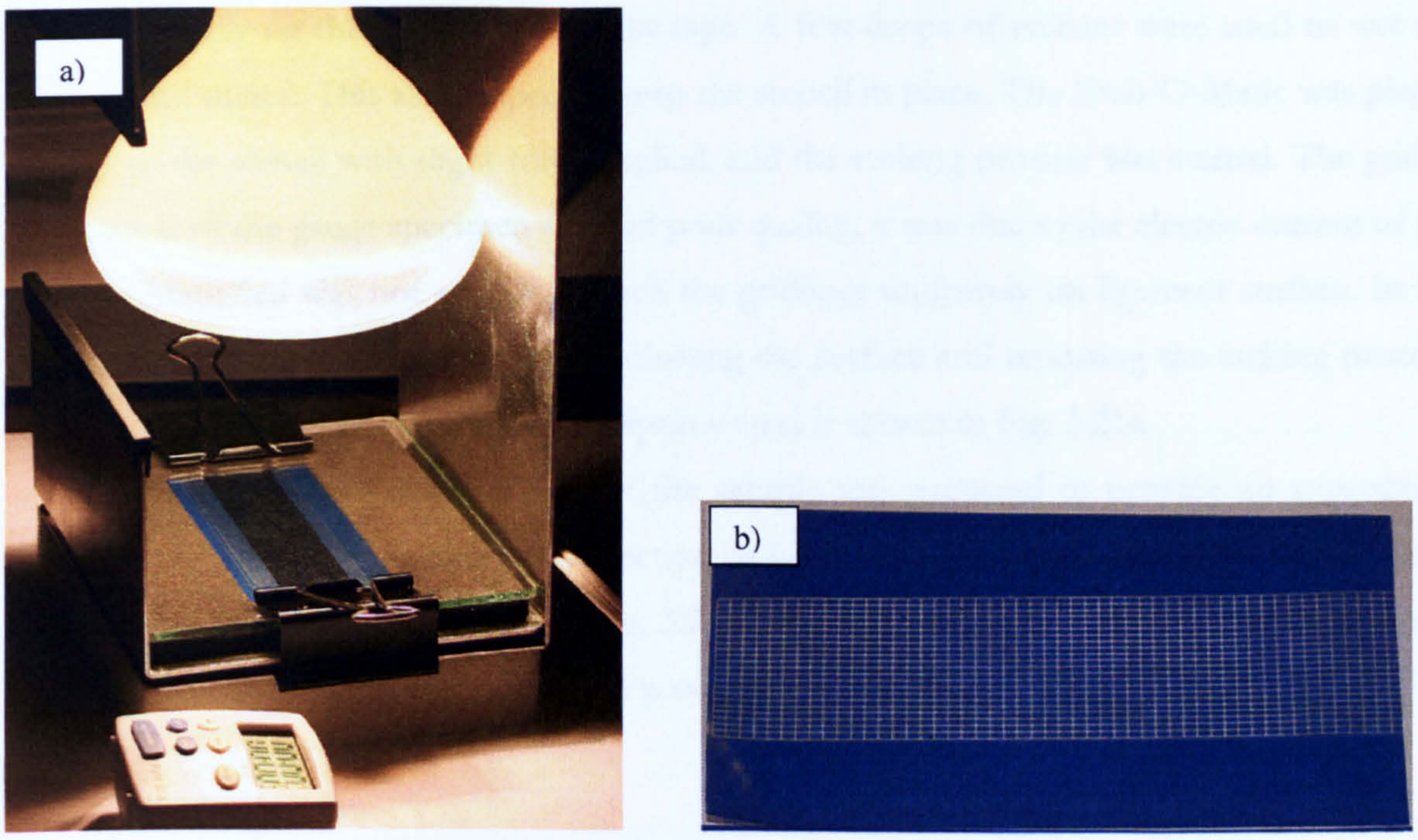

Fig. 3.19 Photograph of: a) UV exposure unit and b) resultant stencil

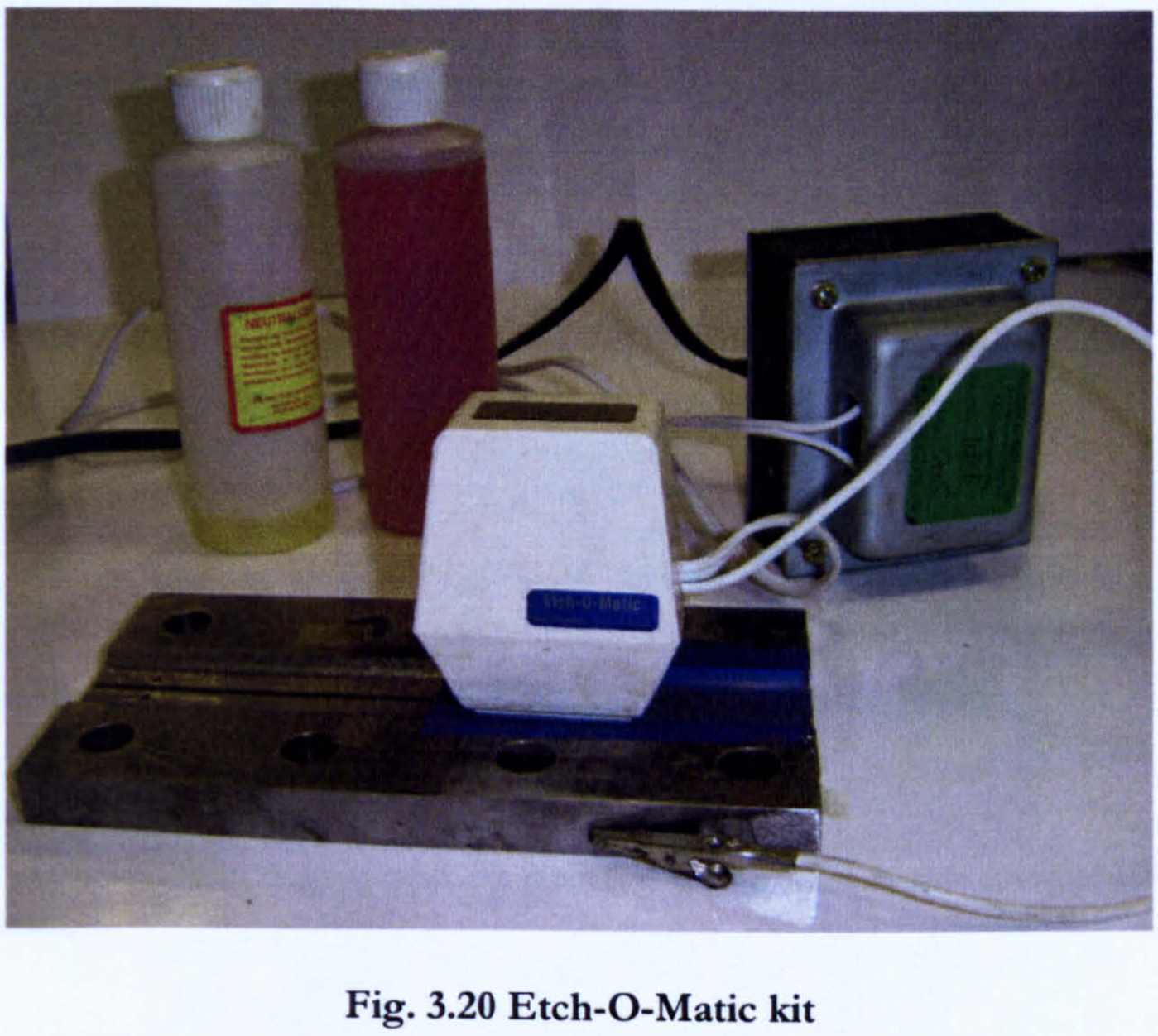

Fig. 3.20 Etch-O-Matic kit

The quality of the resultant grid was dependant on the etching time, amount of etchant used, force applied, geometry of the specimen and type of material. In this tear specimen, the stencil

was held firmly on the surface with sticky tape. A few drops of etchant were used to wet the surface and stencil. This also helped to keep the stencil in place. The Etch-O-Matic was placed on top of the stencil with slight force applied, and the etching process was started. The grid in some parts of the gauge specimen showed poor quality, it was due to the electric current of the Etch-O-Matic kid was not enough to etch the gridlines uniformly on ligament surface. In the event of bad etch; it was removed by polishing the surface and repeating the etching process. The resultant etched grid on the X100 pipeline steel is shown in Fig. 3.21a.

For the DIC technique another face of the sample was prepared to provide an appropriate contrast and to reduce the effect of reflection by lightly spraying with white paint and diffusely spraying black paint on the surface (Fig. 3.21b). This technique required little preparation of the gauge surface for the acquisition and processing of the images.

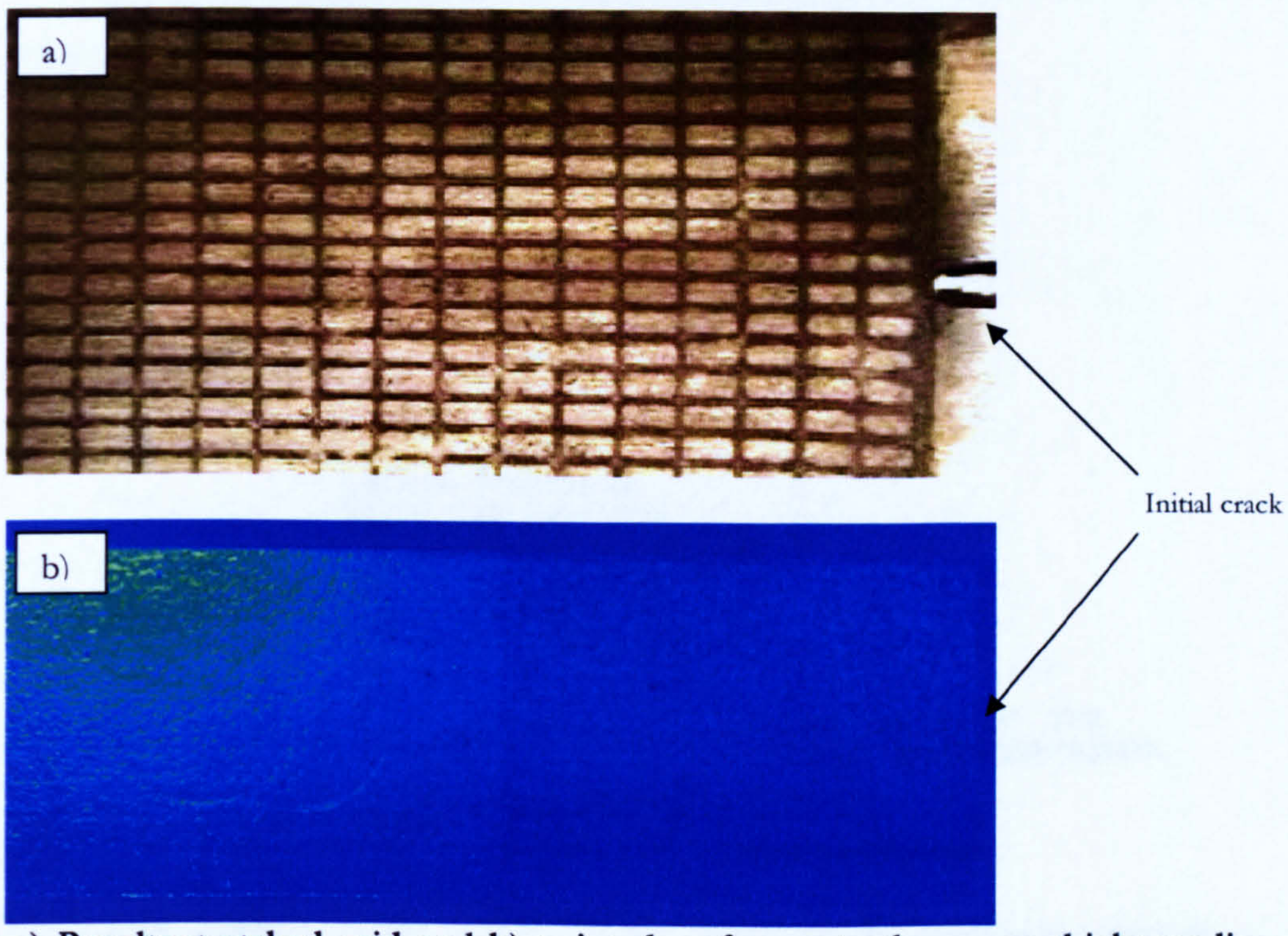

Fig. 3.21 a) Resultant etched grid and b) painted surface onto the gauge thickness ligament specimen.

3.4 TEST RECORD OF TENSILE SPECIMENS AND MATERIAL CHARACTERIZATION

3.4.1 Test record of cylindrical tensile tests

Each experiment produced data in terms of voltage which was converted into axial deformation, transverse deformation, load and displacement data stored in a text file containing five columns including the time of each test.

Data recorded from the smooth specimens were used to evaluate the mechanical properties of the X100 material. Data from notched specimens were used to provide load deformation data for different level states of stress triaxiality to supply sufficient experimental information for calibrating the damage mechanics models to study the flat ductile failure characteristics of the pipeline steel. A total of 58 specimens, smooth and notched cylindrical samples, were tested and their information recorded for three different sets and four different orientations.

Fig. 3.22 shows the nomenclature used to represent the specimen orientation and transverse extensometer position.

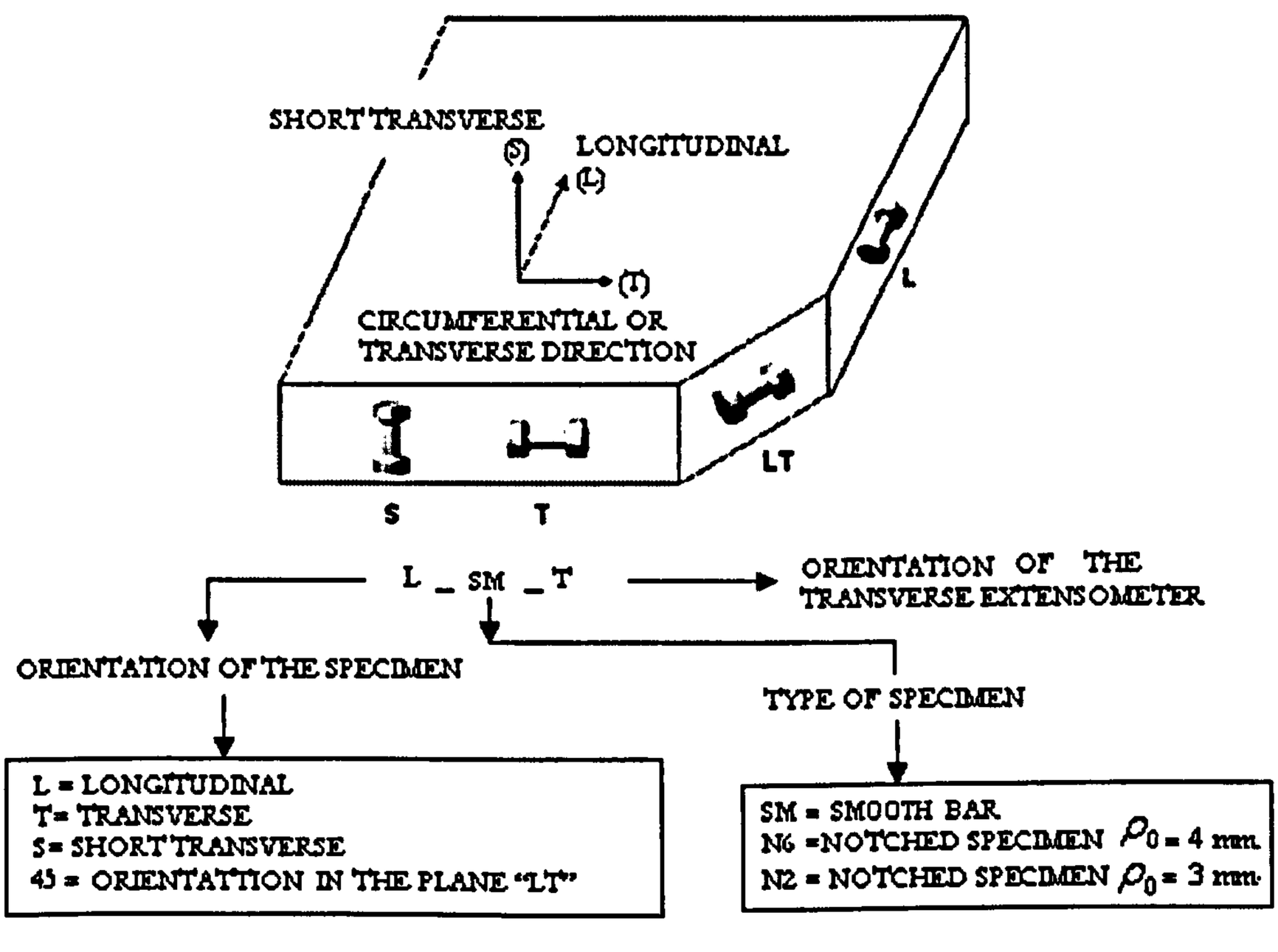

Fig. 3.22 Nomenclature used in order to represent the orientation of tensile specimens and the direction of transverse extensometer to measure the diametral contraction

Fig 3.23 illustrates an example of the load and diametral contraction behaviour of a smooth tensile test in the L direction. The transverse extensometer was fixed on the cross section area in two principal orientations in order to capture the diametral contraction of the considerable ovalisation of the specimens during the tensile test. The procedure to capture such ovalisation was as following: from two tests in the longitudinal direction, the transverse extensometer was attached in the transverse orientation in one test. Whilst in the other test, it was located in the thickness orientation.

The graph of results shows that the deformation up to the point of hardening displays isotropic behaviour and after that point, the softening shows anisotropic damage. It also shows that the strain to failure is much greater in the thickness orientation than in the circumferential one.

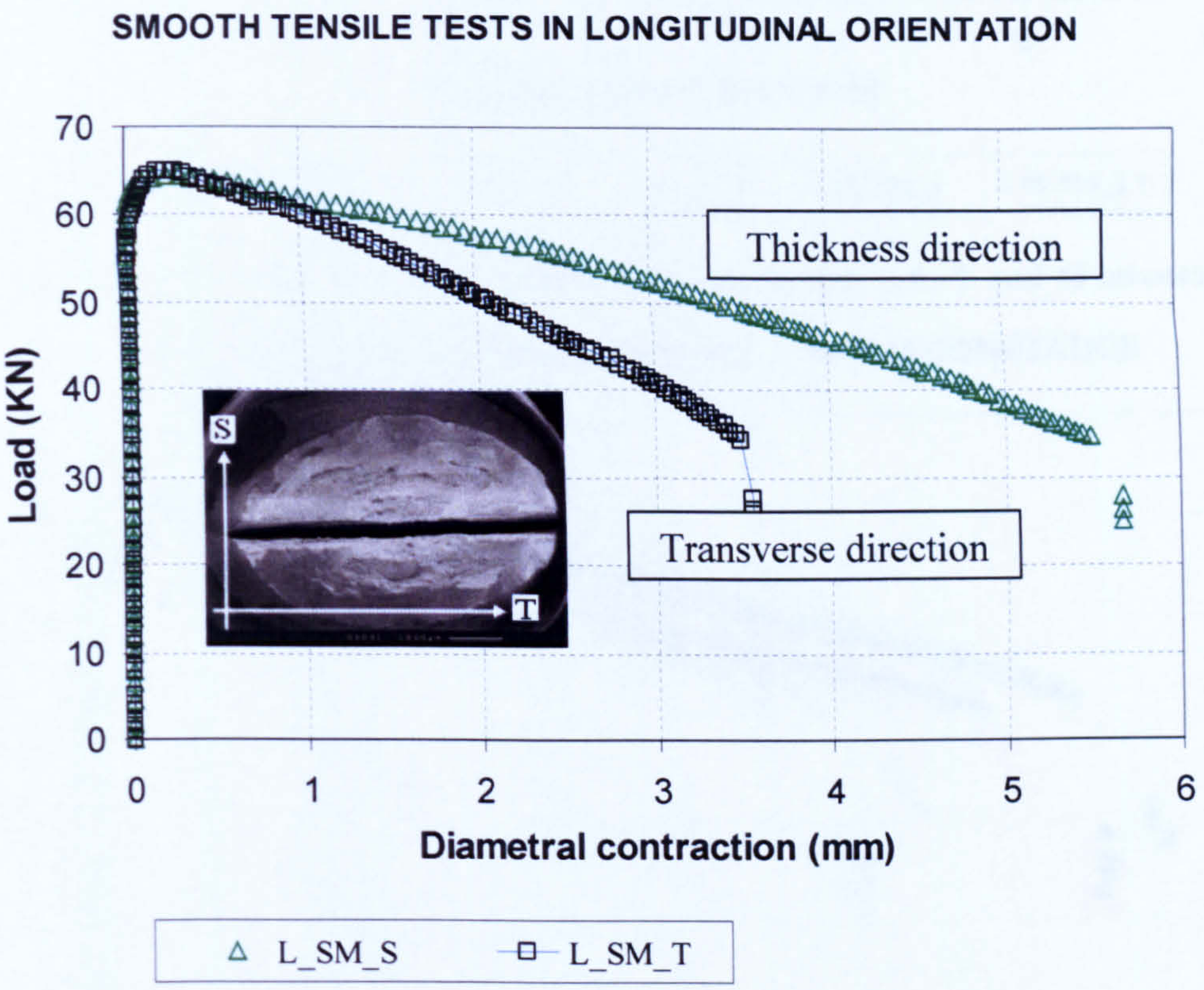

Figs. 3.23 Load – diametral contraction curves of smooth specimens orientated in L direction

According to the above nomenclature, average of load-diametral contraction results of all laboratory specimens in L, T, 45 and S direction are shown in Fig. 3.24 to 3.27.

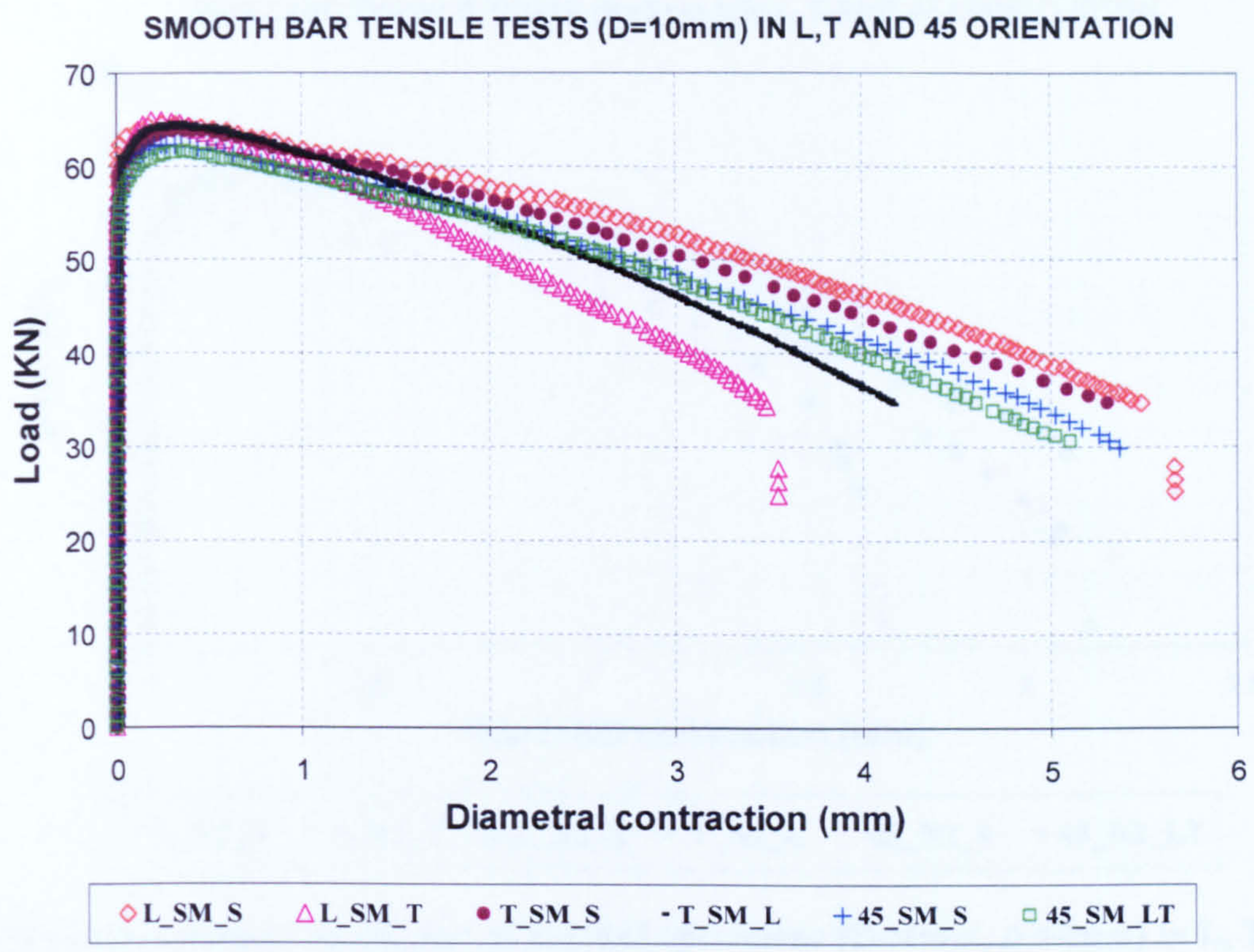

Fig. 3.24 Load-diametral contraction of smooth specimens in L, T and 45 orientation

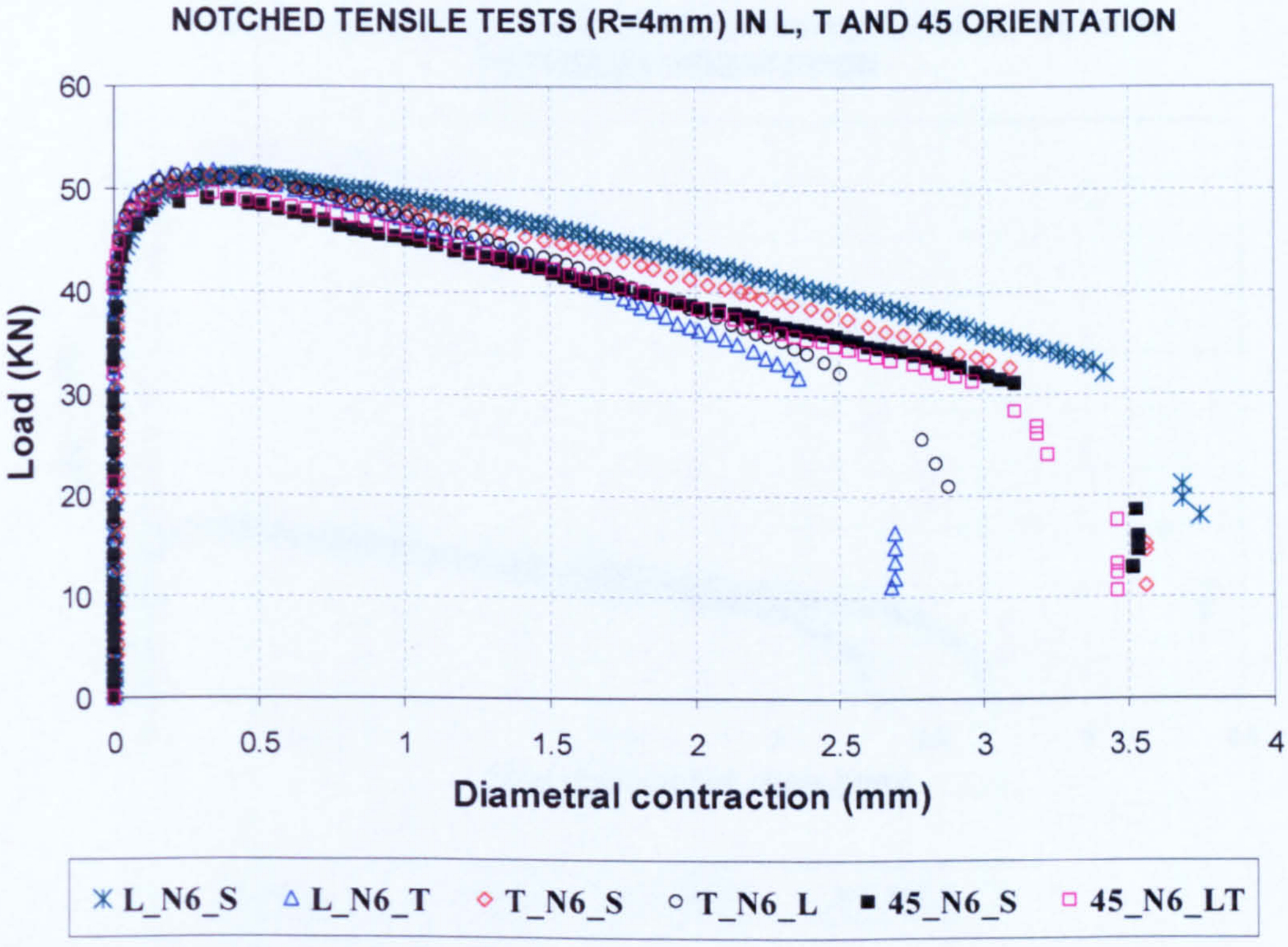

Fig. 3.25 Load-diametral contraction of notched specimens (D=8mm, ρ =6mm) in L, T and 45 orientation

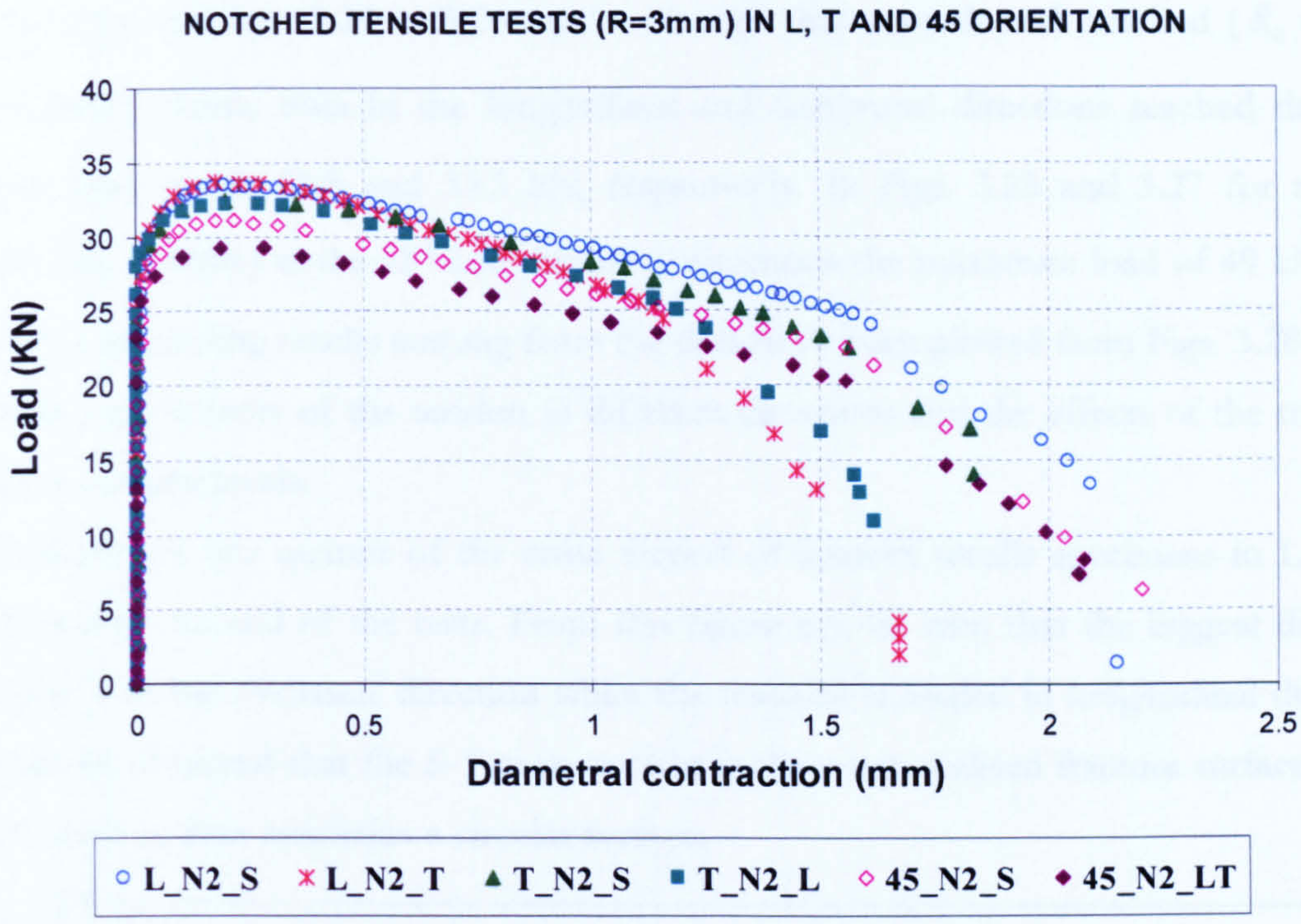

Fig. 3.26 Load-diametral contraction of notched specimens (D=6mm, ρ =2mm) in L, T and 45 orientation

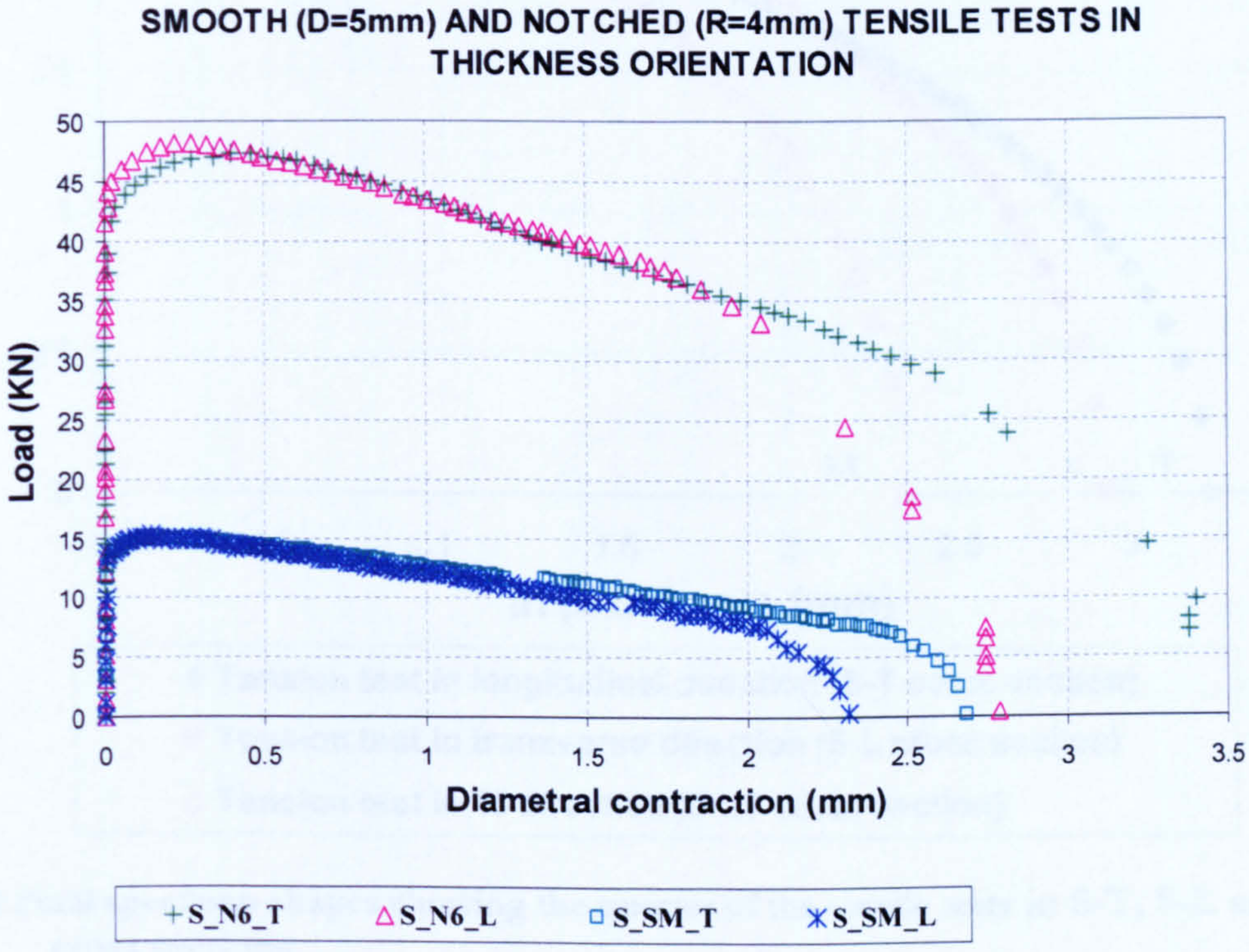

Fig. 3.27 Load-diametral contraction of smooth and notched specimens in thickness orientation

From the previous Figs. 3.24 to 3.26 can be noticed that smooth and notched ($R_0 = 4mm$ and $R_0 = 3mm$) tensile tests in the longitudinal and transverse directions reached the same maximum load of 65, 51.5 and 33.5 kN, respectively. In Figs. 3.25 and 3.27 for notched specimen ($R_0 = 4mm$) in the 45° and thickness directions the maximum load of 49 kN is the same. Other interesting results coming from the data have been plotted from Figs. 3.28 to 3.30 representing the severity of the tension in different directions and the effects of the triaxiality of unlike constraint levels.

Fig 3.28 illustrates one quarter of the cross section of smooth tensile specimens in L, T and 45° direction at the end of the tests. From this figure can be seen that the biggest diametral contraction is in the thickness direction when the material is loaded in longitudinal direction. Also it can be observed that the S-T cross section is the most ovalised fracture surface, whilst the S-LT cross section maintains a circular surface.

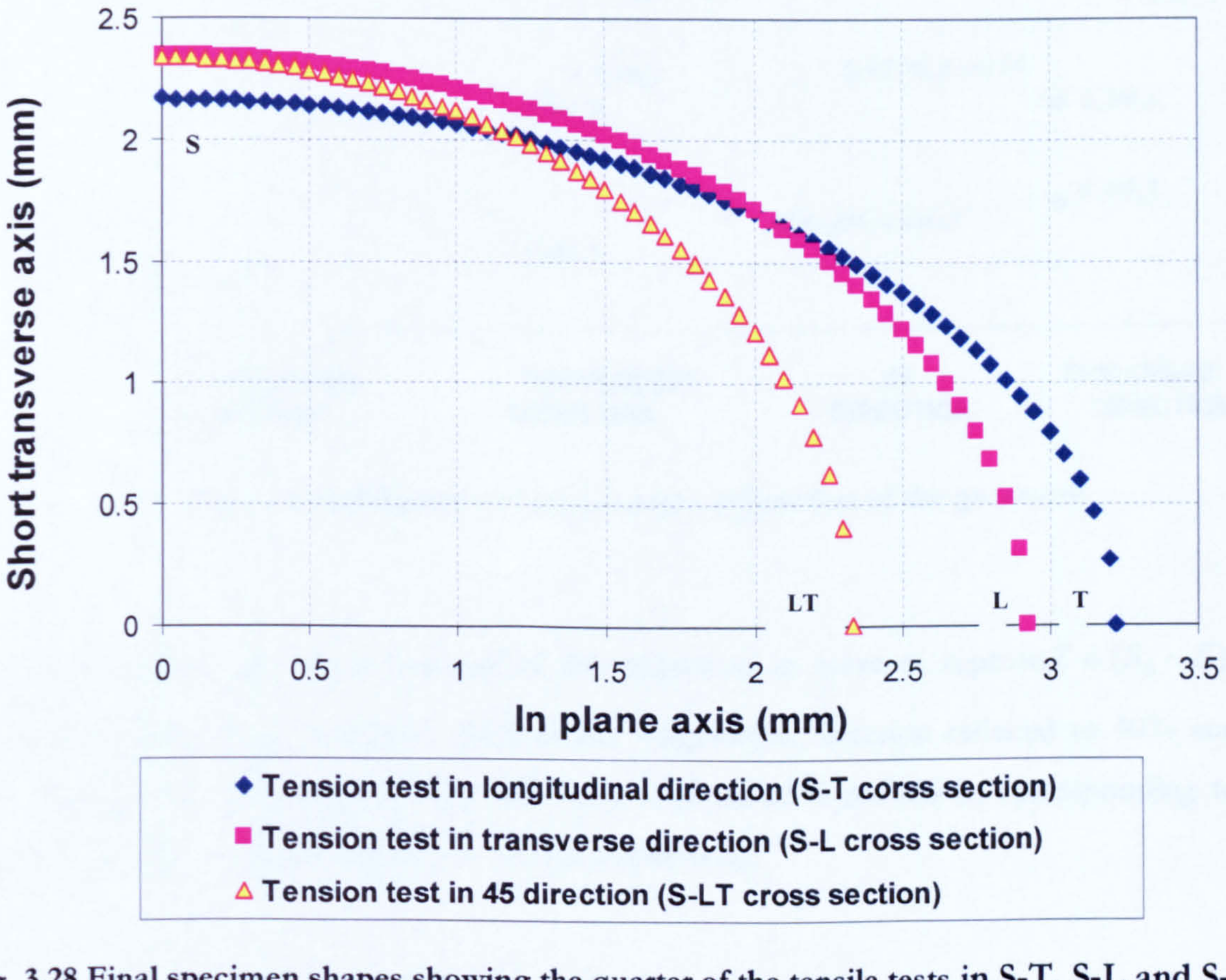

Fig. 3.28 Final specimen shapes showing the quarter of the tensile tests in S-T, S-L and S-LT cross sections.

The evolution of the deformation of coalescence, $\bar{\varepsilon}_{(c)} = \Delta\Phi_c / \Phi_0$, as a function of the geometry is presented in detail in Fig. 3.29. $\Delta\Phi_{(c)}$ is the diametral contraction at the point in the curve where there is a quick change of plastic deformation due to the macroscopic coalescence and Φ_0 is the initial diameter of the gauge section. The factor $\bar{\varepsilon}_{(c)}$ represents the severity of the tension in different directions. From this plot can be seen that notched specimen of $R_0 = 3mm$ in L_N2_S direction has the main severity of tension and effects of the triaxiality because of the high constraint level and material behaviour.

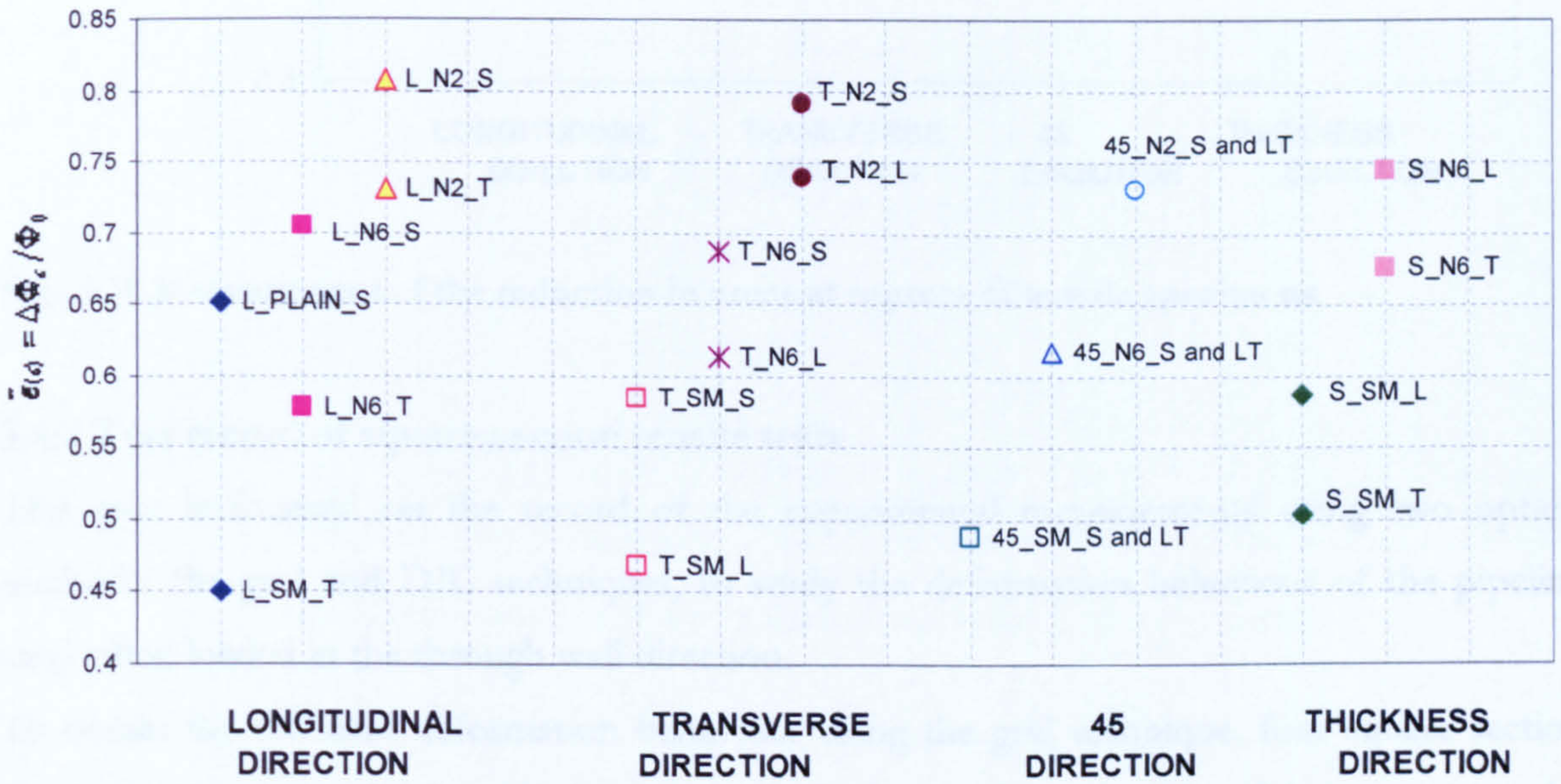

Fig. 3.29 Deformation of coalescence in function of the geometry

Fig. 3.30 reports the measurements of the reduction in areas at rupture $Z = (S_0 - S)/S_0$. Notched specimen of $R = 3mm$ (N2) in the longitudinal direction reduced to 40% and the smooth specimens in the 45° direction showed about 80% reduction, corresponding to the minimum and maximum reductions of area respectively.

Fig. 3.30 Measurement of the reduction in areas at rupture of tensile specimens

3.4.2 Test record of square section tensile tests

This part is focused on the record of the experimental measurements using two optical methods, the grid and DIC techniques, to study the deformation behaviour of the pipeline steel when loaded in the through wall direction.

To obtain the full field deformation behaviour using the grid technique, four square section specimens were tested. The calculation of the displacements was achieved by comparing the deformed grid with the original one. It was possible by the use of video frames (e.g. Fig. 3.31) and a series of photographs (e.g. Fig. 3.32) that were taken of the gauge surface. Acquisition of the images from the still camera was not as good as the ones obtained from the video camera, due to the difficulty of focussing on the small grid pattern throughout the loading process. The engraved lines can clearly be seen from the video frames, although the width of the lines is significant compared with the pitch. This is important since the reliability of this method depends primarily upon the quality of the pictures in terms of contrast, brightness and width of the engrave lines.

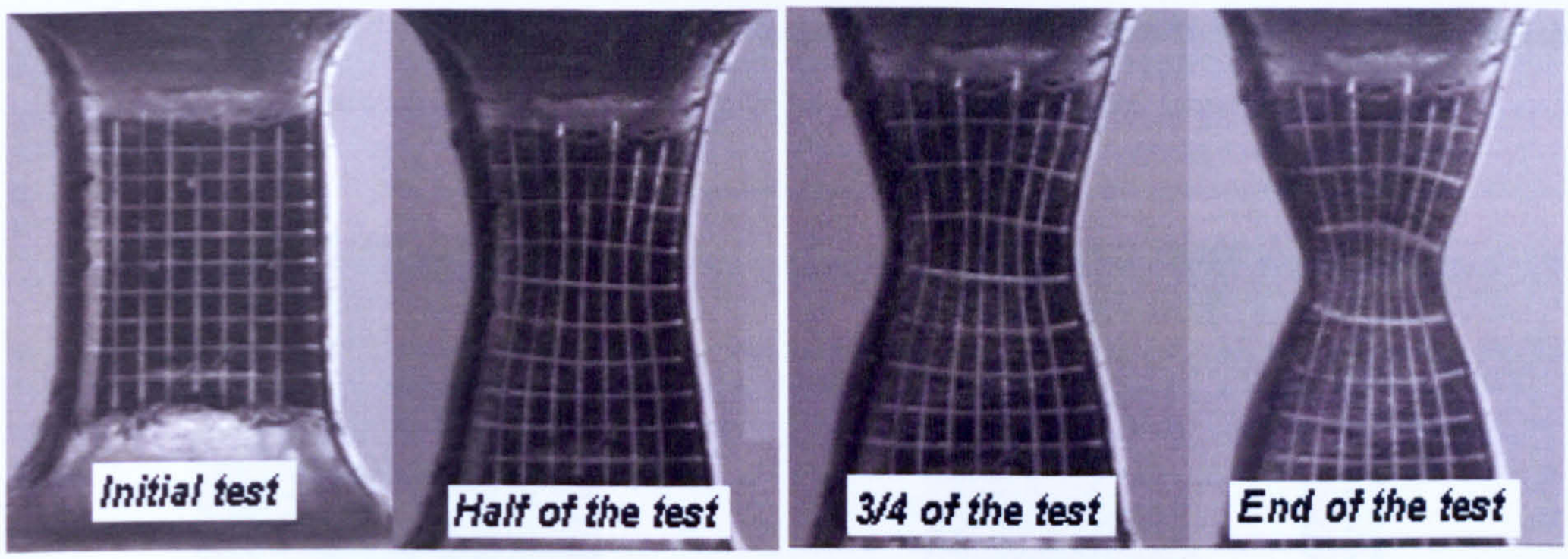

Fig. 3.31 Example of close up pictures coming from video camera

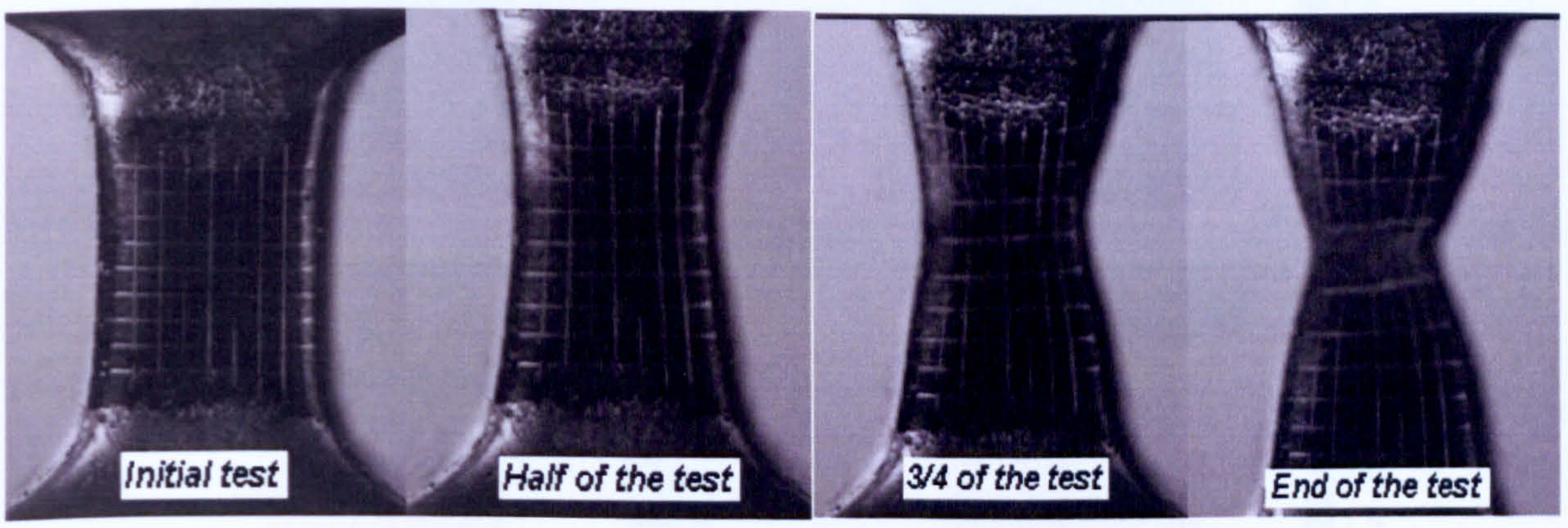

Fig. 3.32 Example of close up pictures coming from still camera

The deformation gradient and the strain in the tensile tests were calculated by analysing the deformed grid and comparing it to the undeformed one. The experiments showed that at the scale of the grid-pitch, a square (0.5mm x 0.5mm) in the undeformed state transforms into a rectangular or trapezium after deformation. Therefore the deformation gradient tensor, which contains information on the deformation of the element, appears to be a linear mapping between the initial and final states.

A MATLAB script (Gutierrez, 2005) was used to extract the deformation measurement from the grid, at the centroid of each single grating, when manually clicking on grid intersections. In the script, text output files were created as deformation gradients, engineering and logarithmic strains of the grid. These text output files were then used to plot the contours of the whole field deformation behaviour in the loading direction using a surface mapping software

(SURFACE 8, 2002). Fig. 3.33a-d show the original image when the macroscopic crack starts to grow in the centre of the gauge section and its corresponding plot contours.

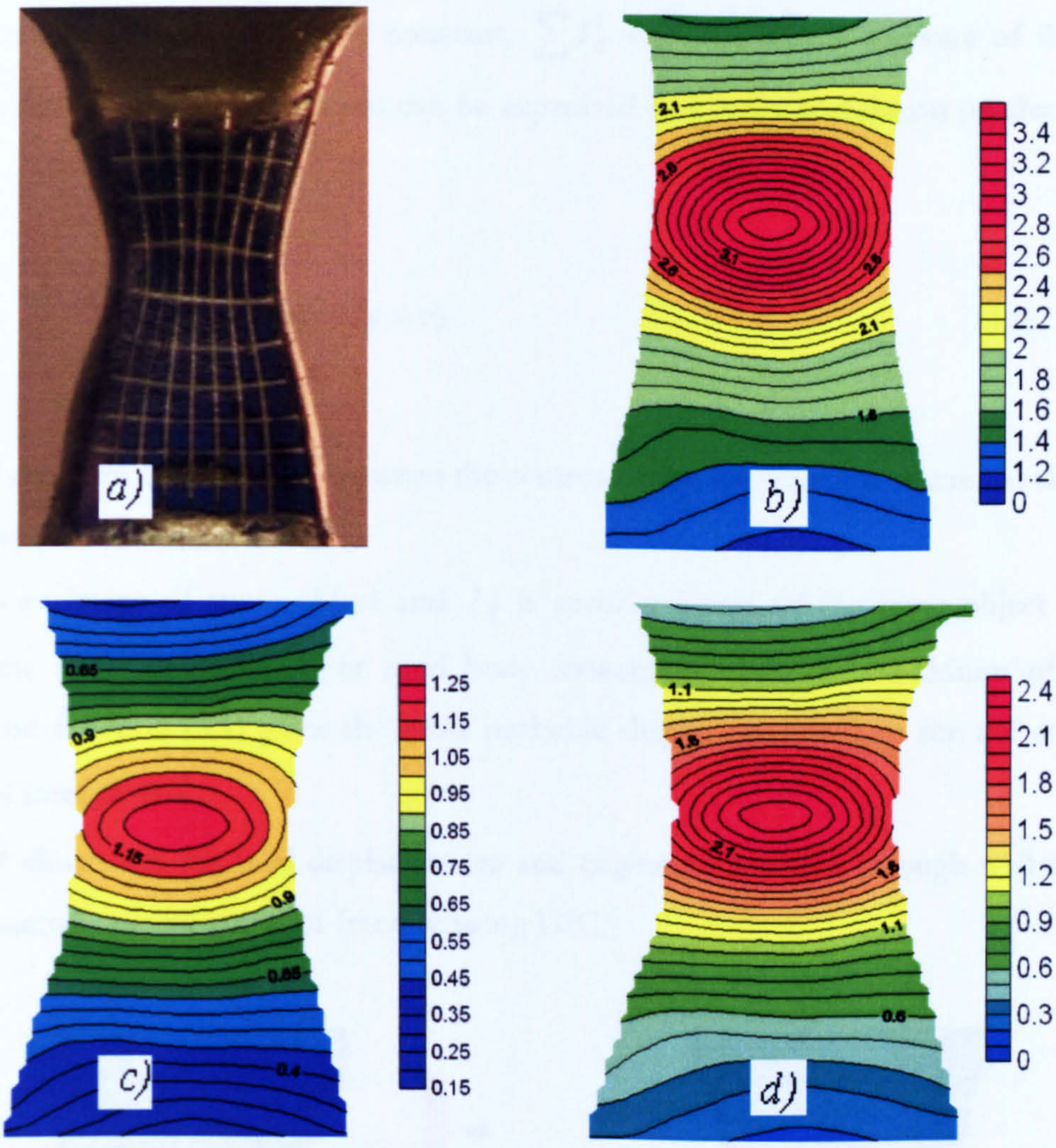

Fig. 3.33 (a) Original image with grids engraved on its gauge surface. (b) Displacement gradients in mm, (c) logarithmic and (d) engineering strains in mm/mm at the loading direction

A commercial DIC package DaVis by LaVision was used to obtain the experimental measurements of the abraded surface. In this implementation the images are first transformed into the frequency domain using a fast Fourier transform. Then the cross-correlation function Eq (3.1) is calculated in the frequency domain.

The principle of two-dimensional DIC is simple (Da Fonseca, 2005). A digital image comprises a two-dimensional array of intensity values, I(x,y). Given two images, I_A and I_B, a N × N pixel region of interest, known as an interrogation window, is defined in each image. If the image brightness is approximately constant, $\sum I_A^2 \approx \sum I_B^2$, then a measure of the similarity between the two regions of interest can be expressed as a cross-correlation product (Clocksin, 2002):

$$c(u,v) = \sum_{x=-m}^{n} \sum_{y=-n}^{n} I_1(x,y) I_2(x+u, y+v) \qquad (3.1)$$

where u and v are the distances between the centres of the two regions of interest along x and y respectively, and n=N/2.

If I_A is an image of some object and I_B is another image of the same object after it has undergone some deformation or rigid body movement, then the maximum of the cross-correlation function (3.1) gives the most probable displacement values for the centre of the region of interest in I_A.

Fig. 3.34 shows the full field displacements and engineering strains through wall direction up to the macroscopic initiation of fracture using DIC.

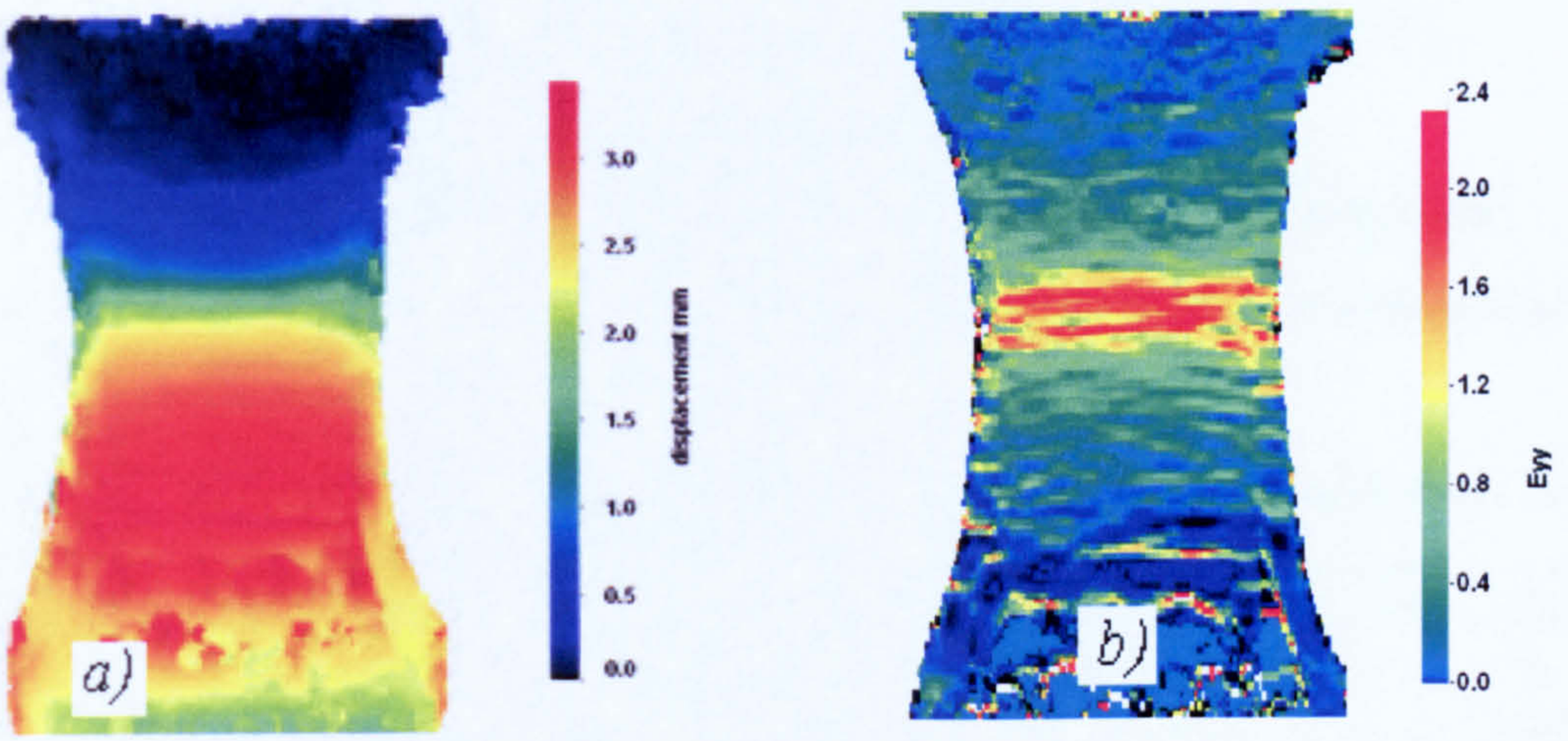

Fig. 3.34 (a) Displacement gradients in mm and (b) engineering strains in mm/mm at the loading direction up to the initiation of fracture

3.4.3 Evaluation of mechanical properties

Fig. 3.35 shows the nominal stress-strain data from the four orientations of the smooth tensile experiments. The stress-strain result curve in the through pipe wall thickness direction was obtained from both cylindrical (smooth) and square section specimens. The average values of the measured mechanical properties of the material are reported in Table 3.4.

The 0.2% yield stress for the transverse tensile was of 760 MPa . As the hoop stress in a gas pipe is the maximum stress, this range of the yield stress met the target values $(\sigma_y > 689MPa)$ for X100 pipeline steel. A comparison of the yield stress (0.2%) of the four tensile directions can be valuated in Fig 3.36.

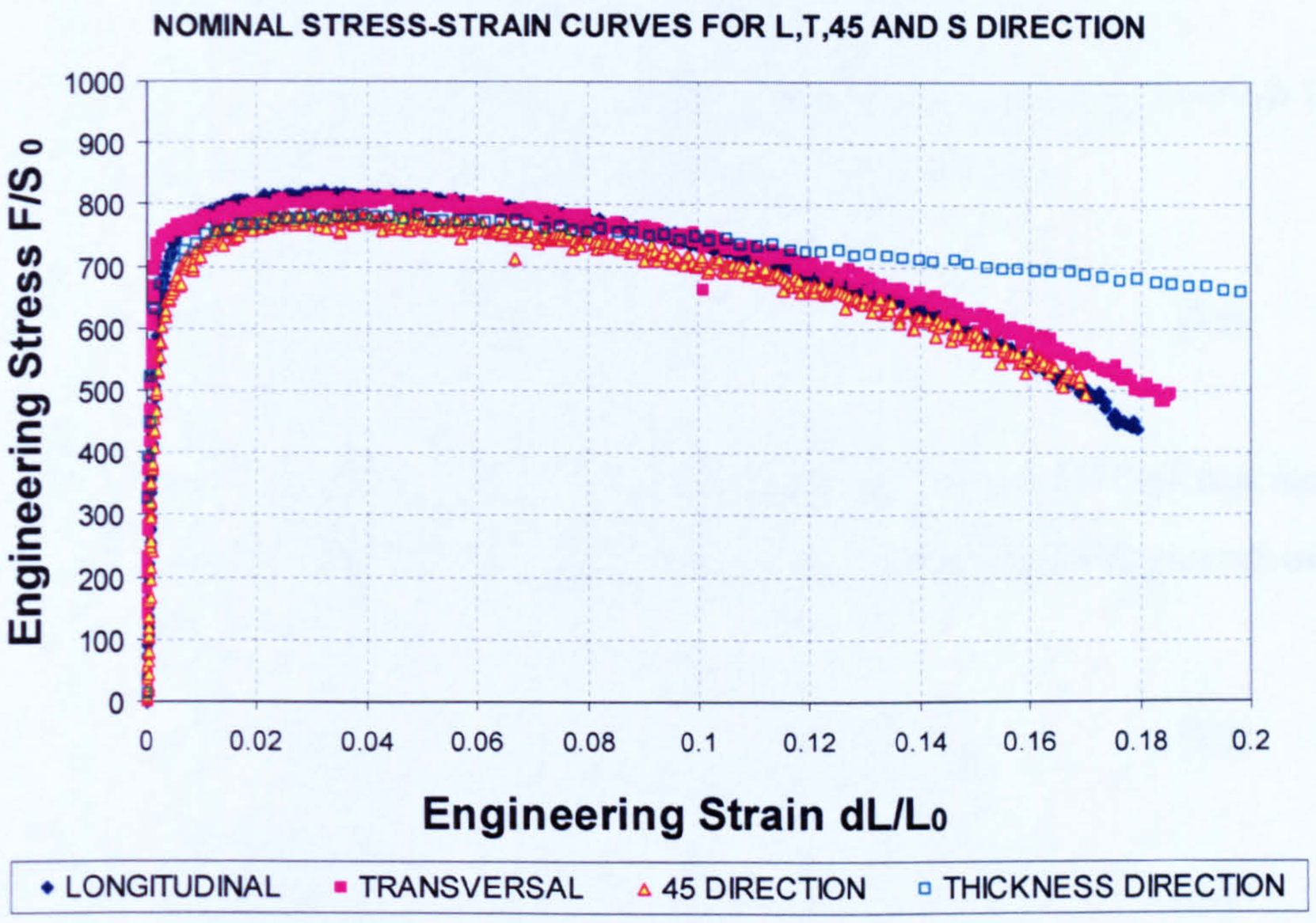

Fig. 3.35 Nominal stress-strain data of the plain bar tensile tests in four orientations of X100 steel.

Table 3.4 Summary of the mechanical properties from the smooth tensile tests in four orientations (X100 pipeline steel)

Tensile specimen	σ_Y (0.2% proof stress) MPa	σ_{UTS} MPa	E GPa	elongation %	reduction of area %	$\sigma_T = K\varepsilon_T^n$ n	K MPa
Longitudinal	631	876	210	18.63	71.51	0.0769	1130.5
Transverse	760	878	210	19.40	72.05	0.0611	1051.4
45	569	839	210	20	78.19	0.0929	1141
Thickness	644	848	210	45	74.67	0.069	1042

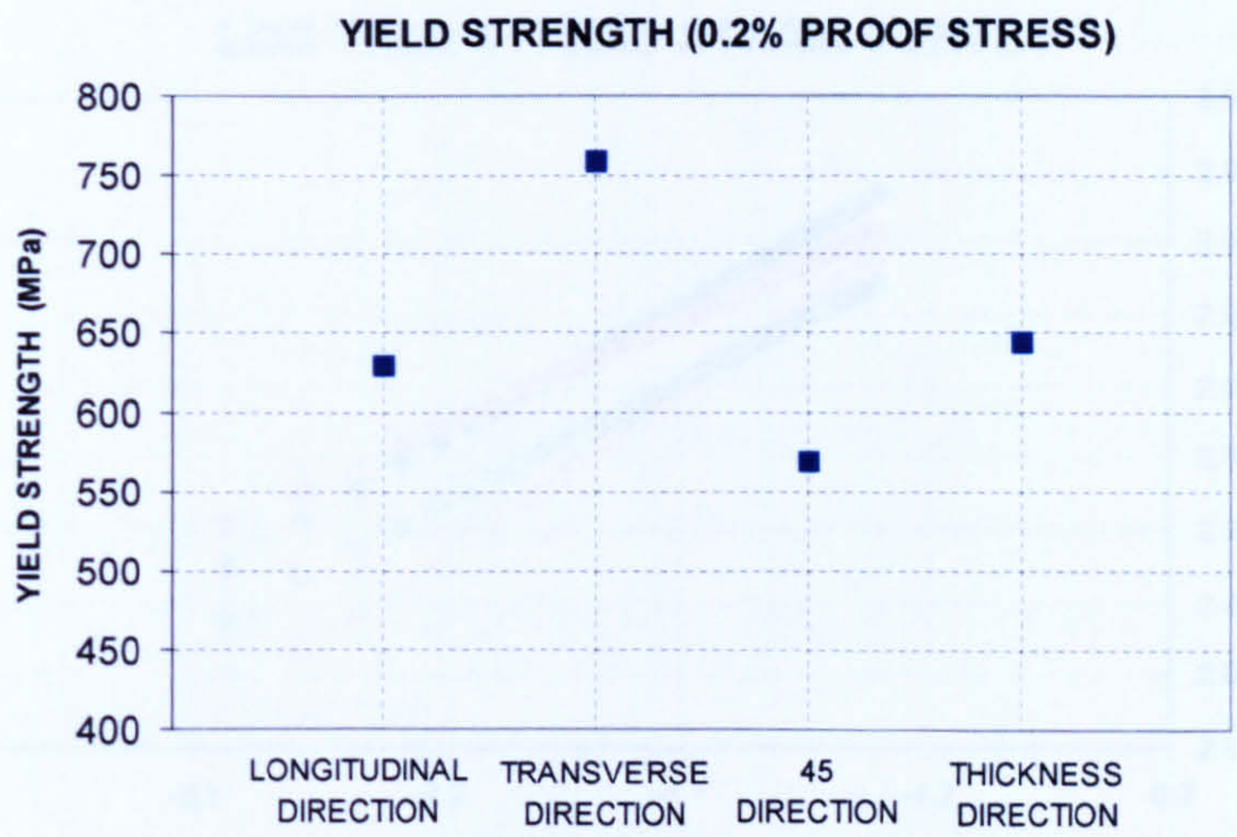

Fig. 3.36 Comparison of yield stress in L,T, 45° and S direction.

The logarithmic true stress-strain curve for X100 was derived assuming a power law strain hardening for the test data between yield and tensile strength (Eq. 3.2):

$$Log(10)\sigma_T = Log(10)K + nLog(10)\varepsilon_T \tag{3.2}$$

where σ_T and ε_T are true stress and true strain, respectively. To estimate the true stress-strain values before the necking of the tensile specimens, the following relationships were used:

$$\sigma_T = \frac{F}{A_T} \tag{3.3}$$

$$\varepsilon_T = \ln\left(\frac{l_i}{l_0}\right) \tag{3.4}$$

where F is the load, A_T true value of cross section area, l_i instantaneous length, and l_0 original gauge length of the tensile specimens.

The estimated data from equations 3.3 and 3.4 were input into relation (3.2) to plot true stress-strain on logarithmic scale as shown in Fig. 3.37. The strain hardening component n and strength coefficient K, calculated for each test, are given in Table 3.4.

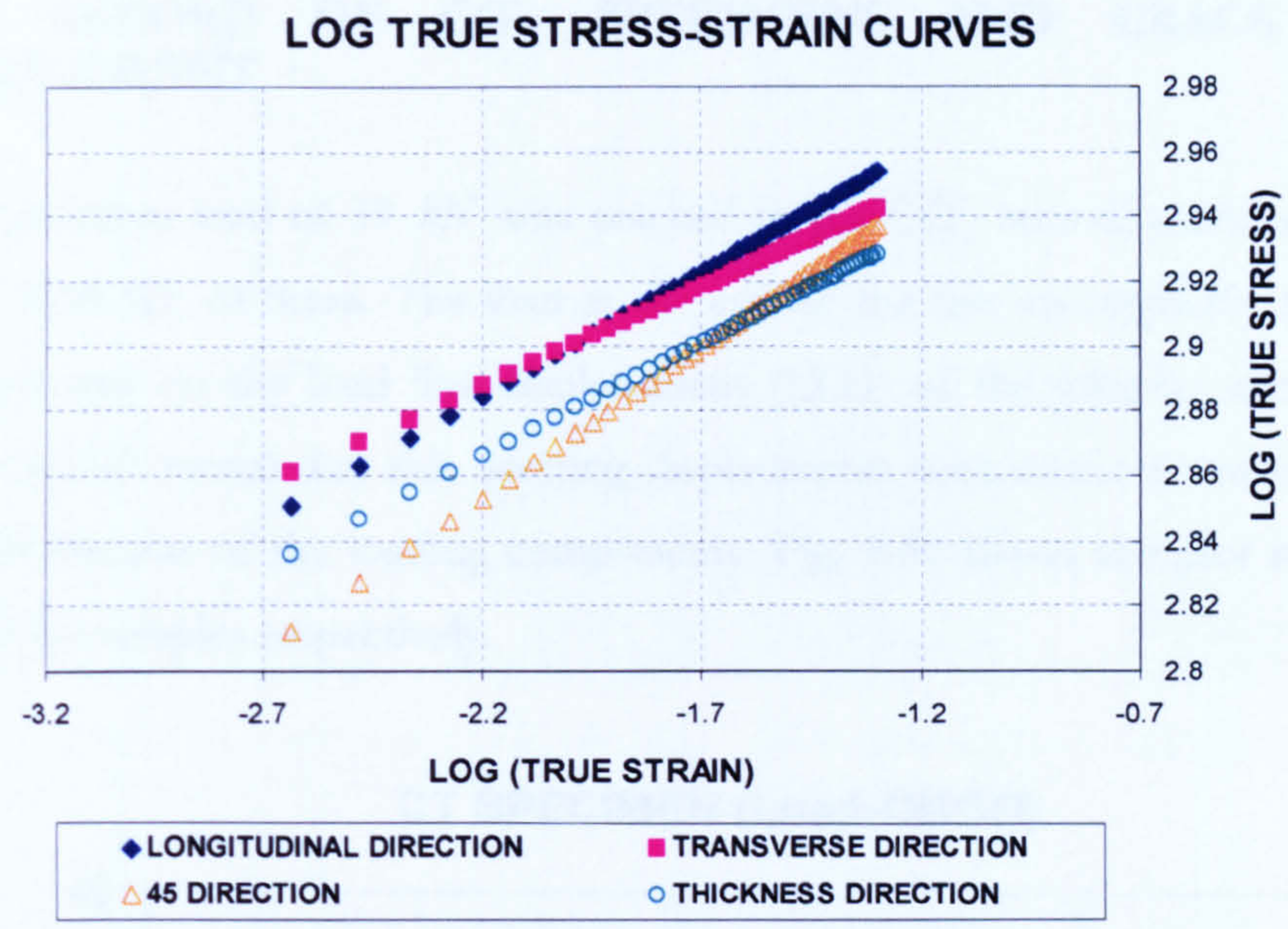

Fig. 3.37 Logarithmic true stress-strain record from the smooth specimens in four different orientations

The power law function of the form $\sigma_T = K\varepsilon_T^n$ was fitted to the smooth tensile experimental data and used to extend the yield curve beyond uniform elongation of the specimen. Fig. 3.38 shows the fitted true stress-strain curves from the four orientations. This data is required as a material property in the computer simulation.

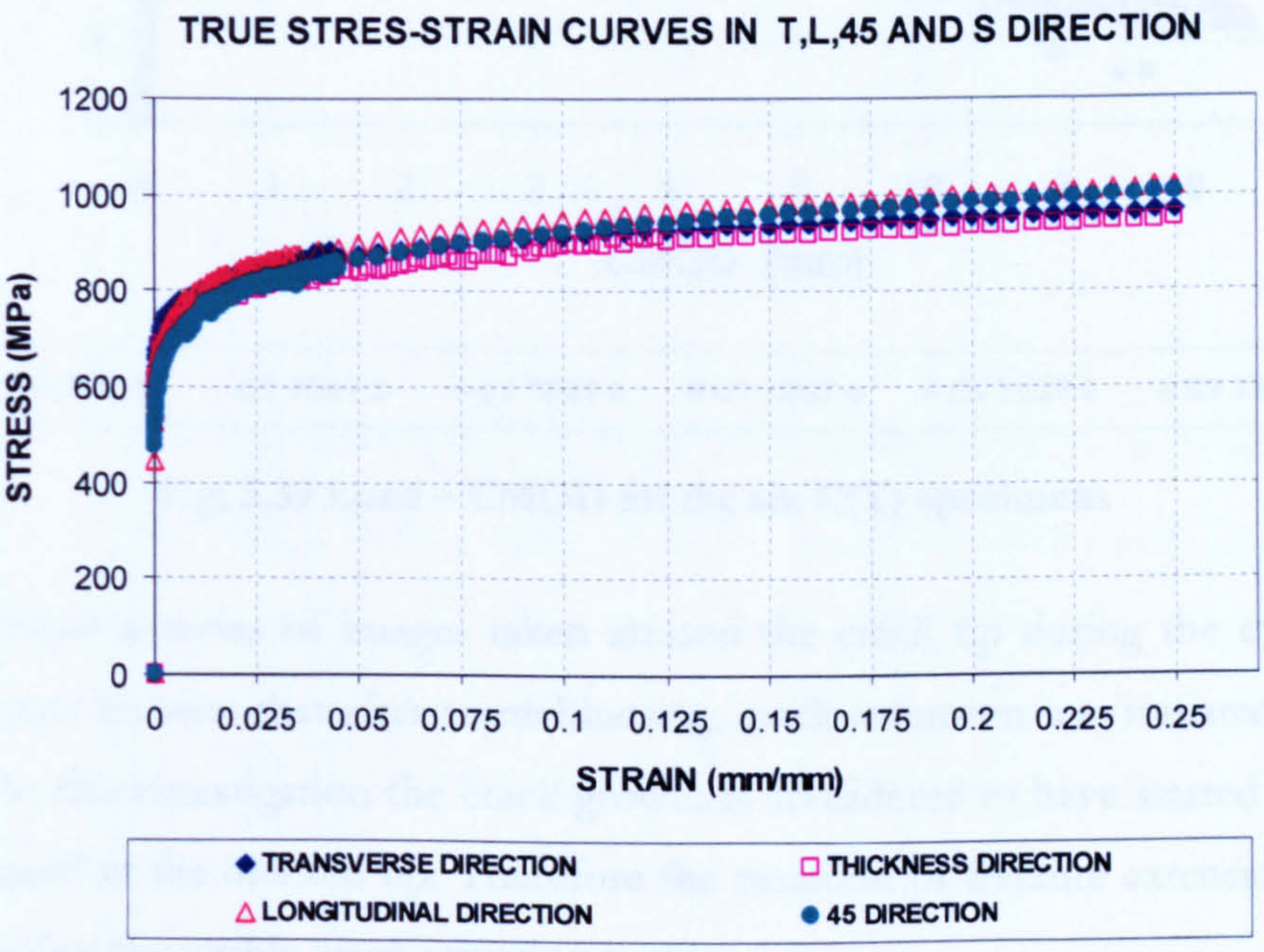

Fig. 3.38 True stress data as a function of true strain from the smooth specimens in four different orientations

3.5 TEST RECORD OF C(T) SPECIMENS AND CRACK GROWTH MEASUREMENT

An average maximum load of 39 kN was reached in the C(T) tests at crack mouth opening displacement (CMOD) of 8mm. The load at the end of the test was typically 5 kN. CMOD data was monitored on the load line displacement (LLD) of the samples and far from the loading point, which means that this opening displacement measurement was not affected by the elastic deformation of the loading components. Fig. 3.39 shows the plot results of load-CMOD of the six samples respectively.

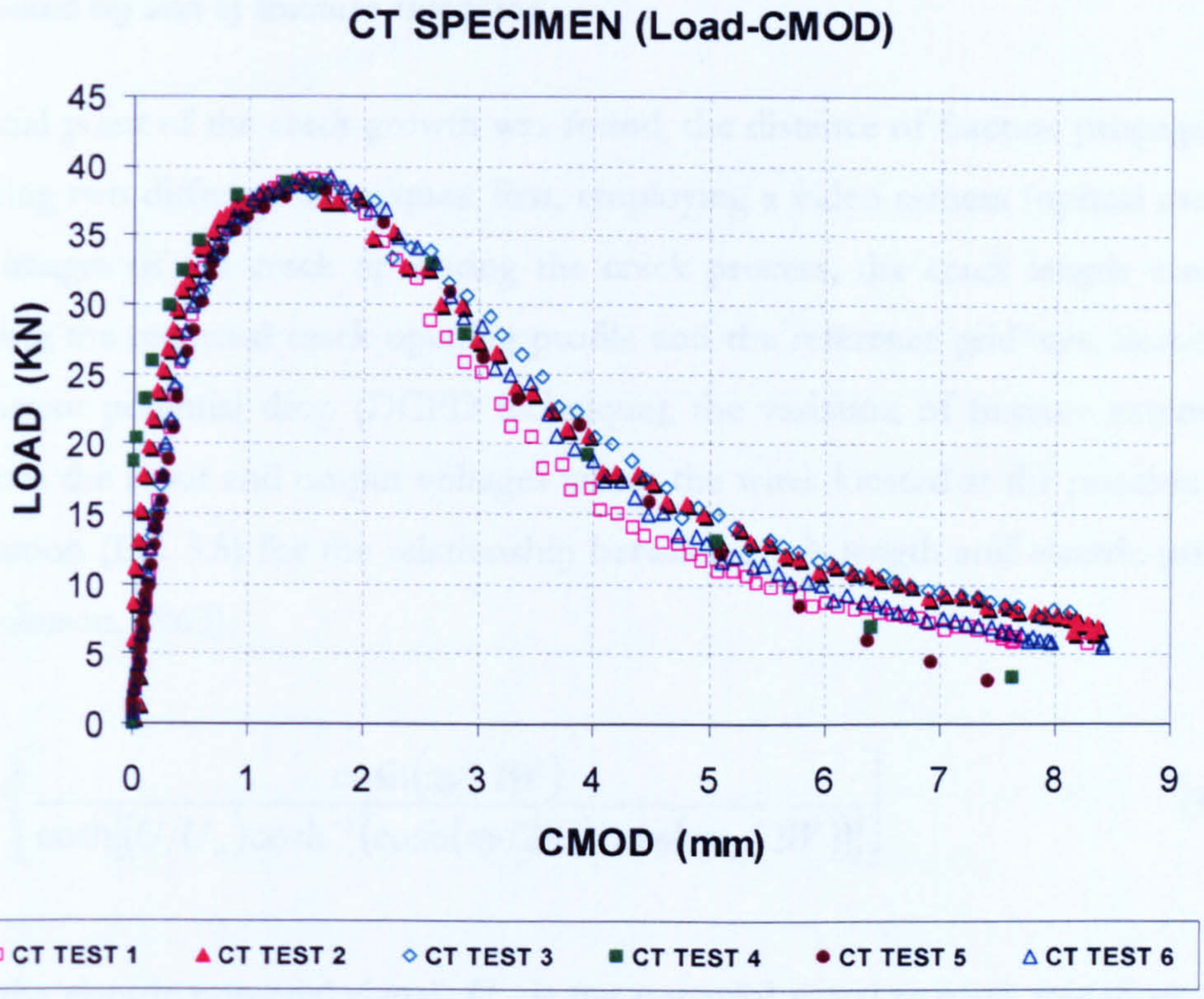

Fig. 3.39 Load – CMOD for the six C(T) specimens

Fig. 3.40a-c shows a series of images taken around the crack tip during the experiment. In these pictures can be seen that after some blunting, crack extension was initiated from the tip of the crack. In this investigation the crack growth is considered to have started when a small fracture is formed at the blunted tip. Therefore the variation of fracture extension for all data was evaluated after the visible crack initiation point.

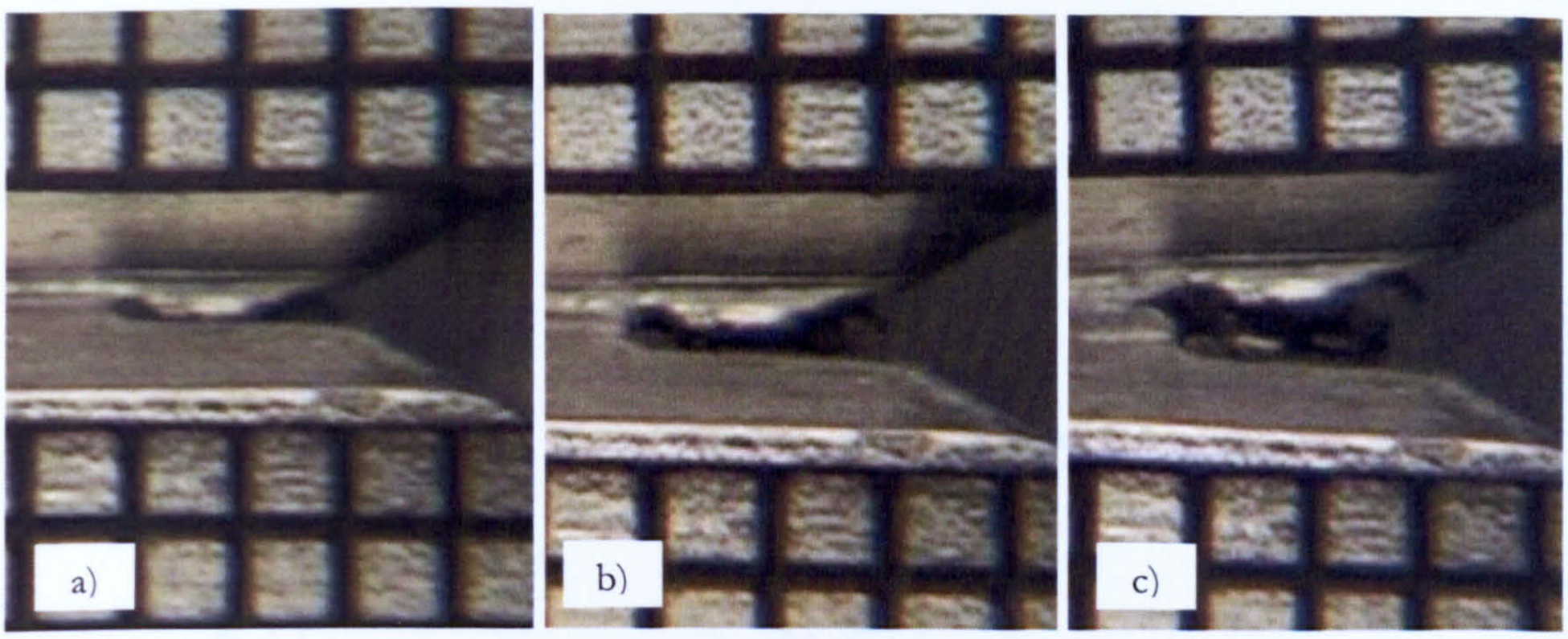

Fig. 3.40 Photographs around the crack tip in a C(T) specimen: a) initial crack length, b) blunted tip and c) fracture extension

Once the initial point of the crack growth was found, the distance of fracture propagation was calculated using two different techniques: first, employing a video camera (optical method) to capture the images of the crack tip during the crack process, the crack length was directly measured using the recorded crack opening profile and the reference gridlines. Second, using the direct current potential drop (DCPD technique), the variation of fracture extension was calculated from the input and output voltages where the wires located at the position that the Johnson equation (Eq. 3.5) for the relationship between crack length and electric potential is applicable (Johnson, 1965).

$$\frac{a}{W}=\frac{2}{\pi}\cos^{-1}\left[\frac{\cosh(\pi y/2W)}{\cosh\left[(U/U_o)\cosh^{-1}\left(\cosh(\pi y/2W)/\cos(\pi a_o/2W)\right)\right]}\right] \tag{3.5}$$

where U is the electric potential signal, U_0 is the potential signal at crack initiation, a is the crack length, a_0 is the initial crack length, W is the specimen width, and $2y$ is the initial spacing of the potential probes.

Fig. 3.41 shows the variation of the crack growth extension (Δa) as a function of CMOD using six C(T) specimens for the DCPD method and three of them marked with a reference grid for the optical technique.

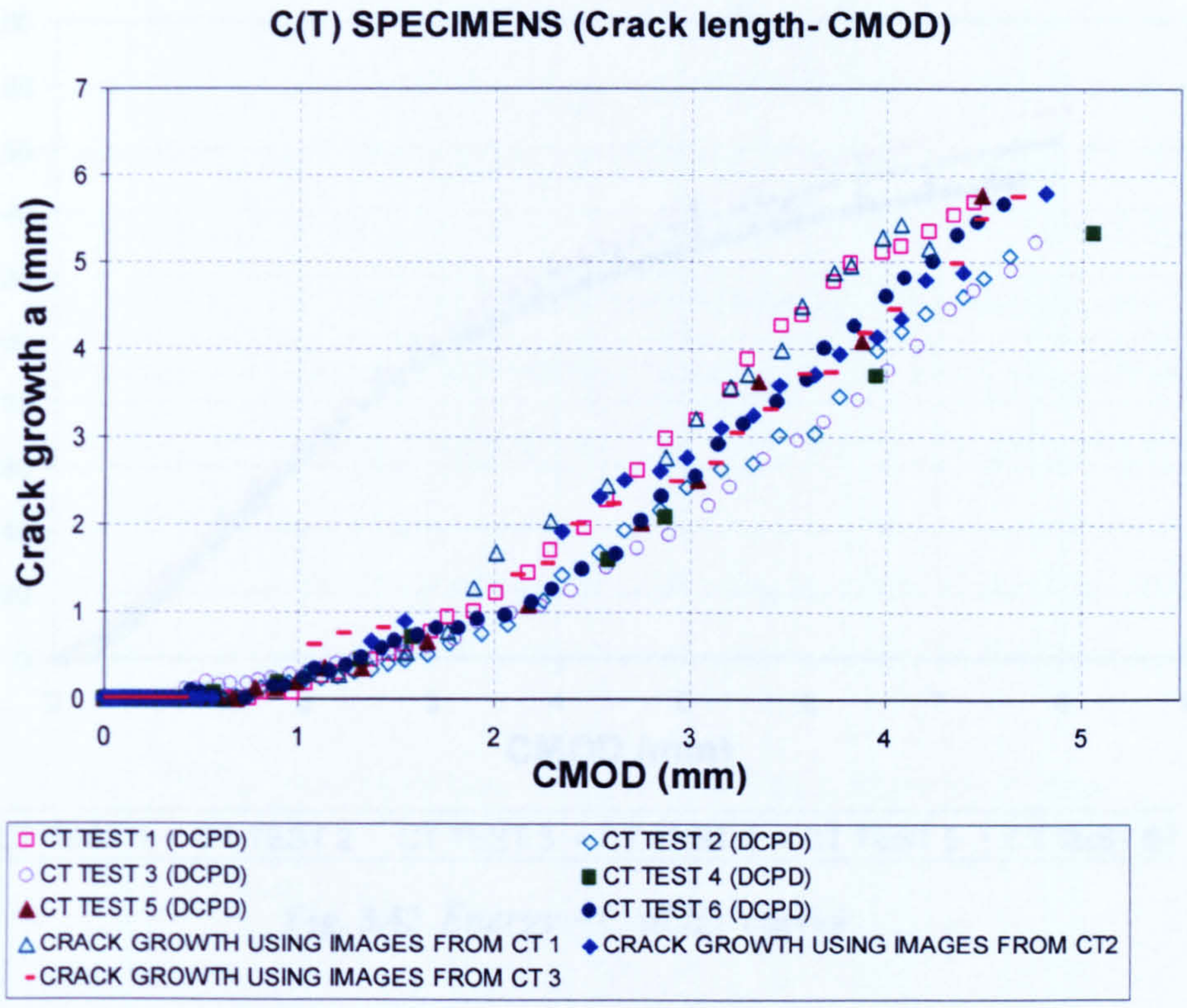

Fig. 3.41 Δa -CMOD curves results from DCPD and optical method

Test data from Fig. 3.39 was used also to estimate the energy release rate in flat fracture propagation. The measurement of the energy rate consisted of numerically calculating the area under the load-displacement graph. Fig. 3.42 shows the variation of energy versus CMOD and Fig. 3.43 displays the measurement of the rate energy against crack length.

To measure the specific flat fracture energy, the initiation energy was subtracted from the total fracture energy. The obtained energy was divided by the total fractured area, which gave a value of 1.4 J/mm^2 .

All this information is used later for the purpose to calibrate the conventional FE and CAFE methods and analyses of the ductile flat fracture of the X100 pipeline steel.

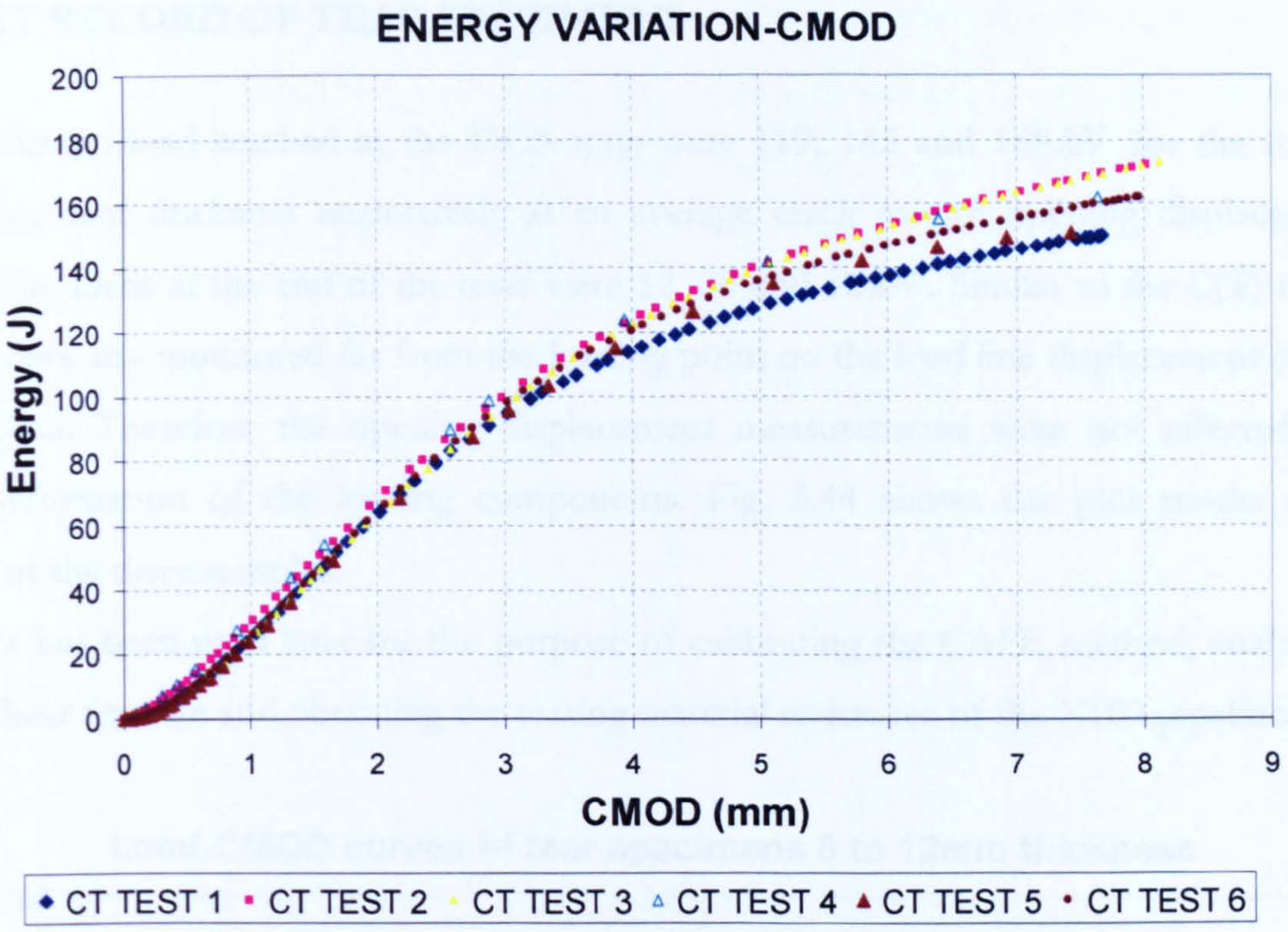

Fig. 3.42 *Energy – CMOD* **curves**

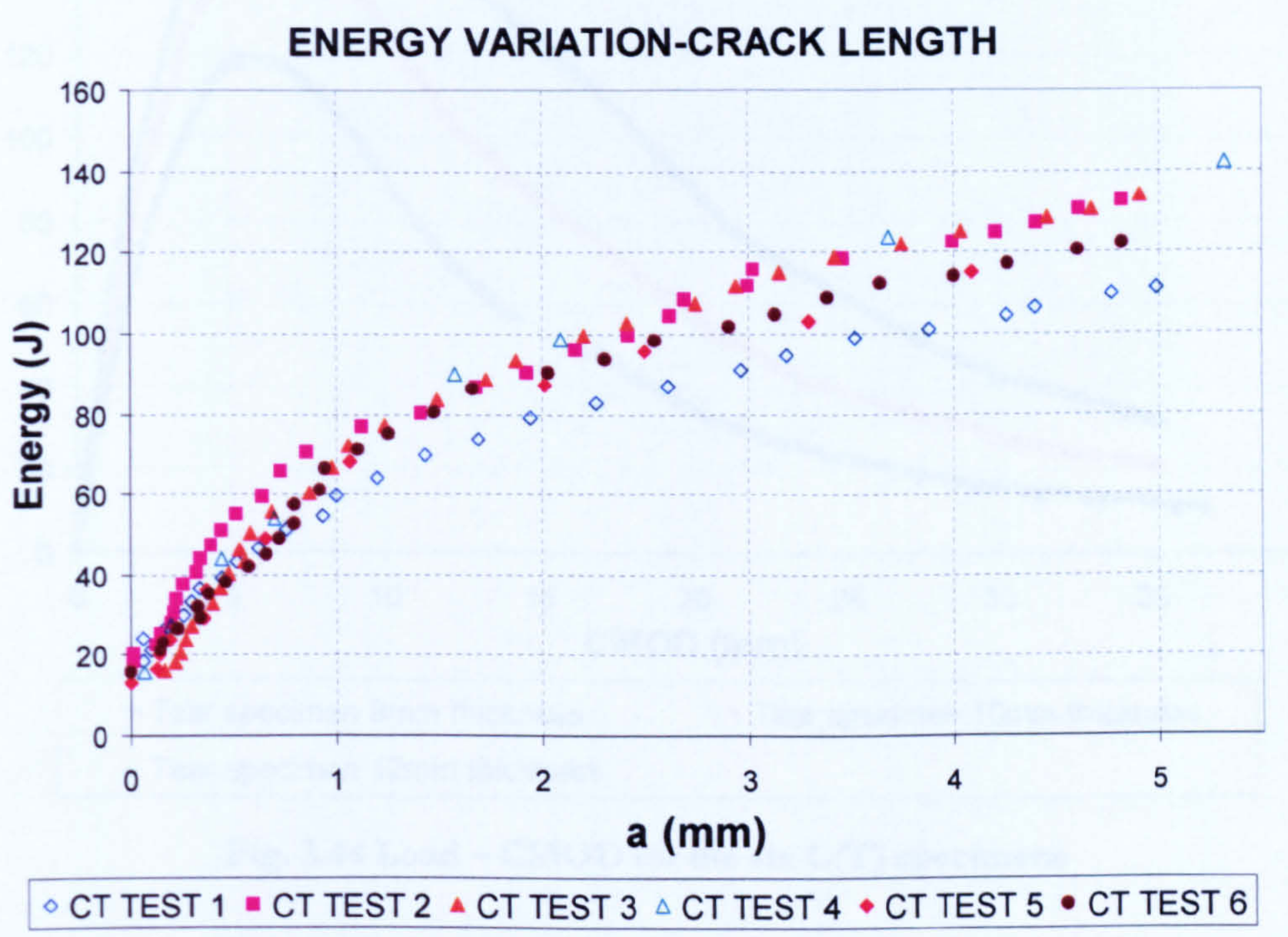

Fig. 3.43 *Energy – Δa* **curves**

3.6 TEST RECORD OF TEAR SPECIMENS

The maximum load reached in the DCB tests were 119, 145 and 168 kN for the 8, 10 and 12mm ligament thickness respectively at an average crack mouth opening displacement of 35mm. The loads at the end of the tests were 12, 20 and 32 kN. Similar to the C(T) tests, the CMOD data was monitored far from the loading point on the load line displacement (LLD) of the samples. Therefore the opening displacement measurements were not affected by the elastic deformation of the loading components. Fig. 3.44 shows the plot results of load-CMOD of the three samples.

This data has been used later for the purpose of calibrating the CAFE method, analysing the ductile shear fracture and obtaining the tearing material resistance of the X100 pipeline steel.

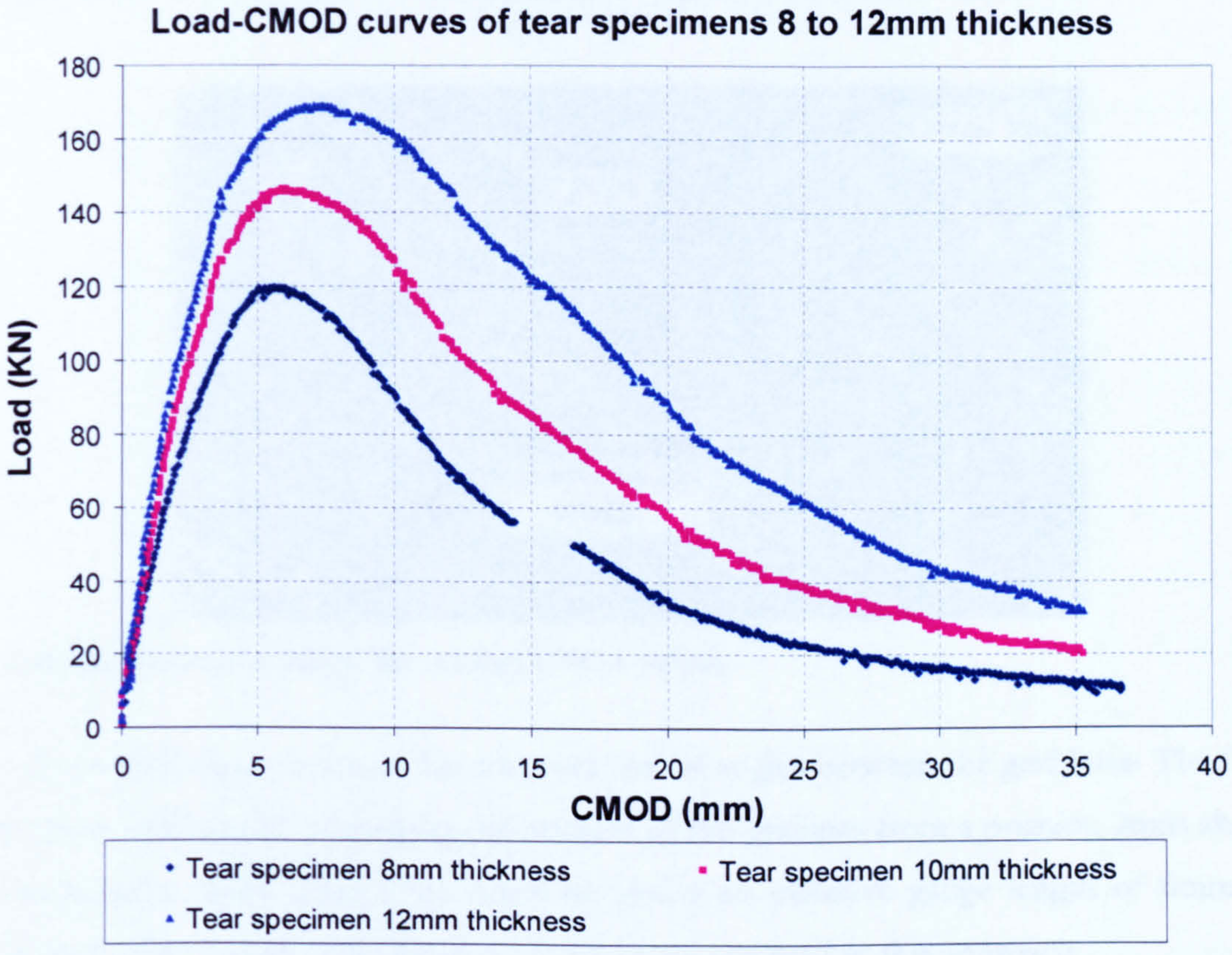

Fig. 3.44 Load – CMOD for the six C(T) specimens

Measurements of CTOA resistance curves were obtained by measuring the angle of the crack edges directly and by measuring the rotation of a grid that was etched onto the surface of the specimens. The measurements were determined from the video history coming from two optical methods used to record the cracking process. All the experimental curves are shown later in chapter five, the results and discussions.

The direct CTOA measurements were determined by recalling an individual image recorded on video tape and images processed from DIC, and a) locating the crack tip, b) locating points on both crack surfaces at some distance, x, behind the crack tip c) fitting straight lines between the crack tip and each point, and d) computing the angle between the straight lines.

To obtain reliable CTOA, values were taken from 3 measurements within the range of 1.5 to 2.5mm behind the current crack tip and averaged to get representative values of the stable tearing event. Fig. 3.45 shows the measurement range for the CTOA values.

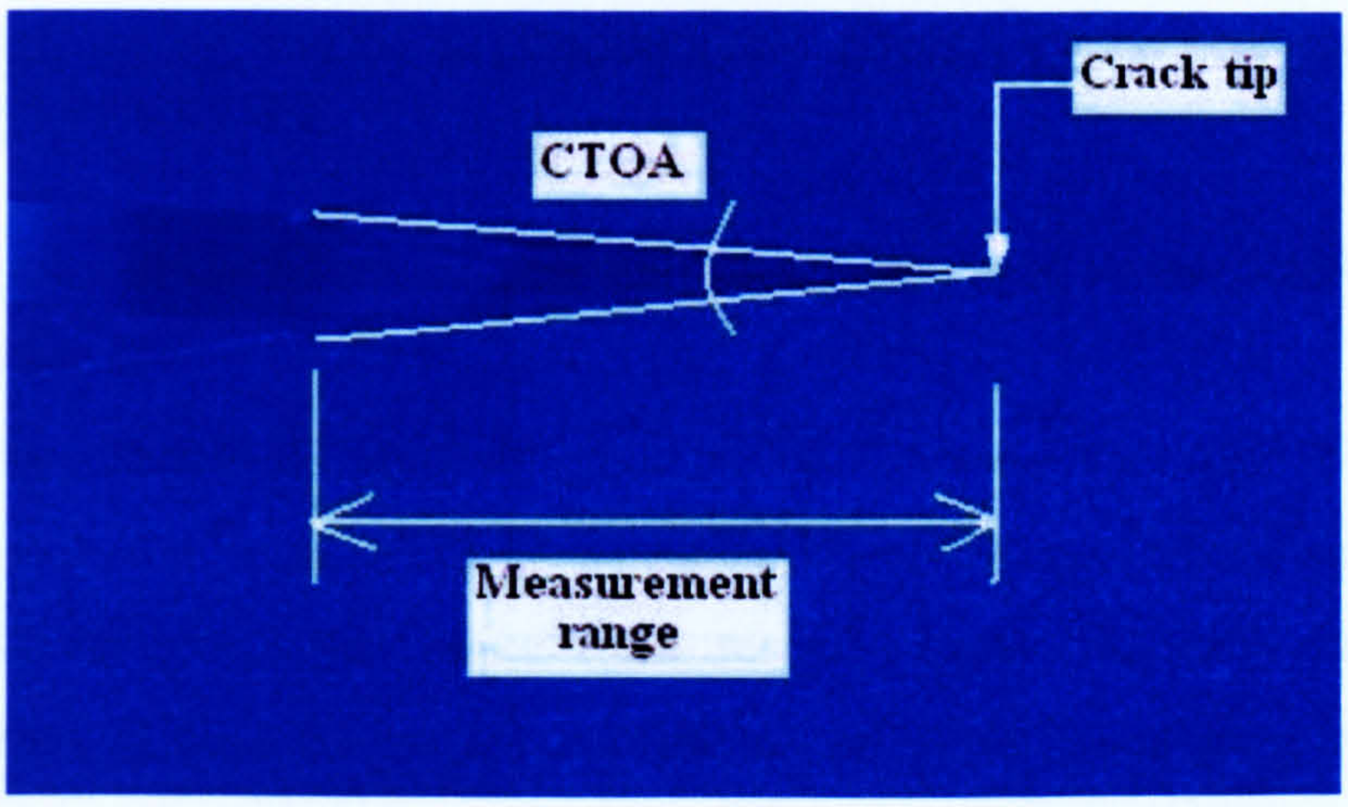

Fig. 3.45 Measurement range for critical CTOA values.

The second technique involved the measurement of angles between the grid lines. The CTOA values were obtained by measuring the rotation of the gridlines from a position 2mm ahead of the crack tip to 4mm behind the crack tip giving an effective gauge length of 6mm. This technique is indirect since data from crack edges are not used in this approach.

To obtain the representative value of the stable tearing, CTOA measurements were taken and averaged from the three first inclined lines of the deformed mesh close to the crack flanks. Fig. 3.46 illustrates the measurement range of the critical CTOA using the grid method. The grid had a pitch of 1x2mm which provided adequate resolution for the purposes and it also facilitated in tracking the crack.

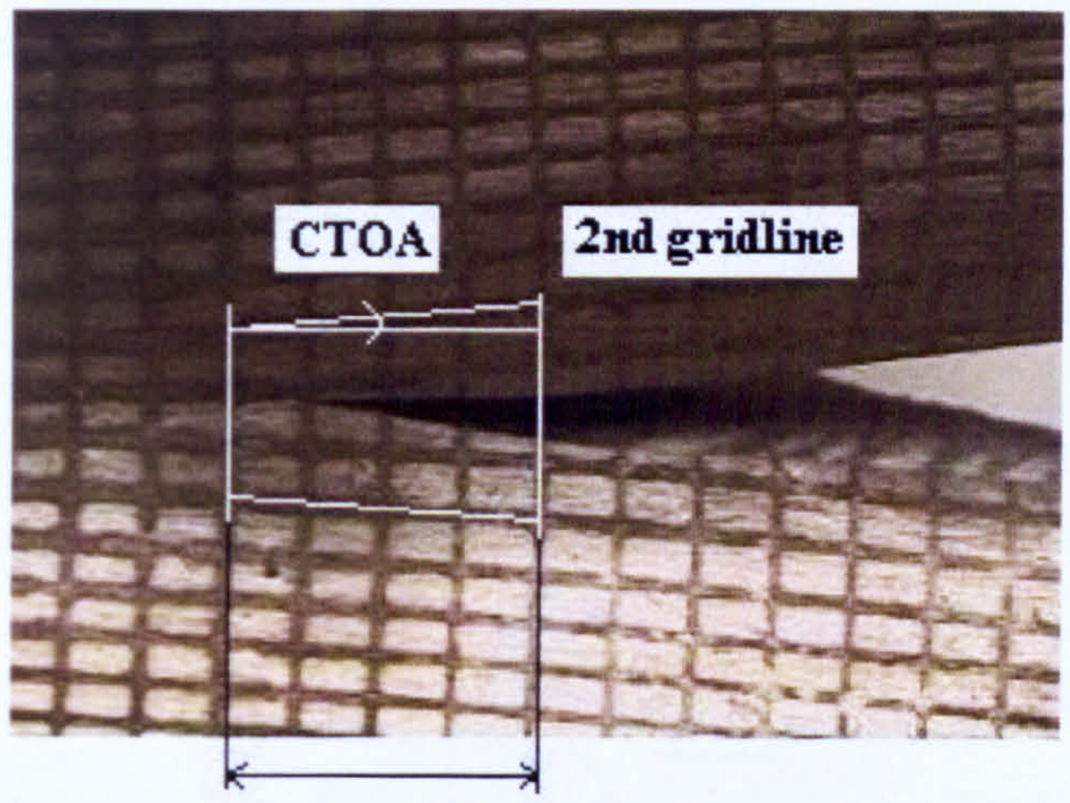

Fig. 3.46 Measurement of the CTOA values from the grid method.

3.7 SCANNING ELECTRON MICROSCOPY OBSERVATIONS (SEM) OF THE MICROSTRUCTURE

SEM metallography of the microstructure, etched with 2% nital, of the X100 pipeline steel is shown in Fig. 3.47a-f.

Fig. 3.47a-b shows the revealed microstructure in the L-T plane of the steel. Fig. 3.47c-d is the microstructure observed in the S-L plane, which has revealed very marked strips oriented along the longitudinal direction. This arises from recent progress in the technology for the controlled-rolling (CR) and thermo-mechanical control (TMC) processing of steels. Finally, Fig. 3.47e-f is that corresponding to the S-T plane. This plane area displayed some marked strips along the transverse direction, but these strips are not as noticeable as those observed in the S-L plane.

The observed microstructure under SEM is similar to that acicular ferrite (AF) observed for low carbon Mn-Mo-Nb micro-alloyed steels, which presents various fine nonequiaxed grain sizes distributed in a random manner (Xiao F. et al. 2005, Xiao F. et al. 2006, Shanmugam S. et al. 2006, Zhao et al. 2003, Zhao et al. 2005 and Sharma U. and Douglas G. 2000). The acicular ferrite microstructure is becoming an optimal microstructure for pipeline steels because it satisfies the high strength and toughness requirement.

The term of acicular ferrite steel was firstly described by Smith et al. in the early 1970, and it has been widely accepted in pipeline engineering as an independent microstructure different from the conventional pipeline steels with ferrite-pearlite microstructure. This acicular ferrite microstructure is defined as a highly substructured non-equiaxed phase, which is formed during the continuous cooling process by mixed diffusion and shear transformation mode at a temperature range slightly higher than upper bainite (Smith et al. 1972 and Smith et al. 1976).

The experimental results of the researchers above have indicated that in order to obtain the good combination of the high strength and toughness for acicular ferrite pipeline steel, it is necessary to control thermo-mechanical control process and cooling conditions parameters, and the chemical compositions of the whole production process. The advanced thermo-mechanical control process is an effective method to obtain good properties by controlling the final acicular ferrite microstructure for micro-alloyed pipeline steels. The hot deformation affects the microstructure refinement by effective nucleation and growth of acicular ferrite, so that, the final microstructure and mechanical properties are depended strongly on controlled rolling parameters and cooling conditions of the plate.

Grain refinement in the steel is enhanced through a combination of controlled rolling and microalloying.

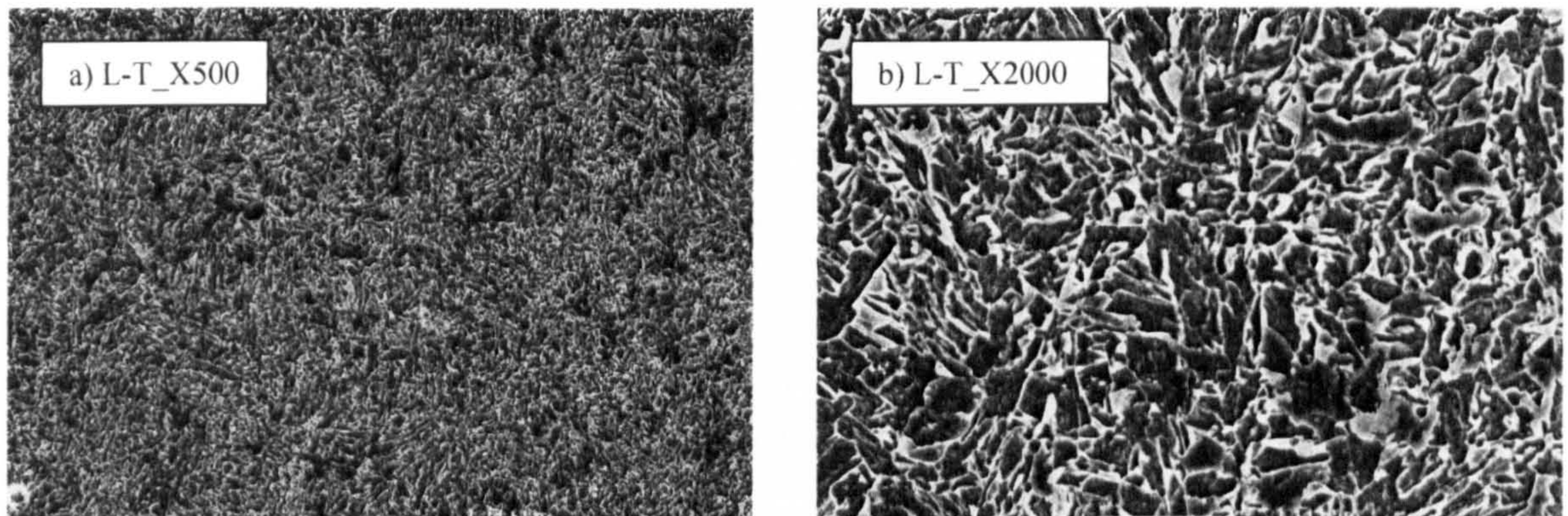

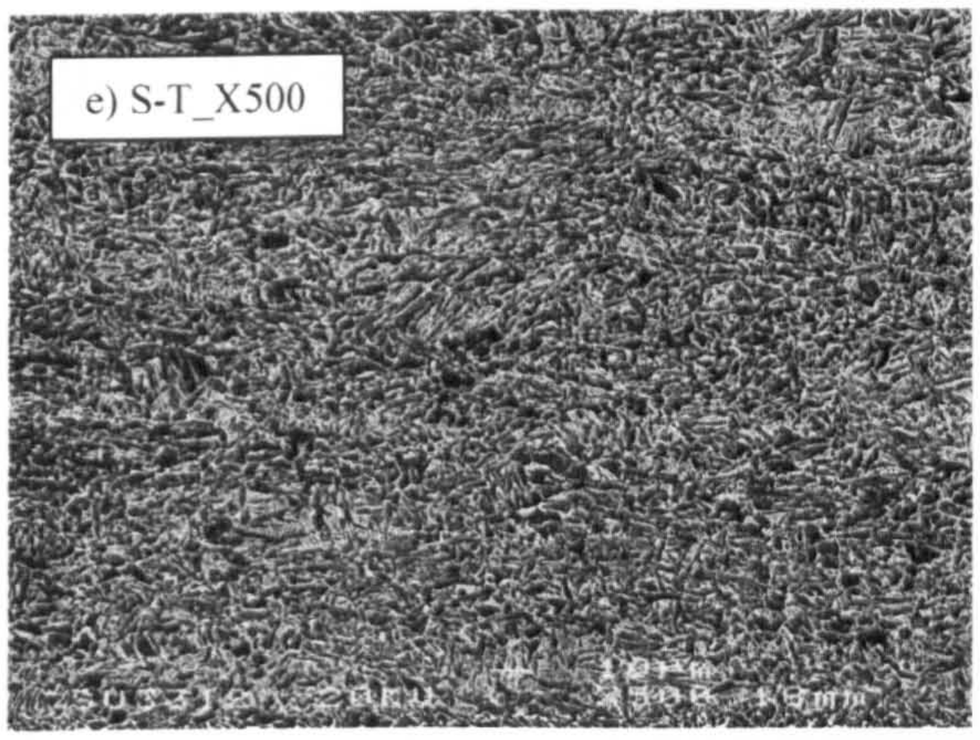

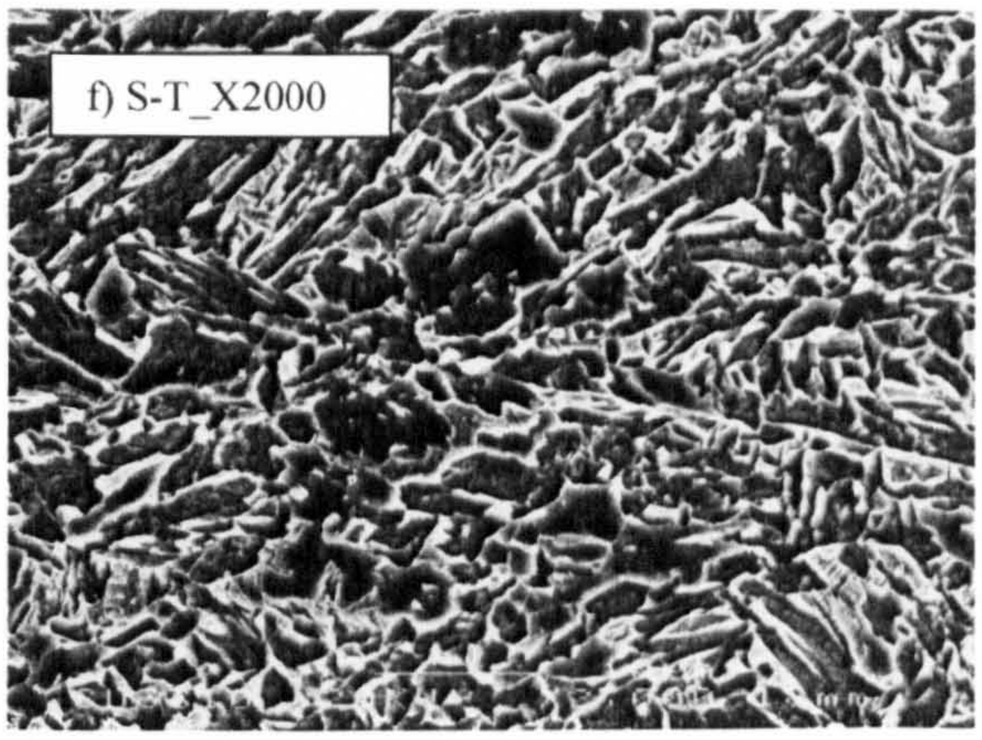

Fig. 3.47 Microstructure revealed (nital 2%) in the planes L-T,S-L and S-T of the X100 pipeline steel

CHAPTER 4

4.1 MICROMECHANICAL DAMAGE MODELS UTILISED FOR THE DUCTILE FRACTURE

The aim of this phase of the computer simulations is to tune the material constitutive damage parameters for the flat and slant cracked specimens. In order to do this calibration, models for porous materials proposed by Rousselier (1987) and the extended Gurson theory (Gurson, 1977a; Tvergaard, 1981) were used in this research to characterise the growth and coalescence process driving the ductile failure. The first was developed based on the thermo-dynamical considerations whereas the second one was derived from micromechanical description of the porous material. In both cases, damage is represented by a single scalar variable: the porosity f. These theories have shown to be very suitable for ductile materials, which is the case for the high strength pipeline steel (API grade X100) studied. The GTN damage model has been employed in a conventional finite element (FE) technique and the Rousselier one is used in a hybrid cellular automata finite element, CAFE, technique.

As referred in chapter two (equations 2.9-2.10), the GTN model is expressed in the form of the yield potential:

$$\Phi = \left(\frac{\sigma_{eq}}{\sigma_Y}\right)^2 + 2q_1 f^* \cosh\left(q_2 \frac{3p}{2\sigma_Y}\right) - \left(1 + q_3 (f^*)^2\right) = 0$$

The function $f^*(f)$ was chosen as:

$$f^*(f) = \begin{cases} f & f \le f_c \\ f_c - \dfrac{f_u^* - f_c}{f_F - f_c}(f - f_c) & f > f_c \end{cases}$$

where σ_{eq} is the von Mises equivalent stress, σ_Y the material yield strength, p the hydrostatic stress, q_1, q_2 and q_3 are material constants, f_c is the critical value of void volume fraction, f_F is void volume fraction at final fracture and $f_u^* = 1/q_1$.

On the other hand, the consistent and simple ductile damage theory introduced by Rousselier, as described in chapter two (equations 2.15-2.18), has the plastic potential model of the form:

$$\frac{\sigma_{eq}}{\rho} - H\left(\varepsilon_{eq}^{p}\right) + B(\beta)D\exp\left(\frac{\sigma_m}{\rho\sigma_1}\right) = 0$$

where:

$$\dot{\beta} = \dot{\varepsilon}_{eq}^{p} D\exp\left(\frac{\sigma_m}{\rho\sigma_1}\right)$$

$$\rho(\beta) = \frac{1}{1 - f_0 + f_0 \exp\beta}$$

$$B(\beta) = \frac{\sigma_1 f_0 \exp\beta}{1 - f_0 + f_0 \exp\beta}$$

where β is a scalar damage variable, B is the damage function, ρ is dimensionless, D and σ_1 are material constants and $H\left(\varepsilon_{eq}^{p}\right)$ is a term describing the hardening properties of the material.

4.2 CALIBRATION OF THE MODELS

Any continuous ductile damage model has to be calibrated for a particular material before it can be used to predict the fracture behaviour of a structural component, so that model parameters can be considered true material properties. The plan to calibrate the constitutive properties of the GTN and Rousselier model for the conventional FE and CAFE techniques respectively consisted of a trial-and-error series of simulations, comparing the experimental record to the simulation data until the model response matched the experimental information.

To find the best-fitted GTN constitutive parameters, five micromechanical parameters q_1, q_2, f_c, f_F and L_{FE} (value of the element size L_{FE} is representative of the large inclusion spacing in the material) were explored in the 3D damage simulations of flat specimens.

In 3D CAFE analysis, the Rousselier damage parameters D and σ_1 were adjusted by trial and error simulations for the flat and slant cracked specimens. The parameters of mean critical

value of the damage variable ($\bar{\beta}_F$), standard deviation of the critical value of the damage variable that is used for normal distribution of the elements over the fracture plane, which are removed during the crack growth process $STD\beta_F$ and number of cells per linear finite element $\sqrt[3]{M_D}$ were adjusted as well for the good prediction of the material behaviour. The total number of cells per ductile CA, M_D, was chosen so that the linear size of an individual CA cell is close to the ductile damage cell size, L_D. The finite element in this case only was refined enough to provide adequate resolution of the stress-strain fields in the damage zone and the cellular automata deal with the evolution of damage at the correct micro-structural scale. If a cubic finite element of size $L_{FE} \times L_{FE} \times L_{FE}$ is assumed then the Eq. (4.1) can be used to choose M_D:

$$\frac{L_{FE}}{\sqrt[3]{M_D}} = L_D \tag{4.1}$$

Where $\sqrt[3]{M_D}$ is the number of cells per dimension of a cubic ductile CA.

The other model parameter which requires proper tuning in the CAFE model for the ductile array is, c_D, the concentration factor for ductile CA array. If there is a dead ductile cell then all neighbouring cells which lie on or near the plane perpendicular to the direction of the maximum principal stress will receive some strain concentration. This condition reflects the strain concentration in the material surrounding a void. The value of $c_D = 1.4$ was used for all simulations as proposed in Shterenlikht (2003) for the modelling of a Charpy test. Shterenlikht has stated that the value of this parameter was based on rough guess and some data fitting, and a more detailed understanding of the fracture process at the micro-scale might help to find metallurgically meaningful values.

The term f_0 is the initial void volume fraction, which can be calculated from Franklin's formula (1969) as following:

$$f_0 = f_v \frac{(d_x d_y)^{1/2}}{d_z} \tag{4.2}$$

$$f_v = 0.054\left(S\% - \frac{0.001}{Mn\%}\right) \tag{4.3}$$

where d_x, d_y and d_z are the average dimension of the inclusions. If a spherical inclusion shape is assumed, Eq. (4.2) gives $f_0 = f_v$. From this an initial void volume fraction $f_0 = 3x10^{-5}$ was found for this steel.

To account for strain hardening, the experimental stress-strain curves determined by the uniaxial tension tests (Fig. 3.31) were used in the simulations.

4.3 NUMERICAL MODELS TO CHARACTERISE FLAT FRACTURE

To characterise the flat fracture, two sets of 3D computational analyses were conducted for the flat specimens and the results compared. The first set was a conventional finite element (FE) method in which the element size must be chosen with regard to the micro-structural scale of the ductile damage process. The second set of analyses used the hybrid cellular automata finite element, CAFE, technique.

The 3D conventional finite element analyses were performed using the commercial code ABAQUS/Explicit code (version 6.4) and the CAFE modelling was realised via the user material subroutine VUMAT in the same FE software. This allowed the material properties and the model dimensionality to be combined. The plasticity model used in the FE software followed the Prandtl-Reuss formulation with a von Mises yield criterion and isotropic hardening. For all models, the geometry, mesh, the set of nodes and elements for the loads and boundary conditions were previously designed in ANSYS (version 7.0) and HyperMesh (version 9.0) codes, and exported to ABAQUS to obtain all the simulation results. All simulations were performed in a PC Pentium 4 CPU 3.2 GHz, 1 GB of RAM and 120 GB disk capacity. Appendix 1 shows the code used for the simulations in ABAQUS for the classic FE and CAFE methods in tensile tests. It should be pointed out here that the same input files can be modified to suit the geometry and boundary conditions of flat C(T) specimens.

4.3.1 Computer modelling of tensile tests

For the tuning process, experimental data of Load-Diametral contraction (Chapter 3) of three sets of laboratory specimens (smooth and notch tensile bars) with different constraint levels were used.

3D models of the tensile tests in the L, T, and 45 directions are shown in Fig. 4.1. Due to the symmetry, only one quarter of the smooth and notched bars were modelled. All 3D meshes

consisted of 8-node reduced integration brick elements (C3D8R). Loads and boundary conditions were imposed on the specimens according to their directions. (i.e.) In the tensile test of transverse direction, all nodes located on the vertical symmetry T-L and T-S planes were constrained in the short transverse and longitudinal orientation respectively, and nodes located on the horizontal symmetry S-L plane were constrained in the loading direction. Loading of the model was conducted by imposing a prescribed displacement on the upper face of the model in the transverse direction.

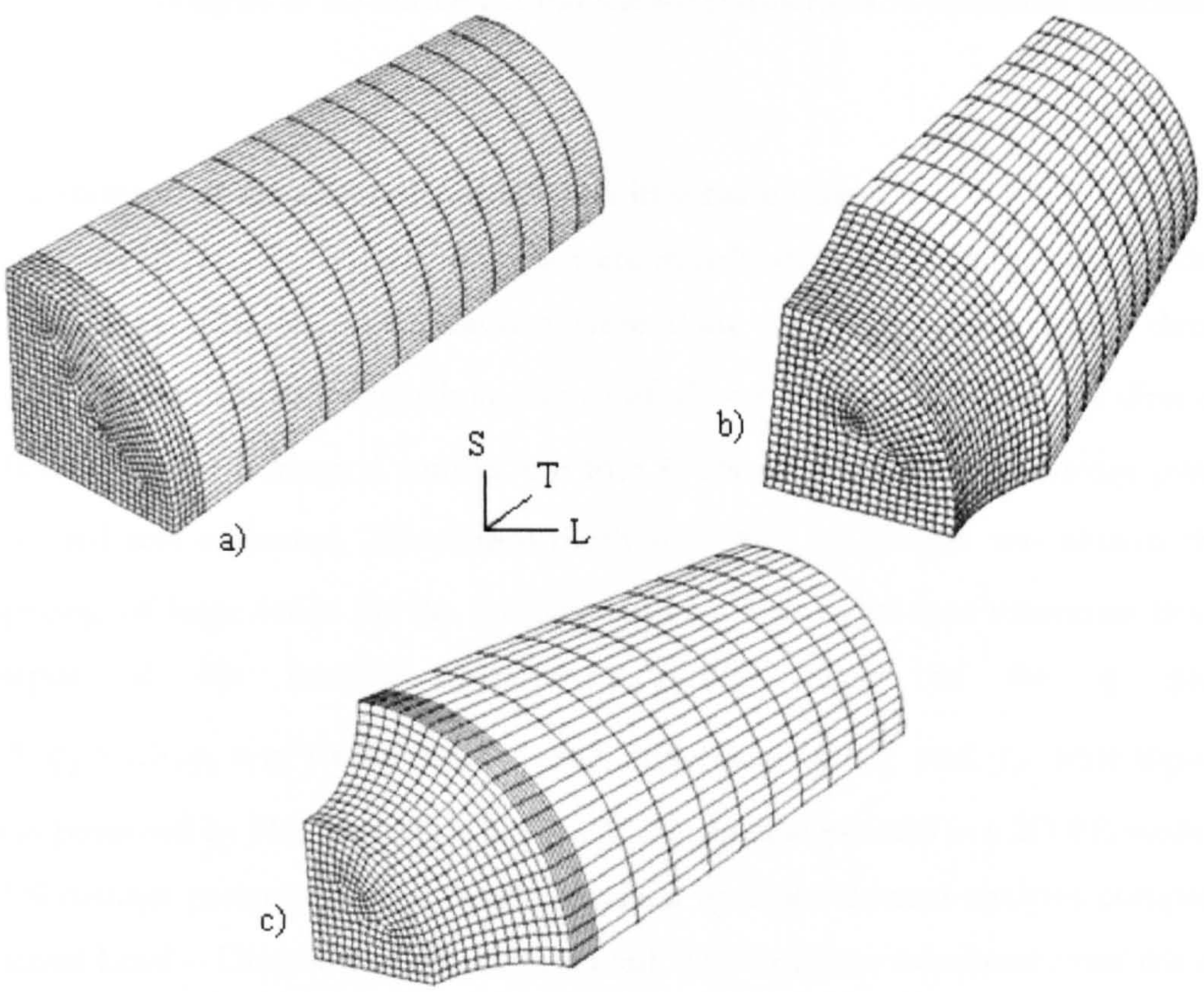

Fig. 4.1 Examples of 3D tensile FE models for simulations in L,T an 45 orientations. a) 3D plain bar, b) and c) 3D notch tensile specimens with a notch radius R_0=4mm and R_0=3mm respectively

Cylindrical and square cross-section 3D FE models were employed for simulating testing in the thickness "S" orientation (Fig. 4.2). For the cylindrical tensile specimens, only one quarter was modelled. For the square tensile samples, in spite of symmetry conditions, a complete model was used to obtain the whole field strain deformation in the damage zone (See Chapter 4). All analyses were carried out using 3D elements (C3D8R).

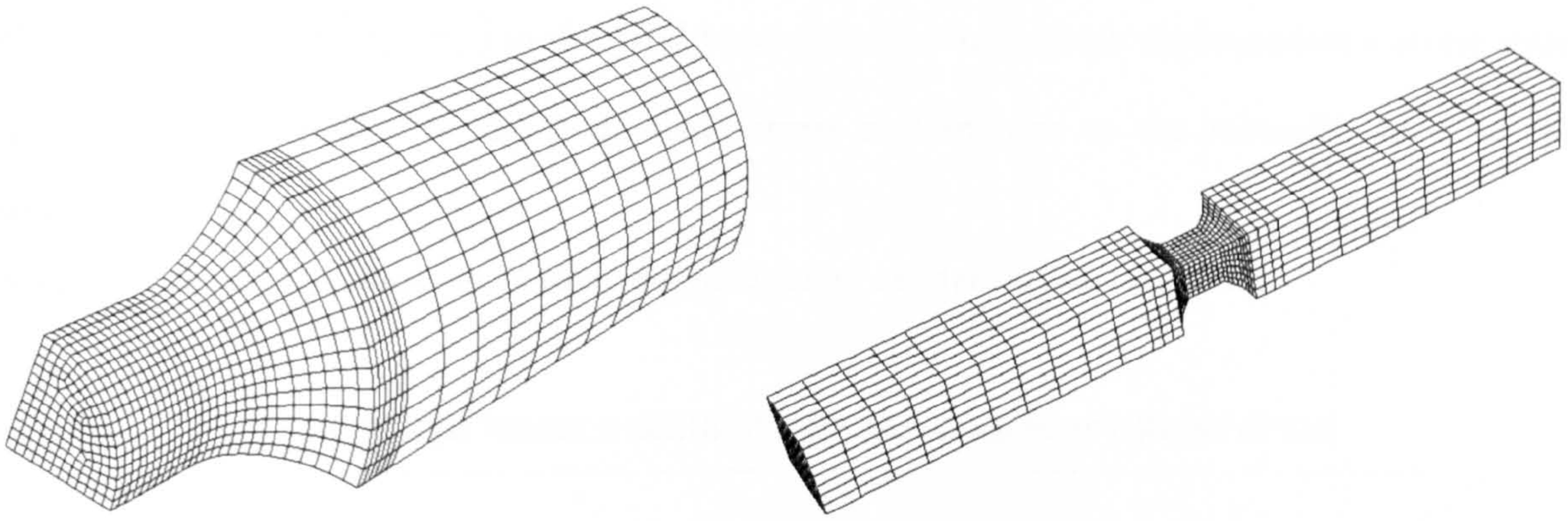

Fig. 4.2 Examples of 3D tensile FE models for simulations in thickness direction

4.3.1.1 Calibration of the damage parameters in tensile tests

3D simulations of isotropic ductile damage were initially carried out for tensile specimens in the 45° direction. The initial simulations were done using the experimental data (load-Φ contraction) from a notched tensile specimen of $R_0 = 4mm$ in the 45_N6_LT direction.

In the first set of 3D numerical studies, the four GTN micromechanical damage parameters were explored and calibrated. The critical mesh size of $l_{FE} = 200\mu m$ was chosen from the mean spacing of large voids on the fracture surface. This value was measured from SEM photographs of flat fracture specimens. Typical values of the q parameter ($q_1 = 1.5, q_2 = 1.0, q_3 = q_1^2$) were initially used, and values of f_c and f_F were input in the analysis as proposed by Hashemi (2004b) for a X100 pipeline material in a 2D FE study.

The GTN damage parameters were finally obtained by finite element analyses comparing the experimental Load – Diametral contraction record. The load was calculated from the reaction at the top surface of the tensile test models, whilst the contraction was monitored in the damage zone.

Plots of the test data and simulations of different values of damage parameters for notched bar tensile specimen of 8mm gauge diameter and 6mm notch radius are shown from Figs.4.3 to 4.6.

From the FE analysis, it has been observed that higher values of q_1 and q_2 accelerate the failure of the material and higher values of f_c and f_F cause a delay in the damage process. It was found that the model was very sensitive to q_2. This sensitivity is directly associated with

the modification of (σ_m/σ_y) in the yield potential equation, which characterises a stress state. Therefore q_2 is related to the hydrostatic stress and in turn to the triaxiality level of the material.

Values of the final calibration of damage parameters are set out in Table 4.1.

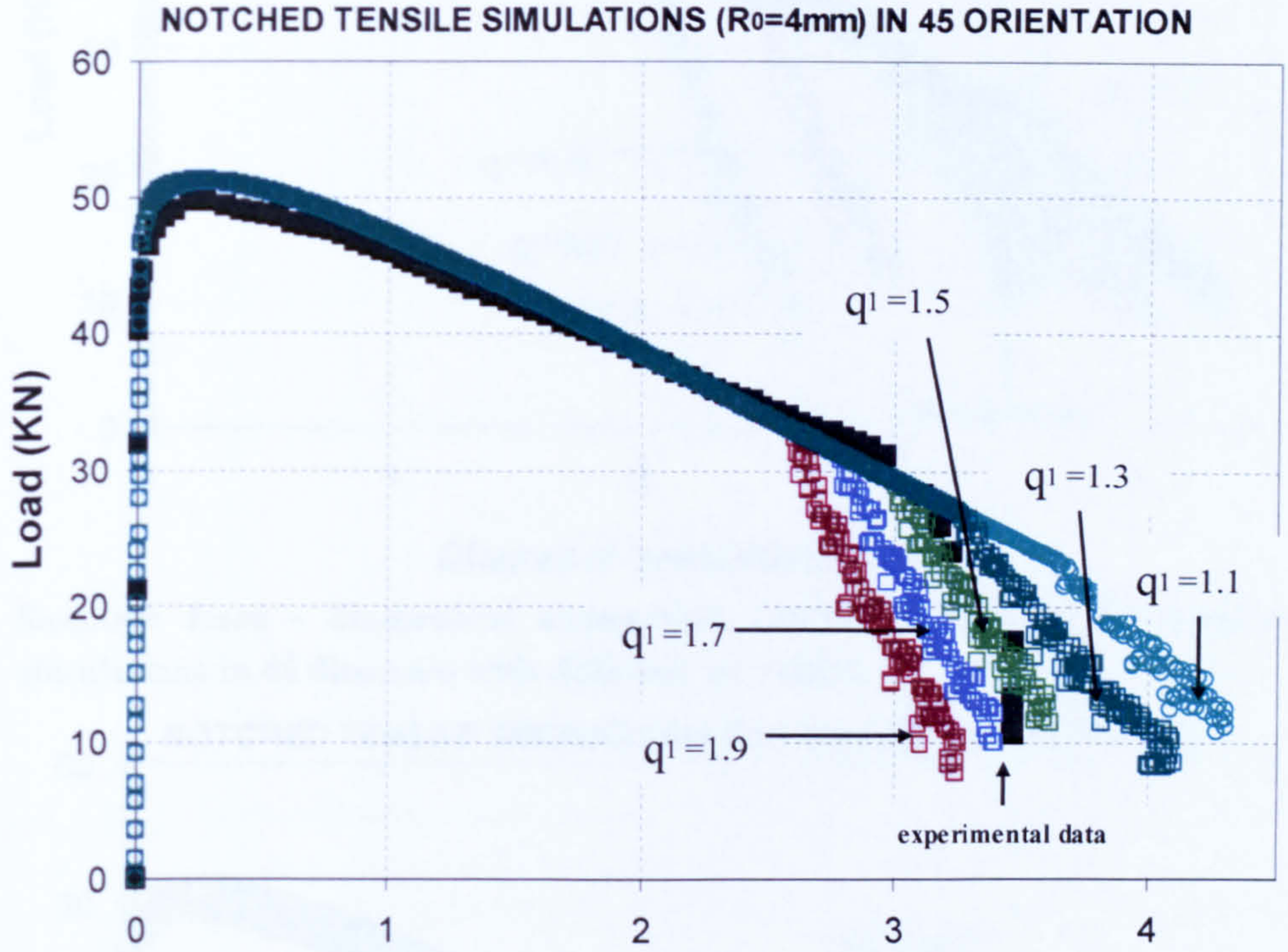

Fig. 4.3 Reaction force - diametrical contraction curves for the 3D FE notched tensile simulations in 45 direction with different q_1 values.

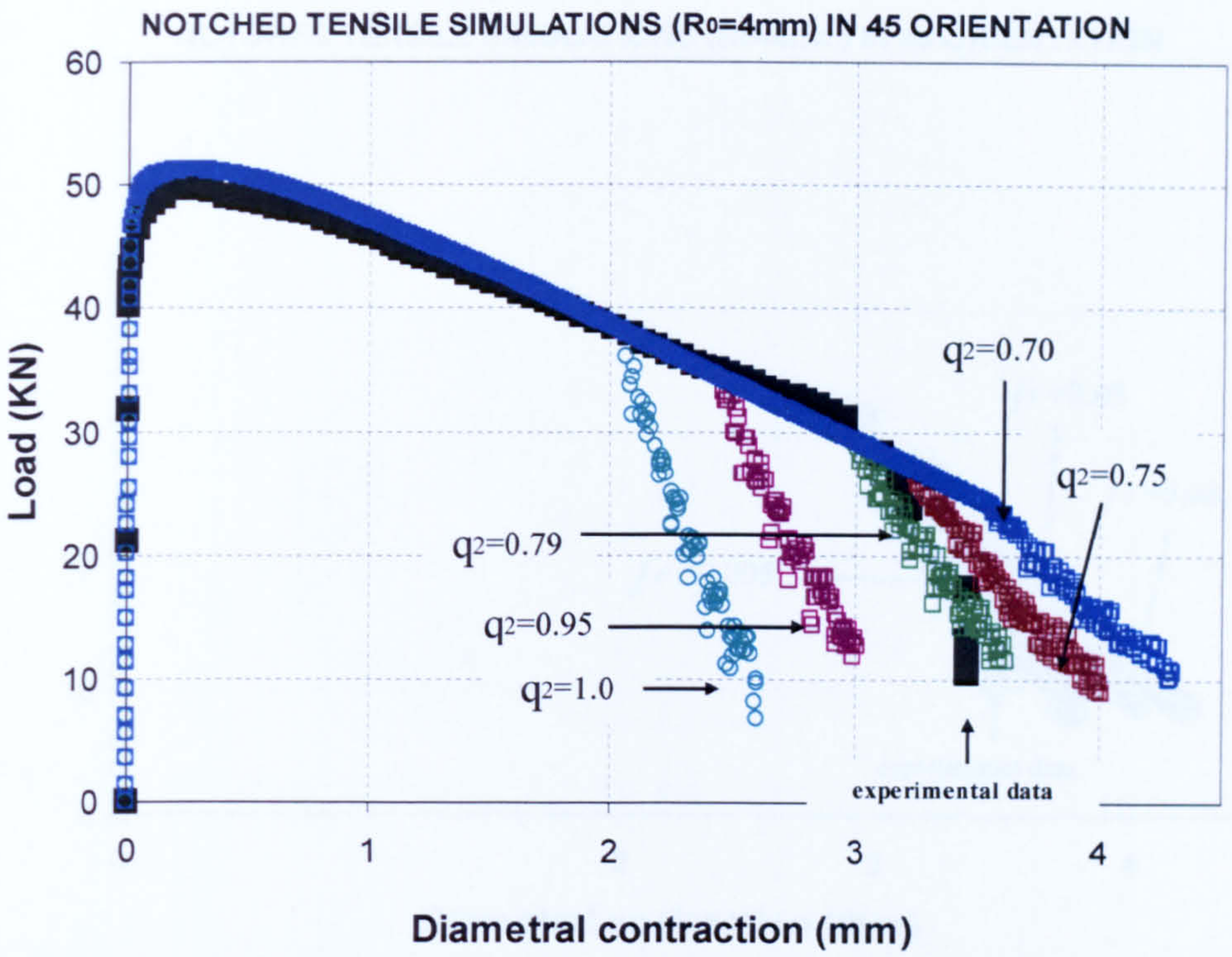

Fig. 4.4 Reaction force - diametrical contraction curves for the 3D FE notched tensile simulations in 45 direction with different q_2 values.

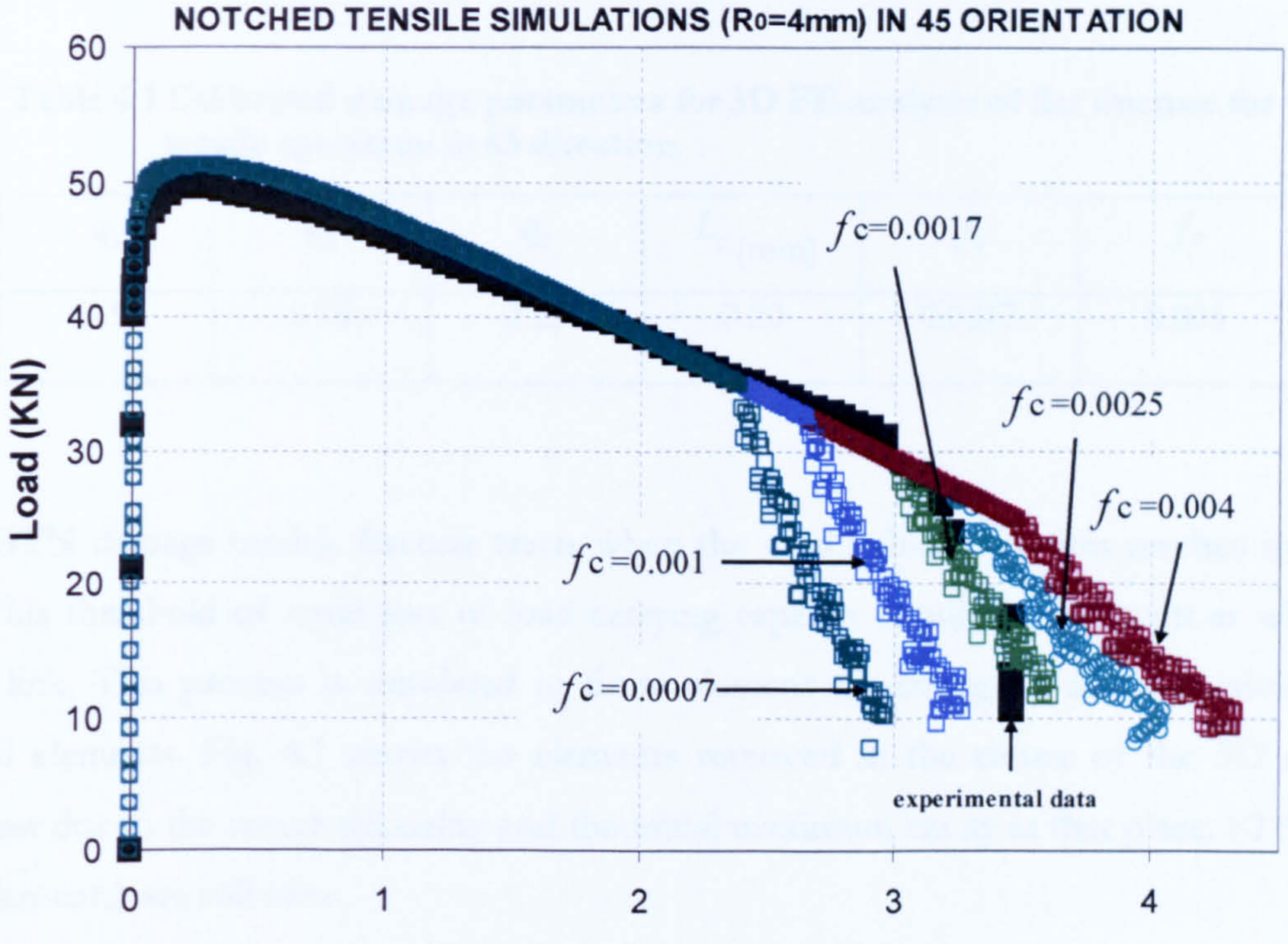

Fig. 4.5 Reaction force - diametrical contraction curves for the 3D FE notched tensile simulations in 45 direction with different f_c values.

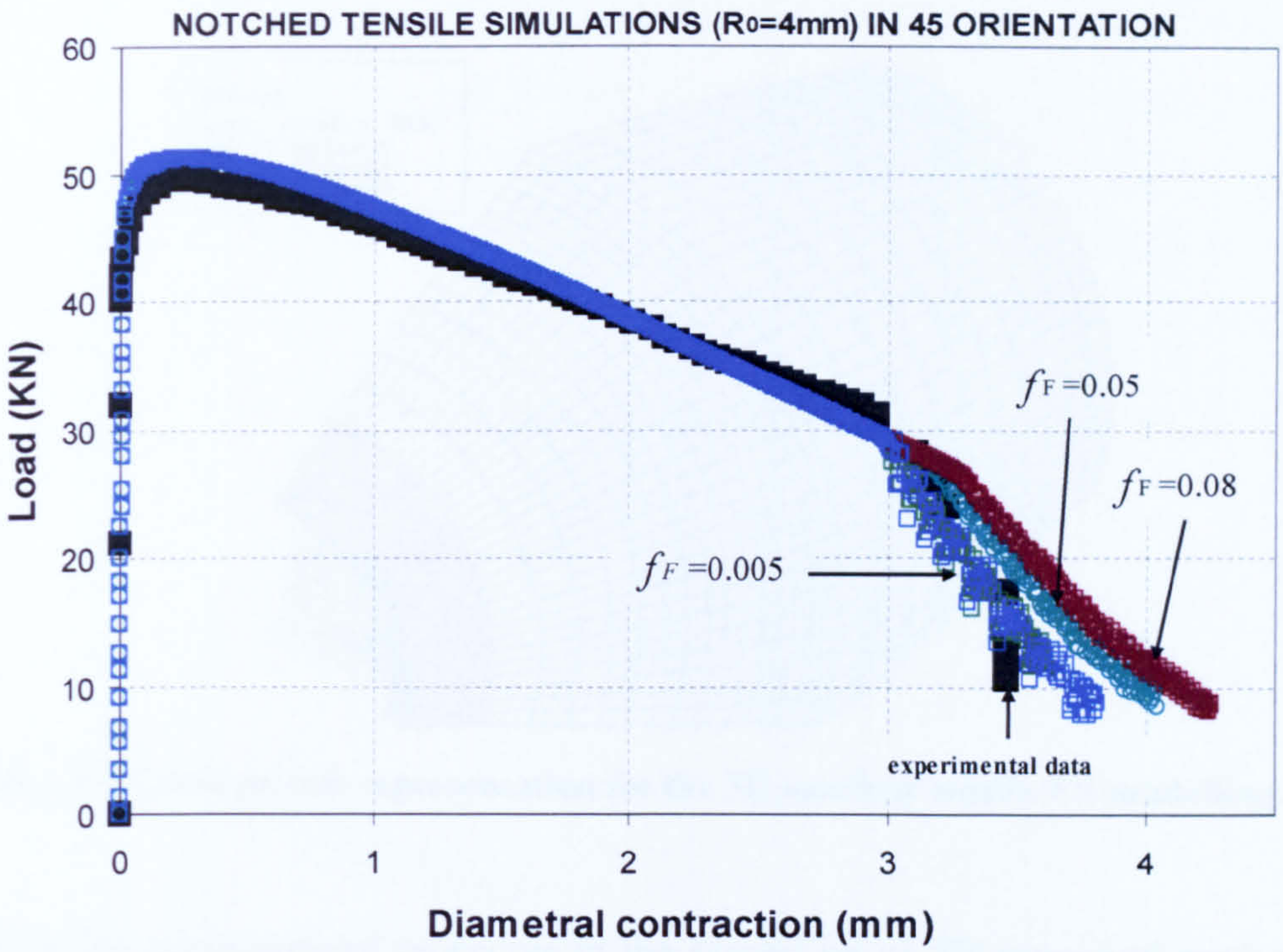

Fig. 4.6 Reaction force - diametrical contraction curves for the 3D FE notched tensile simulations in 45 direction with different f_F values.

Table 4.1 Calibrated damage parameters for 3D FE analysis of flat fracture for tensile specimen in 45 direction.

q_1	q_2	q_3	L_c (mm)	f_c	f_F
1.5	0.78	2.25	0.20	0.0017	0.005

In the GTN damage model, fracture starts when the void volume fraction reaches its critical value. This threshold of rapid loss of load carrying capacity simulates the point at which the cavities link. This process is simulated in finite element modelling by the extinction of the damaged elements. Fig. 4.7 shows the elements removed in the centre of the 3D notched tensile test due to the severe triaxiality and the initial maximum cavity at that place. STATUS = 1 (red elements) are still alive.

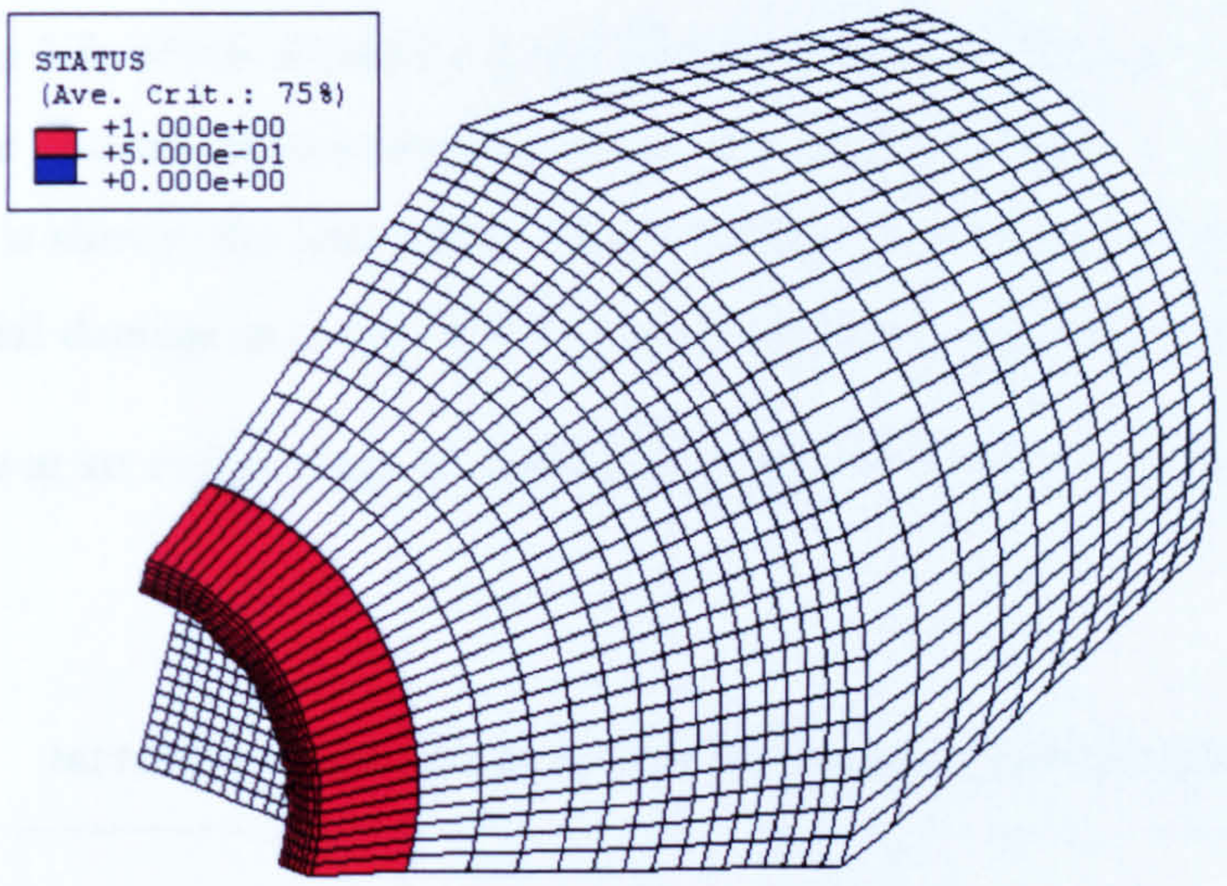

Fig. 4.7 Crack growth representation for the 3D notched tensile FE modelling.

Applying similar computational procedure in the second set of 3D numerical predictions for the CAFE model as used for the classical FE analysis, the two micromechanical damage parameters in Rousselier model: D and σ_1 were adjusted to represent the experimental area reductions at fracture. Values recommended by Rousselier (1987) of $D = 2$ and $321MPa$ were input in the initial simulations. The initial void volume fraction was obtained from Franklin's formula ($f_0 = 3x10^{-5}$). A suitable FE size of 0.8mm was chosen to give adequate and fast resolution of the stress-strain field behaviour in the damage zone, such that four ductile cells were attached at each FE providing a cell size of 0.2mm, which is representative of the large inclusion spacing in the material. Initial inputs values of $STD\beta_F = 1.25$ and $\bar{\beta}_F = 8$ were initially used as proposed in Shterenlikht (2003). These initial values however lead to an underestimation of the ductility (See Fig. 4.8). Therefore trial and error simulations were carried until the model response matched the experimental data.

Plots of simulation data with different values of the Rousselier damage parameters, D and σ_1, and the mean critical value of the damage variable ($\bar{\beta}_F$) are shown from Figs. 4.8 to 4.10 for the notched bar tensile specimen of 8mm gauge diameter and 6mm notch radius. In these figures the variables $\bar{\beta}_F$ and σ_1 have been denoted as BFM and S respectively. The best

values for the standard deviation of the critical value of the damage variable ($STD\beta_F$) were in the range of 1.3 to 1.5, which allowed a good distribution of the element removed during the crack growth. The chosen damage parameters in the CAFE model are set out in Table 4.2. Also in this table is shown the best tuned values for the other orientations in the assumption of effective material damage isotropy. It was observed that the general effect of increasing D causes the damage at an earlier stage of loading and higher values of σ_1 and $\bar{\beta}_F$ delayed the failure process.

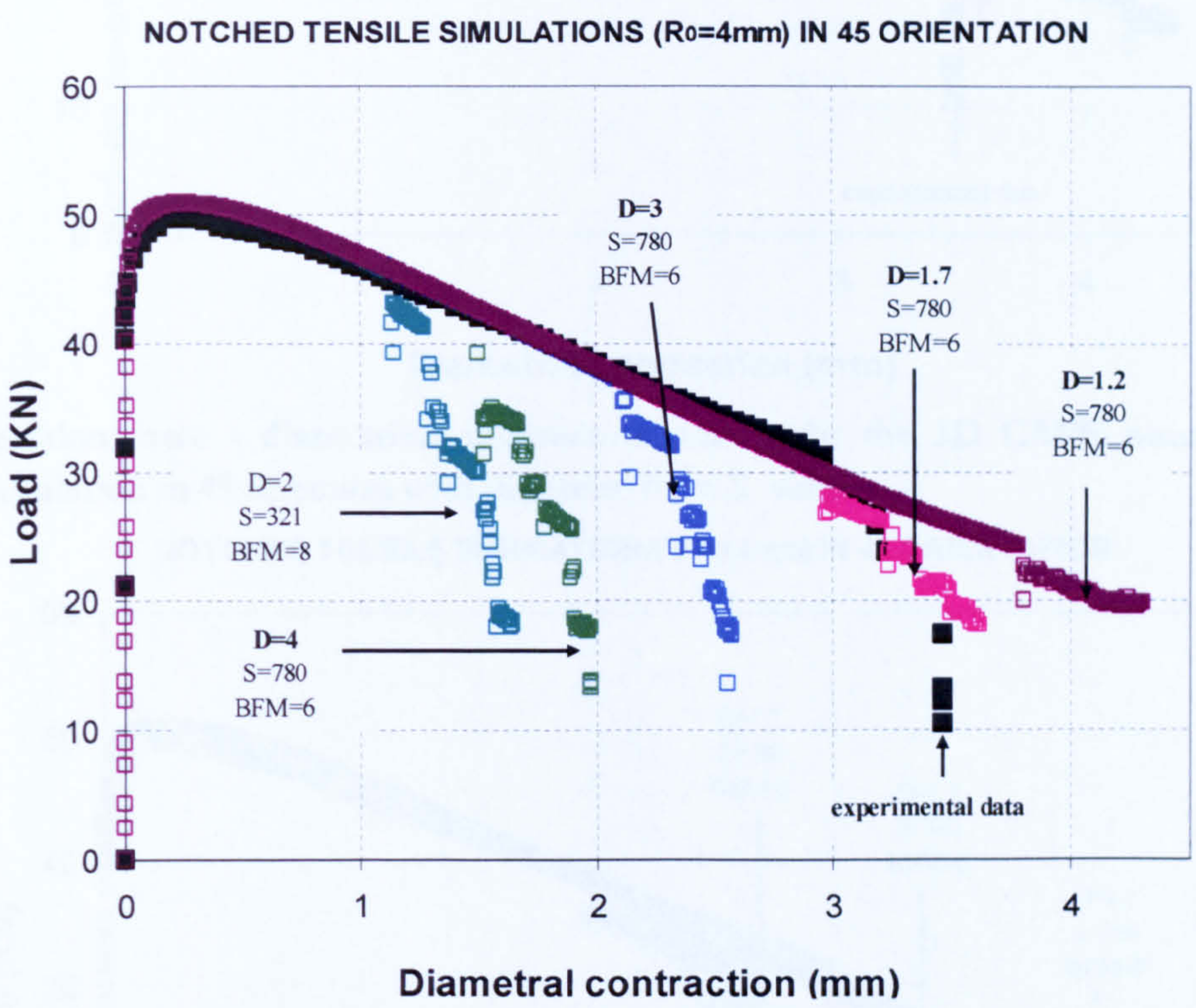

Fig. 4.8 Reaction force - diametrical contraction curves for the 3D CAFE notched tensile simulation in 45 direction with different D values.

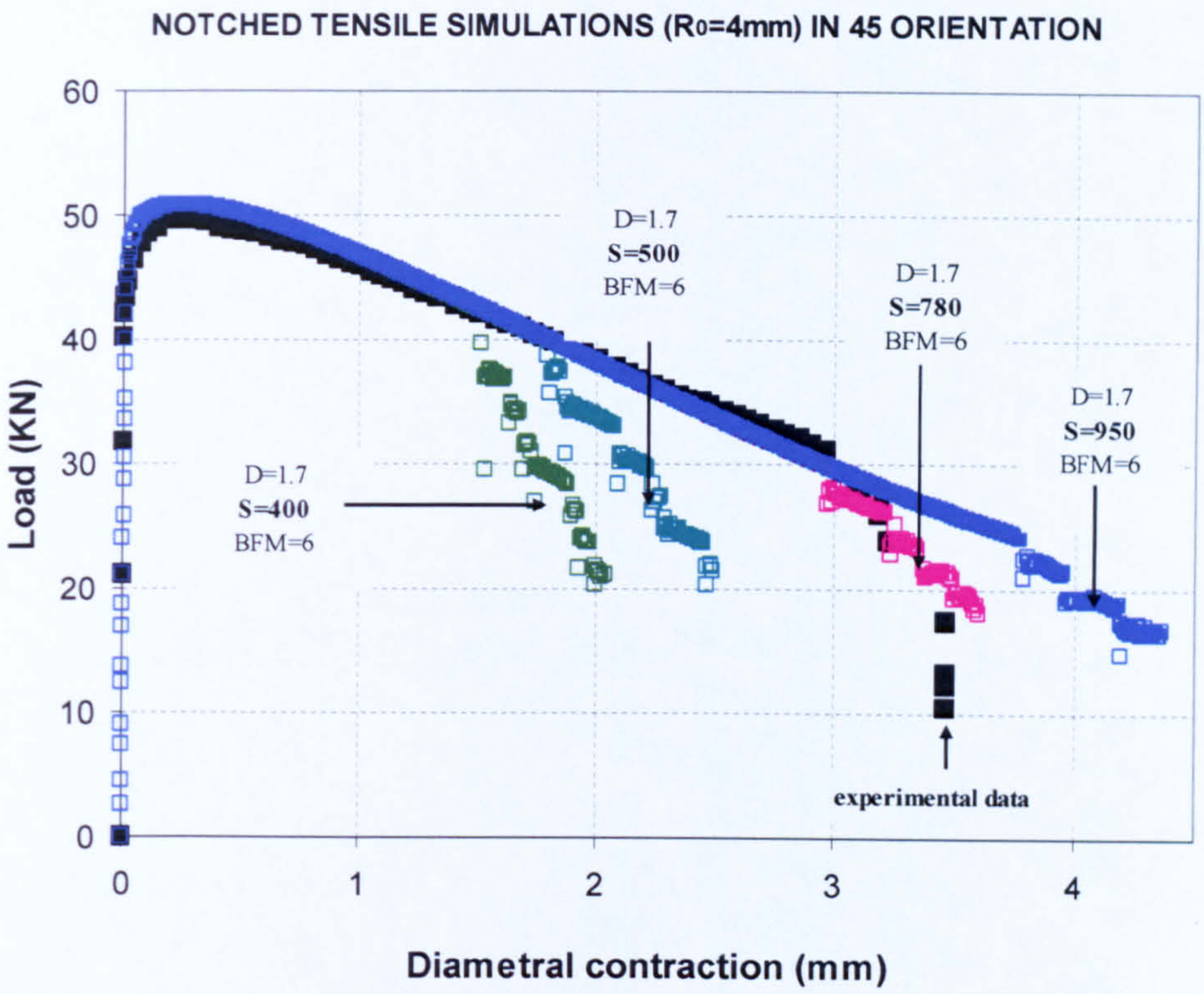

Fig. 4.9 Reaction force - diametrical contraction curves for the 3D CAFE notched tensile simulation in 45 direction with different $\sigma_1 = S$ values.

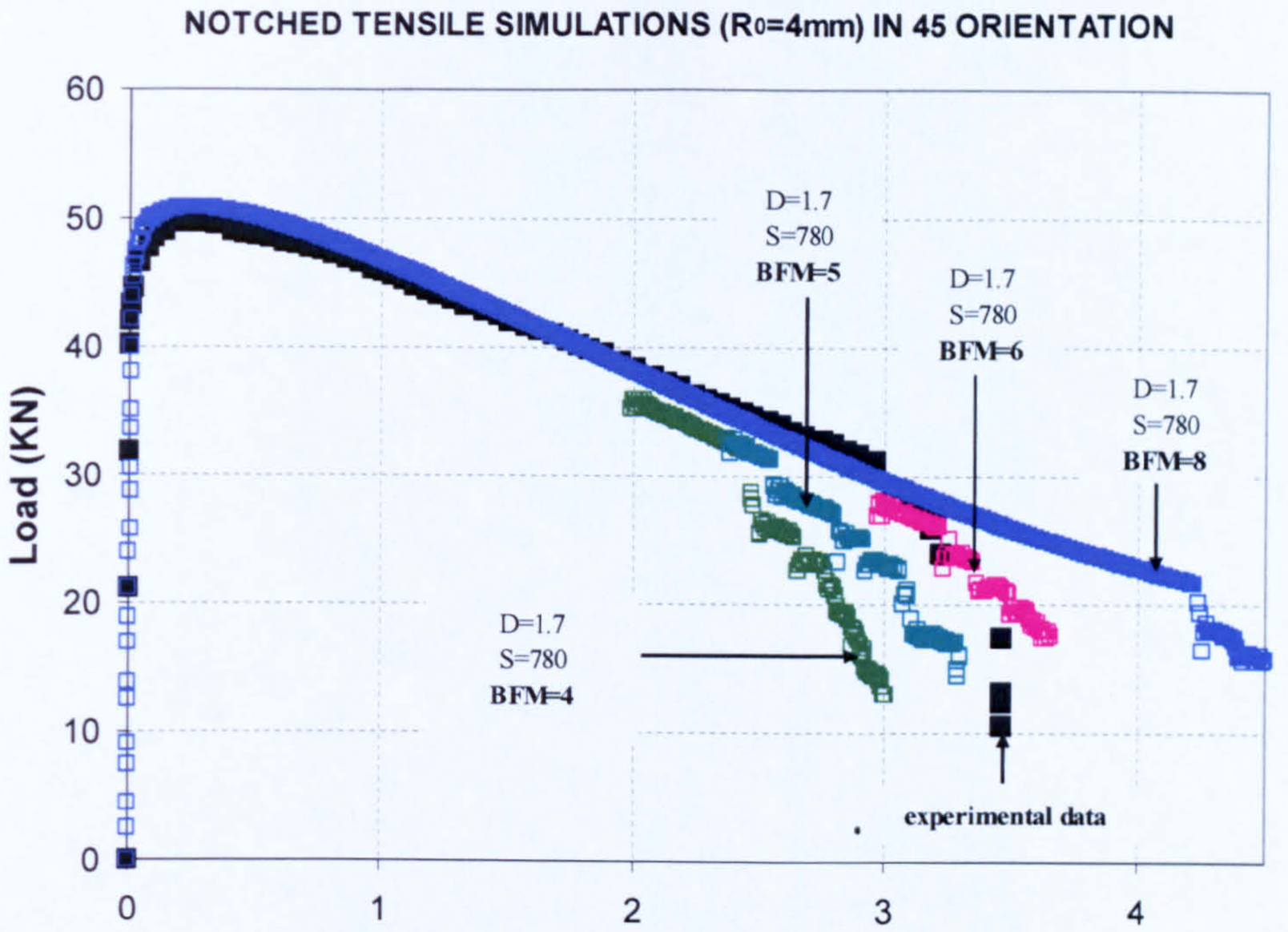

Fig. 4.10 Reaction force - diametrical contraction curves for the 3D CAFE notched tensile simulation in 45 direction with different $\bar{\beta}_F = BFM$ values.

In the CAFE technique, fracture starts when the damage variable distributed across a CA cell exceeds the critical value according to the local strain concentration. When all ductile CA cells assigned at one finite element die at the microscopic level, a dead element at the macroscopic scale is produced as well. Fig. 4.11 shows the simulation of fracture propagation through the microstructure. Variable STATUS=0 (blue elements) symbolise the elements that are completely destroyed and STATUS = 1 (red elements) for the rest that are still alive.

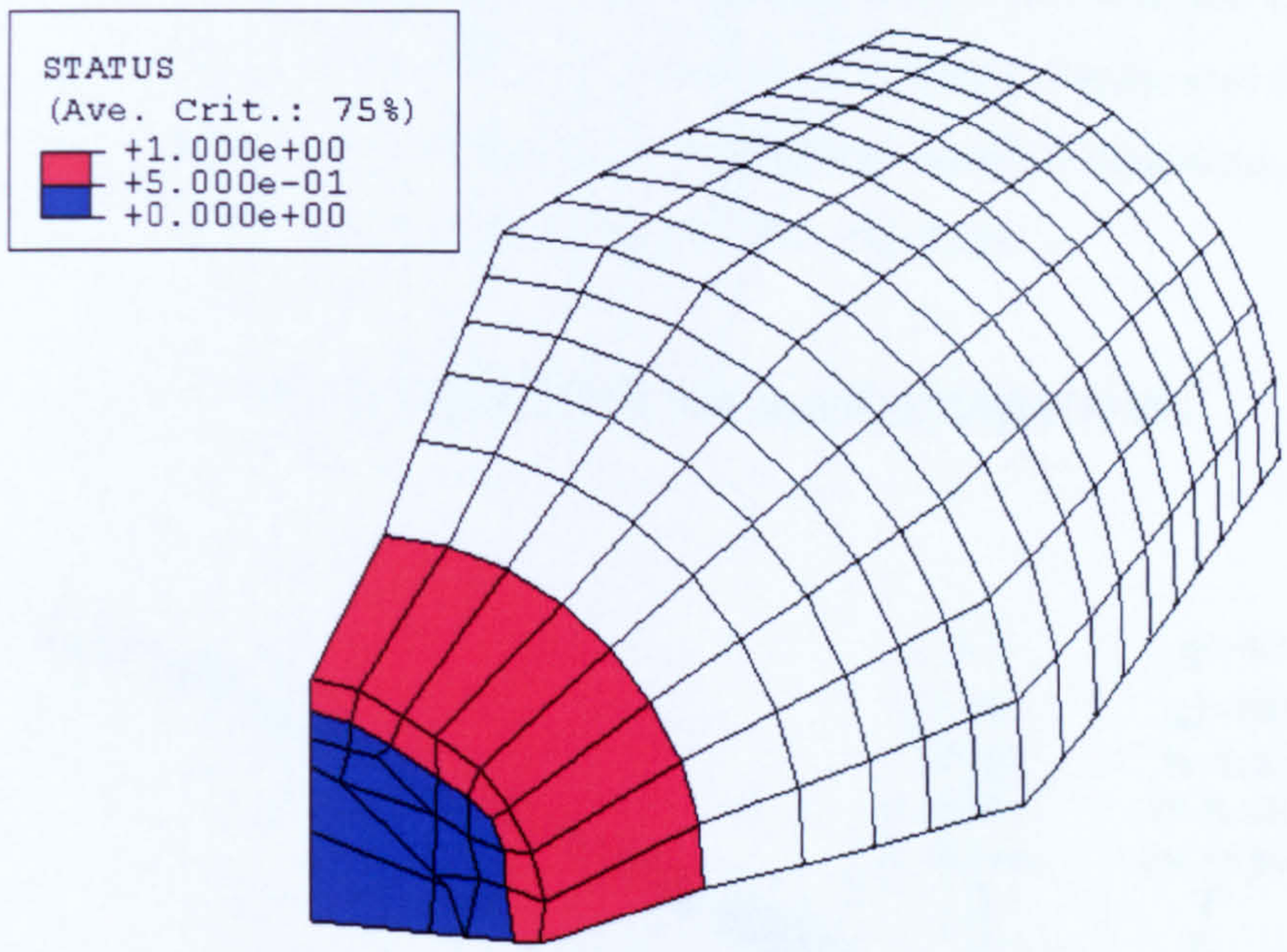

Fig. 4.11 Crack growth representation for the 3D notched tensile CAFE modelling.

Table 4.2 Calibrated damage parameters for 3D CAFE analysis of tensile specimens.

	45 DIRECTION	TRANSVERSE DIRECTION	LONGITUDINAL DIRECTION	THICKNESS DIRECTION
σ_1	780 [MPa]	780 [MPa]	780 [MPa]	780 [MPa]
D	**1.7**	**2.5**	**2.6**	**3.5**
f_0	$3.0x10^{-5}$	$3.0x10^{-5}$	$3.0x10^{-5}$	$3.0x10^{-5}$
$\bar{\beta}_F$	6	6	6	6
L_{FE}	0.8 mm	0.8 mm	0.8 mm	0.8 mm
L_D	0.2 mm	0.2 mm	0.2 mm	0.2 mm
$\sqrt[3]{M_D}$	4	4	4	4

4.3.1.2 Role of the element size

The mesh size is an important parameter in the damage modelling. As stated earlier, it is a representation of the average inter-particle distance and can be determined from SEM examination of the fracture surface.

Simulation analyses with different mesh size values were carried out using the conventional FE and GTN damage model for a 3D notch specimen ($R_0 = 4mm$) to study the role of the element size. In order to represent the different average spacing between the large voids, it was necessary to make three FE models with elements of 0.2mm, 0.4mm and 0.8mm. Analysis results showed that the size of the mesh is a dependence material behaviour; a smaller mesh size accelerates the damage process of the material (See Fig.4.12).

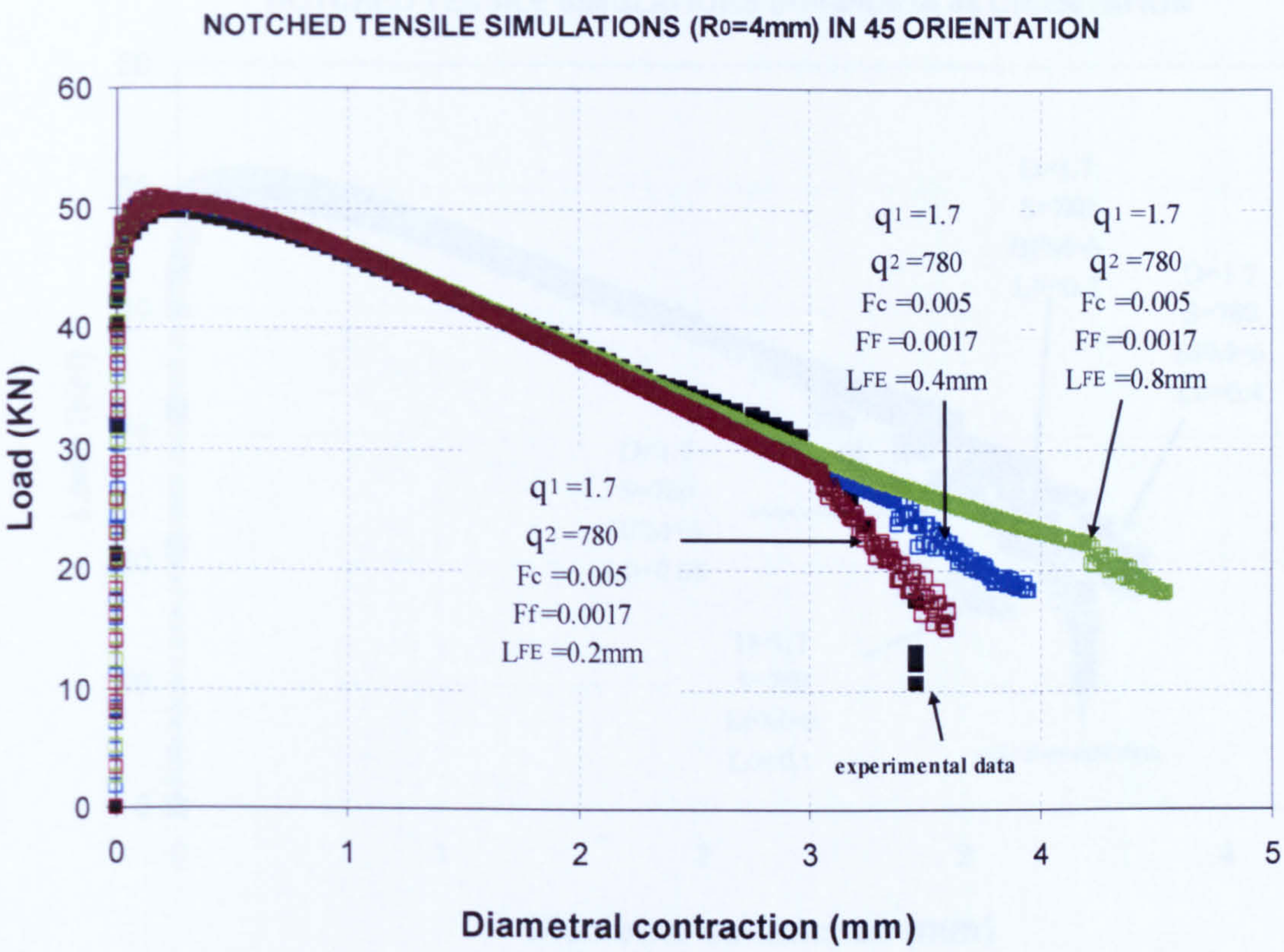

Fig. 4.12 Reaction force - diametrical contraction curves for the 3D FE notched tensile simulation in 45 direction with different L_{FE} values.

Similar damage behaviour was obtained from CAFE simulations when varying the cell size. The advantage of this technique is that only one FE model was needed to deal with the same micro-structural scale. Fig. 4.13 shows the results of the simulation curves using the CAFE and

Rousselier damage model for a 3D notch specimen ($R_0 = 4mm$) with different cell size values. A finite element model with element size (L_{FE}) of 0.8mm was created and different ductile damage cell sizes (L_D) were chosen to represent the average spacing between the large voids. CAFE simulations demonstrated that smaller cell size produces early damage failure of the material.

The studies carried out in this section were with the intention to show the important of the mesh size role in the modelling. For the further analysis $L_{FE} = 0.2mm$ has been used as the characteristic length of the X100 pipeline steel of the flat fracture surface of tensile and C(T) specimens.

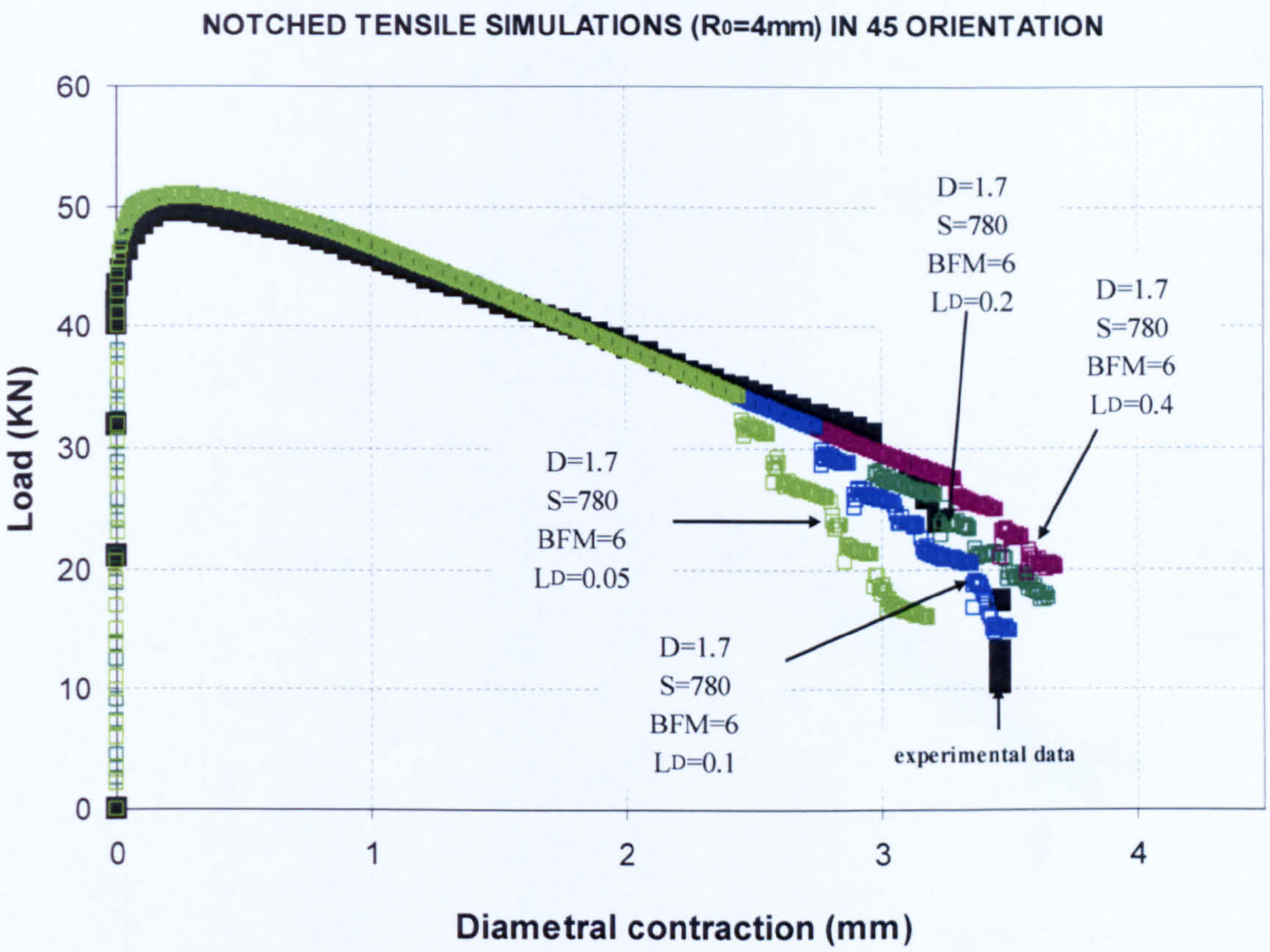

Fig. 4.13 Reaction force - diametrical contraction curves for the 3D CAFE notched tensile simulation in 45 direction with different L_D values.

On the other hand, with the aim of showing the effectiveness of the CAFE technique in reducing computing time to obtain comparable results of damage prediction, four cylindrical tensile specimens with different size element, but the same cell size in the damage zone were

created. A value of $L_D = 0.1mm$ for the cell size was chosen and models with element size L_{FE} of 0.2mm, 0.4mm 0.6mm and 0.8mm were made. These models decreased the number of elements with VUMAT properties (NEL) in the damage zone from 130 to 93, 45 and 23 elements respectively.

Calibration was achieved using the model with $L_{FE} = 0.8mm$ because of the fast simulation results and the fitted data was input to the other three models. CAFE simulations demonstrated that for the same values of Rousselier damage parameters with different element size but equal internal cell size, the results are comparable and the running time is reduced considerably. Fig. 4.14 shows the plots of the simulated results and experimental data. Specific values of each simulation are set out in Table 4.3. It should be pointed out that models with element size larger than 0.8mm in the damage zone ($L_{FE} = 1mm$ and $L_{FE} = 1.2mm$) gave poor results, since the FE models were not refined enough to capture the deformation behaviour accurately.

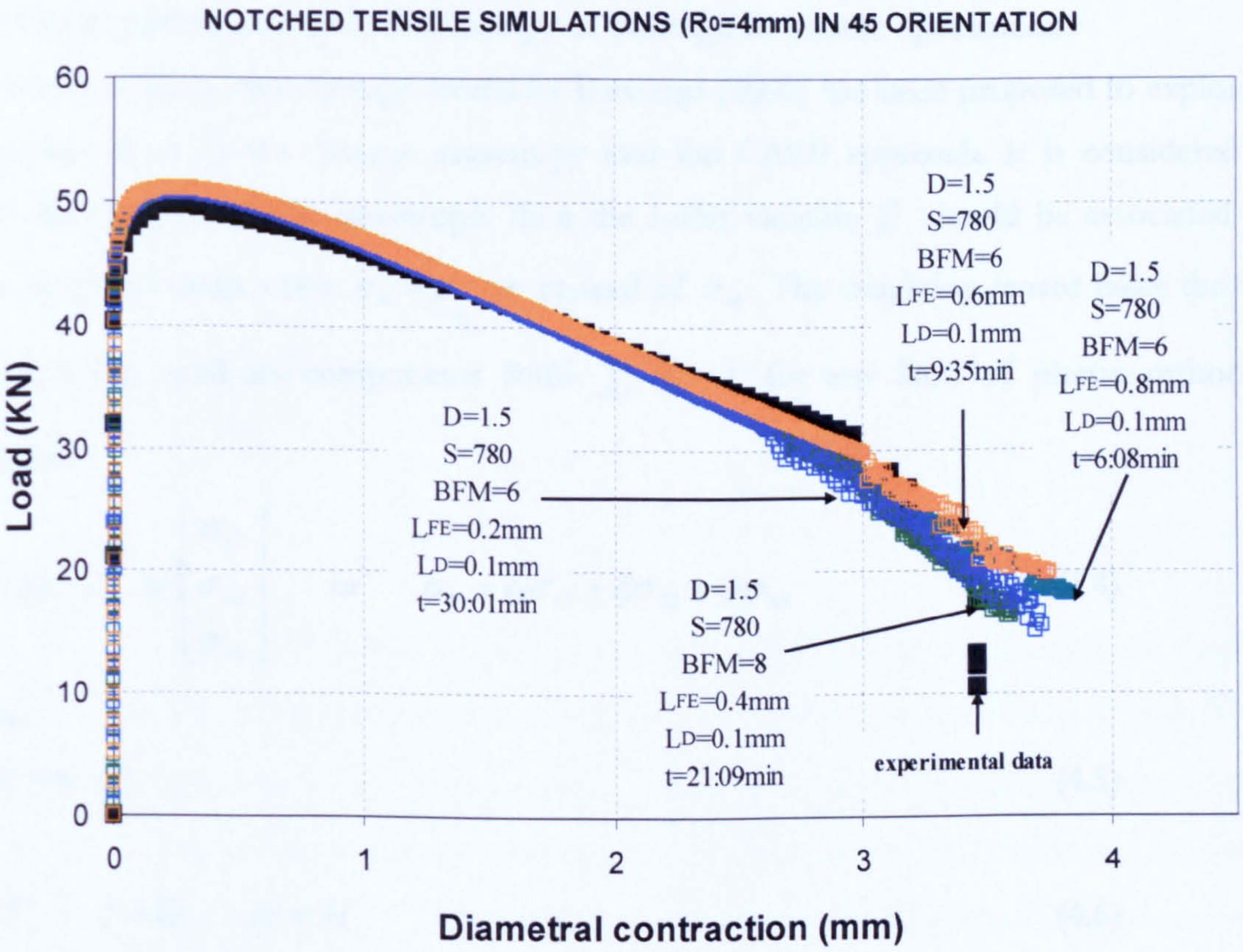

Fig. 4.14 Reaction force - diametrical contraction curves for the 3D CAFE notched tensile simulation in 45 direction with different L_{FE} values.

Table 4.3 Damage modelling parameters calibrated for: $L_{FE} = 0.8mm$, $L_{FE} = 0.6mm$, $L_{FE} = 0.4mm$ and $L_{FE} = 0.2mm$ tensile models

	1	2	3	4
σ_1	780 [MPa]	780 [MPa]	780 [MPa]	780 [MPa]
D	1.5	1.5	1.5	1.5
f_0	$3.0x10^{-5}$	$3.0x10^{-5}$	$3.0x10^{-5}$	$3.0x10^{-5}$
L_{FE}	**0.8 mm**	**0.6 mm**	**0.4 mm**	**0.2 mm**
L_D	0.1 mm	0.1 mm	0.1 mm	0.1 mm
$\sqrt[3]{M_D}$	8	6	4	2
$\bar{\beta}_F$	6	6	6	6
NEL	23	45	93	130
time	**6:08 min.**	**9:35 min.**	**21:09 min.**	**30:01 min.**

4.3.1.3 Calibration for plastic anisotropy of damage in tensile specimens

The extended Rousselier damage model by Benzerga (2000) has been proposed to explore the incorporation of ductile damage anisotropy into the CAFE approach. It is considered that when damage plasticity is anisotropic then the scalar variable β should be associated with some weighted mean stress $\sigma_h = \underset{\sim}{J}_h : \underset{\sim}{\sigma}$ instead of σ_m. The weighting tensor takes the form $\underset{\sim}{J}_h = X_i \underset{\sim}{e}_i \otimes \underset{\sim}{e}_i$ and its components fulfil $\sum_i X_i = 1$ for any kind of plastic orthotropy. Therefore:

$$\sigma_h = \begin{bmatrix} \alpha & \xi & \psi \end{bmatrix} \begin{bmatrix} \sigma_{11} \\ \sigma_{22} \\ \sigma_{33} \end{bmatrix} \quad \text{or} \quad \sigma_h = \alpha\sigma_{11} + \xi\sigma_{22} + \psi\sigma_{33} \tag{4.4}$$

where,

$$\alpha + \xi + \psi = 1 \tag{4.5}$$

and,

$$\alpha = F \qquad \xi = G \qquad \psi = H \tag{4.6}$$

where F, G and H are the constants obtained by tensile tests in different orientations, defining anisotropic yield behaviour on the basis of strain ratios (Lankford's R values). R_L is the coefficient of Lankford in the L direction and hence:

$$R_L = \frac{\varepsilon_T}{\varepsilon_S} = \frac{2a+2b-c}{2a+2c-b} \tag{4.7}$$

$$R_T = \frac{\varepsilon_L}{\varepsilon_S} = \frac{2b+2a-c}{2b+2c-a} \tag{4.8}$$

$$R_S = \frac{\varepsilon_L}{\varepsilon_T} = \frac{2c+2a-b}{2c+2b-a} \tag{4.9}$$

$$R_{LT} = \frac{\varepsilon_{ll}}{\varepsilon_S} = \frac{9d}{a+b+4c} - \frac{1}{2} \tag{4.10}$$

$$R_{TS} = \frac{\varepsilon_{st}}{\varepsilon_L} = \frac{9e}{4a+b+c} - \frac{1}{2} \tag{4.11}$$

$$R_{SL} = \frac{\varepsilon_{ls}}{\varepsilon_T} = \frac{9f}{a+c+4b} - \frac{1}{2} \tag{4.12}$$

The correspondence among F, G, H, L, M, N and a, b, c, d, e, f are:

$$F = (-a+2b+2c)/9 \qquad a = -F+2G+2H \tag{4.13}$$

$$G = (2a-b+2c)/9 \qquad b = 2F-G+2H \tag{4.14}$$

$$H = (2a+2b-c)/9 \qquad c = 2F+2G-H \tag{4.15}$$

$$L = e \qquad d = N \tag{4.16}$$

$$M = f \qquad e = L \tag{4.17}$$

$$N = d \qquad f = M \tag{4.18}$$

According to the experimental tensile tests, the corresponding coefficients of Lankford were $R_L = 1.13$, $R_T = 0.89$ and $R_S = 1.5$, and the calculated constants of F, G and H were 0.40, 0.48 and 0.12 respectively. These values were input via user material subroutine VUMAT in the ABAQUS software, which allowed the simulation of the condition of damage anisotropy as shown in Fig. 4.15 for a 3D notch specimen ($R_0 = 4mm$) in the transverse direction. The best fitted data of damage parameters for L, T and S orientation are set out in Table 4.4. Constants of L, M and N were not used for anisotropic damage. Anisotropic yield behaviour and anisotropic plastic flow were not employed for this calculation.

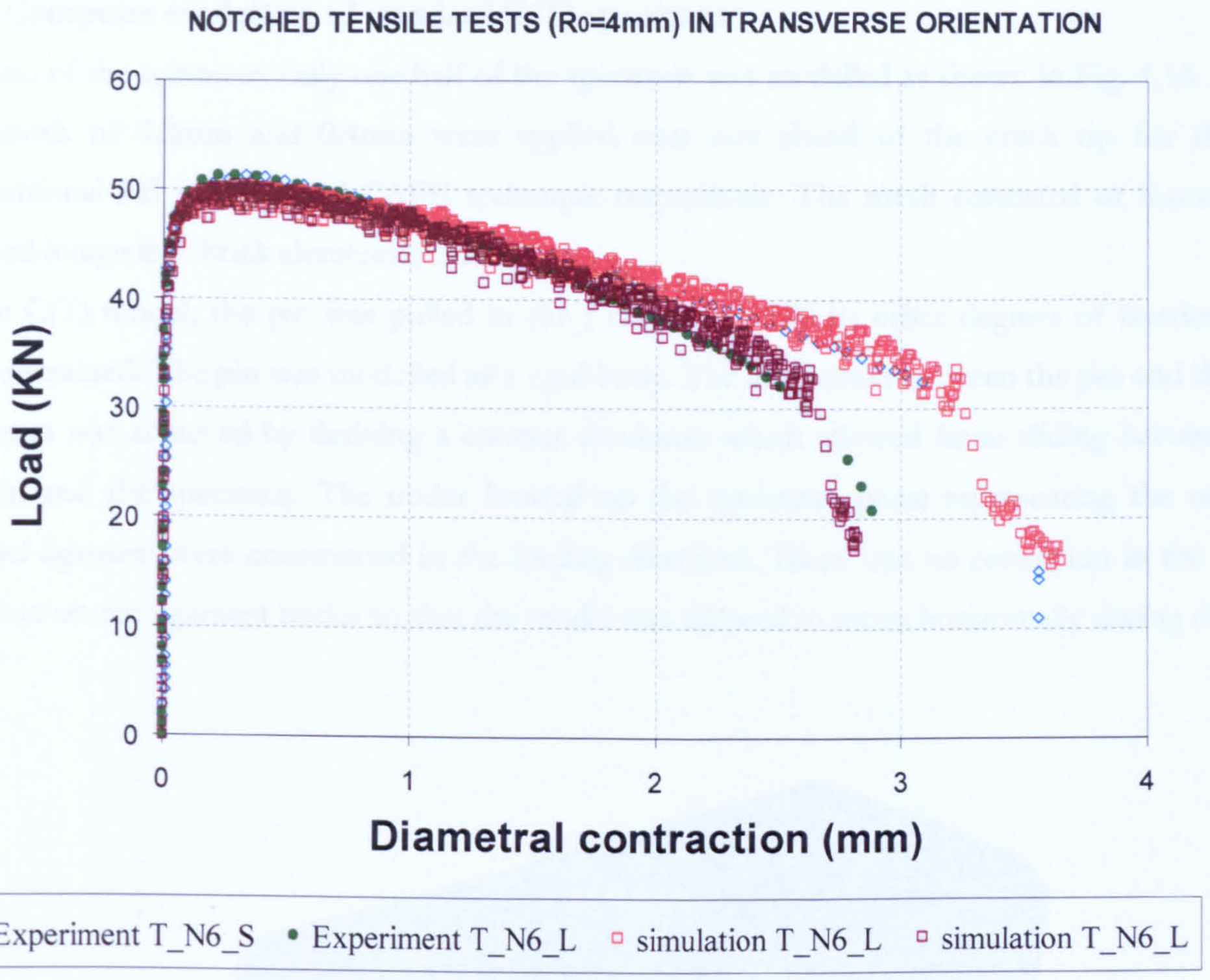

Fig. 4.15 Plots results of reaction force - diametrical contraction curves for the 3D anisotropic CAFE notched tensile simulations in transverse direction.

Table 4.4 Calibrated damage parameters for 3D anisotropic CAFE analysis of tensile specimens.

	TRANSVERSE DIRECTION	LONGITUDINAL DIRECTION	THICKNESS DIRECTION
σ_1	780 [MPa]	780 [MPa]	780 [MPa]
D	**0.80**	**0.87**	**1.2**
f_0	$3.0x10^{-5}$	$3.0x10^{-5}$	$3.0x10^{-5}$
$\bar{\beta}_F$	6	6	6
L_{FE}	0.8 mm	0.8 mm	0.8 mm
L_D	0.2 mm	0.2 mm	0.2 mm
$\sqrt[3]{M_D}$	4	4	4

4.3.2 Computer modelling of standard C(T) specimens

Because of the symmetry only one half of the specimen was modelled as shown in Fig. 4.16. A fine mesh of 0.2mm and 0.4mm were applied near and ahead of the crack tip for the conventional FE method and CAFE technique respectively. The mesh consisted of 8-node reduced integration brick elements (C3D8R).

In the C(T) model, the pin was pulled in the *y* direction while its other degrees of freedom were restrained. The pin was modelled as a rigid body. The interaction between the pin and the specimen was achieved by defining a contact condition which allowed finite sliding between the pin and the specimen. The nodes located on the symmetry plane representing the un-cracked ligament were constrained in the loading direction. There was no restriction in the *x* direction on the ligament nodes so that the model was allowed to move horizontally during the test.

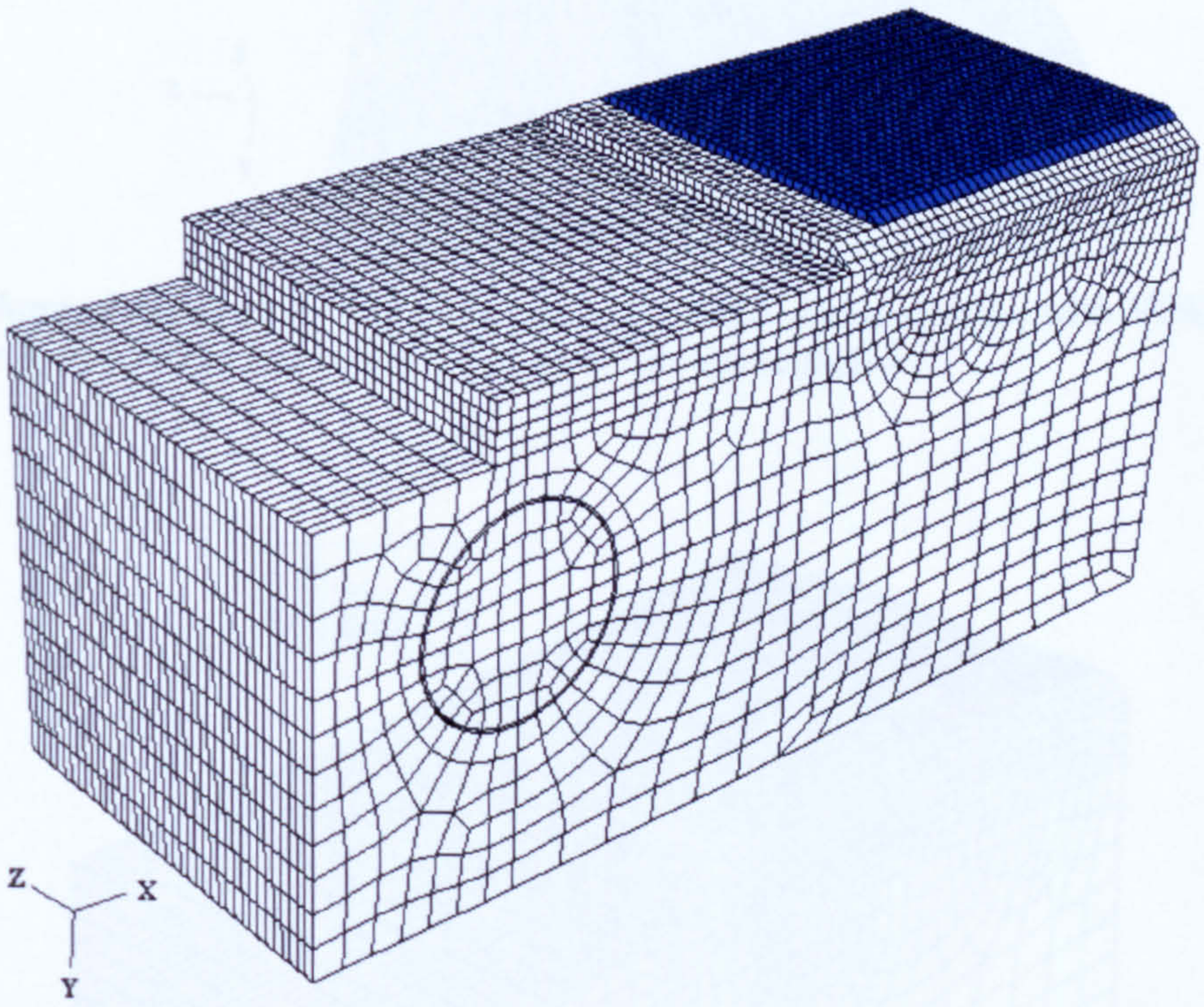

Fig. 4.16 Example of 3D compact test FE model

As a first attempt at a 3D analysis, a quarter of the C(T) specimen without side grooves was constructed with the aim to simplify the complexity of creating the lateral groove in the damage zone, where the mesh size is of the order of average inter-particle distance. But the finite element contour plot with STATUS variable (Fig. 4.17) showed that the conventional FE

and CAFE simulations were showing crack tunnelling, because the material near the outer surface is in a state of low stress triaxiality giving wrong results in the load-CMOD data. Accordingly, side grooves were introduced in the half of 3D modelling to maintain a straight crack front (Fig. 4.18). It should be pointed out that the symmetry of half of the CT specimen enforces fracture of damage on a flat plane.

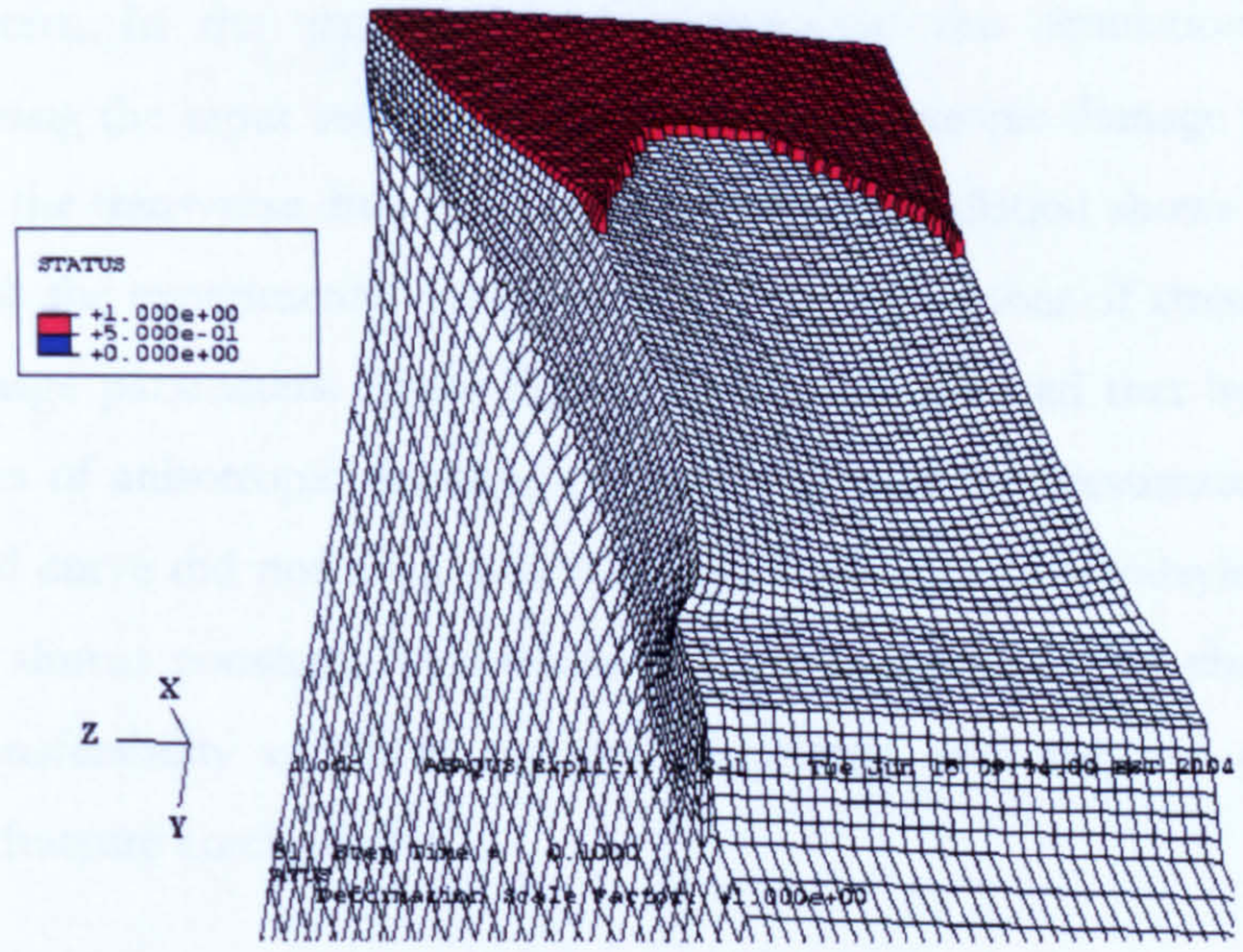

Fig. 4.17 Deformed mesh of the 3D C(T) specimen without side groove, with STATUS variable at the end of the simulation. Red elements are still alive.

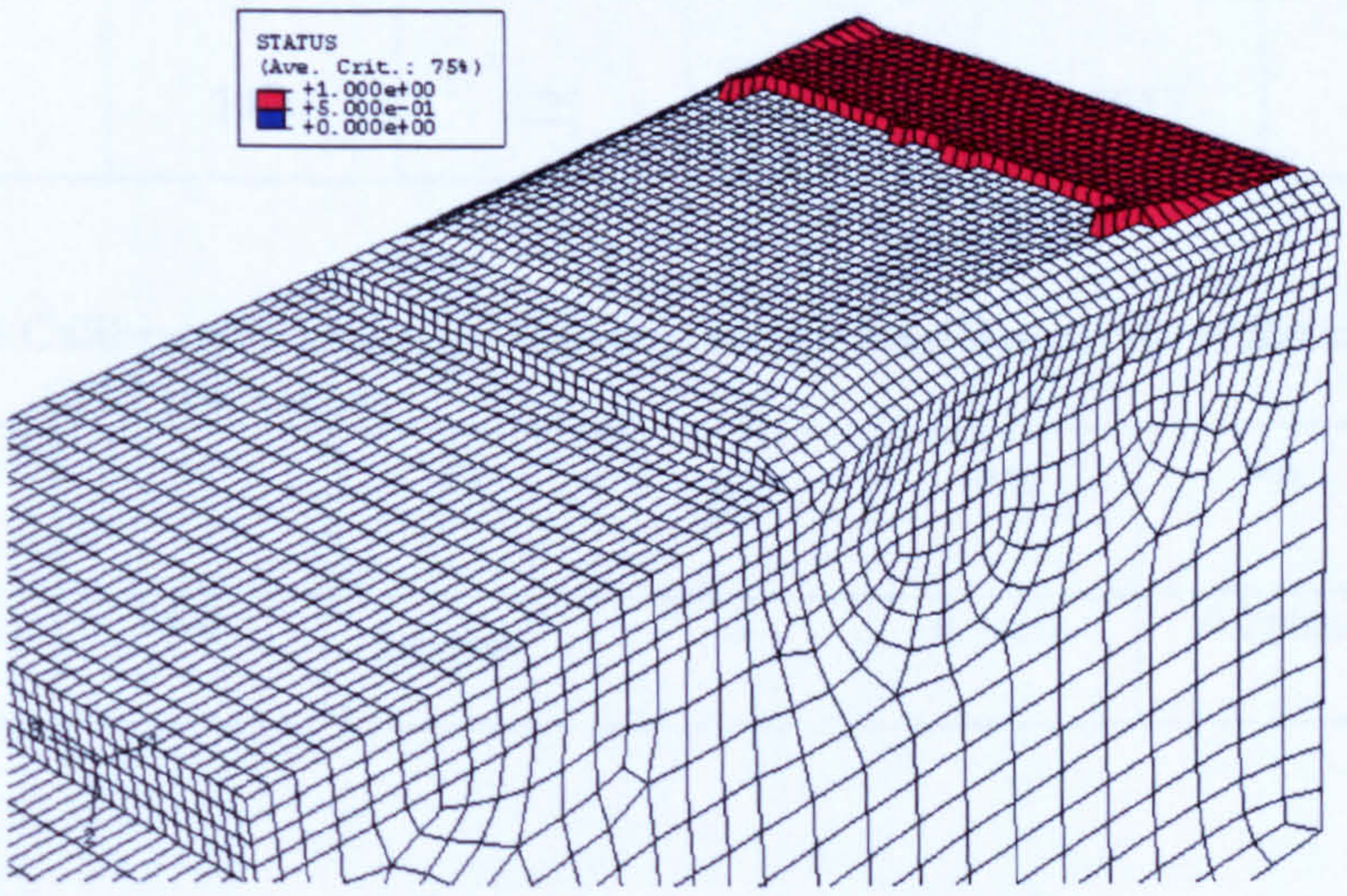

Fig. 4.18 Deformed mesh of the 3D C(T) specimen with side groove, and STATUS variable at the end of the simulation. Red elements are still alive.

4.3.2.1 Calibration of the damage parameters in C(T) specimens

3D analyses were performed employing the same computational techniques of damage mechanics that were used in the preceding calibrations of material properties of tensile test specimens. Tables 4.5 and 4.6 show the values of the best fitted GTN and Rousselier damage parameters that were obtained according to the results of the trial and error series of conventional finite element and CAFE analysis respectively. Fig. 4.19 shows the plots of these calibrated parameters. In the same figure is represented the simulation curve for the anisotropic case using the input values of the calibrated anisotropic damage parameters from the tension test in the transverse direction. The anisotropic simulation shows very poor results in comparison with the experimental data, even after a large number of attempts to adjust the values of the damage parameters. From Fig. 4.19 it can be inferred that by using the tuned damage parameters of anisotropic damage, the peak load was underestimated by about 40%. Also the simulated curve did not drop after the peak load; the stress carrying capacity of the model remaining almost constant. This needs further investigation. In chapter five will be discussed the transferability of these damage parameters and the use of them for the calculation of flat fracture crack growth.

Table 4.5 Calibrated damage parameters for 3D conventional FE analysis of flat fracture for C(T) specimens.

q_1	q_2	q_3	L_D(mm)	f_c	f_F
1.5	1.05	2.25	0.20	0.0017	0.005

Table 4.6 Calibrated damage parameters for 3D CAFE analysis of flat fracture for C(T) specimens.

σ_1	D	f_0	$\bar{\beta}_F$	L_{FE}	L_D	$\sqrt[3]{M_D}$
780 [MPa]	4.5	$3.0x10^{-5}$	6	0.4mm	0.2mm	2

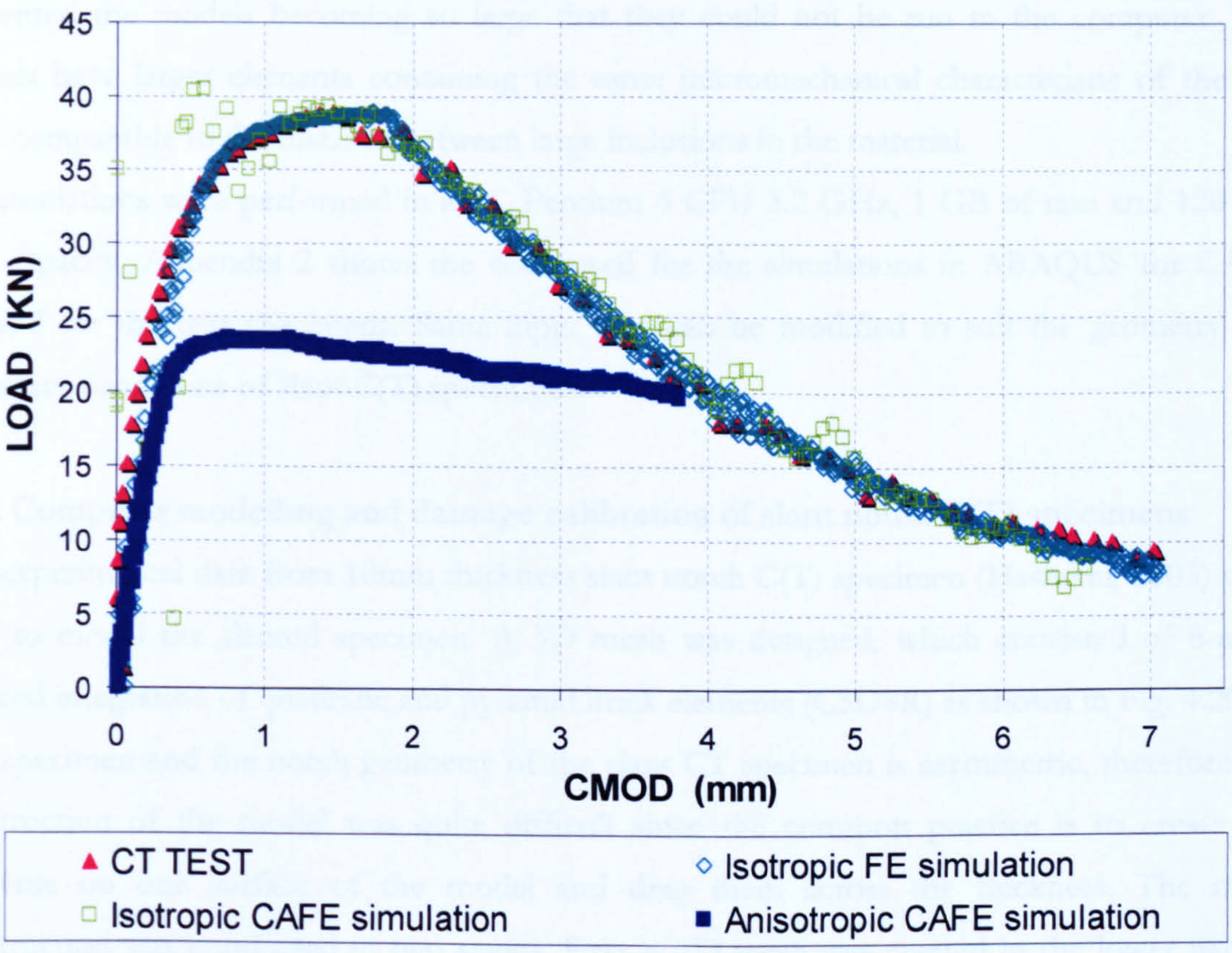

Fig. 4.19 Reaction load - CMOD curves of the experimental data and simulation results from isotropic conventional FE, isotropic CAFE and anisotropic CAFE techniques.

4.4 NUMERICAL MODELLING TO PREDICT SHEAR FRACTURE

3D models of slant notch C(T) and tear specimens were designed to represent the three dimensional effects of the constraint ahead of the crack tip. They were run in Abaqus/Explicit to calibrate and analyse the shear fracture characteristics of the X100 pipeline steel. As in the numerical modelling of flat fracture, the geometry, meshes, the set of nodes and elements for the loads and boundary conditions were designed in ANSYS and HyperMesh codes, and exported to ABAQUS to obtain all the simulations results.

For the 3D computational analysis, the combination of cellular automata (CA) and finite element (FE) techniques (CAFE method) was used. The use of CAFE modelling was appropriated in these numerical modelling due to that a very fine mesh is required to represent the micro-structural characteristics, which is of the order of five times smaller than the element

size utilised for the flat specimens. This avoided the lengthy calibration time and also prevented the models becoming so large that they could not be run in the computer. The models have larger elements containing the same micromechanical characteristic of the cell sizes comparable to the distance between large inclusions in the material.

All simulations were performed in a PC Pentium 4 CPU 3.2 GHz, 1 GB of ram and 120 GB disk capacity. Appendix 2 shows the code used for the simulations in ABAQUS for CAFE method for the tear specimens. Same input files can be modified to suit the geometry and boundary conditions of slant C(T) specimens.

4.4.1 Computer modelling and damage calibration of slant notch C(T) specimens

The experimental data from 10mm thickness slant notch C(T) specimen (Hashemi, 2003) were used to model the slanted specimen. A 3D mesh was designed, which consisted of 8-node reduced integration of quadratic and pyramid brick elements (C3D8R) as shown in Fig. 4.20.

The specimen and the notch geometry of the slant CT specimen is asymmetric, therefore the construction of the model was quite difficult since the common practice is to create 2D elements on one surface of the model and drag them across the thickness. The mesh construction was conducted in two stages. First, a 2D mesh was created in the lower part of the front surface of the model. This region was then dragged along 10mm thickness to the upper area of the model leading to 12 layers of 3D quadratic elements of 0.83mm thickness. Second, a 3D automatic mesh was built using 3D pyramid elements of 0.64mm in an area around the slant notch of the model.

In all parts of the model was assure the proper connectivity between the quadratic and pyramid elements. This created a suitable mesh in places where it is necessary to have an optimal resolution of the stress-strain field behaviour in the damage zone. Sixteen ductile cells were attached at each FE providing a cell size of 0.04mm, which is representative of the large inclusion spacing in the material.

In the analysis, the two 7.4mm loading pins were modelled as rigid bodies and contact conditions were defined between pins and specimen. This allowed finite sliding between loading pins and the specimen. All translation and rotational degrees of freedom for the lower pin were constrained. The upper pin was pulled in the y direction while its other degrees of freedom were restrained.

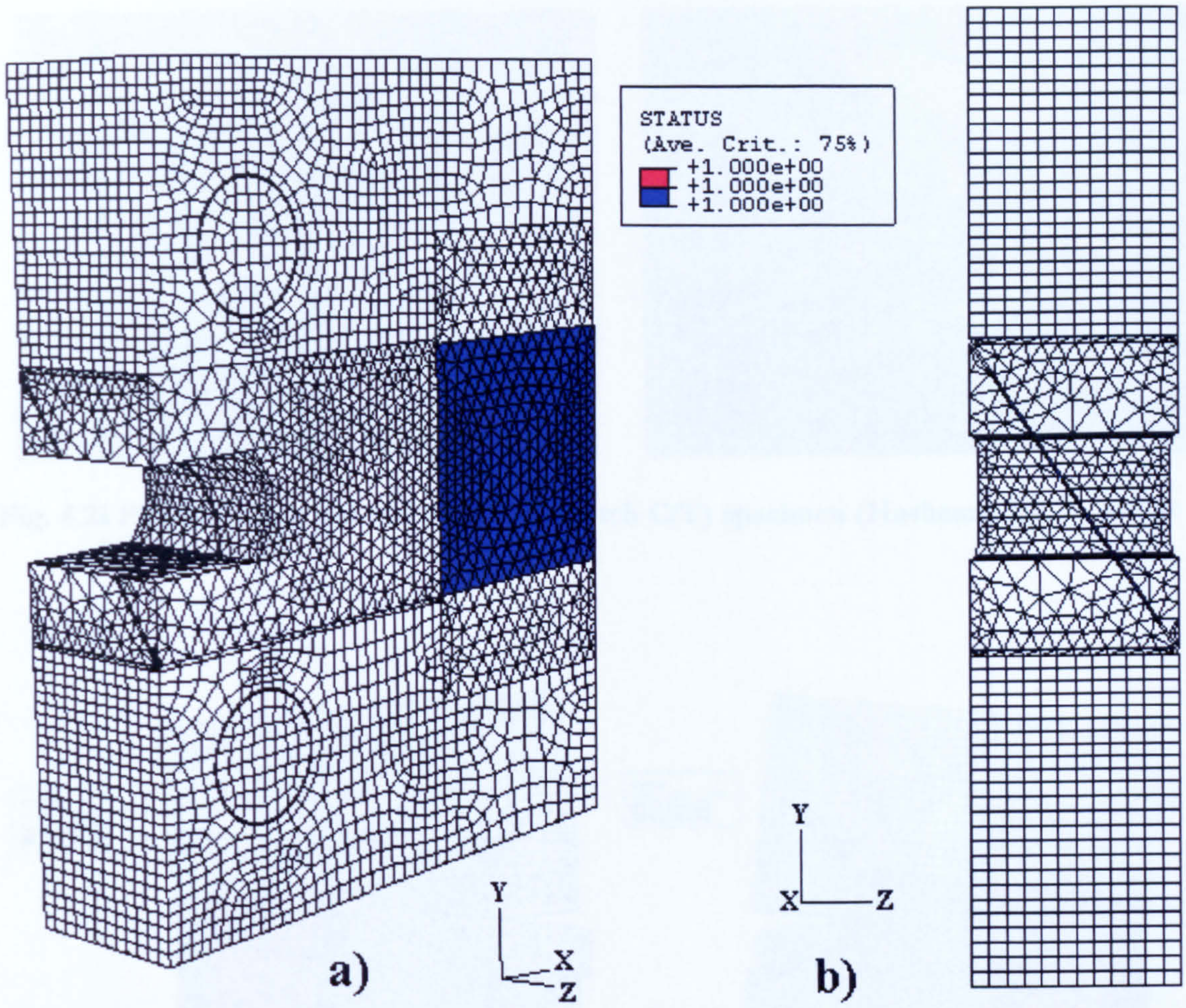

Fig. 4.20 3D slant notch C(T) FE model: a) 3D view, blue elements represent the damage zone and b) it is showing the lateral view of the modelling.

In the model fracture starts when its damage variable distributed across a CA cell exceeds the critical value according to the local strain concentration. Figs. 4.21 and 4.22 show the crack growth of the experimental test and the simulated model of fracture through the microstructure respectively. The damage started ahead of the crack tip, advanced in the vertical direction and then deviated to a 45° orientation. In the simulations the fracture is represented by the STATUS variable in the damage zone. Variable STATUS=0 (blue elements) symbolise the elements that are completely destroyed and STATUS = 1 (red elements) for the rest that are still alive.

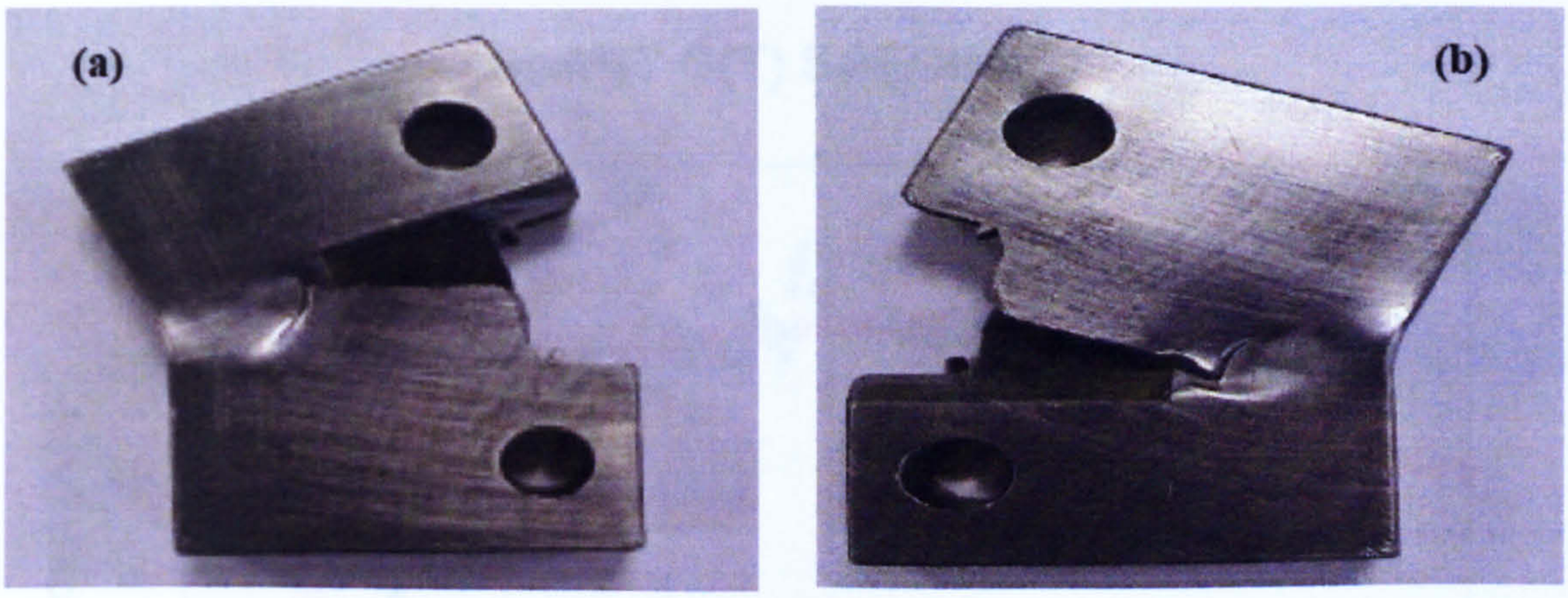

Fig. 4.21 Photograph of the fractured slant notch C(T) specimen (Hashemi, 2003) a)front side b) reverse side

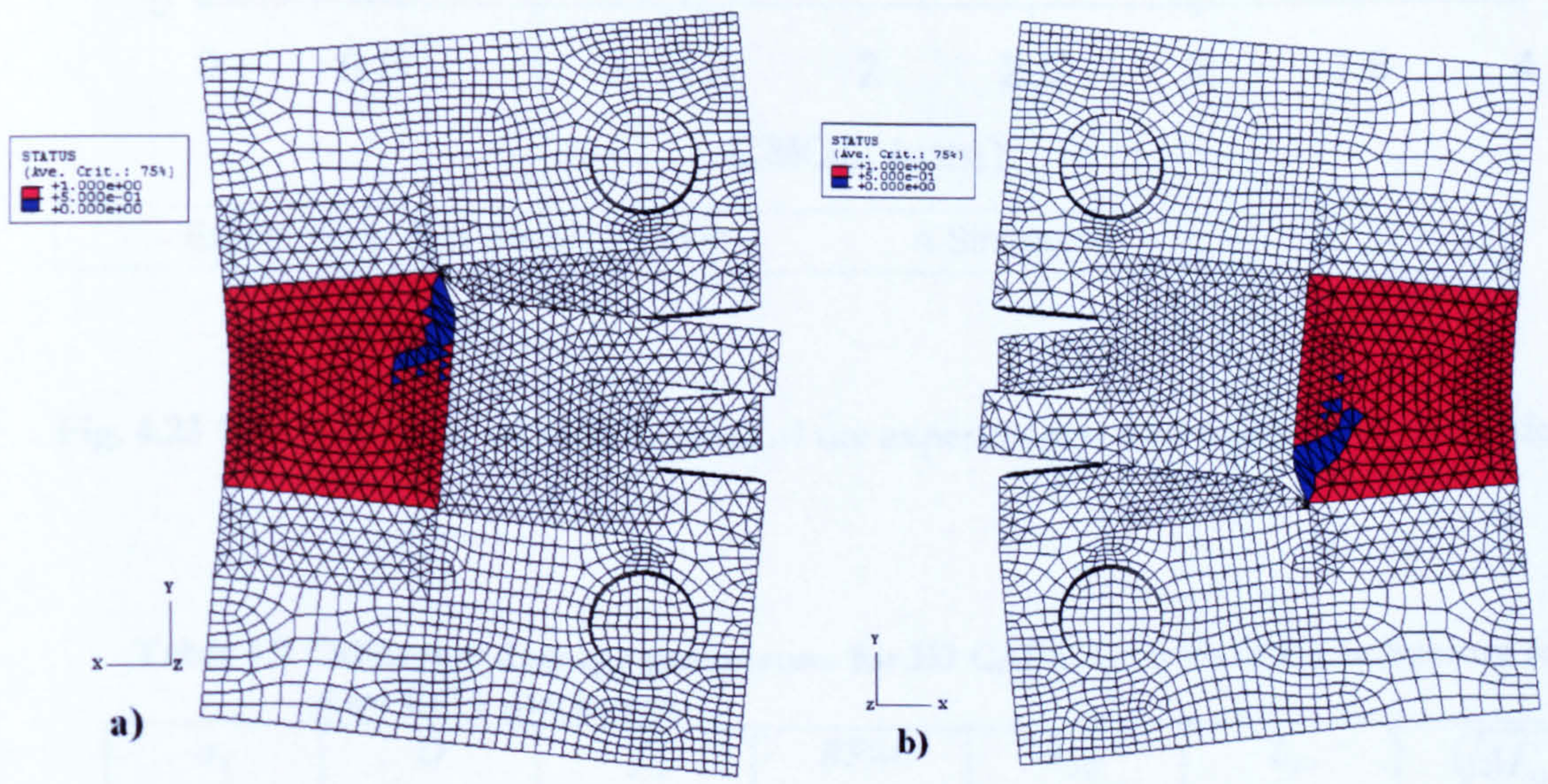

Fig. 4.22 Simulation of the fractured slant notch C(T) specimen a)front side b) reverse side. Blue elements are completed destroyed

A plot of the model response at the end of the analysis is shown in Fig. 4.23. The final tuned parameters for slant fracture from this test are reported in Table 4.7.

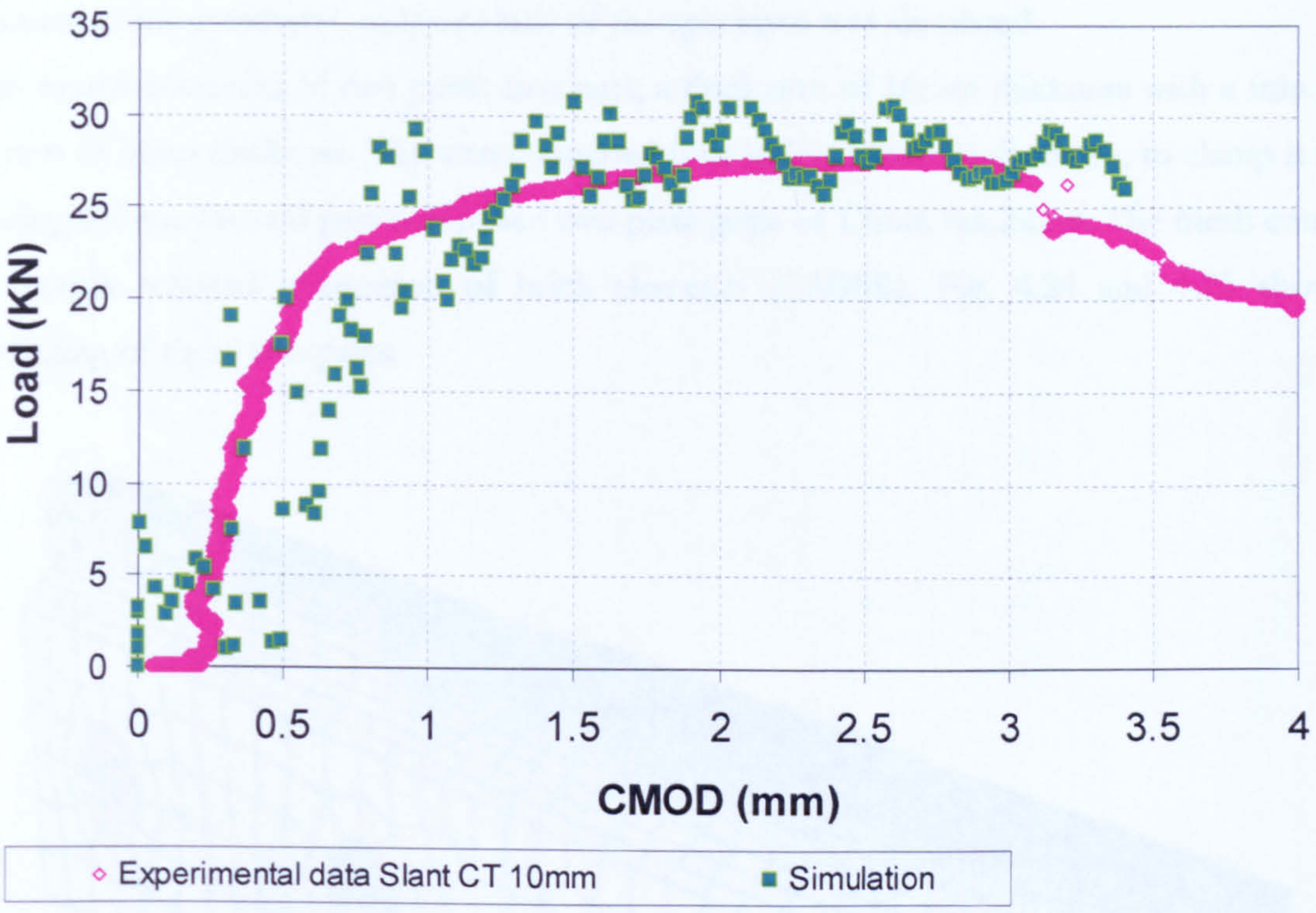

Fig. 4.23 Reaction force – CMOD curves of the experimental data and CAFE simulation.

Table 4.7 Calibrated damage parameters for 3D CAFE analysis of shear fracture for slant C(T) specimens.

σ_1	D	f_0	BFM	L_{FE}	L_D	$\sqrt[3]{M_D}$
780 [MPa]	**3.2**	$3.0x10^{-5}$	6	0.64mm	0.04mm	16

4.4.2 Computer modelling and calibration of damage parameters of tear specimen

A 3D model was designed to calibrate the fracture characteristics of the tear specimens. Because of the symmetry, only one half of the specimen was simulated.

This model consisted of two parts: first part, a thick arm of 16mm thickness with a thin gauge section of 8mm thickness. The arm contained four holes, 14mm in diameter, to clamp it to the loading fixture. Second part comprised two plate grips of 15mm thickness. The mesh consisted of 8-node reduced integration of brick elements (C3D8R). Fig. 4.24 and 4.25 show the modelling of these two parts.

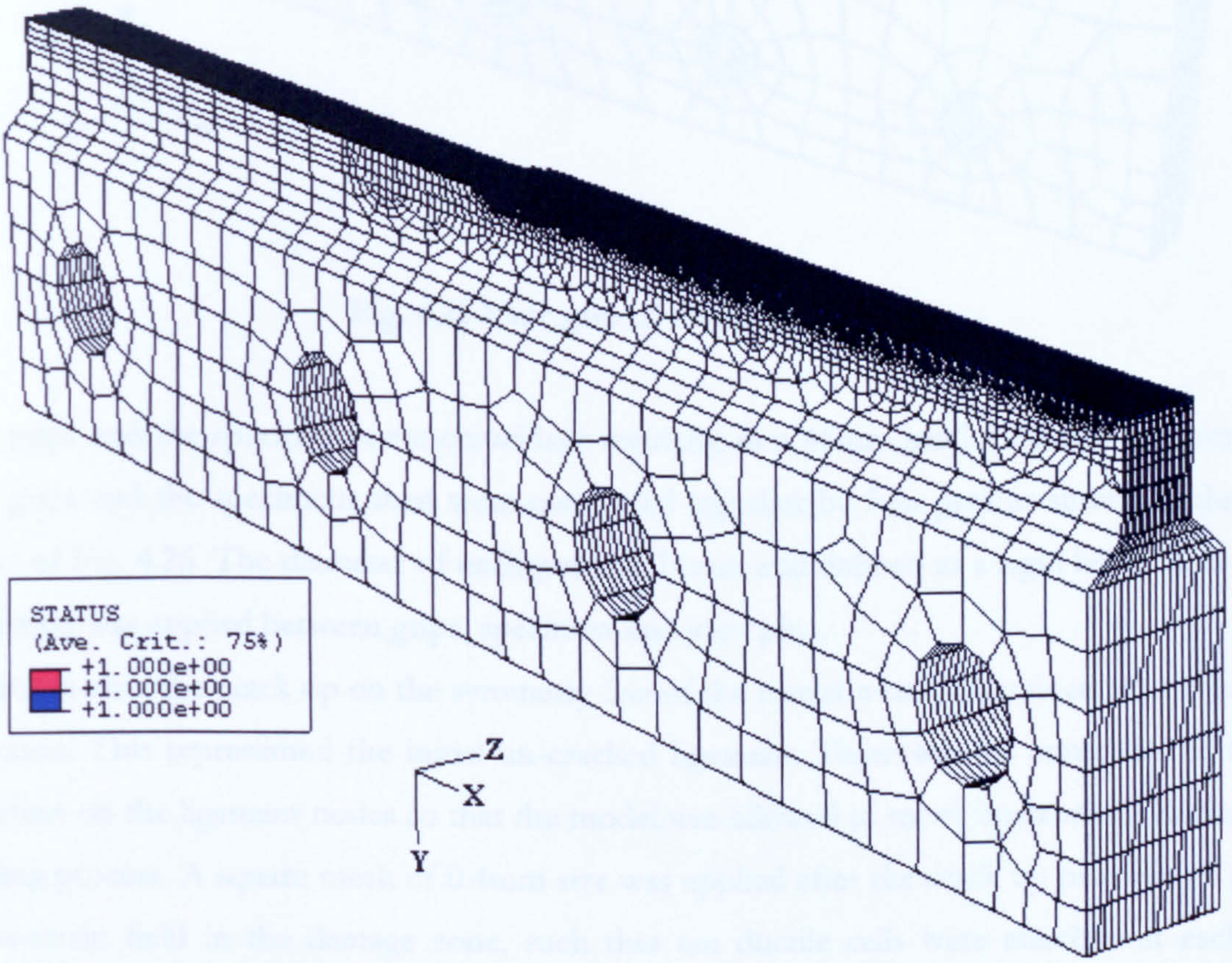

Fig. 4.24 3D FE modelling of tear specimen of 8mm gauge section

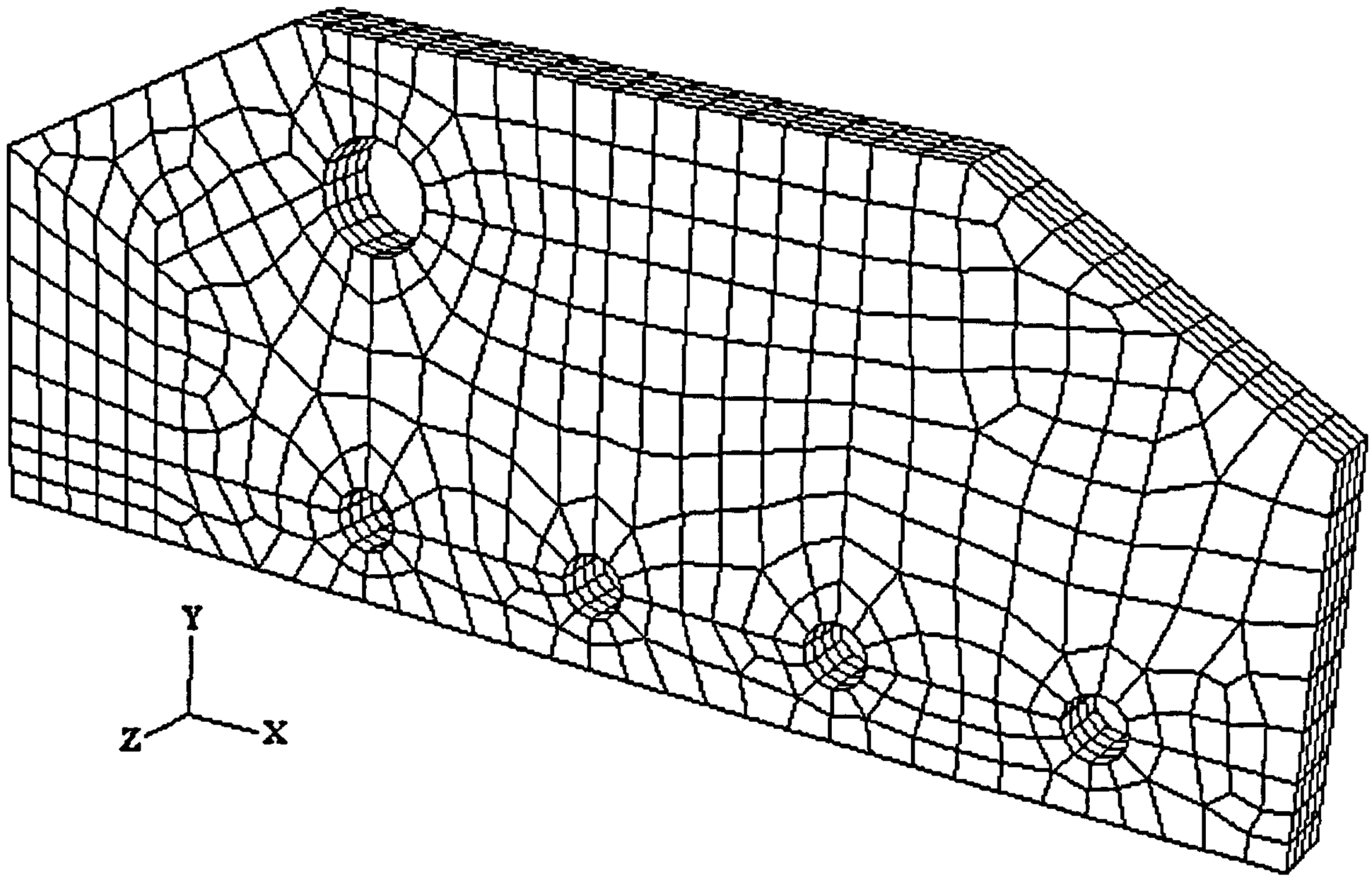

Fig. 4.25 Plate grip of 15mm thickness

The grips and the specimen were coincident resulting in a 46mm total thickness of assembly.

The grips and the specimens then were connected together by four pins as shown in the two views of Fig. 4.26. The diameter of each pin was 14mm and defined as a rigid body. A contact condition was applied between grips, specimen and joint pins.

All nodes after the crack tip on the symmetry line of the model were constrained in the loading direction. This represented the initial un-cracked ligament. There was no constraint in the x direction on the ligament nodes so that the model was allowed to move horizontally during the loading process. A square mesh of 0.4mm size was applied after the crack tip providing a good stress-strain field in the damage zone, such that ten ductile cells were attached at each FE providing a cell size of 0.04mm.

To load the model, the nodes on the surface of the pin of 25mm at the top of the grips were pulled in the y direction. To provide free rotation of grips during the simulations finite sliding was allowed between the load pin and grips.

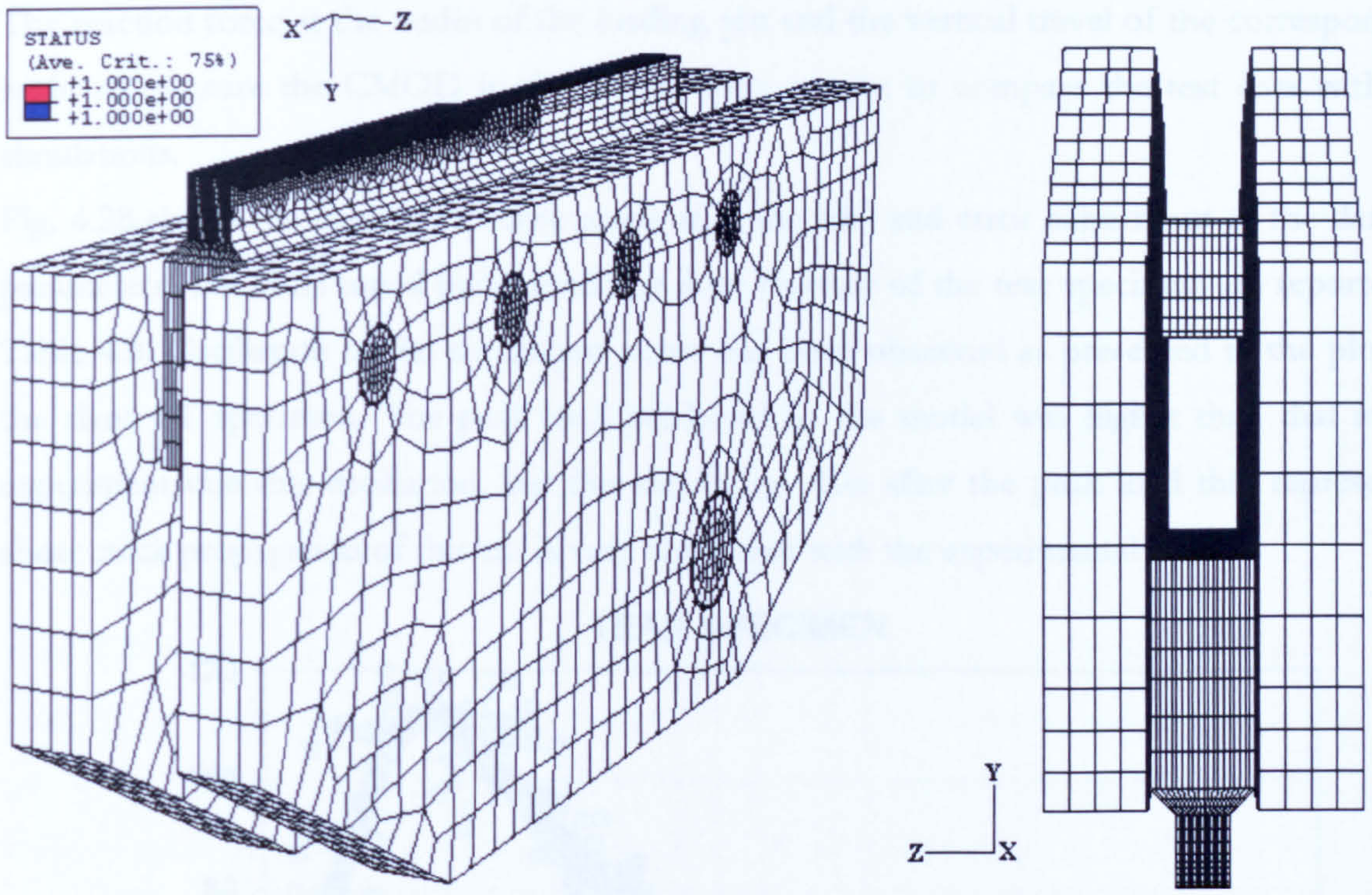

Fig. 4.26 3D views of the assembly of the tear specimen and plate grips

Fig. 4.27 shows the fracture propagation in the model at the end of the simulation, the fracture is represented with the STATUS variable in the damage zone. STATUS = 1 (red elements) for the rest that are still alive. It should be pointed out that some elements remained in the damage zone of the simulated tear tests. This needs further adjustments to allow a good distribution of the element removed during the crack growth process.

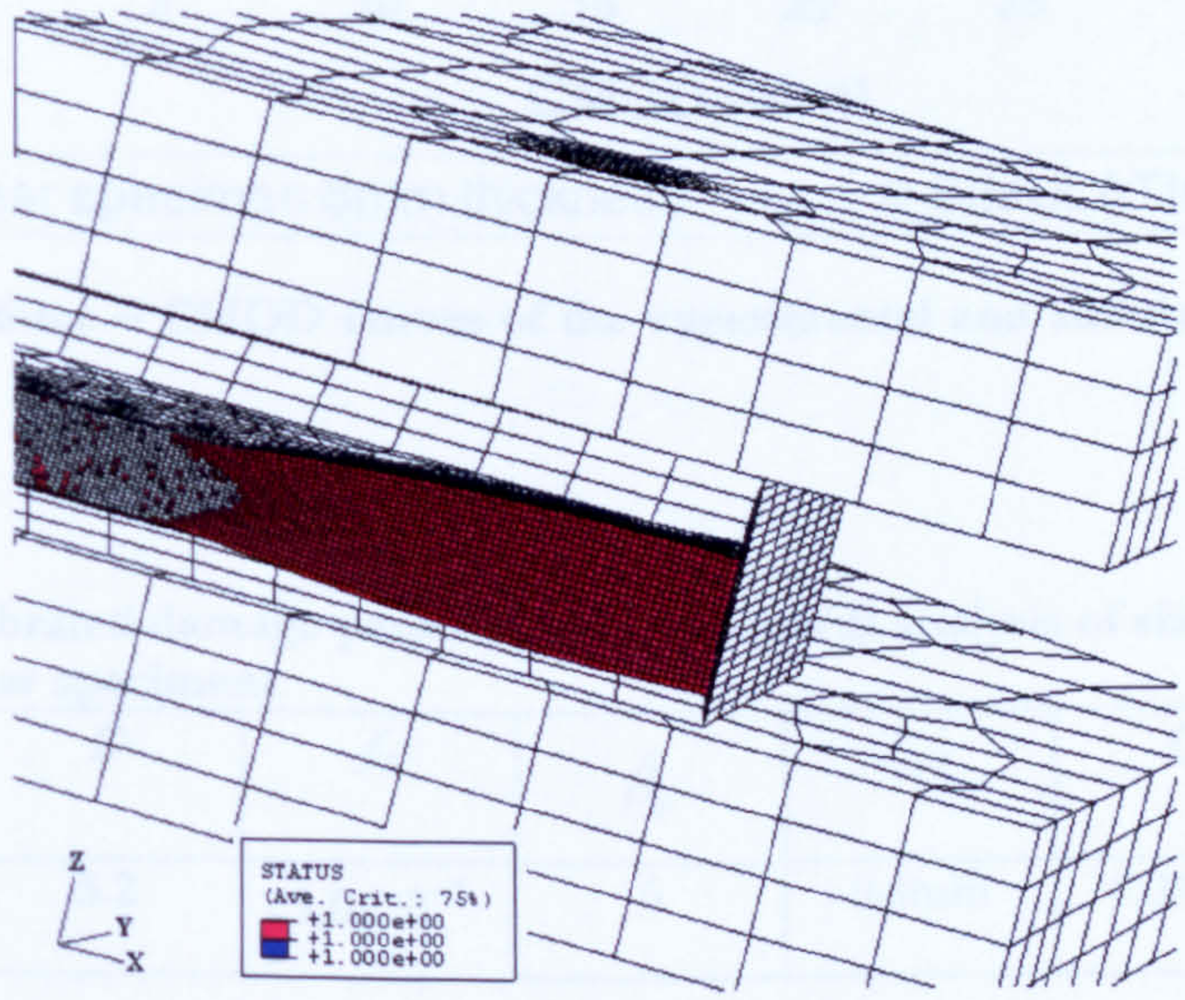

Fig. 4.27 Contour of the crack growth in the damage area

The reaction force at the nodes of the loading pin and the vertical travel of the corresponding node to measure the CMOD in the model were output to compare the test data with the simulations.

Fig. 4.28 shows the best fitted curve result after the trial and error adjustment of the damage parameters. The final tuned parameters for slant fracture of the tear specimen are reported in Table 4.8. Oscillation in the simulation curve has been observed as presented in the plot for the slant CT specimen. The peak load predicted by the model was higher than that in the experiment due this oscillation, but the simulation data after the peak load that represented shear crack propagation of the test is very consistent with the experimental data.

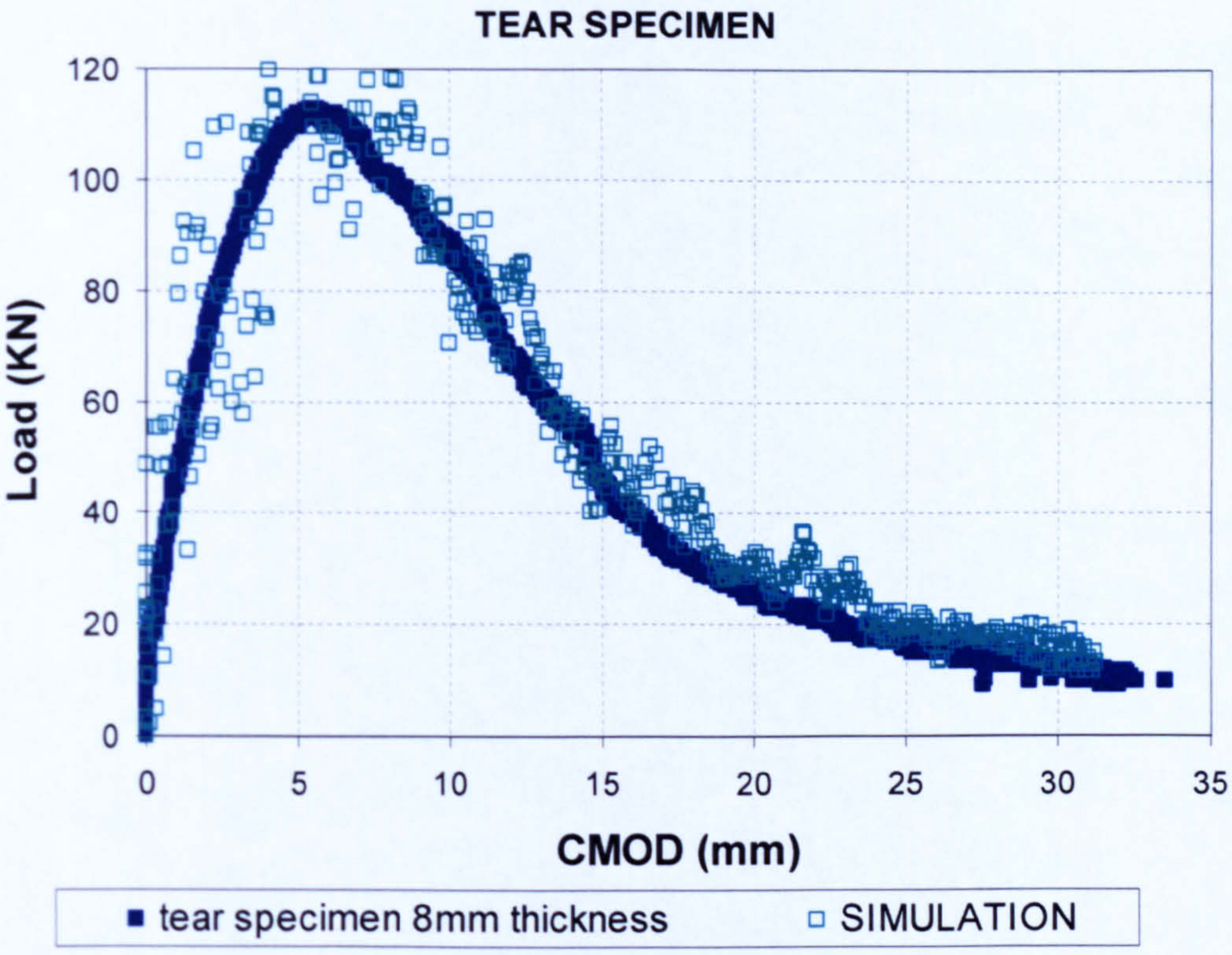

Fig. 4.28 Reaction force – CMOD curves of the experimental and simulation data of the tear test.

Table 4.8 Calibrated damage parameters for 3D CAFE analysis of shear fracture for tear specimens.

σ_1	D	f_0	$\bar{\beta}_F$	L_{FE}	L_D	$\sqrt[3]{M_D}$
780 [MPa]	**3.2**	$3.0x10^{-5}$	6	0.4mm	0.04mm	10

CHAPTER 5

Fractographic observations of the X100 steel used showed that all flat and slanted fracture surfaces were of the ductile dimpled type with some differences on their surface patterns (See more details in section 5.1). The similar macroscopic and microscopic fracture appearance implies that micromechanical models should be transferable between the corresponding specimens independently of constraint and loading conditions.

An illustration of the typical fracture patterns and the spacing measurements between large voids of flat and shear specimens is shown in Fig. 5.1. The micromechanical observations for the X100 pipeline steel revealed that average size of spacing between large dimples of flat fracture were of the order of five times larger than for shear fracture ($200\,\mu m$ and $40\,\mu m$ respectively). These dimensions have introduced different length scales that have been interpreted in the finite element simulations by modifying the mesh size according to the ratio of the large voids mean spacing, d.

In this research, efforts were carried out in the previous chapter to find unique failure parameter values for the corresponding fracture characteristics of the X100 pipeline steel. It has been shown that it was possible to extract the fracture information of the line pipe material from laboratory specimens and their tuned damage models. It should be pointed out that the transferability of the damage parameters worked very well for some models, but did not work for others. This will be discussed in the current chapter making use of the CAFE computational modelling strategy because it has demonstrated its effectiveness in reducing the simulation time whilst maintaining satisfactory damage predictions. The damage prediction modelling has been used finally to assess the fracture resistance of the pipeline material in terms of CTOA fracture criterion.

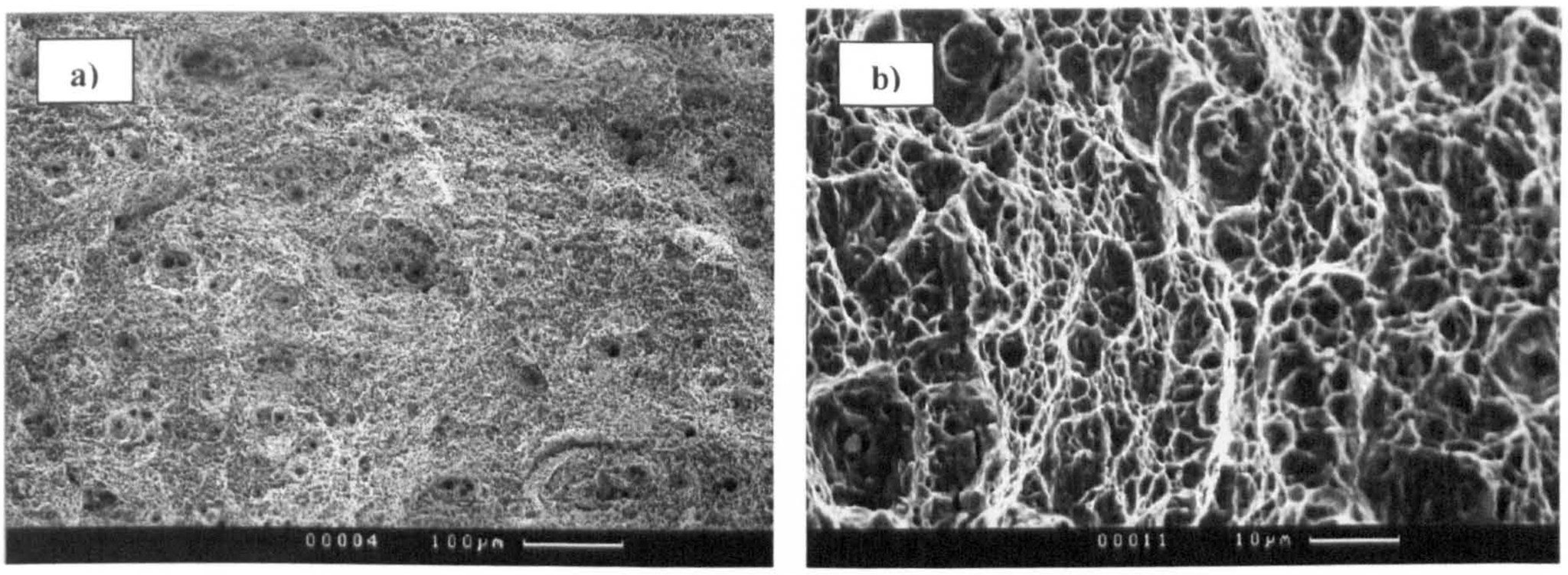

Fig. 5.1 SEM Fractography of the fracture surface of a) tensile test in transverse direction and b) tear specimen pulled out in transverse direction with the initial crack in the longitudinal direction of the pipeline.

5.1 OBSERVATIONS OF THE SPECIMEN FRACTURE SURFACES

5.1.1 Macroscopic fracture surface observations

Different photographs of the macroscopic fracture surfaces from different sets of test specimens (tensile tests, standard C(T) and tear samples) are shown in Figs. 5.2 to 5.4. All specimens showed mainly flat and shear surface fracture characteristics. The macroscopic fracture surface of these specimens can be sorted out according the following categories: (A) flat fracture, (B) shear fracture, and (C) quasi-cleavage.

Fig. 5.2a-d shows a macrospically flat fracture (A) at the centre and slanted rupture (B) at the edges of the smooth tensile specimens for all directions. In particular, small smooth fracture areas of quasi-cleavage (C) at the edges of the tensile test in the thickness direction has been observed, these observation are out of the ordinary in the X100 steel tested at room temperature. However these regions are very small compared with the flat and shear rupture surfaces. The fracture surface obtained for the standard C(T) specimen is shown in Fig. 5.3. It shows flat rupture (A) at the initiation site and throughout the fracture, and it was followed by a cleavage zone after having been broken in liquid nitrogen. Fig 5.4 shows the fracture surface of the 8mm tear specimen, the fracture initiates as triangular ductile flat zone (A), followed by successive beach marks of quasi-cleavage fracture (C). The rest of the region corresponds to ductile shear (B). The 8mm thickness specimen showed full stable surface fracture shearing. In the 10 and 12mm ligament thickness specimens were observed some areas with flat fracture

characteristics after the shear in particular when the fracture path changed angle. This was more noticeable for the thicker specimen.

Details of flat and shear ductile fractures, and quasi-cleavage regions conducted by SEM are given in section 5.1.2.

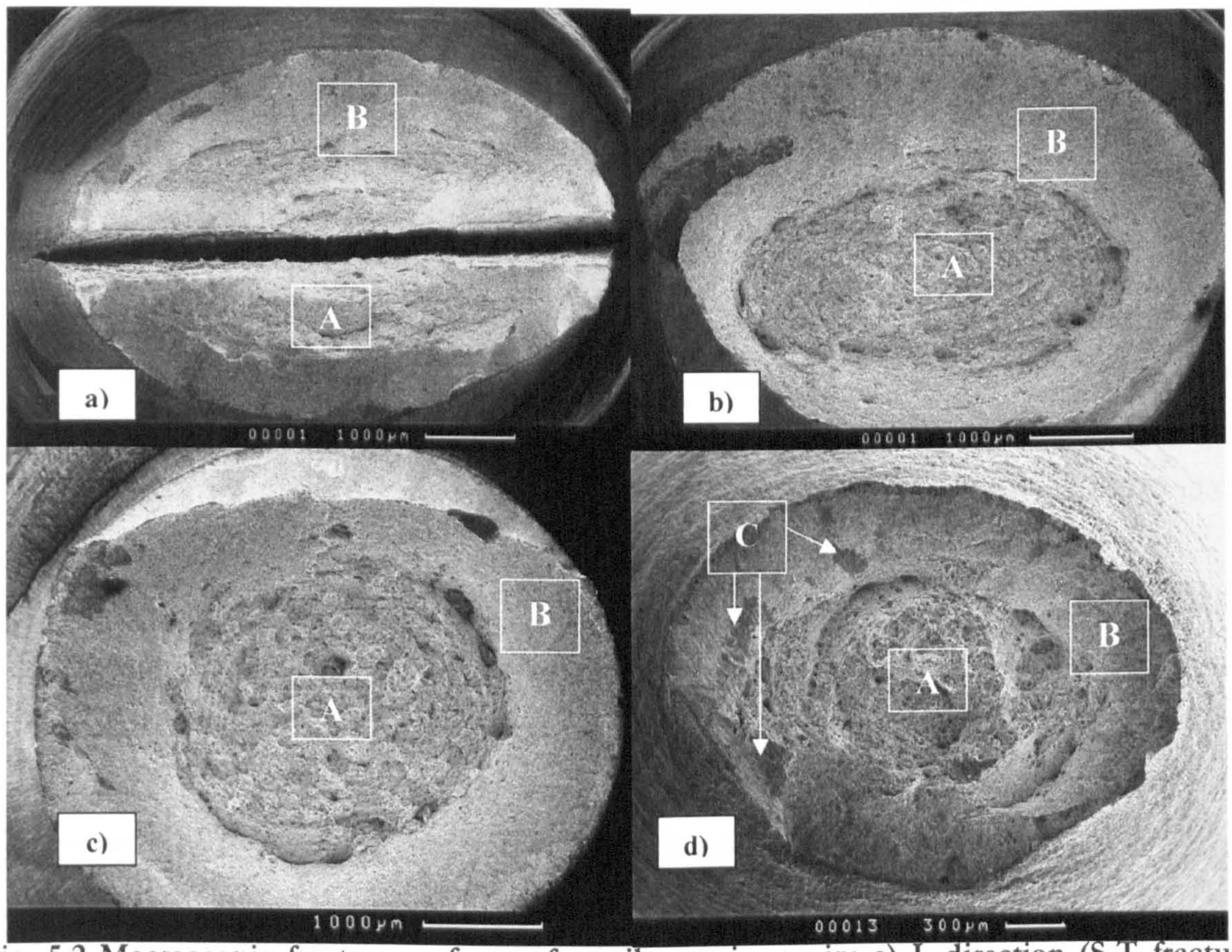

Fig. 5.2 Macroscopic fracture surfaces of tensile specimens in: a) L direction (S-T fracture plane), b) T direction (S-L fracture plane), c) 45 direction (S-LT fracture plane) and d) S direction (L-T fracture plane).

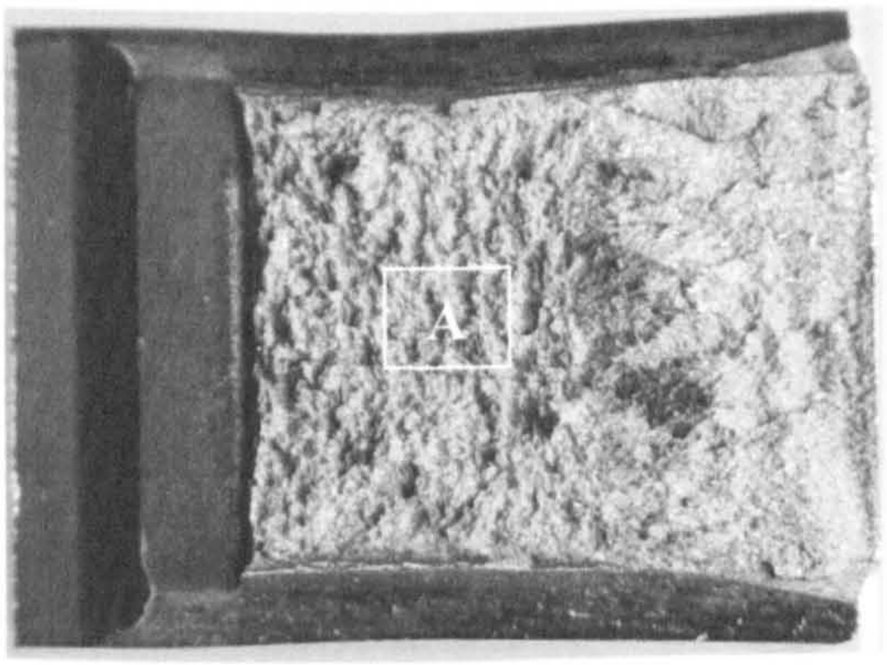

Fig. 5.3 Macroscopic fracture surface of C(T) specimen.

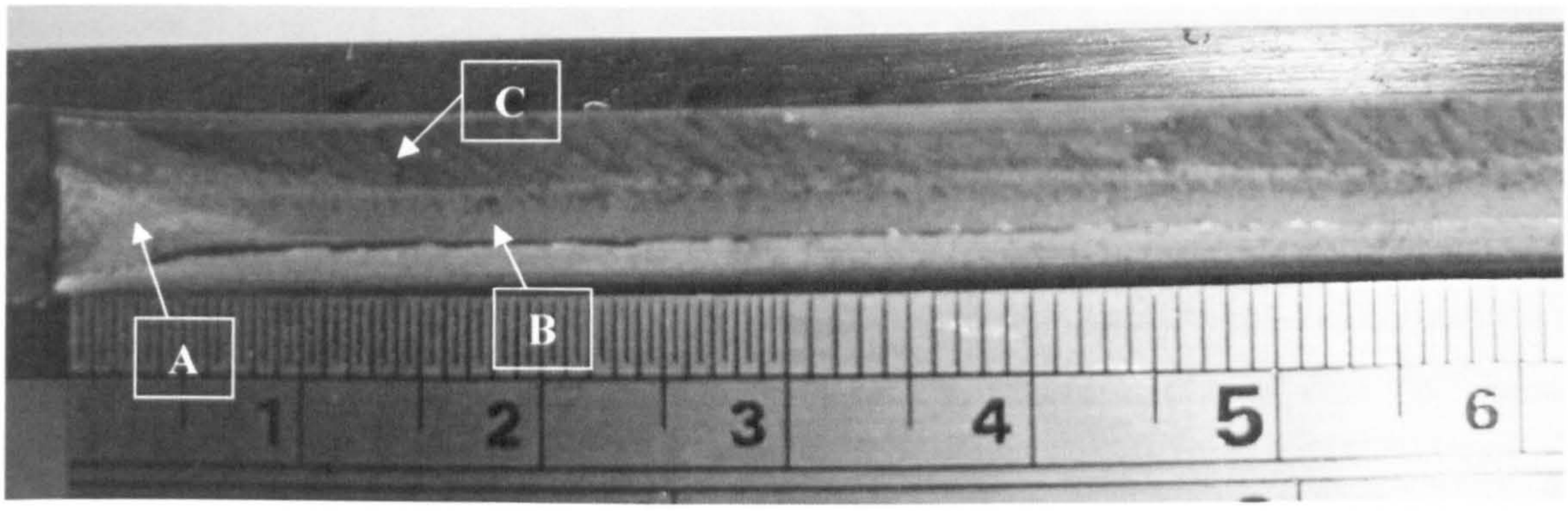

Fig. 5.4 Photographs of the fracture surface of tear test of 8mm ligament thickness.

5.1.2 Microscopic fracture surface observations

At higher magnification, SEM fractography observations showed that all flat and slanted fracture surfaces were of the ductile dimpled type. In slanted planes, the rupture surface also exhibits a few smooth areas where small dimples cannot be seen. These have the appearance of quasi-cleavage fracture. These small areas are more frequent in plain tensile specimens in the thickness direction and in the beach marks of the slant specimens.

The comparison of the microscopic ductile fracture surface obtained on flat and slant specimens are different and indicated two principal failure mechanisms. In flat regions, a void growth mechanism is dominant and large dimples can be seen around second phase particles. In slanted regions, void growth is limited which leads to the formation of smaller voids.

All fracture surface observations at the centre of tensile specimens had cluster of small and large dimples representing the tensile fracture mode. This led to the formation of macroscopic fracture surface type "A". The SEM of the edge of the broken tensile specimens showed that the voids were shallow and had an elongated appearance representing the macroscopic shear crack growth type "B" on the slanted planes. Figs. 5.5 to 5.8 show SEM fractographs of the dimple appearance at the centre and the edges of test bar specimens in all loading directions. In Fig. 5.8c is displayed a close up of the quasi-cleavage fracture surface at the edges of thickness tensile bars.

Flat fracture surfaces of CT specimens (Fig. 5.9) showed dimple appearance similar to the fracture surface at the centre of tensile samples. The fracture at the centre of tensile bars and ahead of the crack tip in C(T) samples was dominated by micro-voids. It should be pointed out that fracture surface in flat specimens differ in size and cluster of micro-voids, but the average spacing between larger dimples or group of larger voids was approximately the same.

In tear specimens, the initial fracture had the features of flat fracture surface with cluster of small and large dimples corresponding to the opening mode as can be seen in the triangular area of Fig. 5.10a and the close up of Fig. 5.10b. The fractographs of the slant specimens had stretched micro-voids representing the shear void growth, and had populations of elongated small and large voids. These elongated voids indicated that shear deformation dominated the final stage of crack growth. These micro-voids lead to the formation of type "B" fracture surfaces.

Fracture surface observations have provided evidence concerning the transferability of micro-mechanisms between the corresponding flat and shear specimens.

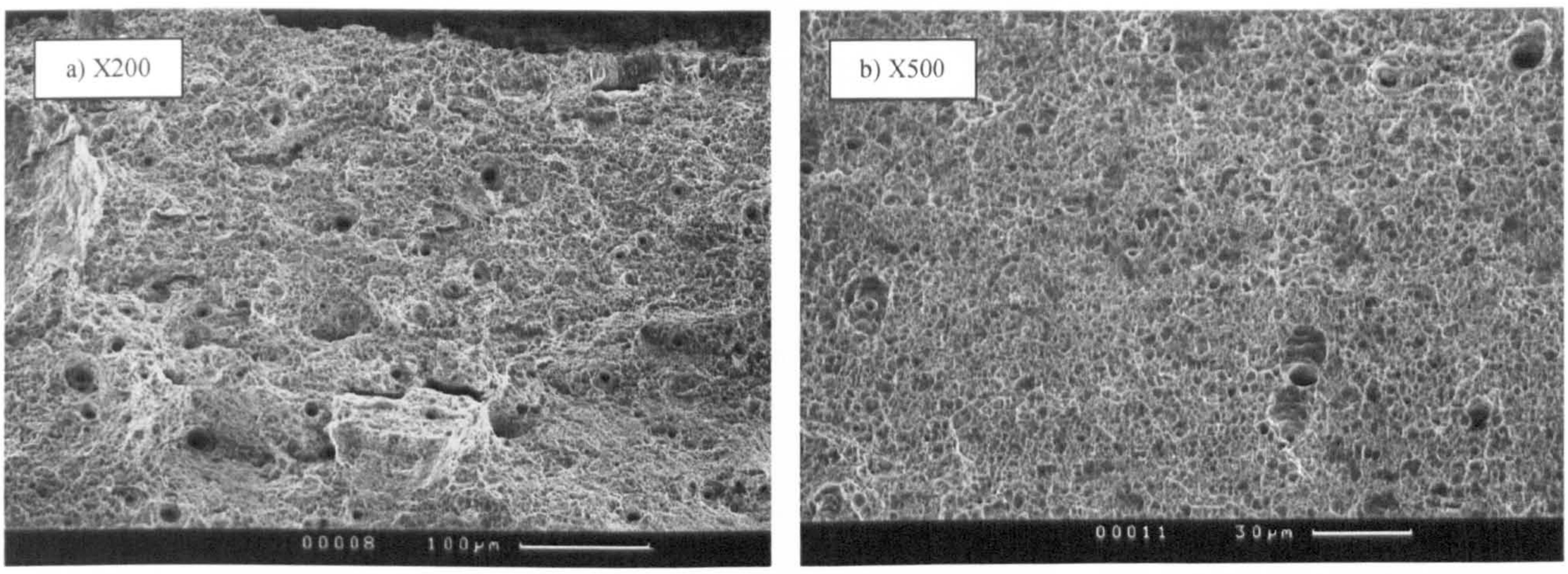

Fig. 5.5 SEM fractography of longitudinal tensile specimen: a) close up of the flat fracture in the centre zone and b) close up of the shear fracture in slanted zone.

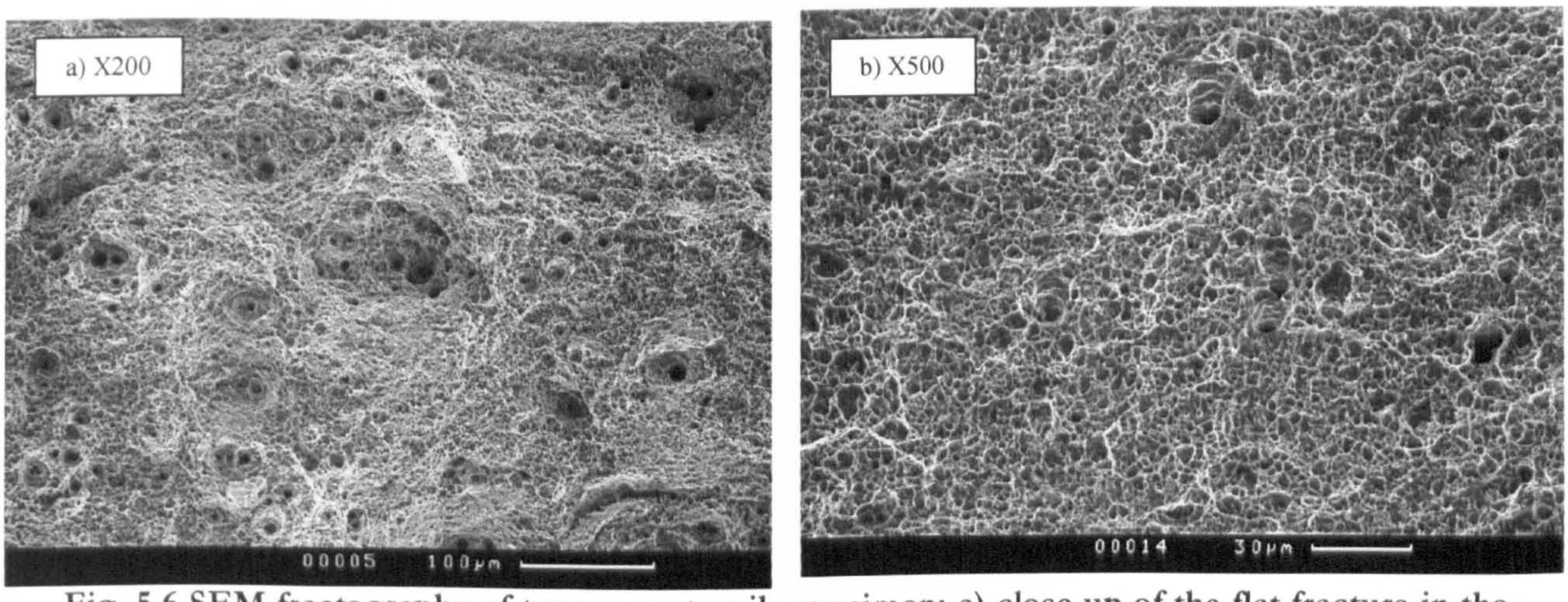

Fig. 5.6 SEM fractography of transverse tensile specimen: a) close up of the flat fracture in the centre zone and b) close up of the shear fracture in slanted zone.

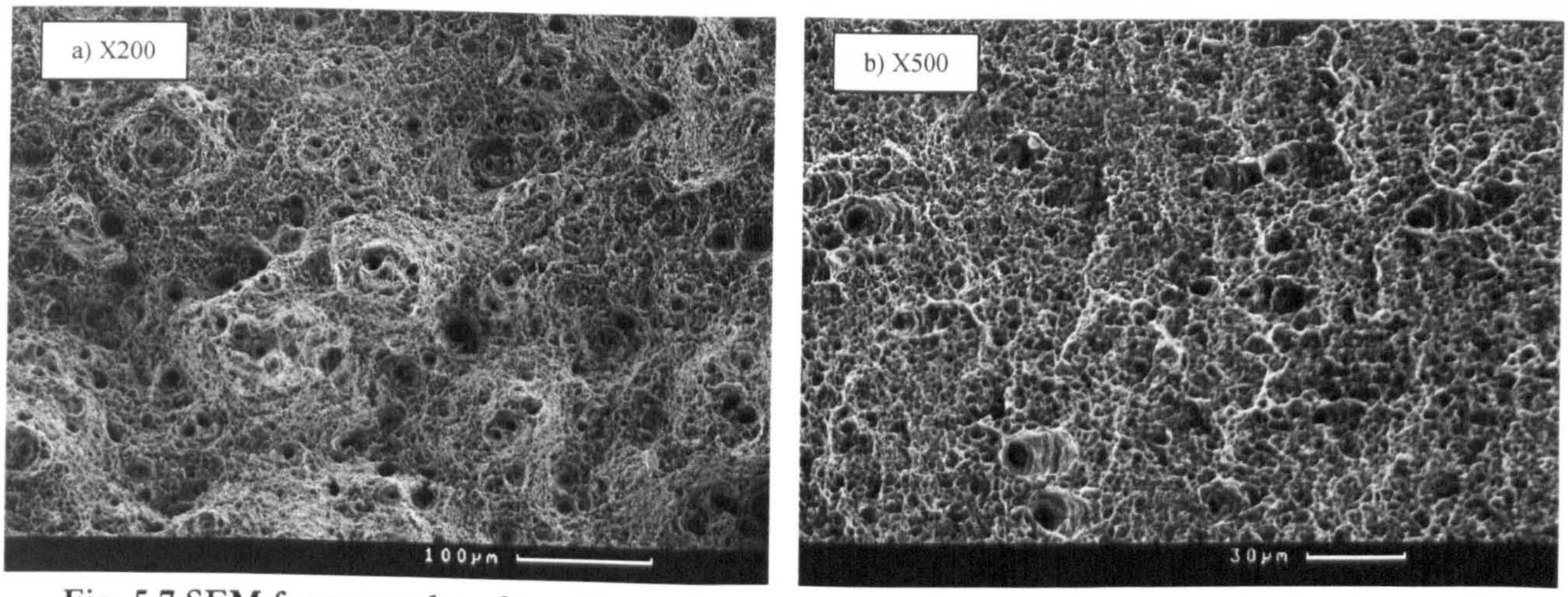

Fig. 5.7 SEM fractography of tensile specimen in 45 direction: a) close up of the flat fracture in the centre zone and b) close up of the shear fracture in slanted zone

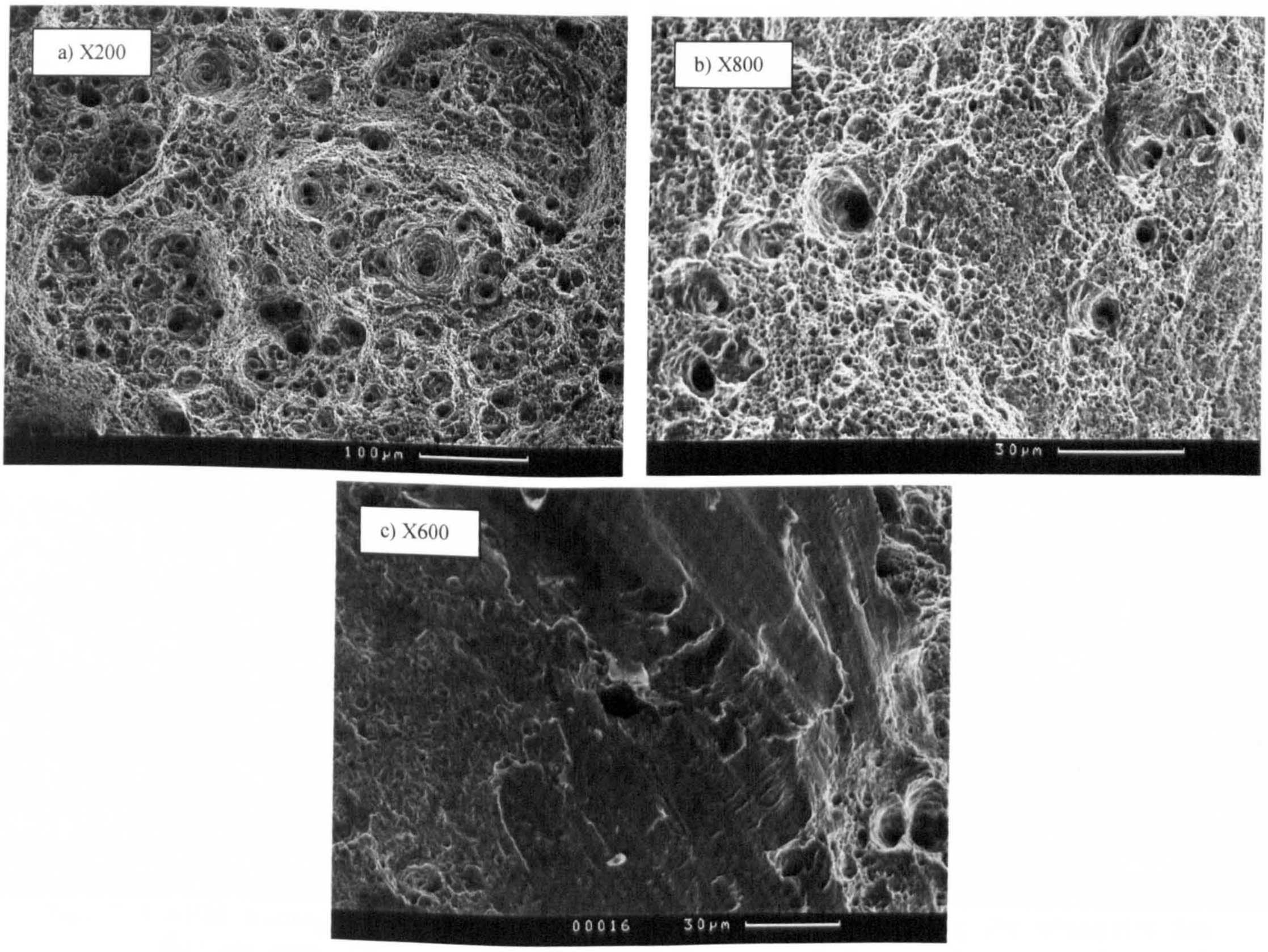

Fig. 5.8 SEM fractography of tensile specimen in thickness direction: a) close up of the flat fracture at the centre zone, b) close up of ductile shear in slanted zone and c) close up of the smooth area (quasi-cleavage fracture) in slanted zone.

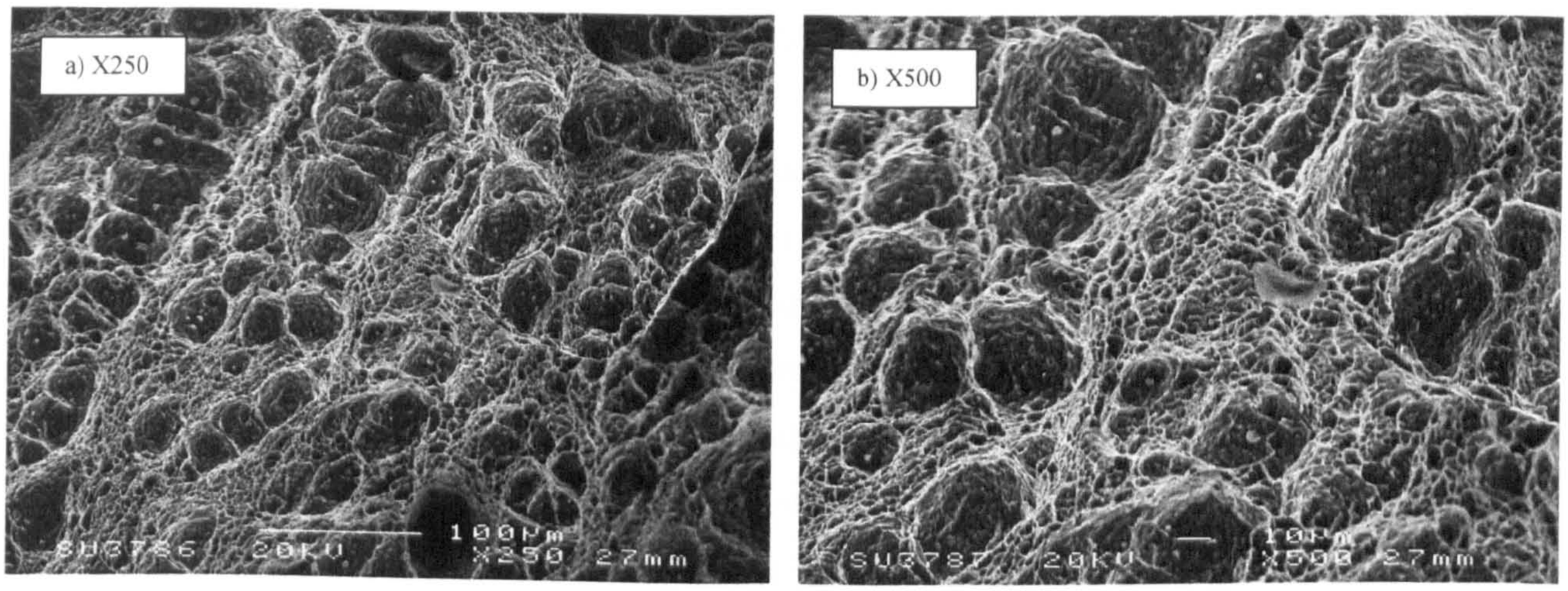

Fig. 5.9 SEM fractography of C(T) specimen: a) and b) close up of the flat fracture in the centre and ahead of the sample

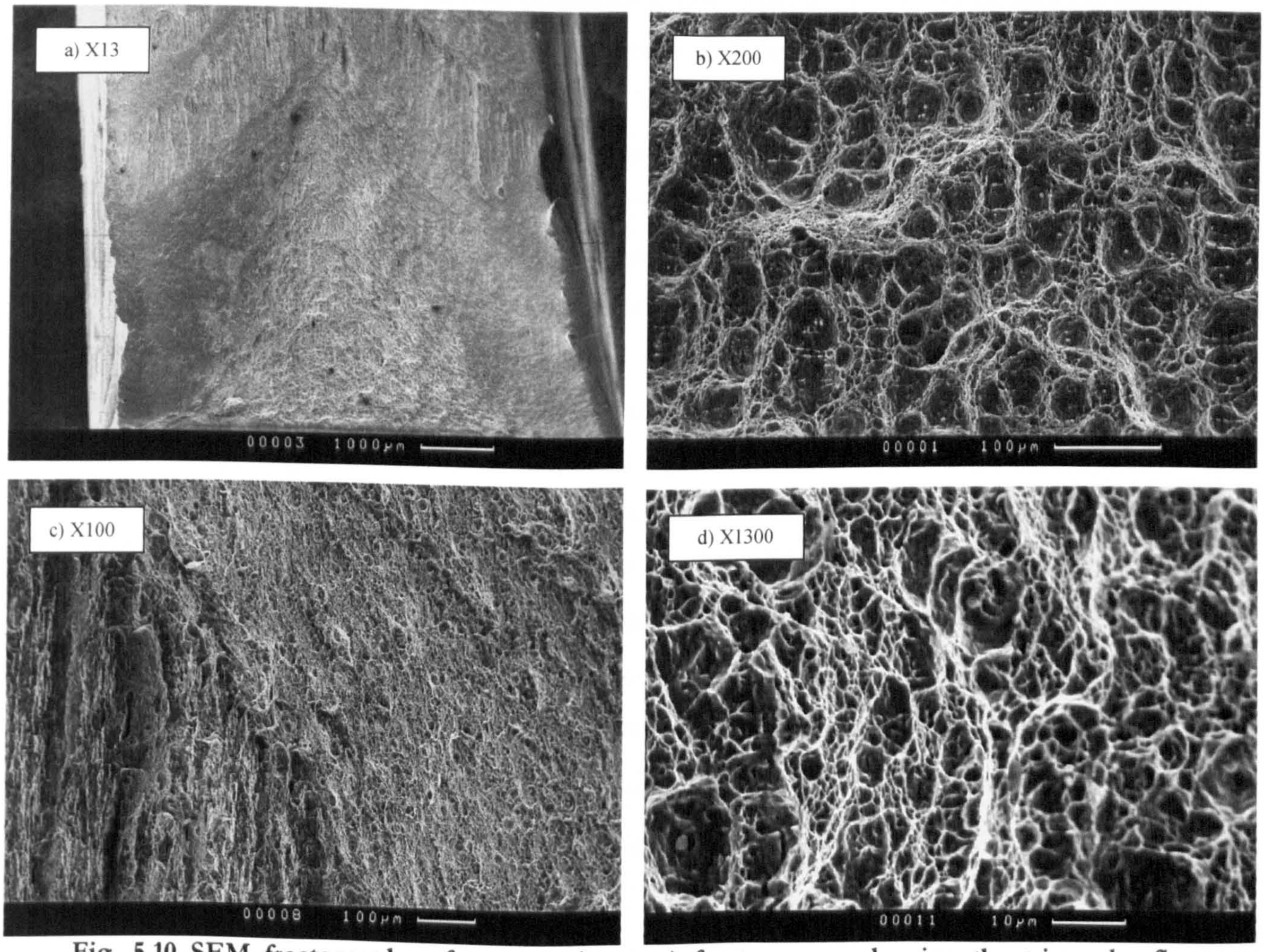

Fig. 5.10 SEM fractography of tear specimen: a) fracture area showing the triangular flat fracture area. The successive beach marks of quasi-cleavage fracture and slanted plane regions b) close up of the large dimples in the flat fracture zone, c) close up of the quasi-cleavage and shear fracture areas d) close up of dimples in the slanted zone of the sample.

5.2 TRANSFERABILITY OF DAMAGE PARAMETERS

5.2.1 Transferability of damage parameters in tensile specimens

CAFE analysis demonstrated that Rousselier damage model was able to reproduce the experimental data of all tensile specimens in each orientation when invoking the assumption of effective material damage isotropy. It was also found that a unique set of micromechanical damage parameters was transferable for the corresponding tensile orientations with different levels of restraint. It is important to note that even though the average spacing between larger dimples was approximately of the same value the damage parameter D differed for all four pipe orientations (Table 4.2). This combined with the differing hardening behaviour and the different fracture pattern in the four orientations, from Figs. 5.5 to 5.8 can be seen the micro-voids on the fracture surface of tensile specimens in different orientations differ in size and quantity of them in a cluster of dimples. Example of the transferability of the tuned micromechanical damage parameters of the tensile tests in 45° direction is shown in Fig. 5.11.

Validation of damage prediction was also carried out in terms of deformation contours on square tensile section specimens in the thickness orientation. It was done by comparing the field of the deformations of experimental and simulation results having used the previous calibrated micromechanical parameters of the corresponding cylindrical tensile specimen. In these samples, using an imaging correlation method and grid technique, the whole deformation field in the loading direction was extracted and represented by contours at the end of the test. This was compared with 3D CAFE numerical simulations that were conducted using the same fixed parameters for corresponding directions listed in Table 4.2. Numerical results at the centre of the specimen at the point that the crack started to growth, $\varepsilon_{CAFE} = 2.1$, has demonstrated that the damage parameters previously calibrated were transferable to predict with sufficient accuracy the experimental engineering strain for the experimental grid $\varepsilon_{\exp-grid} = 2.4$ and DIC technique $\varepsilon_{\exp-DIC} = 2.35$. Fig. 5.12 shows the contour results for the experimental results and CAFE model at the end of the simulations.

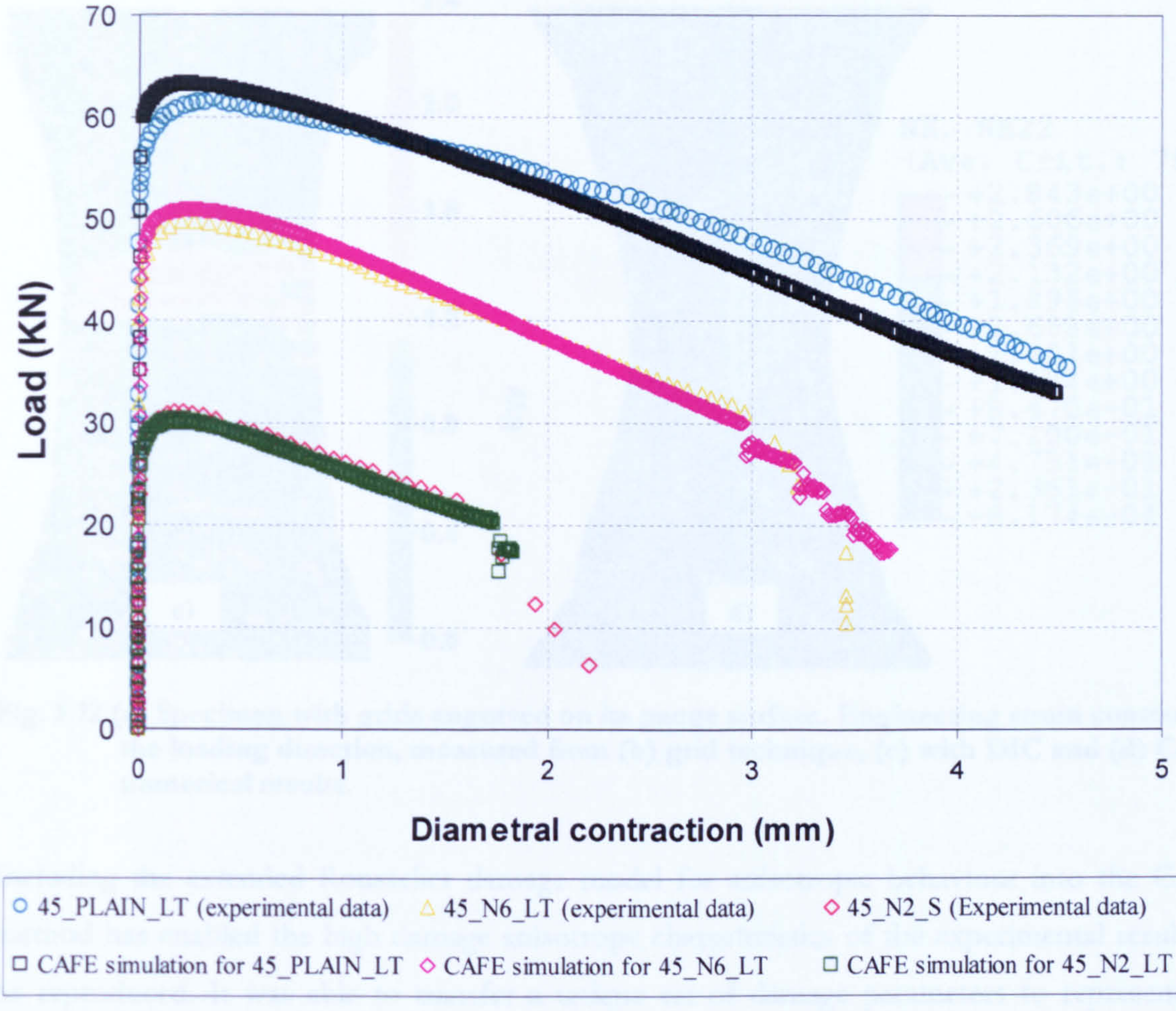

Fig. 5.11 Experimental and best fitted data for GTN and Rousselier damage models.

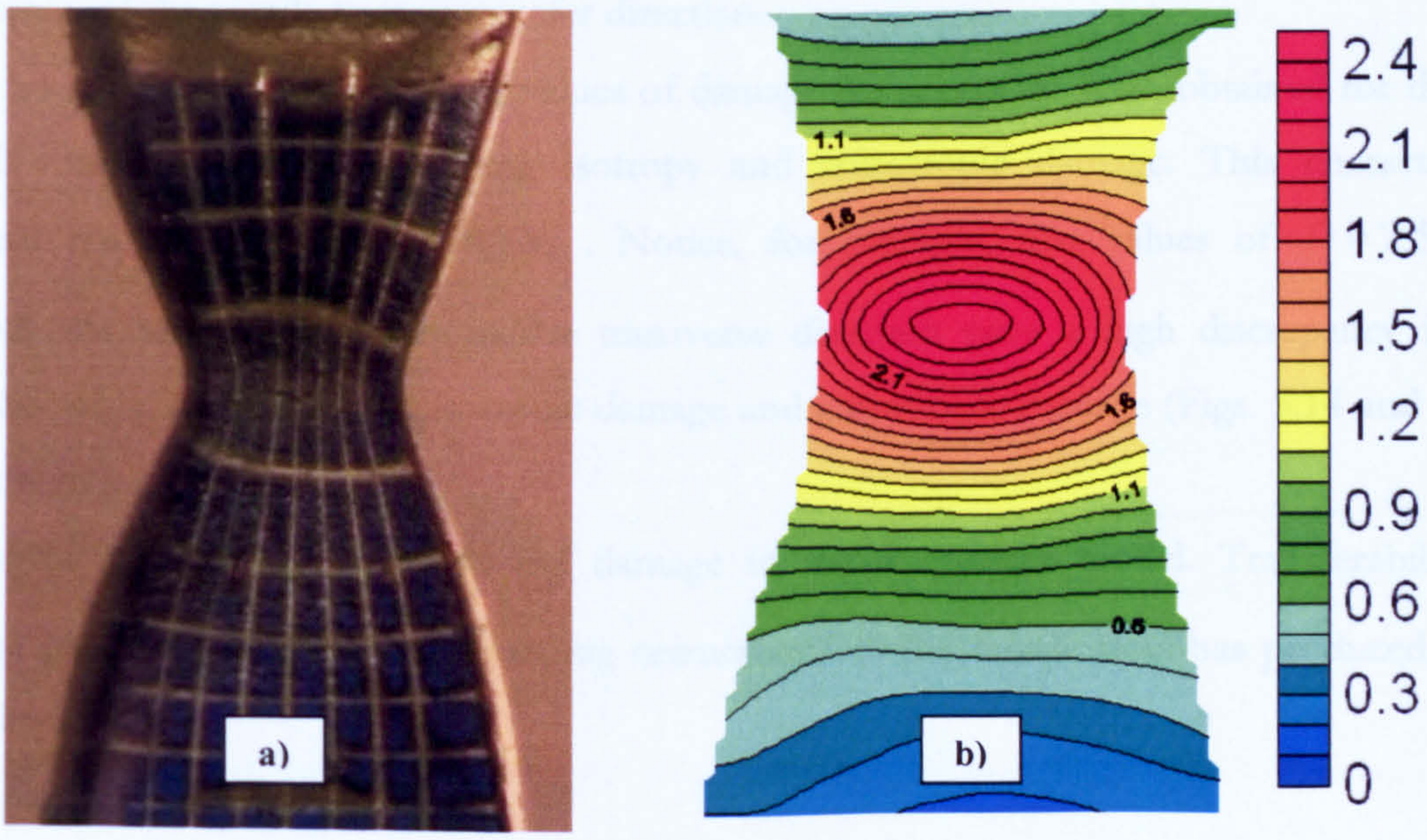

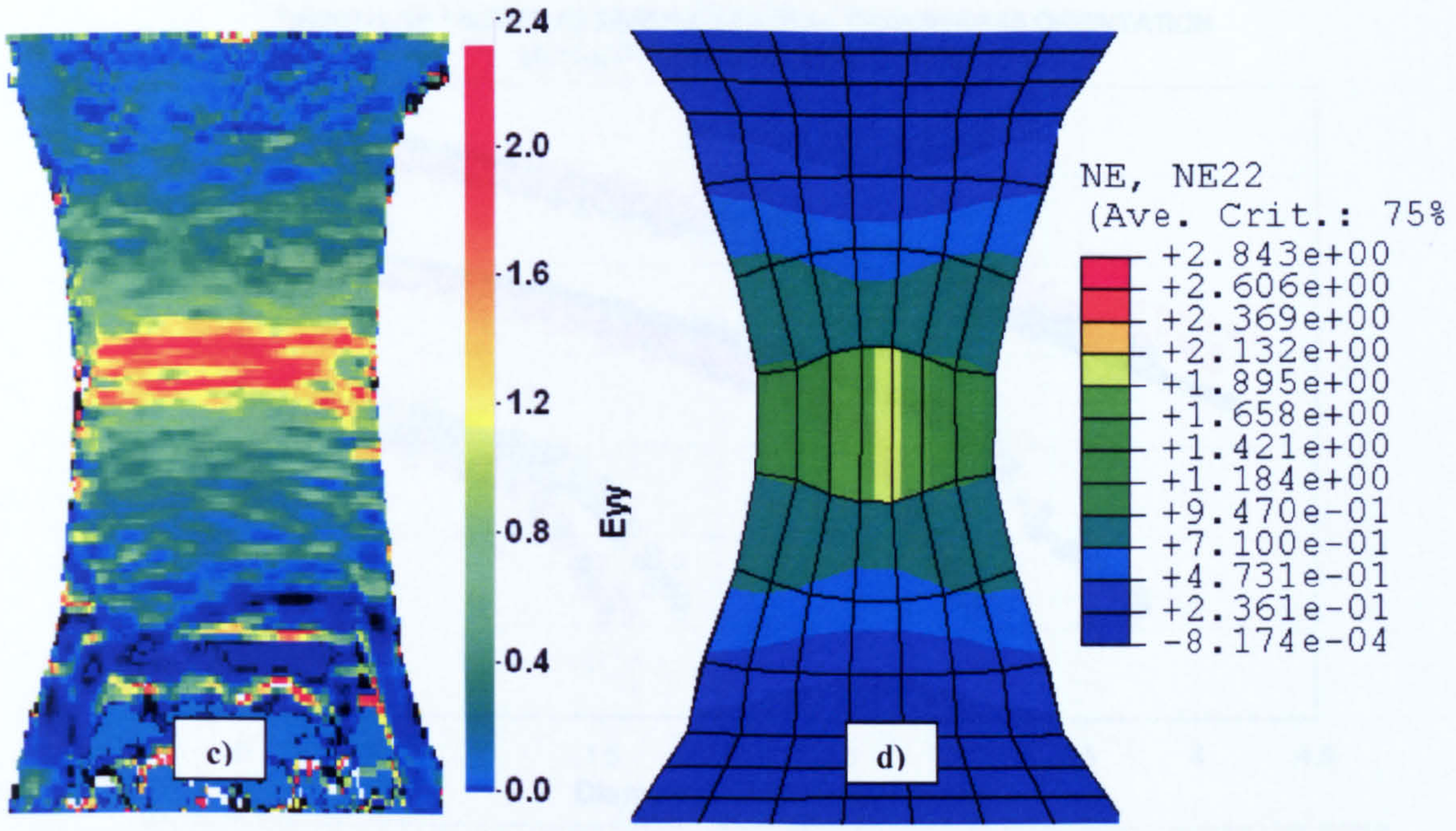

Fig. 5.12 (a) Specimen with grids engraved on its gauge surface. Engineering strain contours in the loading direction, measured from (b) grid technique, (c) with DIC and (d) CAFE numerical results.

Including the extended Rousselier damage model for anisotropic behaviour into the CAFE method has enabled the high damage anisotropy characteristics of the experimental results to be reproduced. It was able to transfer a unique set of damage parameters to represent the considerable ovalisation of the tensile tests at the end of their deformation with different capacities of restraint. Fig 5.13 shows an example of the transferability of the tuned damage parameters of the tensile tests in transfer direction.

It has been observed that different values of damage parameter D were obtained for the 3D CAFE simulations when assuming isotropy and anisotropic damage. This characterised different triaxial stress states σ_m/σ_{eq}. Notice, for example, that values of $D=2.5$ and $D=0.8$ for tensile specimens in the transverse direction gave a high discrepancy in the triaxiality of 0.78 and 0.61 for isotropic damage and anisotropic damage (Figs. 5.14 and 5.15), respectively.

The stress ratio σ_m/σ_{eq} controls the damage in the Rousselier model. Transferability of damage parameters in the corresponding orientations of the tensile tests has produced same triaxiality levels.

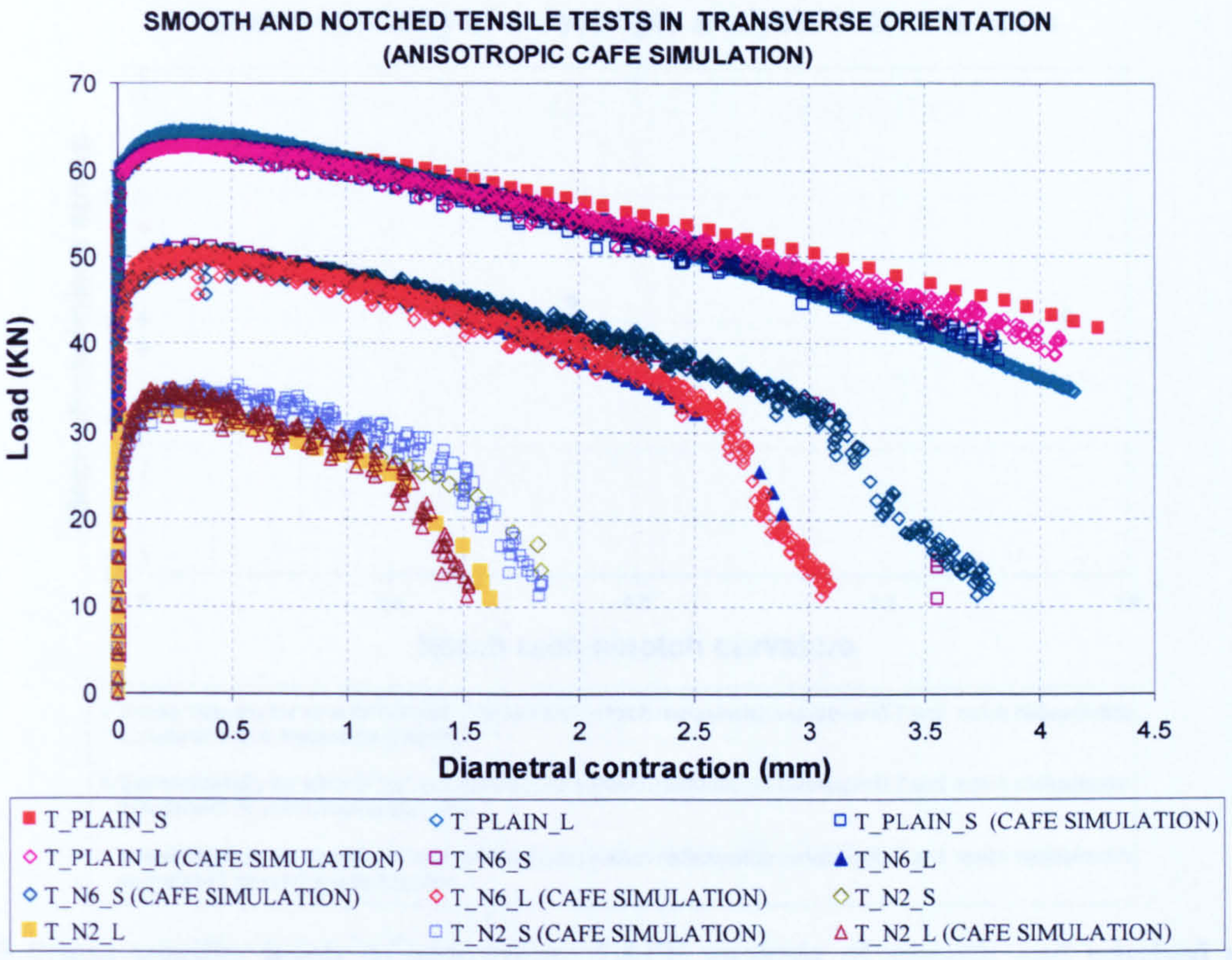

Fig. 5.13 Experimental data and best fitted anisotropic CAFE simulation.

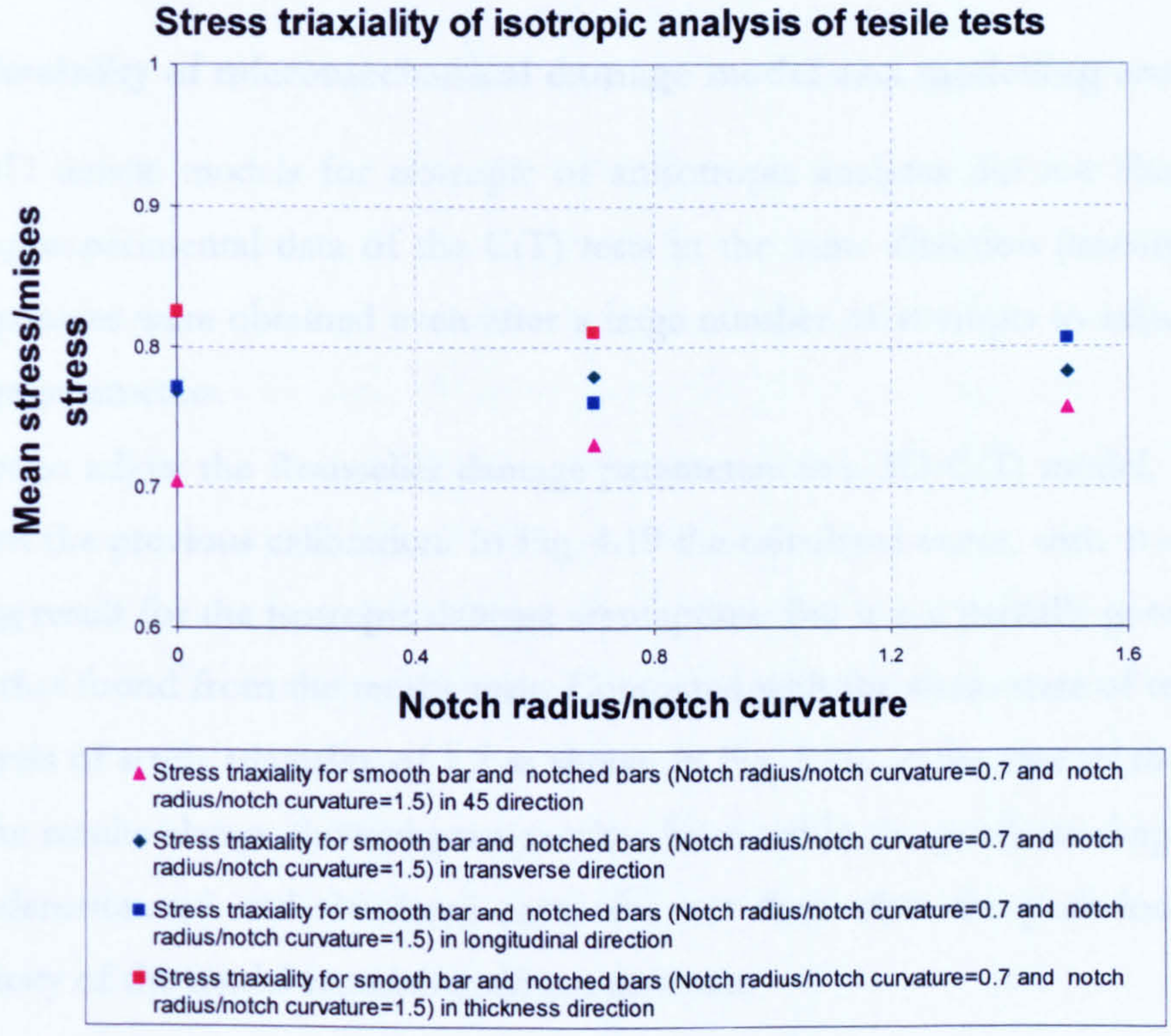

Fig. 5.14 Stress triaxiality levels of isotropic CAFE analysis of smooth and notched tensile tests.

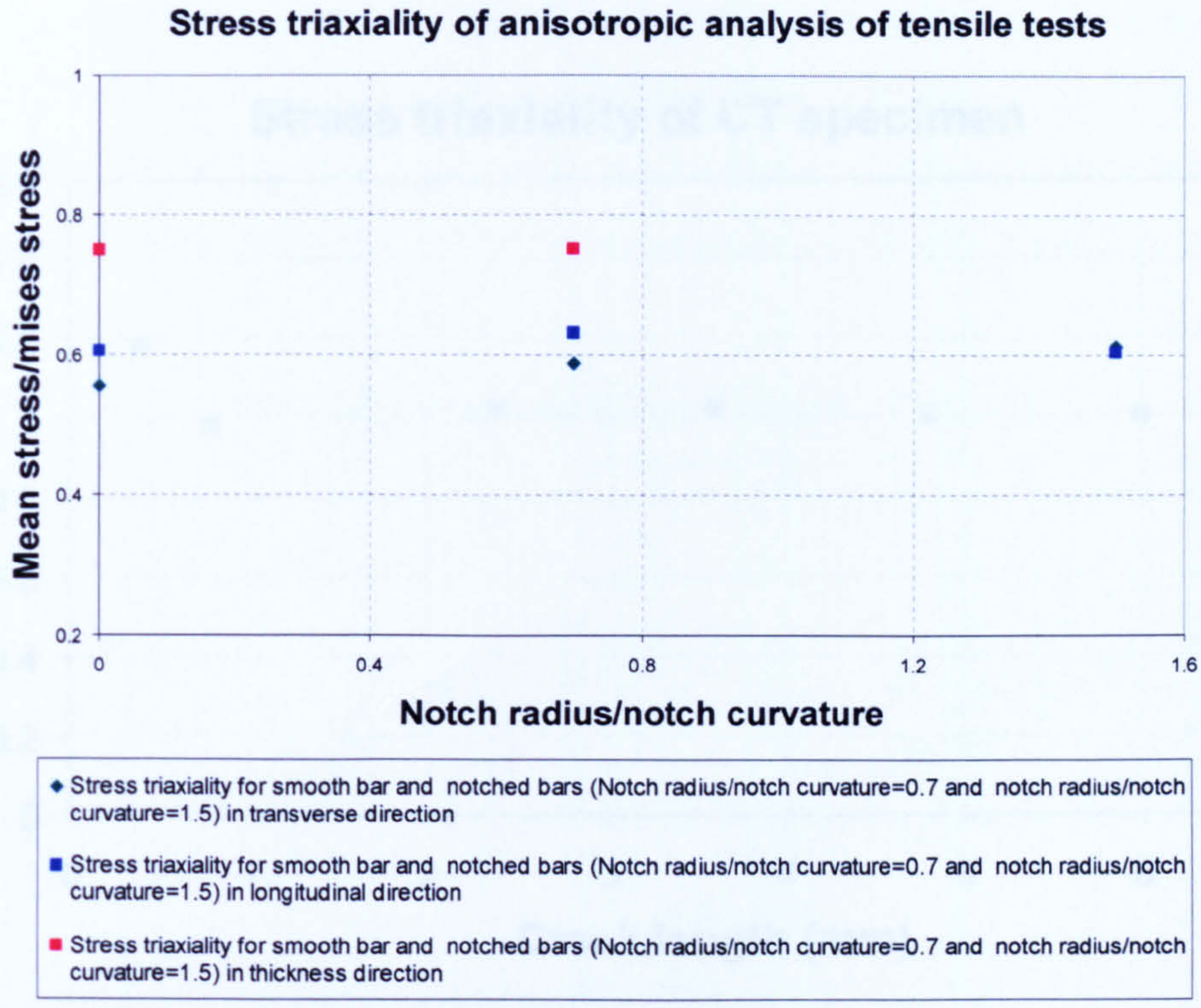

Fig. 5.15 Stress traxility levels of anisotropic CAFE analysis of smooth and notched tensile tests.

5.2.2 Transferability of micromechanical damage model and modelling analysis of CT specimens.

The tuned 3D tensile models for isotropic or anisotropic analyses did not characterise the corresponding experimental data of the C(T) tests in the same direction (transfer direction). These discrepancies were obtained even after a large number of attempts to adjust the values of the damage parameters.

In an attempt to adjust the Rousselier damage parameters in a 3D C(T) model, D has been modified from the previous calibration. In Fig. 4.19 the calculated curve, with $D=4.5$, showed a good tuning result for the isotropic damage assumption. But it is a partially good result, as it differs from that found from the tensile tests. Compared with the stress state of tensile tests, it led higher levels of stress triaxiality of 1.2 as shown in Fig. 5.16. In the case of the anisotropic behaviour, the results always showed poor results. As stated in the previous chapter, the peak load was underestimated and simulated curve did not drop after the peak load; the stress carrying capacity of the model remaining almost constant.

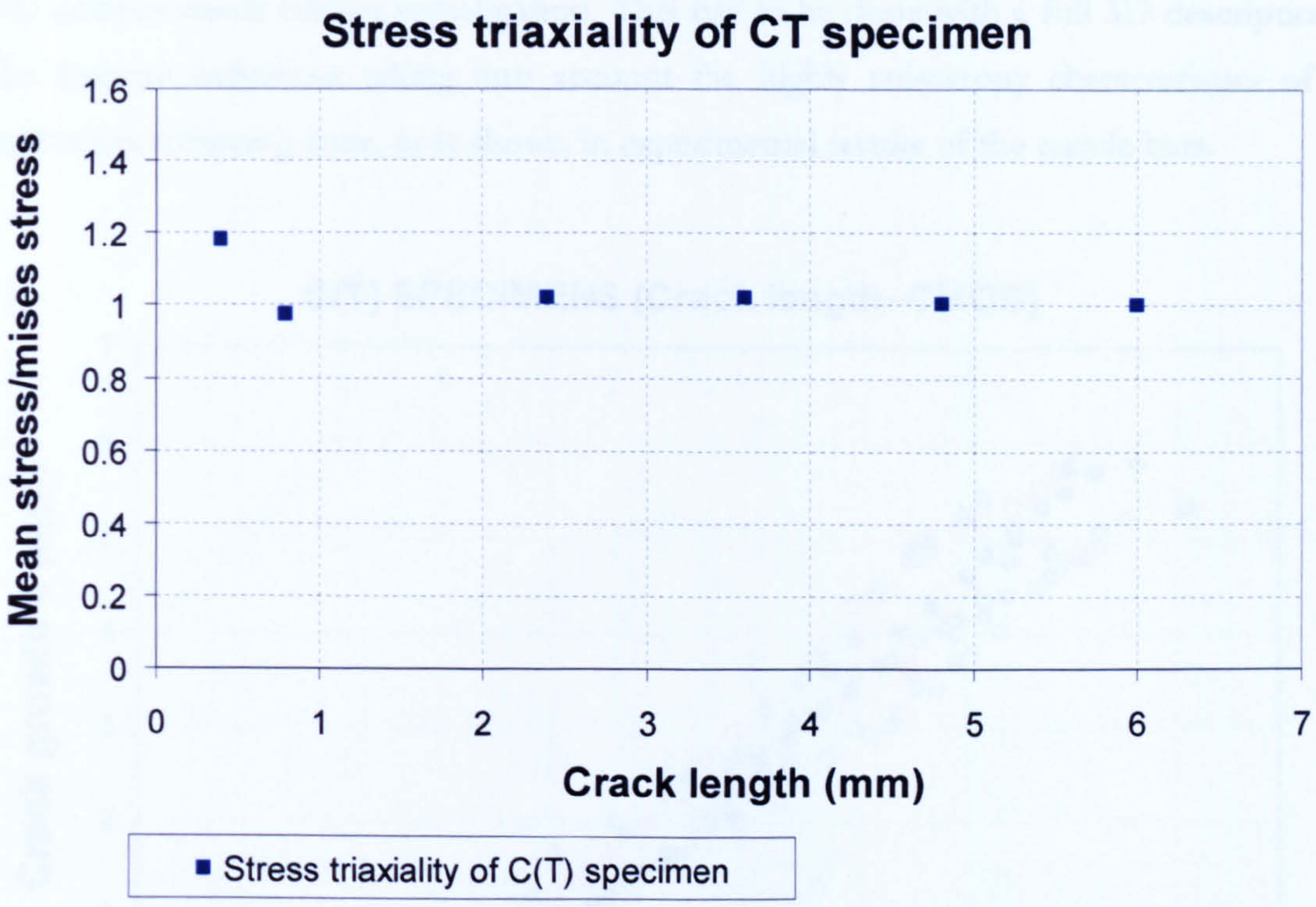

Fig. 5.16 Stress triaxility levels of anisotropic CAFE analysis of C(T) tests.

The damage value of $D = 4.5$ that was needed to tune the experimental data of the CT specimens was used to estimate the crack growth and energy release rate during flat fracture propagation. The estimation of the crack growth from the calibrated CAFE modelling reproduced the experimental data obtained from the measurement using a video camera (optical method), and from the use of a direct current potential drop (DCPD technique). The curve results are shown in Fig. 5.17 as function of CMOD.

The measurement of the energy rate consisted of numerically calculating the area under the load-displacement graph from the CAFE modelling. Fig. 5.18 displays the measurement of the rate energy against crack length.

To measure the specific flat fracture energy, the initiation energy was subtracted from the total fracture energy. The obtained energy was divided by the total fractured area, which gave a value of 1.4 J/mm^2 . This is similar with the value of 1.1 J/mm^2 for the flat fracture specific energy in the same material measured on tensile and standard C(T) specimens (Hashemi, 2004b), and with similar data reported by Stampfl and Kolednik, 2000.

It should be pointed out that proper transferability of the damage values from tensile to C(T) in a 3D analysis needs further investigation. This has to be done with a full 3D description of the flat fracture behaviour taking into account the highly anisotropy characteristics of the material in the softening zone, as is shown in experimental results of the tensile bars.

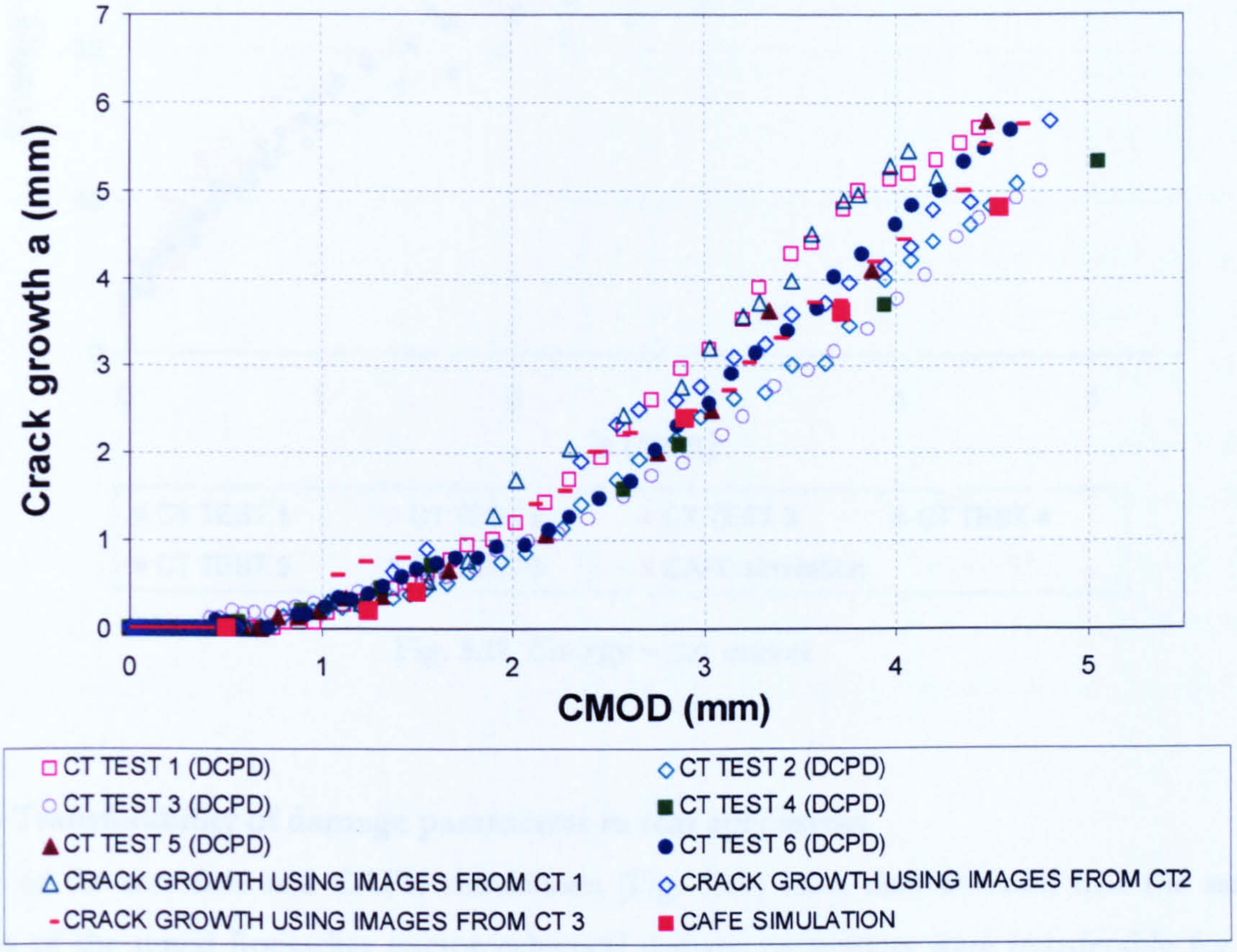

Fig. 5.17 Δa -CMOD curves results from DCPD and optical method

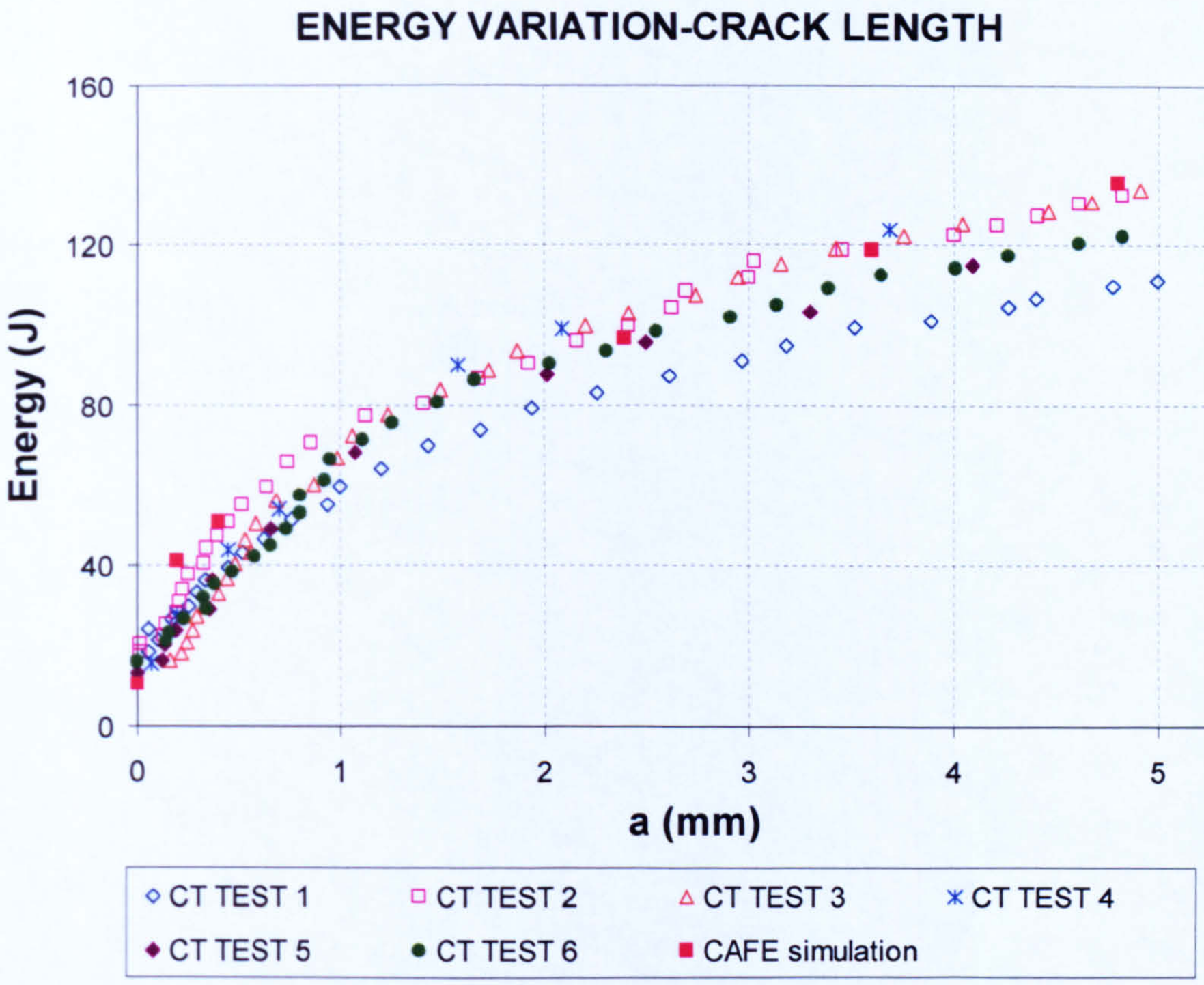

Fig. 5.18 *Energy* – Δa **curves**

5.2.3 Transferability of damage parameters in tear specimens

Plots of the test data and CAFE simulations (Fig. 5.19) have demonstrated that the same values of the tuned Rousselier micromechanical damage parameters were transferable for all the tear tests with different ligament thickness (8 to 12mm). Simulation analysis showed that the triaxiality was higher in the centre than on the surface throughout the crack growth; it also showed that the levels of triaxiality varied in the middle of the ligament test with different thickness, and similar levels of triaxiality were obtained on the surface (Fig.5.20). This difference was because the modelling cannot reproduce the slant fracture and the crack advance remains flat with tunnelling effects through the simulations as can be seen in Fig. 4.27. Even though the simulations of tear specimens were not able to represent the shear crack path, the simulated CTOA values on the surface of the gauge thickness specimens reproduced the experimental CTOA data with good accuracy as is shown in the following sections.

It should be outlined that, in the literature, the flat to slant crack path has not yet been satisfactory simulated. Even though a good representation of mean crack advance has been obtained in recent studies with continuum damage models (Bron et al., 2004) or a 3D cohesive model (Chabanet et al., 2003) the numerically predicted fracture path remained flat. In the research of Bron et al., 2004 has been stated that it is likely that a very fine mesh of about the inter-particle distance is required to perform the calculations of the flat to slant transition.

Validation of these fixed damage parameters was done using the experimental data from Hashemi (2006) for a slanted CT specimen (See section 4.4.1). The 3D computational models that have conditions of plane strain in the middle and plane stress near the surfaces were able to calculate with enough accuracy the relationships between loads and crack mouth opening displacements of the tear specimens with different ligament thicknesses. The simulated curves shows dispersed data at the peak load, but the simulation data after the peak load that represents shear crack propagation of the test has been shown to be very consistent with the experimental data. An interesting result from this transferability of damage parameters was to predict the Load – CMOD curve of a tear specimen with a gauge section of 19mm, which represents a plate of thickness equal to the full pipe wall thickness. It is not possible to test this geometry in practice without deforming the specimen to flatten it because of the curvature of the pipe. This last prediction has been used to assess the fracture resistance of the pipeline material.

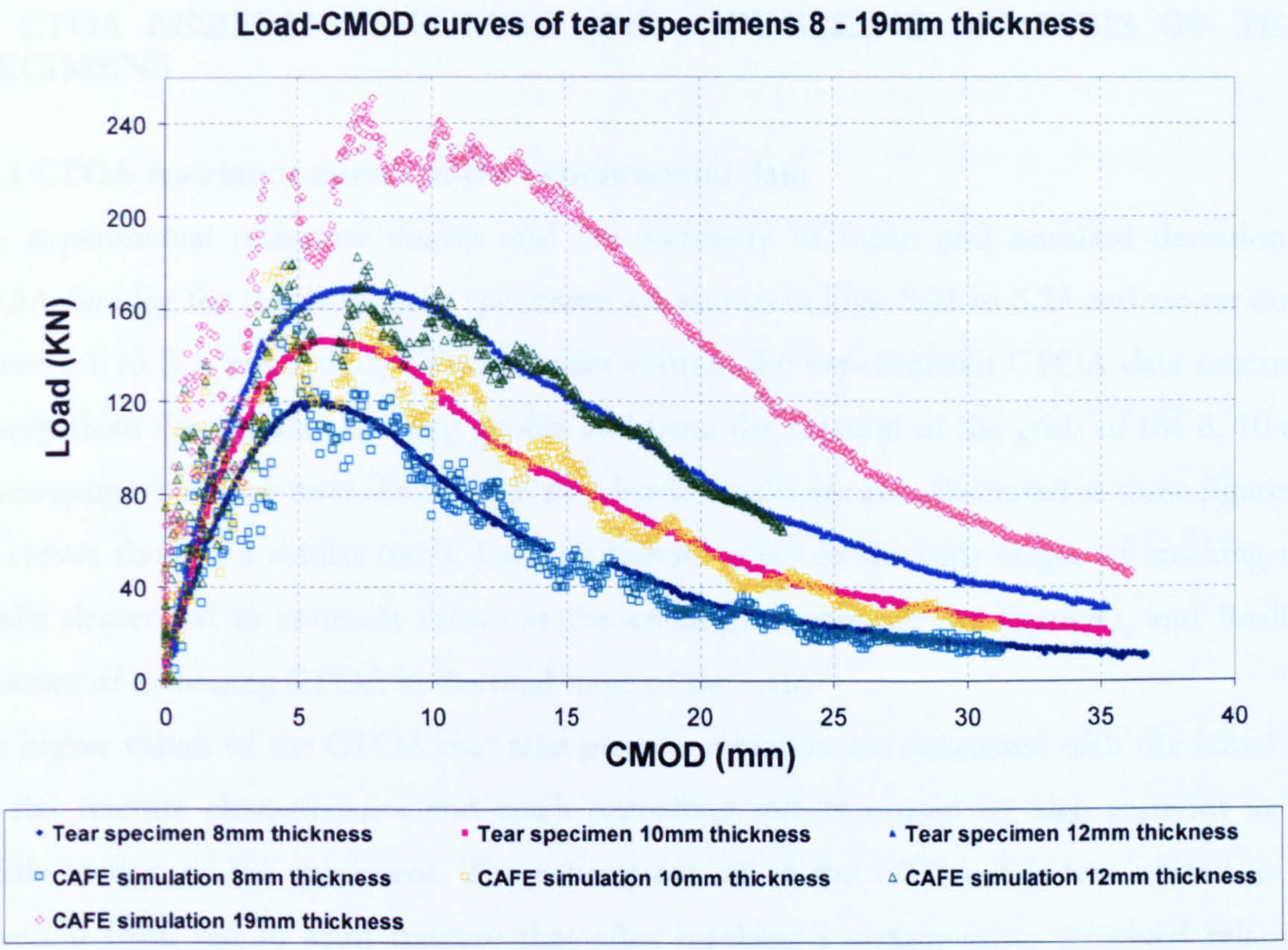

Fig. 5.19 Reaction force – CMOD curves of the experimental and simulation data of the tear tests with different ligament thickness.

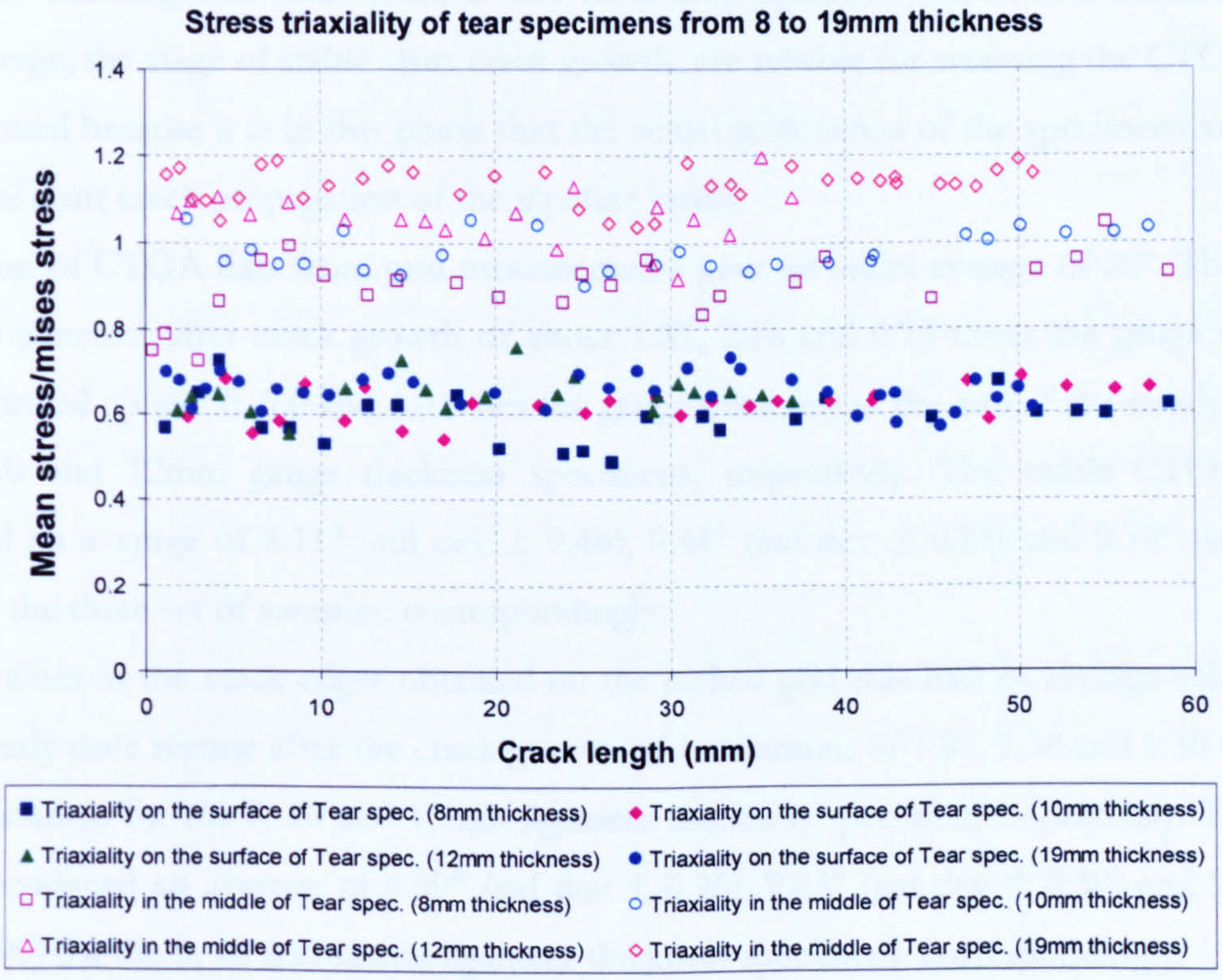

Fig. 5.20 Stress triaxiality – crack length curves on the surface and in the middle of tear tests.

5.3 CTOA RESISTANCE CURVES AND MODELLING ANALYSIS OF TEAR SPECIMENS

5.3.1 CTOA resistance curves of the experimental data

The experimental resistance curves and the summary of mean and standard deviation of CTOA data for the tear laboratory specimens are shown in Figs. 5.21 to 5.23 and are set out in Tables 5.1 to 5.3, respectively. These results contain the experimental CTOA data measured directly from the cracking opening profile and from the rotation of the grids of the 8, 10 and 12mm gauge thickness tests. The CAFE simulation results are also illustrated in these figures.

All curves showed a similar trend. Large initiation values in the early stages of cracking that rapidly descended to constant values as the crack grew through the ligament, and finally a tendency of increasing CTOA in the final stage of the tests.

The higher values of the CTOA that take place at initiation are associated with the initial slit, the flat fracture characteristics and crack tunnelling effects caused by high restraint in the middle section of the specimens. The subsequent fall in the CTOA data was related to the transition from flat to slant fracture that after reaching a certain value remained relatively constant. The rising CTOA data at the final stage of the fracture test was a consequence of the significant buckling that takes place in the remaining ligament. The results obtained in the second stage, the stage of stable slant crack growth, are reliable for assessing the CTOA of the pipe material because it is in this phase that the actual parameters of the specimens are related to the real slant crack propagation of the pipeline steels.

Evaluation of CTOA data from grid measurements gave an initial average of 20°. The CTOA data was constant after crack growth of about 1.87, 2.16 and 0.73 times the gauge thickness and continued up to 7.0, 5.0 and 4.0 times the gauge thickness at the end of the steady state for the 8, 10 and 12mm gauge thickness specimens, respectively. The stable CTOA values produced an average of 8.11° (std dev ± 0.48), 9.44° (std dev ± 0.24) and 9.74° (std dev ± 0.57) for the three set of samples, correspondingly.

CTOA values of the crack edges obtained on the etched grid side had an average value of 25° and a steady state regime after the crack growth of a minimum of 1.87, 1.38 and 1.39 times the gauge thickness for the 8, 10 and 12mm ligament thickness specimen, respectively. The stable CTOA produced an average of 8.59° (std dev ± 0.26), 9.83° (std dev ± 0.30) and 9.84° (std dev ± 0.90) for the 8, 10 and 12mm ligament thickness specimens, correspondingly.

The CTOA measurements of the crack edges from the processing of images by the DIC technique gave an initial average CTOA of 21°, and a steady data of 8.55° (std dev ± 0.16), 10.80° (std dev ± 0.60) and 11.48° (std dev ± 0.92) for the three gauge thickness samples. These values had stabilised after an average crack growth about 3.18, 1.76 and 1.39 times the gauge thickness.

Estimation of the CTOA data from the grid technique has shown that their values were the lowest of the three measurement procedures, and this is probably because the measurements of the grid rotation are taken remote from the crack tip which minimise the crack path and plasticity effects. The slight increase of scatter between different thickness specimens was associated on some occasions with the low quality of the images captured from the video recording and the uncertainty in positioning the measuring lines on the grid lines due to the thickness of the grid. The grid method has an important advantage compared with the direct method of obtaining CTOA values with less scatter particularly for thicker tear plates, where the crack course is not a straight line, as the gridlines reduce the influence of the deflection of the crack path.

Evaluation of the CTOA data from the crack edges, mainly of the thicker specimens, has shown that the scatter and CTOA values are higher than those from the grid lines. These high values are related to the effect of deflection of the fracture path and partly due to the difficulty in precisely locating the crack edges in the images. It should be pointed out that distances, x, below 1.5mm were unsuitable for tear tests due the jagged appearance of the crack flanks close to the crack tip.

It should be highlighted that, with the DIC technique, was intended to evaluate the CTOA values by measuring the relative displacement of two points above and below the crack path using the strain gauge function in the image correlation software DaVis7. But due to the high plastic deformation around the crack tip, the DCB specimens had large body motion during the tests. This meant that the DIC technique was not able to collect the displacement fields of the fracture gauge area effectively in order to measure the CTOA values. Further amendments are needed to capture the displacement data correctly and also to optimise the measurement of the CTOA. It also might help to validate the tuned damage parameters by comparing the full field deformations around the crack of the experimental and simulation data.

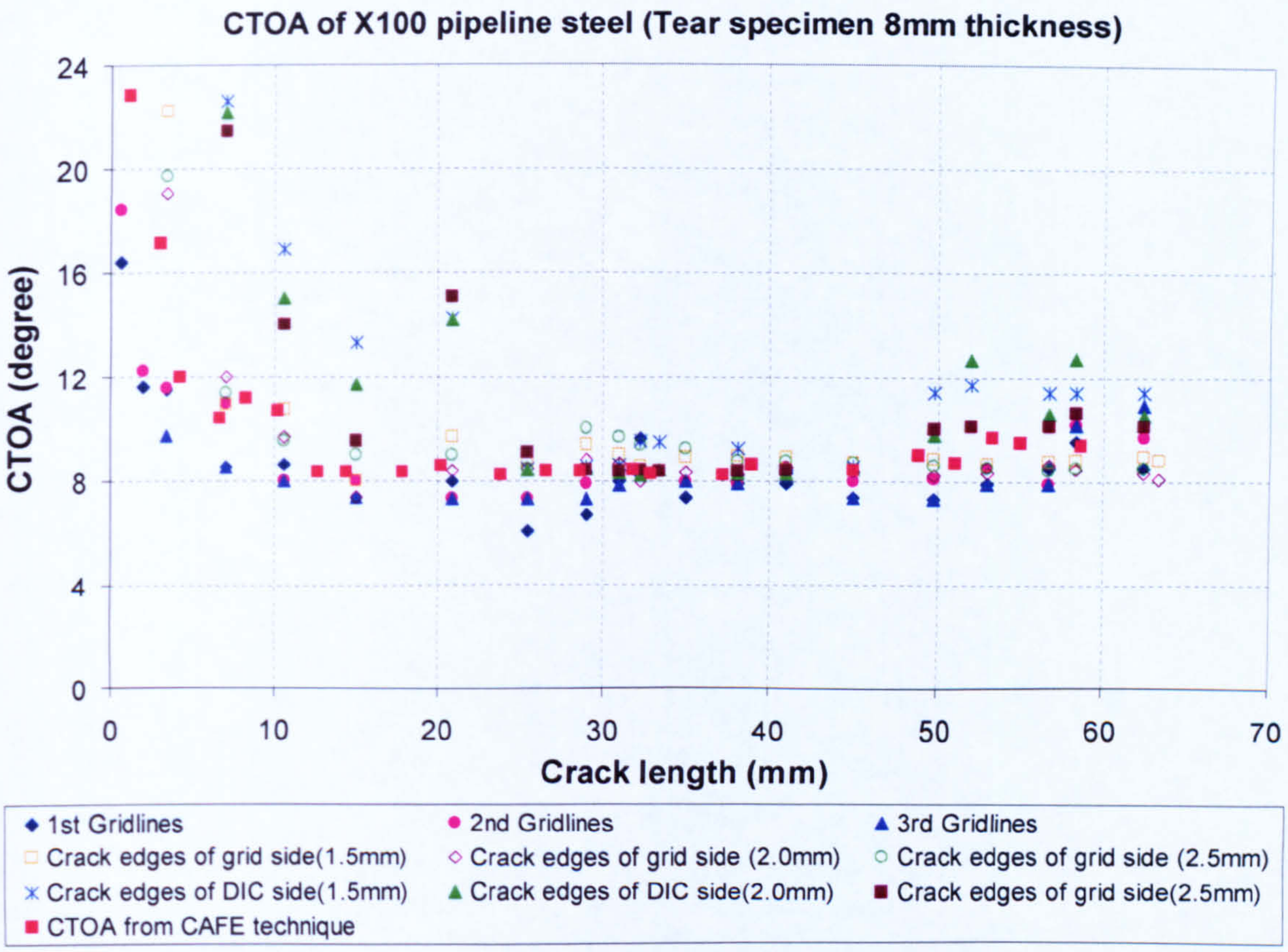

Fig. 5.21 CTOA resistance curves of X100 pipeline steel (8mm thickness of tear specimen) obtained from: a) Gridlines, b) Crack edges (from grid and DIC sides) and c) CAFE technique

Table 5.1 Summary of CTOA values from grid and DIC sides of Tear specimen (8mm thickness)

CTOA from Gridlines	Average of CTOA	SD	Crack length to thickness ratio at the beginning of steady state	Crack length to thickness ratio at the end of steady state
1st gridlines	8.15	0.821	1.875	7.091
2nd gridlines	8.0	0.396	1.875	7.091
3rd gridlines	8.18	0.433	1.875	7.091
AVERAGE	**8.113**	**0.479**	**1.875**	**7.091**
CTOA from Crack edges of grid side(Behind the crack tip)	Average of CTOA	SD	Crack length to thickness ratio at the beginning of steady state	Crack length to thickness ratio at the end of steady state
1.5mm	8.859	0.367	1.875	7.8
2.0mm	8.327	0.335	1.875	7.8
2.5mm	8.402	0.480	1.875	7.8
AVERAGE	**8.596**	**0.266**	**1.875**	**7.8**

CTOA from Crack edges of DIC side (Behind the crack tip)	Average of CTOA	SD	Crack length to thickness ratio at the beginning of steady state	Crack length to thickness ratio at the end of steady state
1.5mm	8.821	0.509	3.182	5.625
2.0mm	8.362	0.096	3.182	5.625
2.5mm	8.482	0.240	3.182	5.625
AVERAGE	**8.555**	**0.163**	**3.182**	**5.625**
CTOA from CAFE TECHNIQUE	Average of CTOA	SD	Crack length to thickness ratio at the beginning of steady state	Crack length to thickness ratio at the end of steady state
AVERAGE VALUES	**8.445**	**0.214**	**1.586**	**6.383**

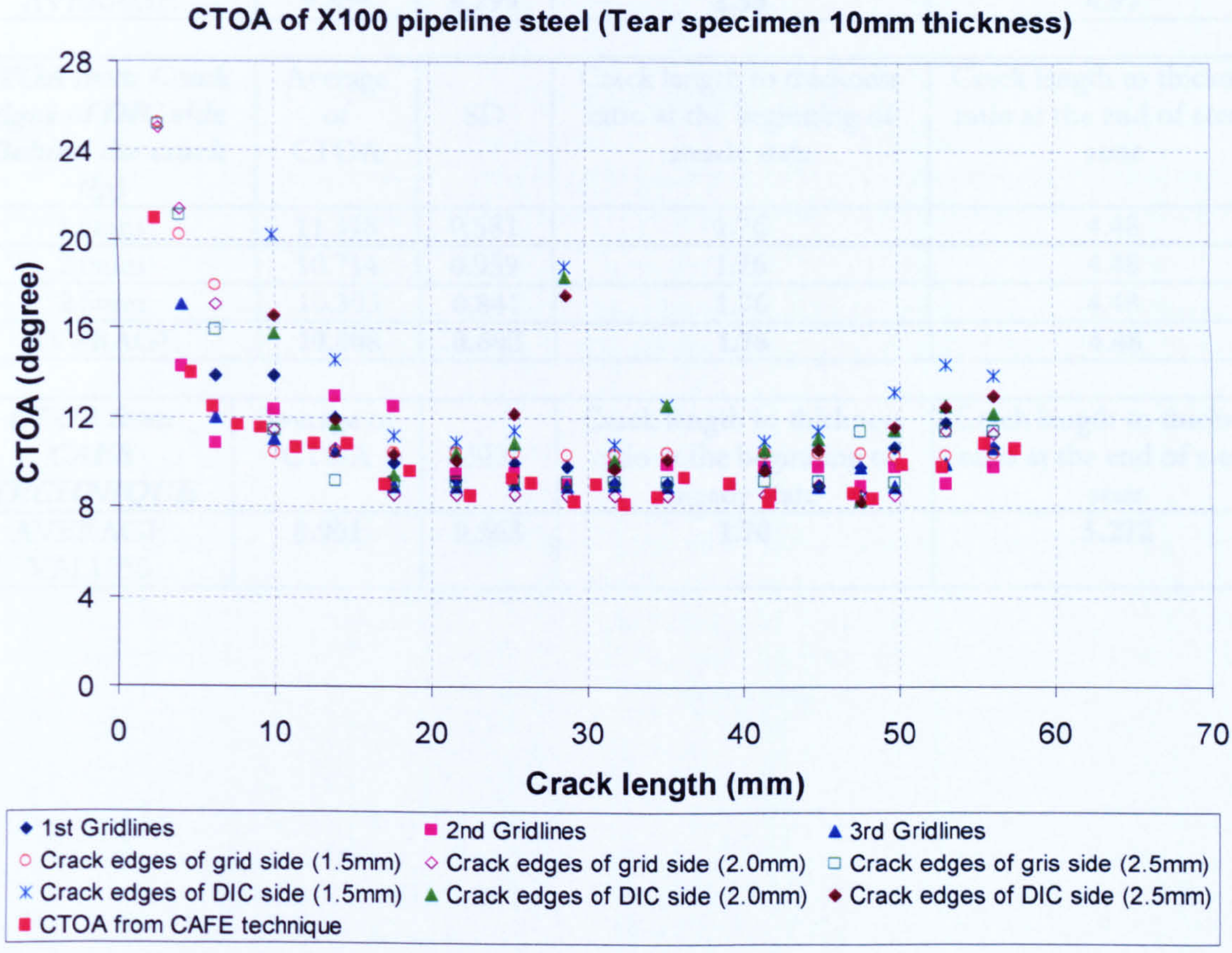

Fig. 5.22 CTOA resistance curves of X100 pipeline steel (10mm thickness of tear specimen) obtained from: a) Gridlines, b) Crack edges (from grid and DIC sides) and c) CAFE technique.

Table 5.2 Summary of CTOA values from grid and DIC sides of tear specimen (10mm thickness)

CTOA from Gridlines	Average of CTOA	SD	Crack length to thickness ratio at the beginning of steady state	Crack length to thickness ratio at the end of steady state
1st gridlines	9.063	0.577	2.16	4.97
2nd gridlines	9.576	0.368	2.16	4.97
3rd gridlines	9.129	0.368	1.76	4.97
AVERAGE	**9.444**	**0.243**	**2.160**	**4.97**
CTOA from Crack edges of grid side(Behind the crack tip)	Average of CTOA	SD	Crack length to thickness ratio at the beginning of steady state	Crack length to thickness ratio at the end of steady state
1.5mm	10.381	0.046	1.38	4.97
2.0mm	8.786	0.617	1.38	4.97
2.5mm	9.334	0.691	1.38	4.97
AVERAGE	**9.834**	**0.299**	**1.38**	**4.97**
CTOA from Crack edges of DIC side (Behind the crack tip)	Average of CTOA	SD	Crack length to thickness ratio at the beginning of steady state	Crack length to thickness ratio at the end of steady state
1.5mm	11.318	0.581	1.76	4.48
2.0mm	10.714	0.959	1.76	4.48
2.5mm	10.393	0.841	1.76	4.48
AVERAGE	**10.808**	**0.608**	**1.76**	**4.48**
CTOA from CAFE TECHNIQUE	Average of CTOA	SD	Crack length to thickness ratio at the beginning of steady state	Crack length to thickness ratio at the end of steady state
AVERAGE VALUES	**8.901**	**0.563**	**1.70**	**5.272**

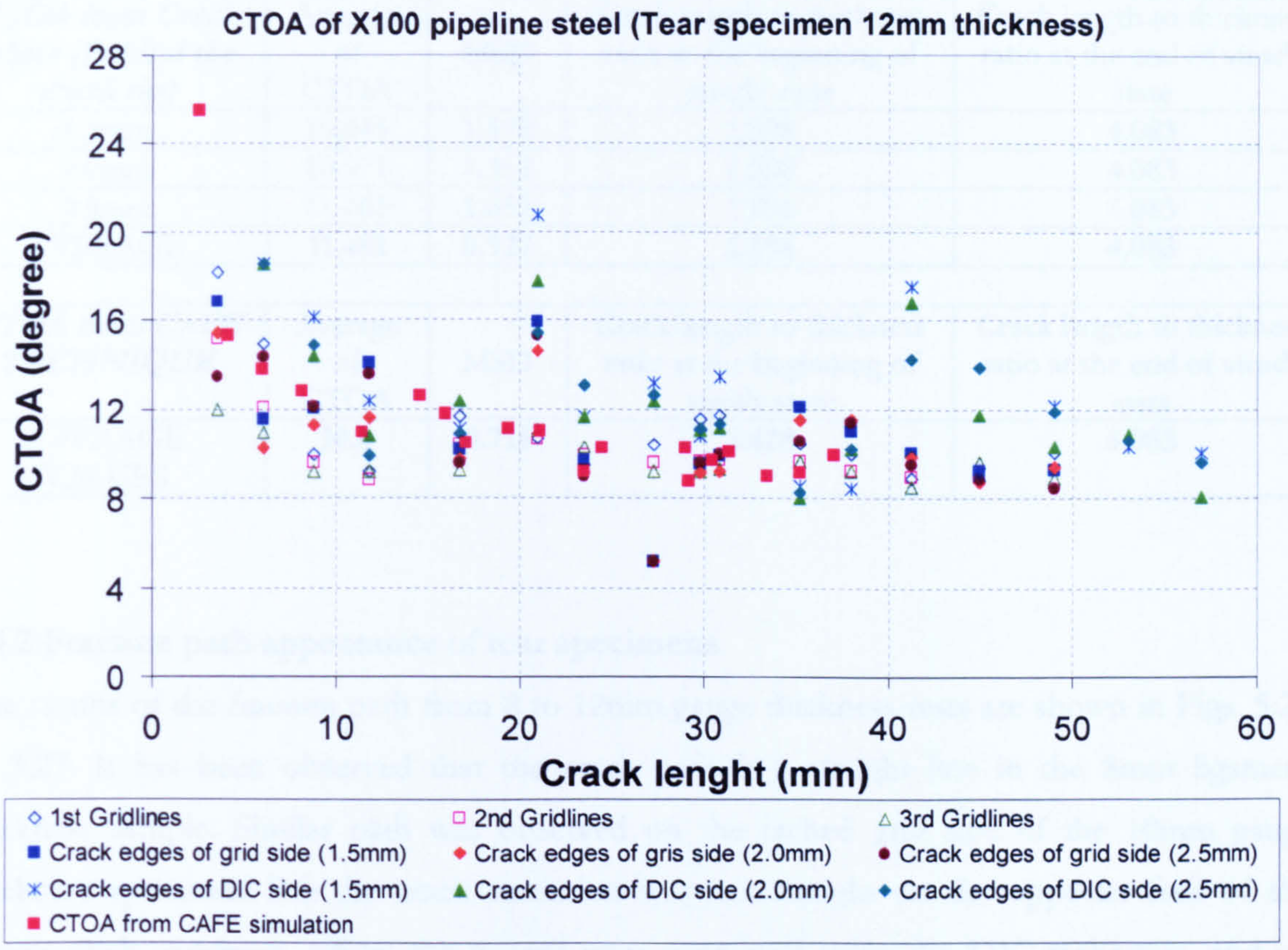

Fig. 5.23 CTOA resistance curves of X100 pipeline steel (12mm thickness of tear specimen) obtained from: a) Gridlines, b) Crack edges (from grid and DIC sides) and c) CAFE technique

Table 5.3 Summary of CTOA values from grid and DIC side of Tear specimen (12mm thickness)

CTOA from Gridlines	Average of CTOA	MSD	Crack length to thickness ratio at the beginning of steady state	Crack length to thickness ratio at the end of steady state
1st gridlines	10.219	0.998	0.735	4.083
2nd gridlines	9.578	0.530	0.735	4.083
3rd gridlines	9.423	0.642	0.735	4.083
AVERAGE	**9.74**	**0.576**	**0.735**	**4.083**
CTOA from Crack edges of grid side(Behind the crack tip)	Average of CTOA	MSD	Crack length to thickness ratio at the beginning of steady state	Crack length to thickness ratio at the end of steady state
1.5mm	10.094	0.919	1.398	4.083
2.0mm	9.788	1.018	1.398	4.083
2.5mm	9.649	0.913	1.398	4.083
AVERAGE	**9.844**	**0.905**	**1.398**	**4.083**

CTOA from Crack edges (Behind the crack tip)	Average of CTOA	MSD	Crack length to thickness ratio at the beginning of steady state	Crack length to thickness ratio at the end of steady state
1.5mm	10.945	1.895	1.398	4.083
2.0mm	10.971	1.358	1.398	4.083
2.5mm	11.461	1.662	1.398	4.083
AVERAGE	**11.481**	**0.927**	**1.398**	**4.083**
CTOA from CAFE TECHNIQUE	Average of CTOA	MSD	Crack length to thickness ratio at the beginning of steady state	Crack length to thickness ratio at the end of steady state
AVERAGE VALUES	**10.0**	**0.715**	**1.428**	**3.083**

5.3.2 Fracture path appearance of tear specimens

The results of the fracture path from 8 to 12mm gauge thickness tests are shown in Figs. 5.25 to 5.27. It has been observed that the crack path is a straight line in the 8mm ligament thickness sample. Similar path was observed on the etched grid side of the 10mm gauge thickness specimen. But the crack extension was not straight on the opposite face of the 10mm thick specimen, where the images were processed using the DIC technique, and on either gauge face of the 12mm specimen. In these specimens the crack path has a zigzag appearance.

The stability of the crack direction can be possibly explained in terms of T-stress, which is the constant stress acting parallel to the crack flank whose magnitude is proportional to the nominal stress in the vicinity of the crack. Cotterell and Rice (1980) showed how the sign of the T-stress determines the stability of straight-ahead mode I cracking; cracks with $T<0$ are stable in this mode while those having $T>0$ are unstable. Results from many experiments in Sherry et al., 1995 and Cotterel 1966 with different cracked specimens showed some analyses consistent with this criterion.

Analyses by Sherry et al., 1995 in double cantilever beams showed that the relative value of T-stress (T/σ) in these specimens is positive and high during the initial test, which decreases as the crack progress. These results also showed that the bigger the ratio of width to length of a DCB specimen, the lower the relative value of T-stress. Also the distribution of the T-stress is more constant as the crack advances. These studies demonstrated that the only way to decrease the level of T-stress of the specimens is to make it either shorter or wider. Work by Shterenlikht et al., 2004 for X80 pipeline steel using a similar DCB sample showed that this

geometry for a thick gauge specimen produced unstable crack growth. In the worst of the cases the crack deviated into the loading arm immediately after initiation (Fig. 5.24).

The geometry was modified to prevent the instability of the crack path and the fracture deviating towards the loading arms. The effective width of the specimen was increased by using loading plates bolted to the specimens. In this current research the specimen geometry following the amendments by Shterenlikht were used.

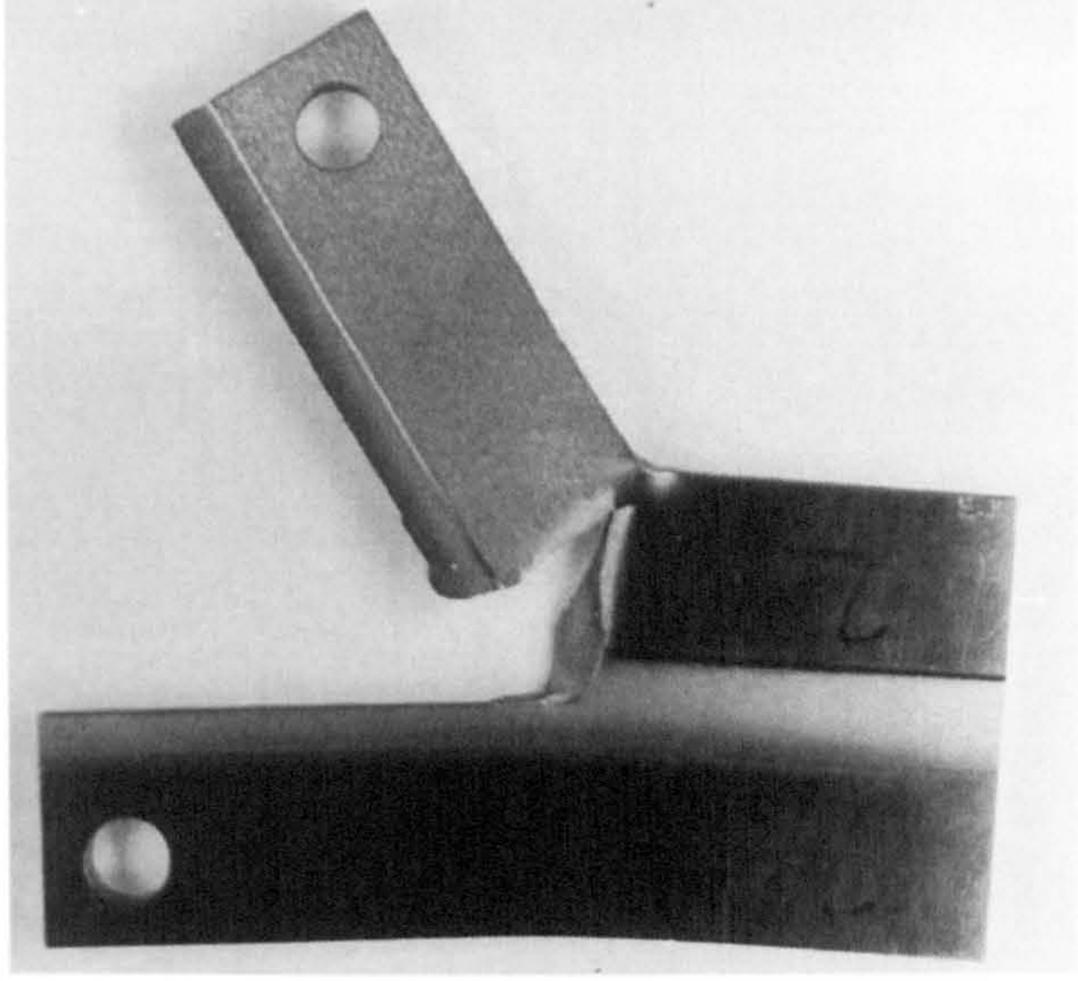

Fig. 5.24 Photograph of the 10mm thick specimen after the test (Shterenlikht et al., 2004)

Negative (compressive) or low values of T-stress cause a reduction in crack tip constraint. The crack tip constraint can be measured in terms of triaxiality factor. In this current investigation, the 8mm thickness specimen has a reduced crack tip constraint in the middle of the specimen (See Fig. 5.20) as a consequent of the difference in the thickness between the middle and the edge regions of the test. This was introduced by thinning of the gauge area and the use of thick loading arms in the tear experiment making the edge areas of the specimen much stiffer than the gauge section. So, the reduction of the test area and the increase of the width of the specimen produced a stable slant crack path. Fig. 5.4 shows the full stable surface fracture shearing developed in this test. The specimens of 10 and 12mm ligament thickness have a higher constraint level than the 8mm one, this in turn probably causes the fracture path changes of inclination angle. The cracking profile of the 10mm gauge thickness on the etched

grid side has a straight fracture path; this is probably showing that the design of the 10mm sample has an intermediate stability of the crack path.

The high scatter introduced in the CTOA measurements for the instability of the crack path in the thicker specimen and the inability to test a thick specimen equal to the full pipe wall thickness make the necessity to develop new specimen designs from the pipeline. One has to take into account the requirement to make the specimens with different gauge thicknesses closer to the pipe wall thickness and make them short enough to provide large amounts of highly consistent CTOA data, and finally to guarantee the stability of the crack advance.

It is worth mentioning that the fracture path in the modified DCB specimens, in Shterenlikht et al., 2004, showed a stair-like appearance in the crack flanks. In several instances a small crack could be seen ahead of the main crack tip that makes the principal fracture jump for several millimetres almost instantaneously and the cracks follow the scribed lines on the surface. This phenomenon was probably due to the scored grid used in those specimens. It should be pointed out that the cracks following the scribed lines have only a local surface effect, but can induce a CTOA measurement error. These events were not seen in this current investigation. The gauge areas to measure the CTOA values were prepared using photochemical etching and appropriate paint for the grid and DIC techniques, respectively.

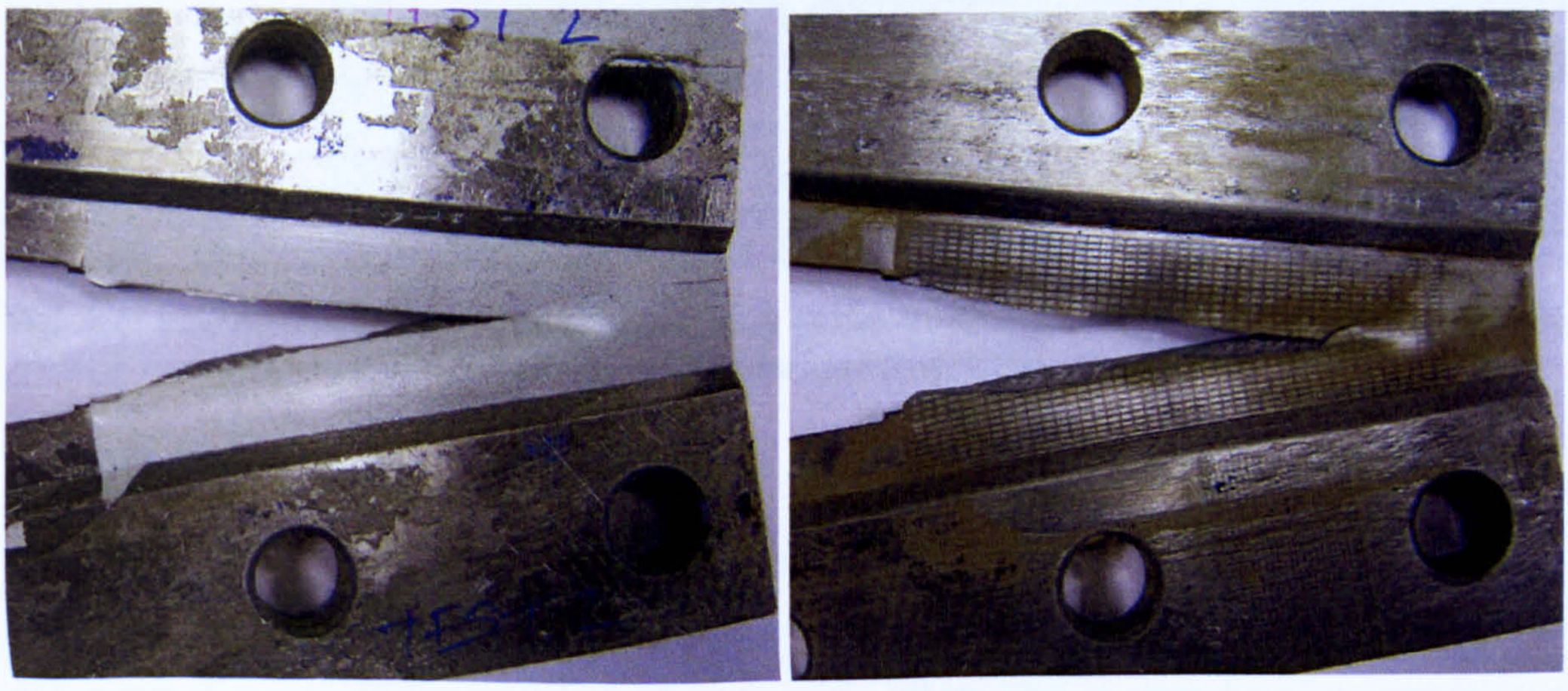

Fig. 5.25 Photographs of fracture of tear test of 8mm thickness. Left image: Image correlation technique, and right image: grid technique (mesh was etched onto the gauge area).

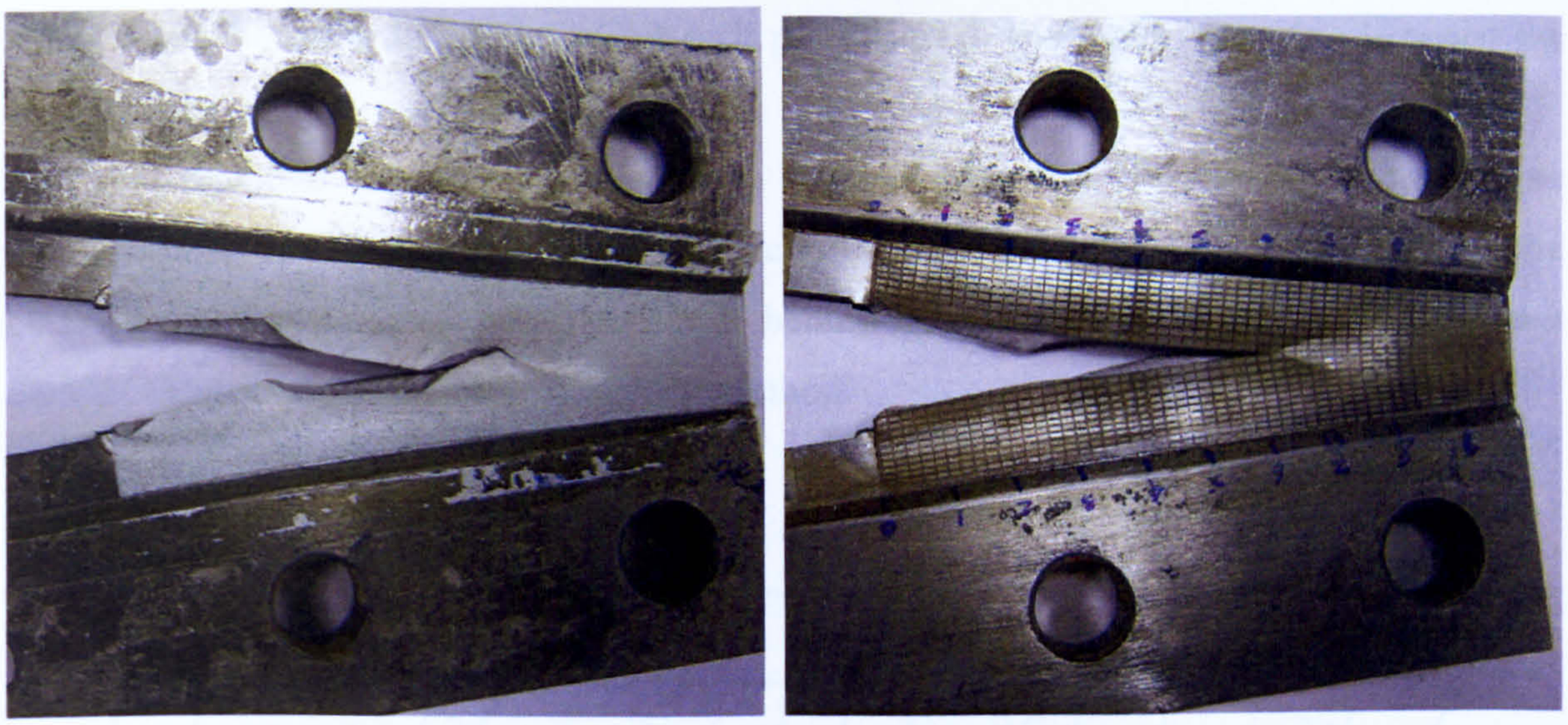

Fig. 5.26 Photographs of fracture of tear test of 10mm thickness. Left image: Image correlation technique, and right image: grid technique (mesh was etched onto the gauge area).

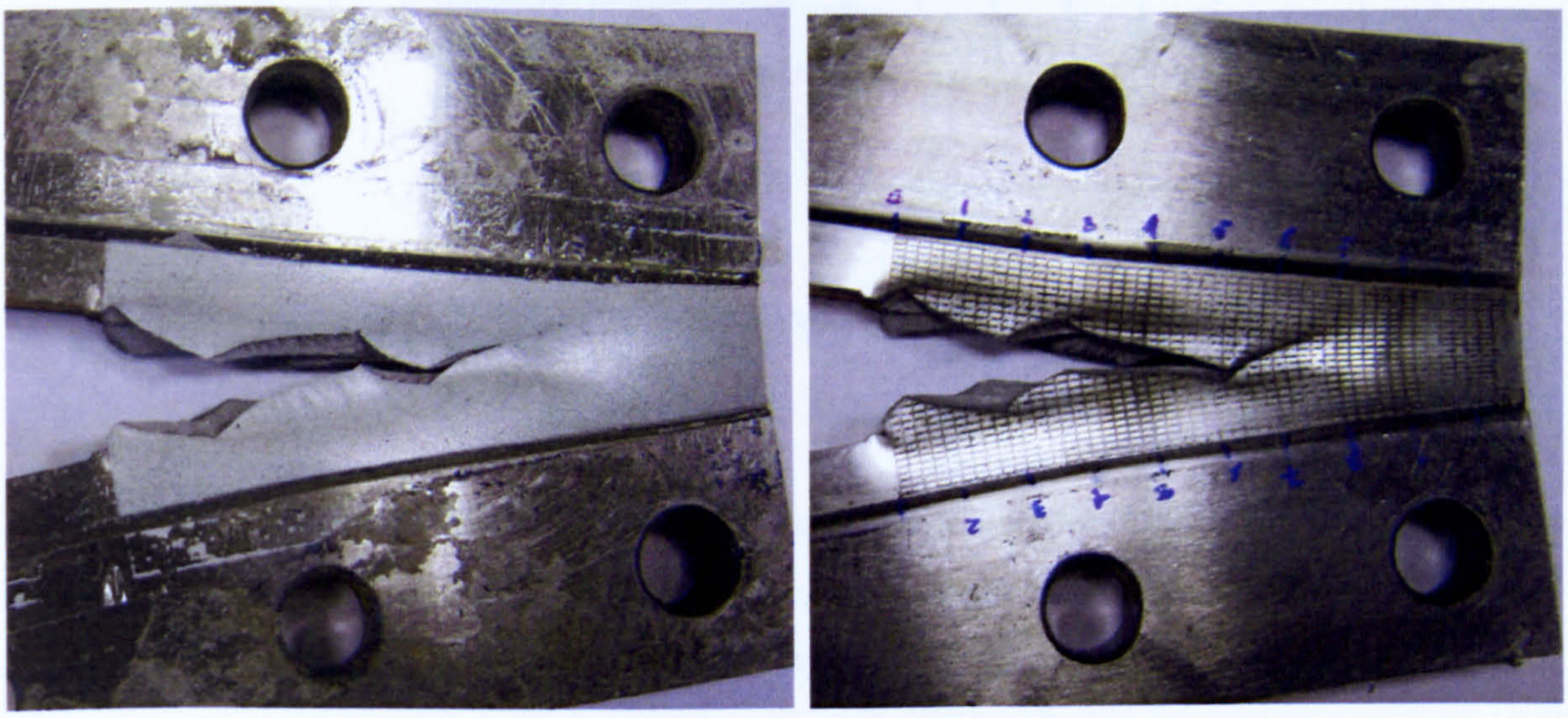

Fig. 5.27 Photographs of fracture of tear test of 12mm thickness. Left image: Image correlation technique, and right image: grid technique (mesh was etched onto the gauge area).

5.3.3 CTOA resistance curves of CAFE simulations

The CTOA data from the 3D CAFE simulation were obtained from successive images of the deformed elements of the model. Analogous to the direct CTOA measurement approach of the crack edges, it was done by a) locating the crack tip after the simulated fracture propagation formed by the removal of damaged elements, b) locating the points on one crack edge and the symmetrical line of the model at some distance, *x*, behind the crack tip, c) fitting

straight lines between the crack tip and each point, and d) computing the angle between the straight lines.

The representative CTOA resistance curve of the simulation was averaged from three measurements of CTOA of the three first inclined lines of the deformed mesh close to the crack edge within the range of 1.5 to 2.5mm behind the current crack tip. Fig. 5.28 illustrates the CTOA measurements using 3D CAFE method.

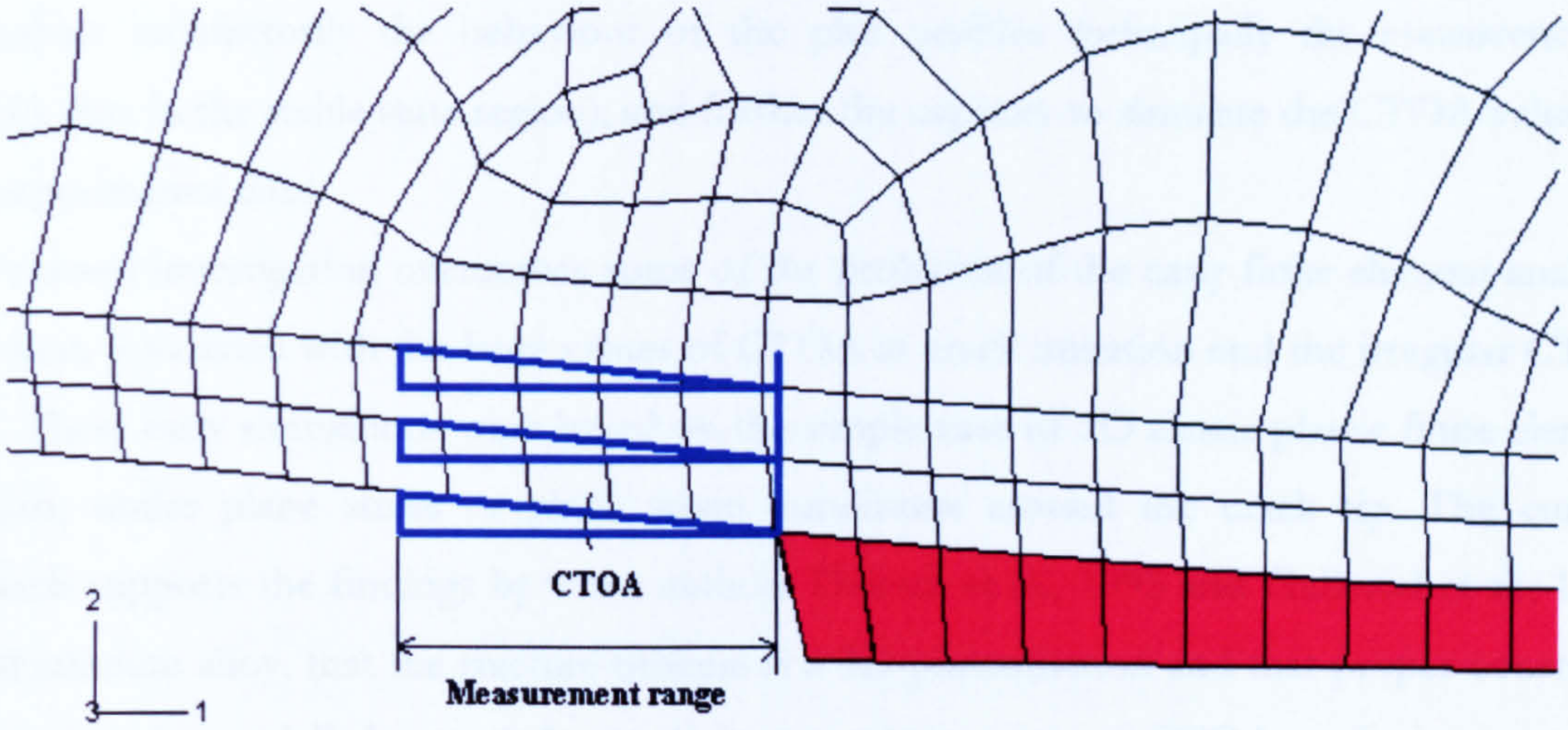

Fig. 5.28 Measurement of the CTOA values from CAFE method.

The CTOA resistance profiles of the CAFE modelling corresponding to the different gauge thickness specimens (8 to 19mm) have been plotted in Fig.5.29, and their resultant mean and standard CTOA values are set out in Table 5.4. One of the important results of this CAFE analysis has been to reproduce the condition of stable crack growth with the thickness equal to the pipe wall of the real structure. This result has an advance on the limiting aspect of the pipe curvature and load capacity of conventional test machines that do not allow tests of full thickness laboratory specimens to be carried out.

All plots have similar characteristics to the experimental data. Three stages were visible: a) high initiation CTOA values, b) followed by the drop to constant values and c) Increasing CTOA at the end of the simulation. The initial CTOA analysis results gave an average of 25° and they decreased to the steady state after crack growth of about 1.58, 1.70, 1.42 and 0.94 times the crack length to gauge thickness ratio and continued at a constant level up to 6.38, 5.27, 3.08

and 4.08 times the ratio for the 8 to 19mm gauge thickness specimens, respectively. The statistical results of the computer modelling showed that the main values and standard deviation data were of 8.44° (std dev ± 0.21), 8.90° (std dev ± 0.56), 10.0° (std dev ± 0.71) and 10.76° (std dev ± 0.53°) for the set of samples, correspondingly. CTOA results showed a trend of increasing in the CTOA values as thicker was the gauge ligament of the specimens, which agree with the experimental data.

The analyses demonstrated the power of 3D CAFE model and the ductile damage theory to reproduce satisfactorily the behaviour of the plot profiles (principally the consistency of CTOA data in the stable state region), and further the capacity to simulate the CTOA values of the experimental data.

The current investigation overcomes some of the problems of the early finite element analyses that were associated with the large values of CTOA at crack initiation and the irregular CTOA data. These early simulations were based on the simple case of 2D elastic plastic finite element analysis, under plane stress or plane strain conditions around the crack tip. The current research supports the findings by some authors Dawick et al., 1995 and Gullerud et al., 1999, for aluminium alloy, that the fracture process is a 3D phenomenon and that proper constraint effects must be modelled around the crack front to obtain accurate CTOA predictions.

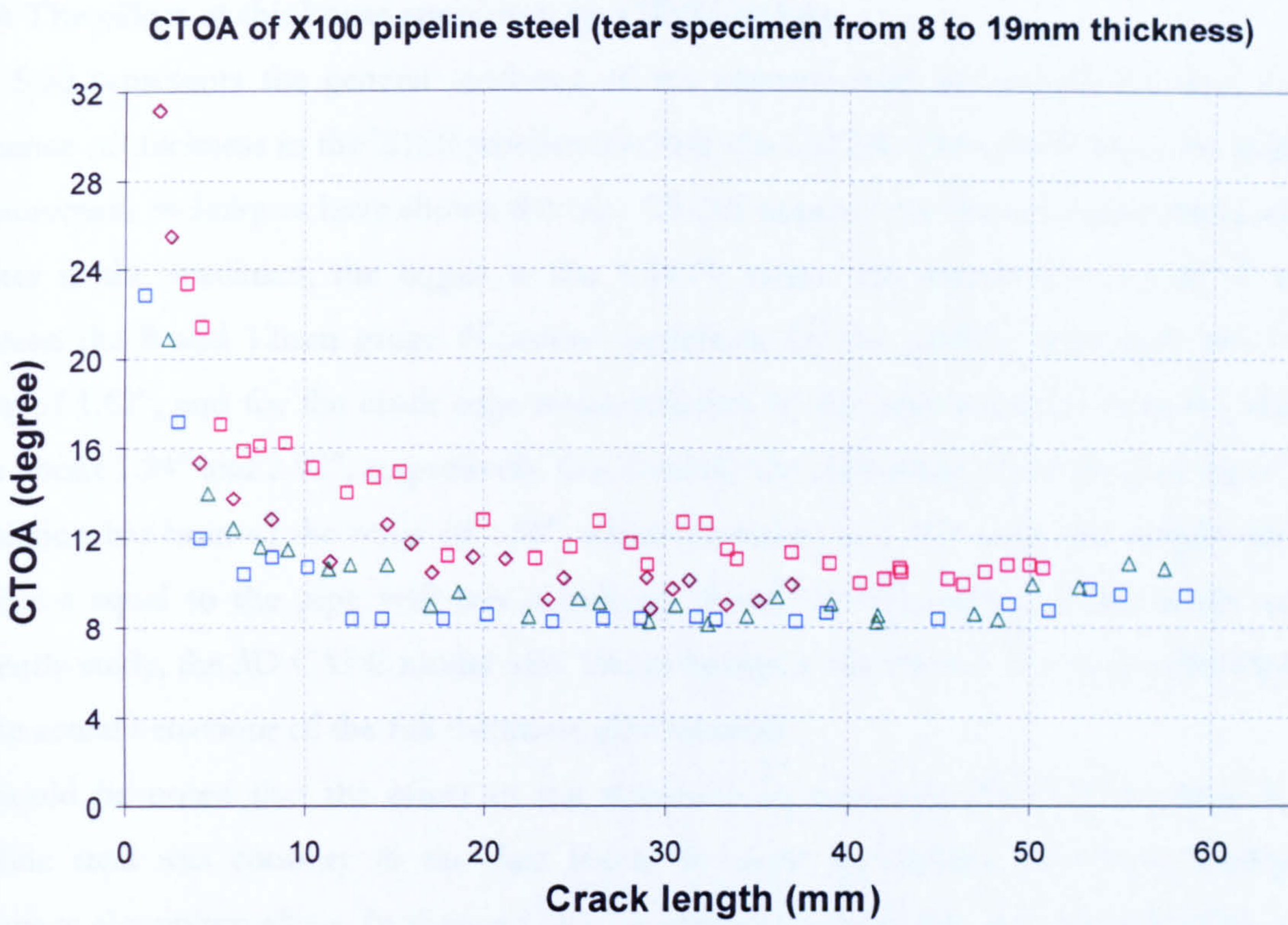

Fig. 5.29 CTOA resistance curves of CAFE simulations of the 8 to 19mm thickness gauge specimens.

Table 5.4 Summary of CTOA values of CAFE simulations of the 8 to 19mm thickness gauge specimens

CTOA from CAFE TECHNIQUE	Average of CTOA	SD	Crack length to thickness ratio at the beginning of steady state	Crack length to thickness ratio at the end of steady state
8mm thickness gauge	8.445	0.214	1.586	6.383
10mm thickness gauge	8.901	0.563	1.70	5.272
12mm thickness gauge	10.0	0.715	1.428	3.083
19mm thickness gauge	**10.762**	**0.532**	**0.947**	**2.673**

5.3.4 The effect of thickness specimen on CTOA values

Fig. 5.30 represents the general tendency of the experimental and simulation data for the influence of thickness in the X100 pipeline steel on the CTOA. The results from the different measurement techniques have shown that the CTOA depends on the specimen thickness; the thicker is the specimen, the bigger is the CTOA value. The difference of CTOA values between the 8 and 12mm gauge thickness specimens for the gridline technique was of the order of 1.62°, and for the crack edge measurements on the grid and DIC sides the changes were about 1.24° and 2.92°, respectively. Consistently the difference of values from the CAFE simulation has been of the order of 1.56°, which increased to 2.31° when the sample with the thickness equal to the pipe wall was simulated. Based on the stable CTOA results of the currently study, the 3D CAFE model with 19mm ligament thickness is the most representative of the actual behaviour of the full thickness pipe material.

It should be noted that the effect of the specimen thickness on the CTOA values in the pipeline steel was contrary to the data found by some researchers who have worked on aerospace aluminium alloys. In these studies on aluminium materials, the critical CTOA values were calculated for sheet and plate 2024 aluminium alloy and they were determined by matching the failure loads on C(T) specimens. The results of these analyses (Fig. 5.31) showed that the critical surface CTOA values continue to decrease for increasing thickness of tempered sheet 2024-T3 (Dawicke., et al., 1999) and for plate 2024-T351 (Mahmoud et al., 2003, and James and Newman., 2002), and may possibly approach a lower limiting value. The plate T351 tended to produce higher CTOA values than the sheet T3. But for a machined plate 2024-T351 (Mahmoud et al., 2003) the CTOA values tended to increase at thicker gauges thickness. It was suspected in this case that the machining operation was removing surface material from the rolled plate that was contributing to the fracture behaviour.

The specimen geometry for the pipeline steel in this current research did not represent the plate equal to the full pipe wall thickness; it was not possible test the full thickness with this geometry because of the curvature of the pipe. Therefore, it is possible that the thinning of the gauge area revealed the microstructure at the centre of the 8mm specimen changed from the microstructure of the full pipe wall. Increasing the gauge thickness meant that the test specimen became gradually more representative of the full pipe microstructure. It appears that in both rolled aluminium alloy and the heavily thermo-mechanically processed X100 steel that there are subtle changes in that damage behaviour at the surface compared with the core.

Further analyses are required to provide more information of this issue.

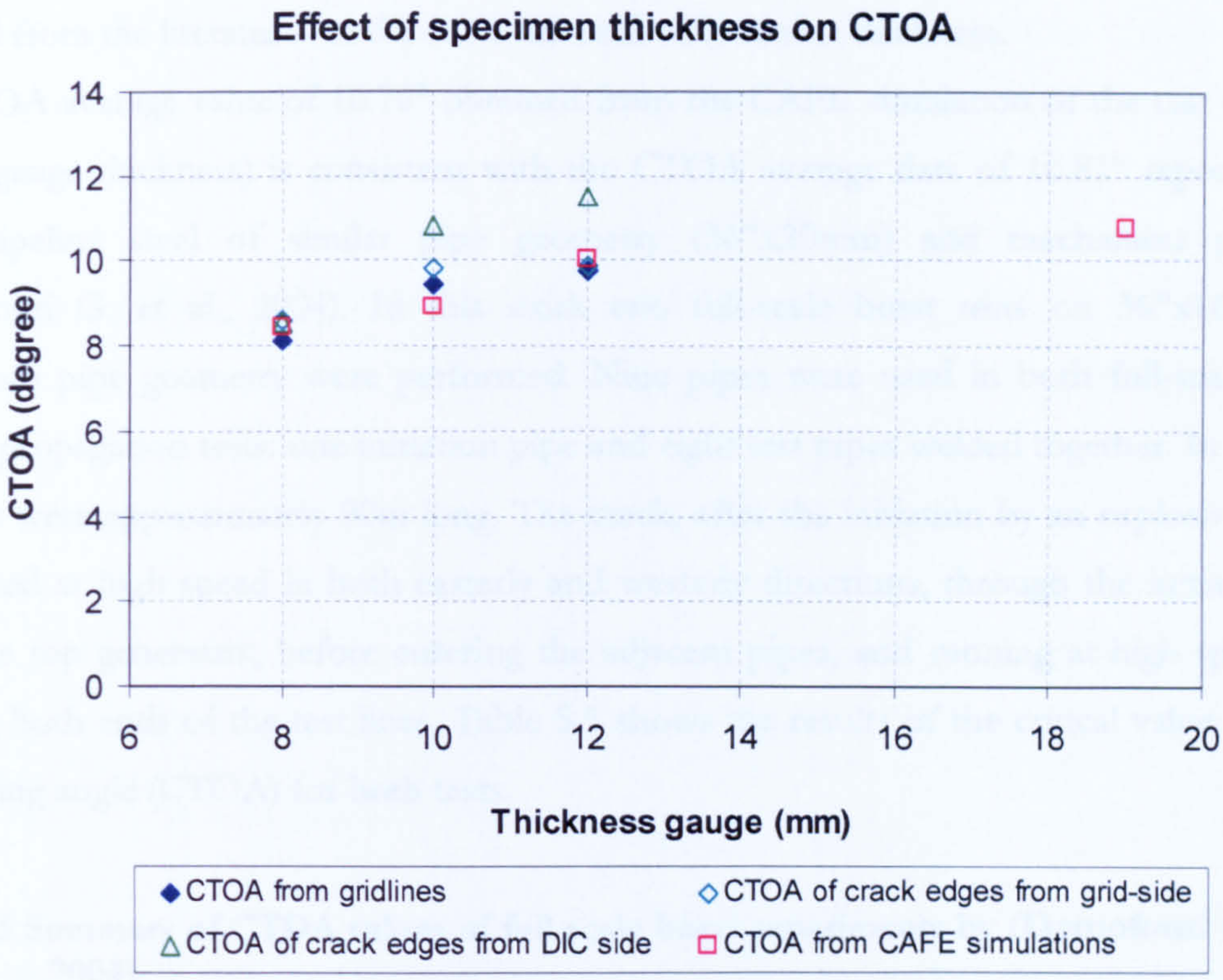

Fig. 5.30 Thickness effect on CTOA values.

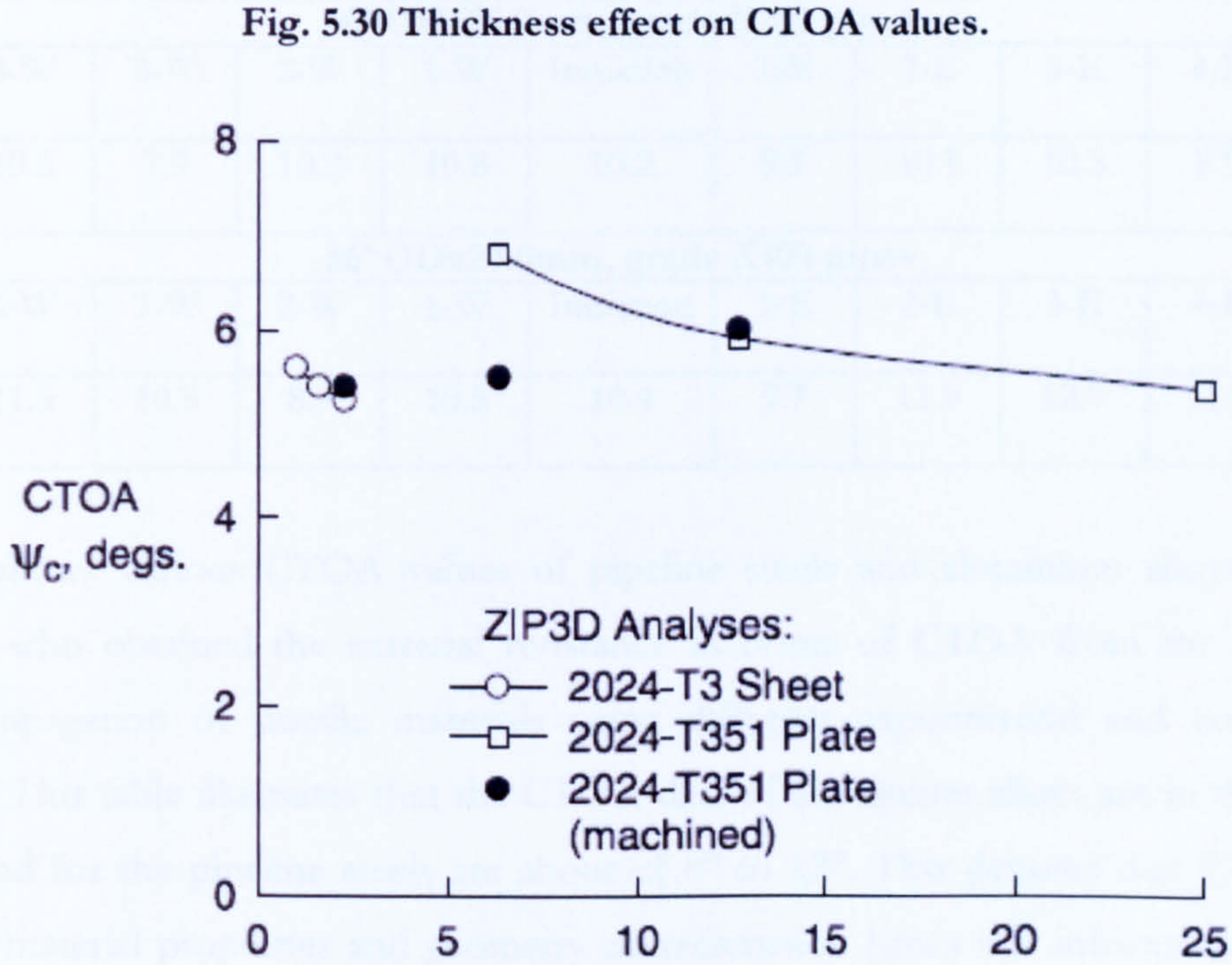

Fig. 5.31 Calculated critical CTOA values for various aluminium material thickness (Newman J.C. Jr et al., 2003)

5.3.5 Comparison of the CTOA data with the literature review

The comparison of the CTOA data from the current research was carried out with data obtained from the literature for the same material with similar thickness.

The CTOA average value of 10.76° obtained from the CAFE simulation of the tear specimen (19mm gauge thickness) is consistent with the CTOA average data of 10.81° reported for a X100 pipeline steel of similar pipe geometry (36"x20mm) and mechanical properties (Demofonti G. et al., 2004). In this work two full-scale burst tests on 36"x16mm and 36"x20mm pipe geometry were performed. Nine pipes were used in both full-scale ductile fracture propagation tests: one initiation pipe and eight test pipes welded together. In total, the test lines were approximately 90m long. The crack, after the initiation by an explosive charge, propagated at high speed in both easterly and westerly directions, through the initiation pipe along the top generatrix, before entering the adjacent pipes, and running at high speed until reaching both ends of the test lines. Table 5.5 shows the results of the critical values of crack tip opening angle (CTOA) for both tests.

Table 5.5 Summary of CTOA values of full scale burst experiments by (Demofonti G. et al., 2004)

36"ODx16.0mm, grade X100 pipes										
Pipe number	4-W	3-W	2-W	1-W	Initiation	1-E	2-E	3-E	4-E	Average
CTOA (degree)	10.6	7.9	10.2	10.8	10.2	9.1	10.1	10.3	8.9	9.78
36"ODx20.0mm, grade X100 pipes										
Pipe number	4-W	3-W	2-W	1-W	Initiation	1-E	2-E	3-E	4-E	Average
CTOA (degree)	11.5	10.5	8.7	10.5	10.4	9.7	11.9	12.9	11.2	**10.81**

Table 5.6 shows various CTOA values of pipeline steels and aluminium alloys by several researches, who obtained the material resistance in terms of CTOA from the steady state fracture propagation of ductile materials using different experimental and computational techniques. This table illustrates that the CTOA data of aluminium alloys are in the region of 4° to 6°, and for the pipeline steels are about of 8° to 12°. This denotes that CTOA values depend on material properties and geometry characteristics. From this information, it can be seen that the CTOA of the current experimental data for 8mm thickness with the etched grid technique (8.11°) and the crack flank measurements of the grid side (8.59°) on the modified

DCB specimen are similar to those obtained (8.39°) by Hashemi et. al., 2004c. Notice that the experimental data from the current research for the 12mm thickness with the etched grid technique (9.74°) and crack flank measurements of the grid side (9.84°) are comparable with the experimental data (9.78°), for similar X100 line pipe 36" X16mm, by Demofonti G. et al., 2004.

Table 5.6 CTOA of different pipeline steels and aluminium alloys

Grade of pipeline steel	Pipe diameter (m)	Wall thickness (mm)	CTOA (deg)	Analysis method	Reference
X65	1.4 (56")	18.7	8.1	Two specimen method	O'Donoghue P. et. al., 1997
			10.9	Analysis model (PFRAC)	
X70	0.91 (36")	14.2	11.8	Full scale burst test	Mannucci G. et. al., 2000
X70	1.06 (42")	12	6.3-10.1	3 point bend test	Pussegoda N. et. al., 2000
X70	1.4 (56")	18.7	10.4	Two specimen method	O'Donoghue P. et. al., 1997
			10.2	Analysis model (PFRAC)	
X80	1.4 (56")	18	11.9	Two specimen method	O'Donoghue P. et. al., 1997
			12.5	Analysis model (PFRAC)	
X80	1.4 (56")	26	8.5-10.5	Full scale burst test	Berardo G. et. al., 2000
			9.0	Analysis model (PICPRO)	
X80	1.2 (48")	13.8 (Machined to 8)	11.2±1.4	Modified DCB specimen	Shterenlikht A. et al. 2004
X80	1.2 (48")	15.3	11.4-14.5	3 point bend test	Pussegoda N. et. al., 2000
X100	1.4 (56")	19.1	8.6-9.6	Full scale burst test	Berardo G. et. al., 2000
			9.5	Analysis model (PICPRO)	
X100	0.91 (36")	16	9.78	Full scale burst test	Demofonti G. et. al., 2004
X100	0.91 (36")	20	10.81	Full scale burst test	Demofonti G. et. al., 2004
X100	0.91 (36")	19 (Machined to 8)	8.39±1.0	Modified DCB specimen (scored grid method)	Hashemi S.H. et. al., 2004c
		19 (Machined to 8)	8.11±0.47	Modified DCB specimen (etched grid method)	

X100	0.91 (36")		8.59±0.26	Modified DCB specimen (crack edges of grid side)	***Current research***
			8.44±0.21	Analysis model (CAFE)	
		19 (Machined to 10)	9.44±0.24	Modified DCB specimen (etched grid method)	
			9.83±0.29	Modified DCB specimen (crack edges of grid side)	
			8.9±0.56	Analysis model (CAFE)	
		19 (Machined to 12)	9.74±0.57	Modified DCB specimen (etched grid method)	
			9.84±0.90	Modified DCB specimen (crack edges of grid side)	
			10±0.71	Analysis model (CAFE)	
		19	10.76±0.5	Analysis model (CAFE)	

Aluminium alloy	**Wall thickness (mm)**	**CTOA (deg)**	**Analysis method**	**Reference**
2024-T3	2.3	4.7	M(T) specimens	Dawicke D.S et. al., 1995
		4-6	Analysis model (3D-FE)	
2024-T3	2.3	6	M(T) specimens	Dawicke D.S and Sutton 1994
2024-T3	5	5.6±0.6	C(T) specimens	Tai Y.H et. al. 2007
2024-T351	2.3	5.24	C(T) specimens	Mahmoud S. and Lease K. 2003
	6.35	5.17		
	12.7	4.92		
	25.4	4.48		
6005A T6	3 (Machined to 2)	4.1±0.4	Modified DCB specimen	Hashemi S.H. et. al., 2004d

5.3.6 Statistical study of CTOA data

A statistical analysis is presented in this section with the aim to examine and compare the results of the experimental and computational data.

The percentage cumulative probability distributions of the steady experimental and CAFE analysis CTOA data of 8 to 12mm gauge thickness samples are illustrated in Figs. 5.32 to 5.34. Similar distributions are shown for the CAFE analysis of 8 to 19mm gauge thickness in Fig. 5.35. These graphs are defined by the following normal probability density function:

$$f(x) = \frac{1}{\sigma\sqrt{2\pi}} e^{-(x-\mu)^2/2\sigma^2} \tag{5.1}$$

The results indicated that there was less than 3% probability of the CTOA being less than 8.0° for the experimental and simulation data of the 8mm thickness specimen, and 9.8° for the 19mm ligament thickness that represents the thickness equal to the pipe.

The statistical study of the CTOA data has showed that the highest variance of CTOA was from the crack edge measurement technique of the thicker specimen (average std dev ± 0.94). It was probably due to the effect of deflections of the fracture path.

The statistical study has also allowed the analysis the probability concerned with the differences between two mean values of the experimental and simulation data of similar thickness specimens. The real difference was evaluated with the null hypothesis (H_0) and alternative hypothesis (H_1) that were taken as following:

$H_0 : \mu_1 = \mu_2$ (There is no difference between the two means and any observed difference is due to a random chance)

$H_1 : \mu_1 \neq \mu_2$ (The means between the samples are different)

A hypothesis test concludes with the decision: H_0 is accepted or H_0 is rejected as shown in Table 5.7.

Since the number of measurements of the sample is $n < 30$, the t-distribution is used to determine the significance level of the tests. The t-distribution applies with:

$$t = \frac{\left|\bar{x}_1 - \bar{x}_2\right|}{\sigma_d \sqrt{\frac{1}{n_1} + \frac{1}{n_2}}} \tag{5.2}$$

where $\bar{x}_1$ and $\bar{x}_2$ are the mean of the first and second sample, respectively; n_1 and n_2 are the number in the first and second sample, correspondingly; and σ_d is the standard deviation for the difference between mean that is given as following:

$$\sigma_d = \sqrt{\frac{n_1 s_1^2 + n_2 s_2^2}{n_1 + n_2 - 2}} \tag{5.3}$$

where s_1 and s_2 are the standard deviation of the first and second sample, respectively.

The results of the tests for difference between two means are shown in Table 5.7. The acceptance of H_0 has been evaluated at the 5% and 1% level of significance for a two-tailed test according to the number of the degree of freedom $\upsilon = n_1 + n_2 - 2$ (See Table of the Appendix 3).

The analysis showed that, at the 5% of the significance level, there is no difference between the experimental mean value of the different measurement techniques and the simulation mean data of the 8mm thickness specimen, except for the test of CAFE-gridline mean data. However in this test, H_0 is accepted at 1% significance level. The analysis of difference between means in the 10mm thickness specimen indicated that H_0 is only accepted at 1% of the significance level for the test CAFE-gridline mean data. In these tests the acceptance of H_0 has been for the gridline measurement technique, which has not been affected by the zigzag of the crack path. The statistical test of difference between the means in the 12mm gauge thickness samples indicated that H_0 has been accepted at the 5% and 1% of significance level for the CAFE analysis - Experimental data of gridlines and CAFE – Experimental data of crack edges of grid side. But H_0 is rejected even at the 1% of significance level for the CAFE–Experimental data of crack edges of DIC side, this may probably be due to the major influence of the zigzag of the crack path in the CTOA measurements.

The statistical analysis has also to test the difference between the means of the CAFE analysis of the 19mm gauge thickness and experimental data of a full scale burst test of similar

mechanical properties and geometry characteristics (Demofonti G. et al., 2004). The results showed that H_0 is accepted at the 5% level of significance. It is 95% certain that there is no difference between the experimental and simulation data.

It is important to notice that the statistical analysis showed that the 3D CAFE modelling was able to simulate with accuracy the CTOA values of the modified DCB specimens and measurement techniques of the pipeline steel; any difference between the experimental and simulation data was due to the zigzag effect of the crack path in the thicker laboratory specimens. The statistics have also shown the capacity of the CAFE analysis to reproduce CTOA values in the same range of other experimental method as the full scale burst test of similar mechanical properties and wall thickness.

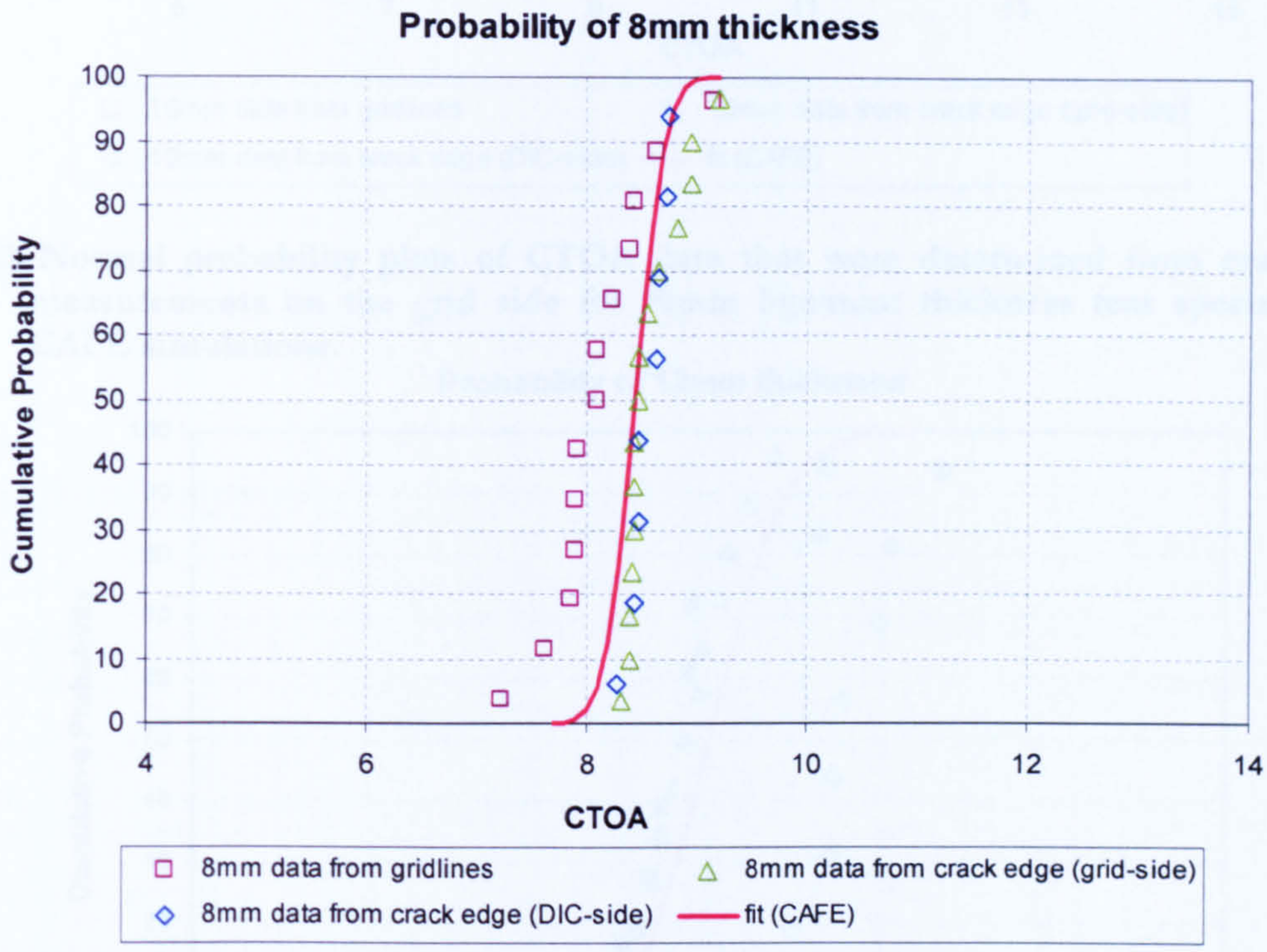

Fig. 5.32 Normal probability plots of CTOA data that were determined from gridlines measurements for 8mm ligament thickness tear specimens and CAFE simulation.

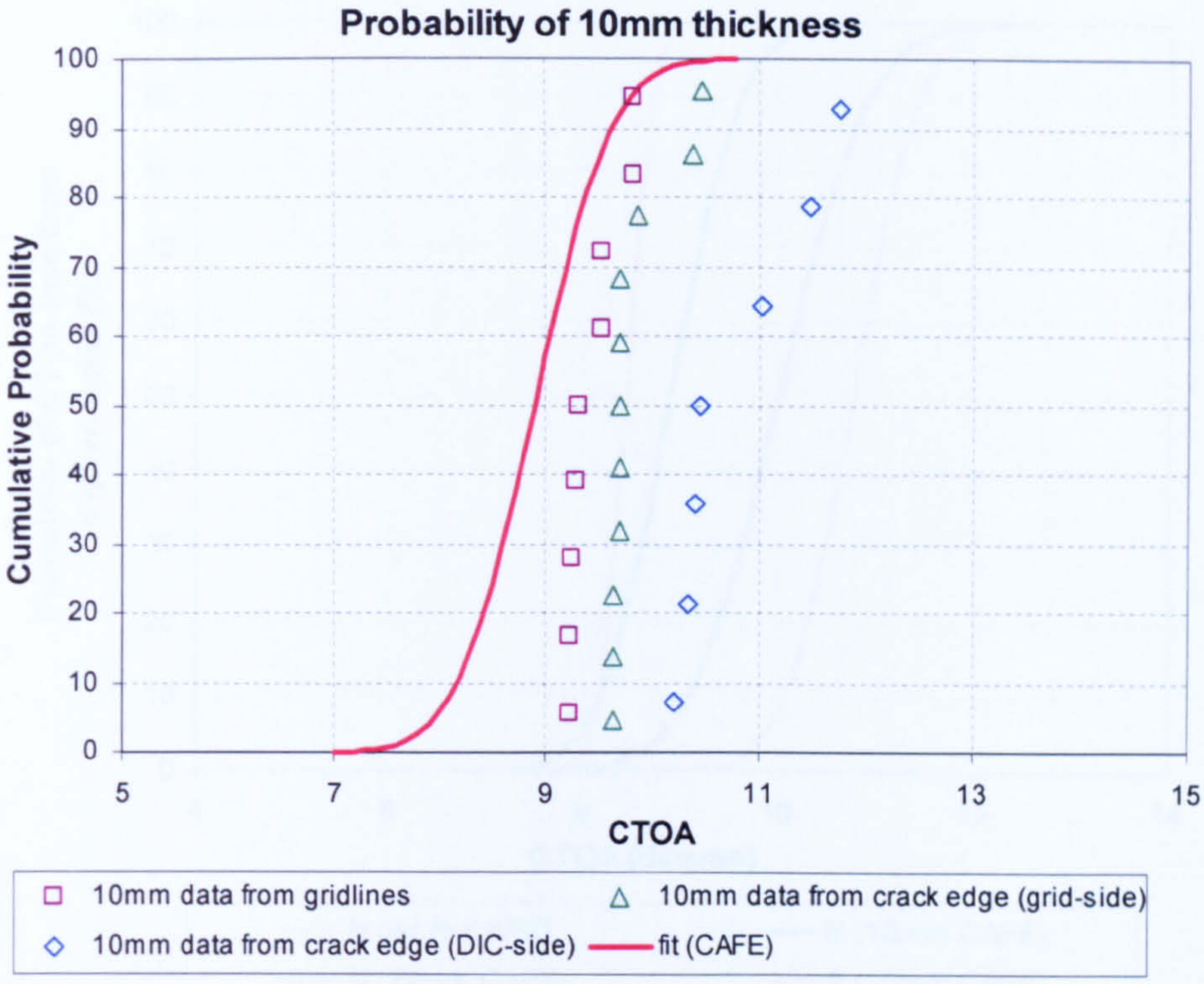

Fig. 5.33 Normal probability plots of CTOA data that were determined from crack edges measurements on the grid side for 10mm ligament thickness tear specimens and CAFE simulations.

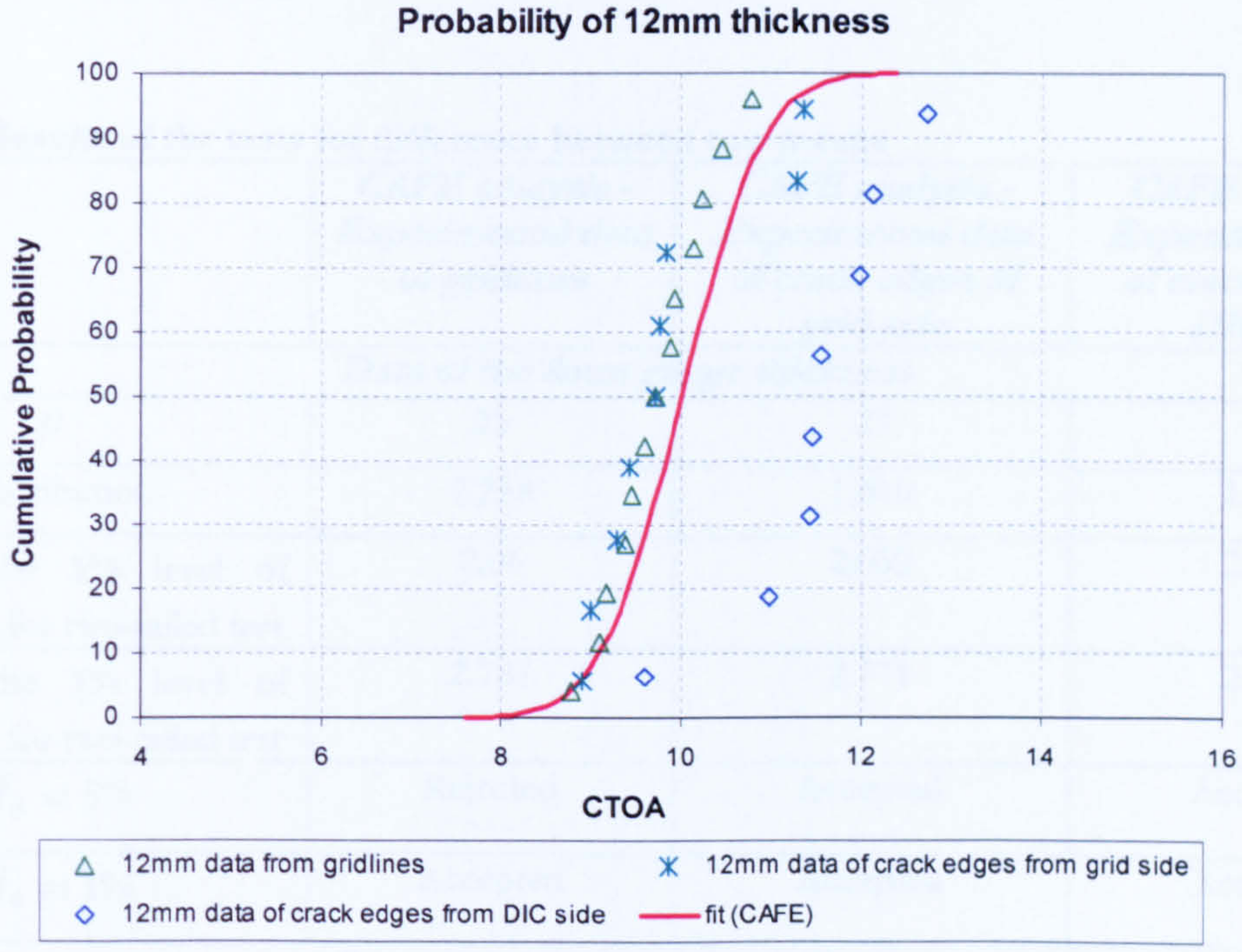

Fig. 5.34 Normal probability plots of CTOA data that were determined from crack edges measurements on the DIC side for 12mm ligament thickness tear specimens and CAFE simulation.

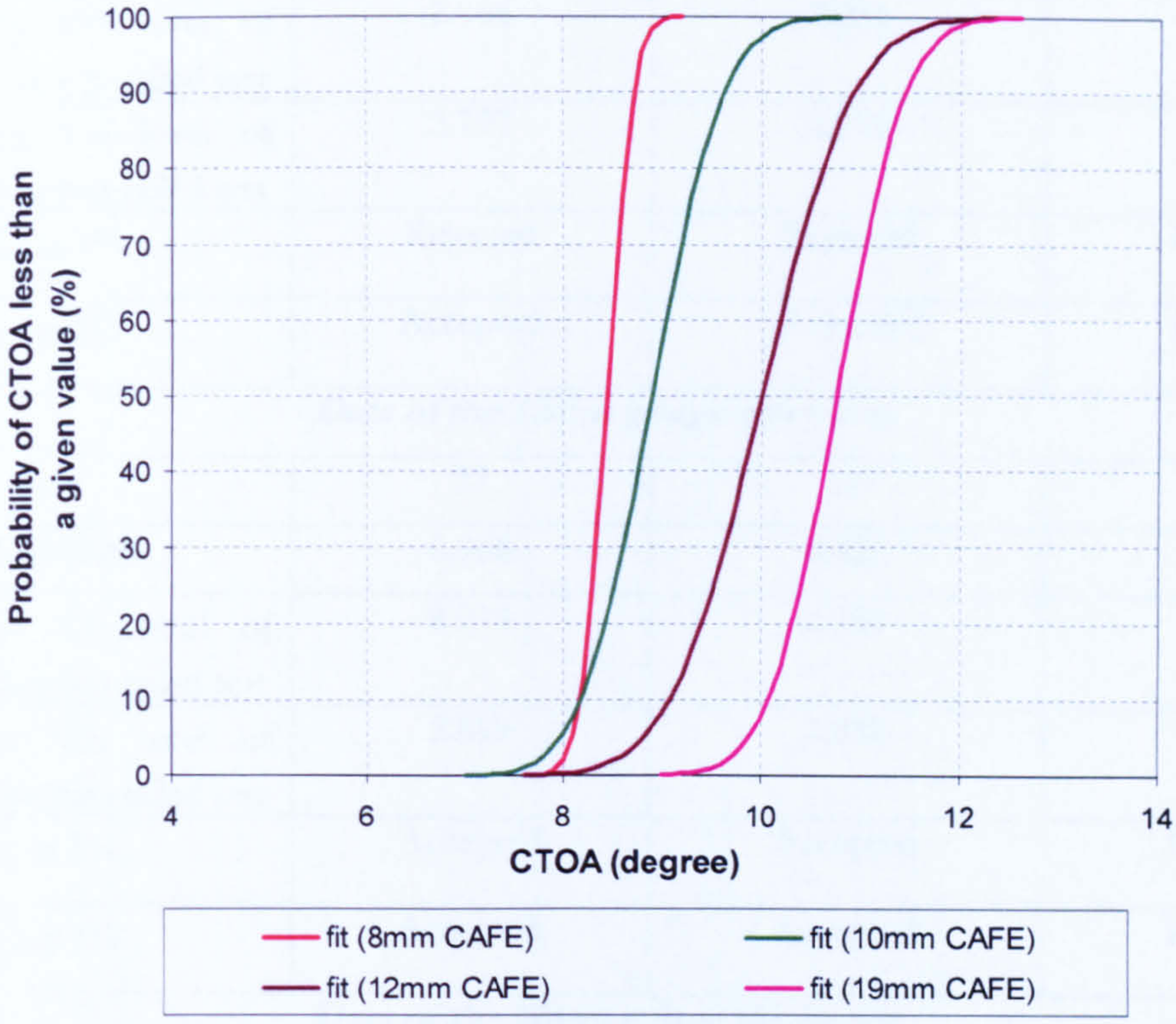

Fig. 5.35 Normal probability plots of CTOA values of CAFE simulations. CTOA data were determined from 8 to 19mm ligament thickness models.

Table 5.7 Results of the tests for difference between two means

	CAFE analysis - Experimental data of gridlines	***CAFE analysis - Experimental data of crack edges of grid side***	***CAFE analysis - Experimental data of crack edges of DIC side***
Data of the 8mm gauge thickness			
υ	25	27	20
t-distribution	2.258	1.610	1.194
$t_{0.025}$ at the 5% level of significance for two-tailed test	2.06	2.052	2.086
$t_{0.005}$ at the 1% level of significance for two-tailed test	2.787	2.771	2.845
H_0 at 5%	Rejected	Accepted	Accepted
H_0 at 1%	Accepted	Accepted	Accepted
Data of the 10mm gauge thickness			
υ	24	26	22
t-distribution	2.648	4.864	7.047

$t_{0.025}$ at the 5% level of significance for two-tailed test	2.064	2.056	2.074
$t_{0.005}$ at the 1% level of significance for two-tailed test	2.797	2.779	2.819
H_0 at 5%	Rejected	Rejected	Rejected
H_0 at 1%	Accepted	Rejected	Rejected
Data of the 12mm gauge thickness			
υ	22	18	17
t-distribution	0.968	0.426	3.698
$t_{0.025}$ at the 5% level of significance for two-tailed test	2.074	2.101	2.11
$t_{0.005}$ at the 1% level of significance for two-tailed test	2.819	2.878	2.898
H_0 at 5%	Accepted	Accepted	Rejected
H_0 at 1%	Accepted	Accepted	Rejected
Data of the 19mm gauge thickness			

	CAFE analysis - Experimental data of full scale burst (Demofonti G. et al., 2004)
υ	26
t-distribution	0.067
$t_{0.025}$ at the 5% level of significance for two-tailed test	2.056
$t_{0.005}$ at the 1% level of significance for two-tailed test	2.779
H_0 at 5%	Accepted
H_0 at 1%	Accepted

CHAPTER 6

CONCLUSIONS

1) In this research the tearing fracture properties of X100 pipeline steel were investigated. A series of experimental tests and computer simulation analysis were carried out to investigate the ductile damage behaviour of the material. The experimental programme consisted of various flat and slanted laboratory specimens having different geometries that were instrumented to obtain the ductile fracture characteristics of the pipeline steel. Tensile tests with different levels of constraint in four different directions provided the mechanical properties and the flat fracture features. The mechanical properties in the through pipe wall thickness direction were obtained by the use of two specially designed cylindrical and square tensile specimens that were friction welded to steel grip extensions. SEM images confirmed that the welding process used to make the specimens did not change the microstructure of the gauge area in the tests. The proposed specimen designs and the data collection technique, extensometry and optical techniques, demonstrated the efficacy of the whole process to get the required data of high strength gas line pipe steel. Standard C(T) and tear specimens (modified DCB samples) with the initial crack in the rolling direction were also tested providing the crack growth, and the flat and shear fracture data of the material, respectively.

2) Another experimental result was the determination of the CTOA resistance curves by the use of a photochemical etching method and an appropriated paint on tear specimens for the processing of images of the grid and DIC techniques respectively in order to obtain the CTOA values. CTOA measurements from the etched gridlines had an important advantage compared with the crack edge measurements in obtaining CTOA values with less scatter and consequently more reliable CTOA values particularly for thicker tear plates, where the crack course is not a straight line. The gridlines reduced the influence of the zigzag appearance of the crack path. The results from the different measurement techniques showed that the CTOA was a function of material thickness; the thicker the specimen, the bigger the CTOA value. This thickness dependence in the CTOA values was more noticeable between 8 and

10mm thickness than between 10 and 12mm one. The small difference of the CTOA values between 10 and 12mm thickness specimens may probably be due to the influence of the zigzag of the crack path in the CTOA measurements in the thicker specimen.

3) SEM observations revealed that all fracture surfaces of the flat and slanted specimens were of the ductile dimple type. The average size of spacing between large dimples of flat fracture was of the order of five times larger than the shear fracture (200 μm and 40 μm, respectively). These findings led to different length scales that were interpreted in the Cellular Automata - Finite Element (CAFE) simulations by modifying the mesh and cell sizes comparable to the distance between large dimples in the material.

4) Research results of the transferability of micromechanical damage parameter showed the following: a) The measured responses of plain and notched specimens of equal orientation could be represented well in 3D CAFE simulations, for the isotropy and anisotropic damage analysis, using a unique set of damage parameters. b) The calibrated micromechanical damage parameters for the tensile tests in isotropic and anisotropic analysis could not predict the data of the 3D C(T) model in the same transfer direction. The anisotropic simulations showed poor results even after a large number of attempts to adjust the values of the damage parameters for the CT specimens. In the case of the isotropic damage analysis the calibration of the simulated curves to the experimental data was possible, but quite different values were needed to give a reasonable simulation of the C(T) data. Transferability between flat specimens needs further investigation. c) The tuned damage parameters used in slant C(T) tests were able to reproduced the experimentally observed data of the tear specimens with different ligament of 8 to 12mm thickness in the assumption of effective material damage isotropy. d) The tuning processes in slanted specimens allowed assessing the CTOA resistance curves of a tear specimen with a gauge section of 19mm, which represents a plate of thickness equal to the full pipe wall thickness. It is not possible to test this geometry in practice without deforming the specimen to flatten it because of the curvature of the pipe.

5) The research results of the CTOA simulations showed the following: a) 3D CAFE tuned models reproduced satisfactorily the consistency of CTOA data in the stable state region. b) Capacity of the numerical model to simulate the CTOA values of the experimental data. The

CTOA average value of 10.76° obtained from the CAFE simulation of the 19mm gauge thickness was in agreement with the available data reported for a X100 pipeline steel of similar pipe geometry (36"x20mm) and mechanical properties. c) 3D CAFE models could represent the dependence of the CTOA values as a function of the material thickness. d) The CAFE technique was shown to be a powerful tool in reducing simulation time whilst maintaining good predictions of damage. This avoided the lengthy calibration time and also prevented the models becoming so large that they could not be run in the computer. This is due to that a very fine mesh is required to represent the micro-structural characteristic which is of the order of 40 μm . In these cases the classic FE models were not appropriated.

CHAPTER 7

FUTURE WORK

1) Key findings from the CTOA techniques indicated that the critical surface CTOA values continue to reduce for decreasing thickness material. This behaviour was contrary to the investigations normally found in the literature for sheets and plates of aluminium materials. The actual specimen geometry did not represent the plate equal to the full pipe wall thickness; it was not possible test the full thickness with this geometry because of the curvature of the pipe. It is suggested to create new specimen designs to support that the CTOA values were not introduced for the excessive thinning of the gauge area. Further solutions might probably be to make the gauge area: a) with the thickness close to the pipe wall, b) short enough to provide highly consistent CTOA data and c) finally weld it to steel arm extensions to give stability in the crack path in the specimens. Measurements of the CTOA values with different ligament specimens might possibly be introduced from different pipe wall thicknesses or by machining one of the sides of a thicker pipe wall and weld them to the steel arm extensions.

2) Due to the high plastic deformation around the crack tip, the DCB specimens had high body motion during the tests. This meant that the DIC technique was not able to collect the displacement fields of the fracture gauge area effectively in order to measure the CTOA values. The use of an instrument of motion that allows the CCD camera to follow the crack tip to capture the displacement data correctly is recommended. This might make the DIC technique well suited to obtain the CTOA values by measuring the relative displacement of two points above and below the crack path using the strain gauge function in image correlation software. It also might help to validate the tuned damage parameter by comparing the full field deformations around the crack of the experimental and simulation data.

3) Experimental investigation of CTOA measurements in high strain rates of laboratory specimens are recommended, the insight of this tests might give information about of any dependence of the CTOA data on the dynamic fracture propagation.

4) Difficulties in transferring the tuned damage parameters between the corresponding flat and slanted specimens in anisotropic behaviour were found in the computer simulation. Work in this direction is recommended for the future. Further suitable anisotropic damage models into the present CAFE structure is needed for the accurate representation of the performance of steels like the X100 tested

5) Even though it has been obtained a good representation of mean crack advance and CTOA measurements in recent studies with isotropic continuum damage models, it should be outlined that the ductile shear fracture has not yet been simulated. The Rousselier continuous damage model in the CAFE structure can only account for volumetric void growth. It is suggested to introduce an additional criterion to estimate the onset of shear instability in the ductile damage model.

6) The findings of the micro-structure fracture observations led to the use of two sets of damage mechanics parameters values, one set for the flat-type fracture and another for the slant-type. A theory for each ductile fracture type could be developed in the CAFE method, with each FE being associated with both arrays of flat and slant cells. The one type of cell would dominate the damage according to whether hydrostatic or shear macroscopic conditions evolved in the overlying FE.

REFERENCES

Anderson H. (1973). Finite Element Representation of Stable Crack Growth. Journal of Mechanics and Physics of Solids. Vol. 21, pp. 337-356.

Andrews, R.M., Howard, I.C., Shterenlikht, A. and Yates, J. R. (2002). In the Proceedings of the 14th Biennial Conference on fracture, ECF14, Edited by Neimitz, A. et al. EMAS Publication, Sheffield, 65-72.

Argon A.S. and Im J. (1975), Separation of second phase particles in spheroidized 1045 steel, Cu-0.6% Cr Alloy, and Maraging Steel in Plastic Straining. Metallurgical Transactions. A 6, pp. 839-851.

Argon A.S., Im J. and Safoglu R. (1975). Cavity Formation from Inclusions in Ductile Fracture. Metallurgical Transactions. A6, 825-837.

ASTM: Standard Test Method for Measurement of Fracture Toughness (2001), E1820-01, American Society for Testing and Materials, West Consohocken, Pennsylvania.

Benzerga, A. A. (2000). Rupture Ductile des Toles Anisotropies. PhD Thesis, Ecole des Mines de Paris, France,

Benzerga A. and Besson J. (2001). Plastic Potentials for Anisotropic Porous Solids. Eur. J. Mech. A/Solids, 20, 397-434.

Benzerga A.A., Besson J. and Pineau A. (2004). Anisotropic Ductile Fracture Part II: Theory. Acta Materialia, 52, 4639-4650.

Beynon J.H., Das S., Howard I.C. and Shterenlikht, A. (2002). Extending the Local Approach to Fracture: Methods for Direct Incorporation of Microstructural Effects into Finite Element Models of Fracture. New and Emerging Computational Methods: Applications to Fracture, Damage and Reliability ASME2002. Vol. 438, pp. 229-237.

Berardo G., Salvini P., Mannucci G. and Demofonti G. (2000). On Longitudinal Propagation of a Ductile Fracture in a Gas Line Pipe: Numerical and Experimental Analysis. In Proceeding of the 2000 International Pipeline Conference, Calgary, Canada.

Berg, C.A. (1970). Plastic Dilation and Void Interaction. Inelastic Behaviour of Solids, McGraw-Hill, New York,171-210.

Bilby B.A., Howard and Li Z.H. (1994). Mesh Independent Cell Models for Continuum Damage Theory. Fat. Fract. Engng. Mat. Struct. 17, 1221-1233.

Broberg, K. B. (1975). On Stable Crack Growth. Journal of Mechanics and Physics of Solids. Vol. 23, pp. 215-237.

Brocks W. Sun D.Z., Honing A. (1995). Verification of the Transferability of Micromechanical Parameters by Cell Model Calculation with Visco-plastic Materials. International Journal of Plasticity 11(8), 971-989.

Bron F. and Besson J. (2004). A Yield Function for Anisotropic Materials Application to Aluminum Alloys. International Journal of Plasticity 20, 937-963.

Bron F., Besson J. and Pineau A. (2004). Ductile Rupture in Thin sheets of Two Grades of 2024 Aluminum Alloy. Material Science and Engineering A 380, pp. 356-364.

Bron F. and Besson J. (2006). Simulation of the Ductile Tearing for Two Grades of 2024 Aluminum Alloy thin Sheets. Engineering Fracture Mechanics 73, 1531-1552.

Burstow M.C. and Howard I.C. (1996). Predicting the Effects of Crack Tip Constraint on the Material Resistance Curves Using Ductile Damage Theory. Fat. Fract. Engng. Mat. Struct. 19, 461-474.

Cabral, M.A and Kimber M. J. (1997). Pipeline fracture experiences in Australia and North America, Proceedings of the International Seminar on Fracture control in Gas Pipelines, 1.1-1.22, Sydney, Australia.

Chabanet, O., Steglich D., Besson J., Heitmann V., Hellmann D., Brocks W. (2003). Comput. Mater. Sci. Vol. 26, pp. 1-12.

Clocksin W F, Quinta da Fonseca J, Withers P J, and T. P. H. S (2002) Image processing issues in digital strain mapping. In Proceedings of SPIE 4790, 384 – 395.

Cotterell B. (1966). Notes on the Paths and Stability of Cracks. International Journal of Fracture. Vol. 2, pp. 526-533.

Cotterell B. and Rice J.R. (1980). Slightly Curved or Kinked Cracks. International Journal of Fracture, Vol. 16, No. 2, pp. 155-169.

Da Fonseca J.Q., Mummery P.M. and Withers P.J. (2005). Full-field strain mapping by optical correlation of micrographs acquired during deformation. Journal of Microscopy. Vol. 218 (1), pp. 9-21.

Das S. (2002). The effect of Boundary Conditions and Material Data Representation on the Simulation of Deformation During Hot Rolling, PhD Thesis, Department of Engineering Materials, the University of Sheffield, UK.

Das S., Palmiere E.J. and Howard (2001). CAFE: A New Approach to the Modelling of Multipass Hot Rolling, in Proceedings of Modelling of Metal Rolling Processes Symposium 11- Through Process Modelling, The Institute of Materials, London, pp. 33-40.

Das S., Palmiere E.J. and Howard (2003). CAFE: a tool for Modelling Thermomechanical Processes, in E. J. Palmire, M. Mahfouf and Pinna, Eds, Thermomechanical Processing: Mechanics, Microstructure and Control, Proceeding of the International Conference, Sheffield, 23-26 June, 2002, IMMPETUS, BBR Solutions, Chesterfield, UK, pp. 296-301.

Dawicke D.S., Newman Jr J.C. Starnes Jr. J.H., Rose C.A, Young R.D., Seshadri B.R., 1999, Residual Strength Analysis Methodology: Laboratory Coupons to Structural Components, Third Jint FAA/DoD/NASA Aging Aircraft Conference, Albuquerque, N.M., September 20-23.

Dawicke D.S. and Newman Jr. J.C. (1998). Residual Strength Predictions for Multiple Site Damage Cracking Using a Three Dimensional Finite Element Analysis and CTOA Criterion. Fatigue and Fracture Mechanics: 29th Volume, ASTM STP 1332.

Dawicke D.S., Newman Jr. J.C. and Bigelow C.A. (1995). Three Dimensional CTOA and Constrain Effects During Stable Tearing in a Thin-sheet Material. Fracture Mechanics: 26th Volume, ASTM STP 1256, pp. 223-242.

Dawicke D.S., Piascik R.S and Newman Jr. J.C. (1997). Analysis of Stable Tearing in Thick Aluminium Plate Alloy. Fatigue and Fracture Mechanics: 28th Volume, ASTM STP 1321, pp. 309-324.

Dawicke D.S. and Sutton M.A. (1994), CTOA and Crack-Tunneling Measurements in Thin Sheet 2024-T3 Aluminum Alloy. Experimental Mechanics. Vol. 34, pp. 357-368.

Demofonti G., Mannucci G., Hillenbrand H.G. and Harris D. (2004) Evaluation of the Suitability of X100 Steel Pipes for High Pressure Gas Transportation Pipelines by full Scale Tests. International Pipeline Conference, October 4-8, Calgary, Alberta Canada.

Demofonti G., Buzzichelli G., Venzi S. Kanninen M. (1995). Step by Step Procedure for the Two Specimen CTOA Test. Pro. 2nd International Pipeline Technology Conference. R. Denys Ed., Ostend, Belgium. Vol. 2, pp. 503-512.

Doege E., El-Dsoki T. and Seibert D. (1995). Prediction of Necking and Wrinkling in Sheet-Metal Forming. Journal of Materials Processing Technology. Vol. 50, pp. 197-206.

Faleskog J., Gao X., Shih C.F. (1998). Cell Model for Nonlinear Fracture Analisys-I. Micromechanics Calibration. International Journal of Fracture. Vol. 89(4), pp. 355-373.

Faleskog, J., Shih, C. F., (1997). Micromechanics of coalescence—i. synergistic effects of elasticity, plastic yielding and multi-size-scale voids. Journal of Mechanics and Physics of Solids. Vol. 45, pp. 21–50.

Franklin A.C. (1969). Comparison Between a Quantitative Microscopic and Chemical Methods for Assessment of Non-metallic Inclusions. Journal of the Iron and Steel Institute. Vol. 207, pp. 181-186.

Gandin, C. A., Desbiolles J. L., Rappaz M. and Thevoz P. (1999). A Three dimensional Cellular Automaton – Finite Element Model for the Prediction of Solidification grain Structures, Metallurgical and Materials Transactions A, Vol. 30, pp. 3153-3165.

Gao X., Faleskog J., Shih C.F. (1998). Cell Model for Nonlinear Fracture Analysis-II. Fracture Process Calibration and Verification. International Journal of Fracture. Vol. 89, pp. 375-398.

Garrison W.M, Jr. and Moody, N.R. (1987). Ductile Fracture. Journal of the Physics and Chemistry of solids Vol. 48(11), pp. 1035-1074.

Gollerud A.S., Dodds Jr RH, Hampton R.W., Dawicke D.S. (1999). Three-Dimensional Modeling of Ductile Crack Growth in thin Sheet Metals: Computational Aspects and Validation. Engineering Fracture Mechanics.Vol. 63, pp.347-74.

Grange M., Besson J., Andrieu E. (2000). An Anisotropic Gurson Type Model to Represent the Ductile Rupture of Hydrided Zircaloy-4 Sheets. Vol. 105, pp. 273-293.

Gurson, A.L. (1977a). Continuum Theory of Ductile Rupture by Void Nucleation and Growth: Part I Yield Criteria and Flow Rules for Porous Ductile Media. Journal of Engineering Materials and Technology. Vol. 99, pp. 2-15.

Gurson, A.L (1977b). Porous Rigid-Plastic Materials Containing Rigid Inclusions – Yield Function, Plastic Potential, and Void Nucleation, in D.M.R, ed., Proceedings of the International Conference on Fracture, Vol. 2A, Pergamon Press, pp. 357-364.

Gutierrez G. (2005). Grid Analysis. User's Manual, Department of Mechanical Engineering, The University of Sheffield.

Hashemi S.H. (2003). Assessment of the Fracture Behaviour of High Grade Steel for Gas Pipeline Steel. Thesis in the Department of Mechanical Engineering Department, The University of Sheffield.

Hashemi S.H., Andrews R.M. Howard I.C., Yates J.R. and Edwards A. (2004a). A Single Specimen CTOA Test Method for Evaluating the Crack Tip Opening Angle in Gas Pipeline Steels. In Proceedings of the 5th International Pipeline Conference, (IPC 2004), Calgary, Alberta, Canada. Vol. 1, pp. 1703-1709.

Hashemi S.H., Howard I.C., Yates J.R. and Andrews R.M. (2004b). Micro-mechanical Damage Modelling of Notched Bar Testing of Modern Line Pipe Steel. 15th The European Conference of Fracture. Stockholm, Sweden.

Hashemi S.H., Howard I.C., Yates J.R., Andrews R.M. and Edwards A.M. (2004c). Experimental Study of Thickness and Fatigue Precracking Influence on the CTOA Toughness values of High Grade Gas Pipeline Steel. Proceeding of IPC 2004 International Pipeline Conference, Calgary, Alberta, Canada.

Hashemi S.H., Gay R., Howard I.C., Andrews R.M. and Yates J.R. (2004d). Development of a Laboratory Test Technique for Direct Estimation of Crack Tip Opening Angle. 15th The European Conference of Fracture. Stockholm, Sweden.

Hashemi S.H., Howard I.C., Yates J.R. and Andrews R.M. (2006) Experimental Investigation of Slant Crack Propagation in X100 Pipeline Steel. 16th European Conference of Fracture, Alexandroupolis, Greece.

Howard I.C., Li Z.H, Sheikh M.A., Lidbury DPG and Sherry A.H. (1996). The Simulation of the Fourth Spinning Cylinder Test Using Damage Mechanics. ASME PVP-Vol. 324, Fatigue and Fracture, ed. K. Yoon, American Society of Mechanical Engineers, pp. 251-265.

Howard I.C., Li Z.H and Sheikh M.A. (2000). Modeling the Ductile to Cleavage transition in Steel structures, in Fatigue and Fracture. 30th Volume, P.C. Paris and K Jerina (Eds), ASTM ATP 1360, American Society for Testing and Materials, West Conshohocken, PA, pp. 152-168.

Hill R. (1950). The mathematical Theory of Plasticity. Oxford University Press.

James M.A., Newman Jr. J.C., (2003). The Effect of Crack Tunneling on Crack Growth: Experiments and CTOA Analyses. Engineering Fracture Mechanics. Vol. 70, pp. 457-468.

James M.A. and Newman Jr J.C., 2002, Three Dimensional Analyses of Crack Tip-Opening Angles and δ_5-Resistance Curves for 2024-T351 Aluminium Alloy, ASTM STP 2002;1406:279-97.

Johnson H.H.. Calibrating the Electric Potential Method for Studying Slow Crack Growth. Materials Research and Standards, Vol. 5, pp. 442-445.

Karafillis A.P and Boyce M.C. (1993). A General Anisotropic Yield Criterion Using Bounds and a Transformation Weighting Tensor. J Mech Phys Solids 41(12), 1859-1886.

Kawaguchi S., Hagiwara N., Ohata M., and Yotoda M., (2004) Int. Pipeline Conf., Calgary, Alberta, Canada.

Khvastunkov M.S. and Leggoe J.W. (2004). Adapting Cellular Automata to Model Failure in Spatially Heterogeneous Ductile Alloys. Scripta Materialia. Vol. 51,pp. 309-314

Kim J., Gao X. and Srivatsan T. S. (2004). Modeling of Void Growth in Ductile Solids: Effects of Stress Triaxiality and Initial Porosity. Engineering Fracture Mechanics 71, 379-400.

Knott J.F. (1980). Micromechanisms of Fibrous Crack Extensions in Engineering Alloys. Metal Science 14, 327-336.

Koning A.U. (1977). A Contribution to the Analysis of Quasi Static Crack Growth in Steel Materials, Proceeding of the 4th International Conference of Fracture. Vol. 3, pp. 25-31.

Koplin, J. and Needleman, A. (1988). Void growth and Coalescence in Porous Plastic Solids. International Journal of Solids and Structures 24, 835-853.

Leis, B.N., Eiber, R.J., Carlson, L. and Gilroy-Scott, A. (1998). In Proceedings of International Pipeline Conference Vol. II, ASME, 723-731.

Lemaitre, J. (1985). A Continuum Damage Mechanics Model for Ductile Fracture. Journal of Engineering Materials and Technology 107 (1), 83-89.

Li Z.H, Bilby B.A. and Howard I.C. (1994). A Study of the Internal Parameters of Ductile Damage Theory. Fat. Fract. Engng.Mat.Struct., 17, 1075-1087.

Lloyd W.R (2003). Microtopography for Ductile Fracture Process Characterization Part 1: Theory and Methodology. Engineering Fracture Mechanics. Vol. 70, pp. 387-401.

Lloyd W.R and McClintock. (2003). Microtopography for Ductile Fracture Process Characterization Part 2: Aplication for CTOA Analysis. Engineering Fracture Mechanics. Vol. 70, pp. 403-415.

Luu T.T., Tanguy B., Besson J., Pineau A. and Perrin G. (2006). Unified Constitutive Equations to Describe Elastoplastic and Damage Behavior of an X100 Linepipe Steel. 16th European Conference of Fracture, Alexandroupolis, Greece.

MaClintock, F.A. (1968). A Criterion for Ductile Fracture by the growth of voids, Journal of Applied Mechanics 35, 363-371.

Mahmoud S. and Lease K.B., 2003, The Effect of Specimen Thickness on the Experimental Characterization of Critical Crack-Tip-Opening Angle in 2024-T351 Aluminium Alloy. Engineering Fracture Mechanics, Vol. 70, pp. 443-456.

Mannucci G., Buzzichelli G., Salvini P., Eiber R. And Carlson L. (2000). In Proceedings of the Third International Pipeline Conference, Calgary, Alberta, Canada, Vol. 1, pp. 315-320.

Mannucci G., Demofonti G., Galli M.R. and Spinelli C.M. (1999). Structural Integrity of API 5L X70-X80 Steel Grade Pipeline for High Pressure Long Distance Transmission Gas Lines. In: EPRG/PRCI 12th Biennial Joint Technical Meeting on Pipeline Research, Groningen.

Maxey W.A. (1974). Fracture Initiation, Propagation and Arrest. In: Fifth Symposium on Line Pipe Research, American Gas Association, Houston.

Needleman, A. (1972). Void growth in an elastic-plastic medium. Journal of Applied Mechanics 39, 964-970.

Needleman, A. and Tvergaard V. (1987). Analysis of Ductile Rupture Modes at a Crack Tip. J. Mech. Phys. Solids, 35, 151-183.

Needleman, A. and Tvergaard V. (1991). Numerical Study of Void Distribution Effects on Dynamical, Ductile Crack Growth. Engineering Fracture Mechanics, 38,157-173.

Newman Jr. J.C., Dawicke D.S. and Seshandri B.R. (2003a). Residual Strength Analyses of Stiffened and Un-stiffened Panels – Part I: Laboratory Specimens. Engineering Fracture Mechanics. Vol. 70, pp. 493-507.

Newman Jr. J.C., James M.A. and Zerbst (2003b). A Review of the CTOA/CTOD Fracture Criterion. Engineering Fracture Mechanics. Vol. 70, pp. 493-507.

O'Donoghue P.E., Kaninnen M.F., Leung C.P., Demofonti G. and Venzi S. (1997). The Development and Validation of a Dynamic Fracture Propagation Model for Gas Transmission Pipelines. International Journal of Pressure Vessel and Piping. Vol. 70, pp11-25.

Orowan E. (1949). Fracture and Strength of Solids. Report of Progress in Physics of Solids. Vol. 12, pp. 185-233.

Raabe D. and Becker R.C. (2000). Coupling of Crystal Plasticity Finite Element Model with a Probabilistic Cellular Automaton for Simulating Primary Static Recrystallization in Aluminium, Modelling and Simulation in Materials Science and Engineering. Vol. 8(4), pp. 445-462.

Rice, J.R.. (1968). A Path independent Integral and the Approximate Analysis of Strain Concentration by Notches and Cracks, "ASME Journal of Applied Mechanics. Vol. 35, pp. 379-386.

Rice, J.R. and Tracey, D.M. (1969). On the Ductile Enlargement of Voids in Triaxial Stress Fields. Journal of the Mechanics and Physics of Solids 17, 201-217.

Rivalin F., Besson J., Pineau A., Di Fant M. (2001). Ductile Tearing of Pipeline-steel Wide Plates II. Modeling of in-plane Crack Propagation, Engineering Fracture Mechanics 68, 347-364.

Rothwell A.B. (2000). Fracture Propagation Control for Gas Pipelines- Past, Present and Future. Pipeline Technology, Vol. 1 Edited by R. Denys, Elsevier Science, pp. 387-405.

Rousselier G. (1987). Ductile Fracture Models and Their Potential in Local Approach to Fracture. Nuclear engineering and Design 105 (1), 97-111.

Rousselier G. Devaux J.C. Mottet G. and Devesa G. (1989). A Methodology for Ductile Fracture Analysis Based on Ductile Mechanics: An Illustration of a Local Approach of Fracture, in Nonlinear Fracture Mechanics: Volume II - Elastic -Plastic Fracture, ASTM STP 995. Landes J.D. Saxena A., Merkle J.G Eds., pp. 332-354.

Rudland D.L., Wilkowski G.M., Feng Z., Wang Y.Y., Horsley D. and Glover A. (2003). Engineering Fracture Mechanics. Vol.70, pp. 567-577.

Ruggeri C. and Dodds R.H. (1996). A Transferability Model for Brittle Fracture Including Constraint and Ductile Tearing Effects- a Probabilistic Approach. International Journal of Fracture 79, 309-340.

Schindler, H.J. (1996). International Journal of Pressure Vessel and Piping. Vol. 69, pp. 125-134.

Shanmugam S., Misra R.D.K., Hartmann J. and Jansto S.G. (2006). Microstructure of High Strength Niobium Containing Pipeline Steel. Materials Science and Engineering A 441, pp. 215-229.

Sharma U. and Ivey D. G. (2000). Microstructure of Microalloyed Linepipe Steels. International Pipeline Conference ASME, Vol.1, pp. 193-201.

Sherry A.H., France C.C. and Goldthorpe M.R. (1995). Compendium of T-Stress Solutions for Two and Three Dimensional Cracked Geometries. Fatigue Fract. Engng. Mater. Struct. Vol. 18, No. 1, pp. 141-155.

Shterenlikht A. (2003). 3D CAFE Modelling of Transitional Ductile – Brittle Fracture in Steels. Thesis in the Department of Mechanical Engineering, The University of Sheffield.

Shterenlikht A., and Howard I.C. (2004). Cellular Automata Finite Element (CAFE) Modelling of Transitional Ductile – Brittle Fracture in Steel. The 15th European Conference of Fracture.

Shterenlikht A., Hashemi S.H., Howard I.C, Yates J.R. and Andrews R.M. (2004). A Specimen for Studying the Resistance to Ductile Crack Propagation in Pipes. Engineering Fracture Mechanics. Vol. 71, pp. 1997-2013.

Smith Y. E., Coldren A.P. and Cryderman R.L. (1972). Toward Improved Ductility and Toughness. Tokyo: Climax Molybdenum Company (Japan) Ltd. Pp. 119-142.

Smith Y. E., Coldren A.P. and Cryderman R.L. (1976). *High-Strength, Ductile Mn-Mo-Nb* Steels with a Structure of Acicular Ferrite. Met Sci Heat Treat (English Translation of Metallovedenie i Termicheskaya Obrabotka Metallov). 18(1-2):59-65.

Stampfl J. and Kolednik O. (2000). The Separation of the Fracture Energy in Metallic Materials. International Journal of Fracture. Vol. 101. pp. 321-345.

Surface 8. (2002) Golden Software, Inc.

Sutton M.A., Dawicke D.S. and Newman Jr. J.C. (1995). Orientation Effects on the Measurement and Analysis of Critical CTOA in Aluminium Alloy Sheet. Fracture Mechanics: 26th Volume, ASTM STP1256, pp. 303-318.

Tanguy B. and Besson J. (2002). An Extension of the Rousselier Model to Viscoplastic Temperature dependent Materials. International Journal of Fracture 116, 81-101.

Tai Y.H., Lopez-Crespo P., Ayvar-Soberanis S., Yates J.R., Shterenlikht A. and Withers P.J. (2007). Optical Experimental Methods for Determining Fatigue and Fracture Properties. Fatigue 2007 – The 6th Engineering Integrity Society International Conference on Durability and Fatigue. Cambridge, UK.

Tvergaard, V. (1981). Influence of Voids on Shear Band Instabilities Under Plain Strain Conditions. International Journal of Fracture 17, 389-407.

Tvergaard, V. (1982a), Ductile Fracture by Cavity Nucleation Between Larger Voids, Journal of the Mechanics and Physics of Solids 30(4), 265-286.

Tvergaard, V. (1982b). On Localization in Ductile Materials Containing Spherical Voids. International Journal of Fracture 18(4), 237-252.

Tvergaard, V and Needleman, A. (1984). Analysis of the Cup-Cone Fracture in a Round Tensile Bar. Acta Metallurgica 32, 157-169.

Van Stone R.H., Cox T.B., Low Jr J.R. and Psioda J.A. (1985). Microstructural Aspects of Fracture by Dimple Rupture. Int Met Rev. Vol. 30, pp. 157-179.

Von Neuman J. (1966). Theory of Self-reproducing Autonoma, in A W Banks (Ed), University of Illinois, Urbana.

Wells, A.A. (1961a). Unstable Crack Propagation in Metals: Cleavage and Fast Fracture. Proceeding of the Cranfield Crack Propagation Symposium. Vol. 1, pp. 210-230.

Wells A.A. (1961b). Application of Fracture Mechanics at and Beyond General Yielding. British Welding Journal. Vol. 11, pp. 563-570.

Wells A.A. (1963). Notch Bar Tests, Fracture Mechanics and Brittle Strengths of Welded Structures. British Welding Journal. Vol. 12, pp2-13.

Wilkowski G.M., Maxey W.A. Eiber R.J., 1978, Ductile Fracture Propagation Resistance of Rising Self controlled Rolled Steels. In: ASM Symposium on What Does Charpy Energy Really Mean? Denver, Co.

Wilkowski G.M., Rudland D.L. Wang Y.Y., Horsley D. Glover A. and Rothwell B. (2002) Determination of the Region of Steady State Crack Growth from Impact Tests. In Proceeding of IPC'2002 4th Elsevier. International Pipeline Conference, Alberta, Canada. p.p. 1-7.

Wilkowski G.M., Wang Y.Y. and Rudland D.L. (2000). Recent Efforts on Characterising Propagating Ductile Fracture Resistance of Linepipe Steel. Pipeline Technology. Vol 1, pp359-386.

Wilsforf H.G.F. (1983). The Ductile Fracture of Metals: a Microstructural Viewpoint. Materials Science and Engineering 59, 1-19.

Xia L. and Shih F. (1995). Ductile Crack Growth-I. A Numerical Study Using Computational Cells with Microstructurally –Based Length Scales. J. Mech. Phys. Solids 43(2), pp. 233-259.

Xiao F., Liao B., Ren D., Shan Y. and Yang K. (2005). Acicular Ferritic Microstructure of a Low-Carbon Mn-Mo-Nb Microalloyed Pipeline Steel. Material Characterization 54 (2005), pp. 305-314.

Xiao F., Liao B., Shan Y., Qiao G., Zhong Y., Zhang C. and Yang K. (2006). Challenge of Mechanical Properties of an Acicular Ferrite Pipeline Steel. Materials Science and Engineering A 431. pp. 41-52.

Yamamoto, H. (1978). Conditions for Shear Localization in the Ductile Fracture of Void Containing Materials. International Journal of Fracture 14(4), pp. 347-365.

Zhao M., Yang K., Xiao F. and Shan Y. (2003). Continuous Cooling Transformation of Undeformed and Deformed Low Carbon Pipeline Steels. Materials Science and Engineering A355, pp. 126-136.

Zhao M., Hanamura T., Qiu H. and Yang K. (2005) Lath Boundary Thin Film Martensite in Acicular Ferrite Ultralow Carbon Pipeline Steels. Materials Science and Engineering A 395, pp. 327-332.

APPENDIX I: Code used for the simulation of the CT specimen in ABAQUS input file for the conventional FE

```
****Name of the test and reference of external file containing the model data****
*HEADING
CT test
*INCLUDE, INPUT=3d-ct-mesh-40size-half1.inp
**********************************************************************************
****Printout for the analysis input file processor****
*PREPRINT, ECHO=NO, HISTORY=NO, CONTACT=NO
*RESTART, WRITE, NUMBER INTERVAL=3
**********************************************************************************
****Specify element properties of solid elements****
*SOLID SECTION, ELSET=allel1, MATERIAL=steel1
*SOLID SECTION, ELSET=allel2, MATERIAL=steel2
*SOLID SECTION, ELSET=ele-fine, MATERIAL=steelone
**********************************************************************************
****Description of the material properties for the material steel1****
*MATERIAL, NAME=steel1
*ELASTIC
2.1E5, 0.3
*PLASTIC
*INCLUDE, INPUT=mat.inp
*DENSITY
7.87E-9
**********************************************************************************
**** Description of the material properties for the material steel2****
*MATERIAL, NAME=steel2
*ELASTIC
2.1E5, 0.3
*PLASTIC
*INCLUDE, INPUT=mat.inp
*DENSITY
7.87E-9
**********************************************************************************
****GTN MODEL*******
*MATERIAL, NAME=steelone
*ELASTIC
2.1E5, 0.3
*PLASTIC
*INCLUDE, INPUT=mat.inp
*POROUS METAL PLASTICITY, RELATIVE DENSITY=0.9998952542
1.5, 1.05, 2.25
*POROUS FAILURE CRITERIA
0.005, 0.0017
*DENSITY
7.87E-9
**********************************************************************************

****Definition of the surface or region in the model****
*SURFACE, TYPE=ELEMENT, NAME=ONE
sup-pin1
*SURFACE, TYPE=ELEMENT, NAME=TWO
sup-pin2
```

```
**********************************************************************************************
****Beginning a step****
*STEP, NLGEOM=YES
*DYNAMIC, EXPLICIT
,0.1
**********************************************************************************************
****Mass scaling is often used in ABAQUS/Explicit for computational efficiency in****
****quasi-static analyses and in some dynamic analyses that contain a few very small****
****elements that control the stable time increment****
*VARIABLE MASS SCALIN, TYPE=BELOW MIN, DT=1E-6, FREQUENCY=10
**********************************************************************************************
****This option allows arbitrary time variations to be given throughout a step****
*AMPLITUDE, NAME=BCAMP, TIME=TOTAL TIME, VALUE=ABSOLUTE, SMOOTH=0.05
0,0,0.1,5
**********************************************************************************************
****Define surfaces that contact each other****
*CONTACT PAIR
ONE, TWO
**********************************************************************************************
****Specify boundary conditions****
*BOUNDARY
node-fine,2,
nodeup,1,
nodeup,3,
nodebs,1,
nodebs,3,
*BOUNDARY, TYPE=DISPLACEMENT, AMPLITUDE=BCAMP
nodeup,2,2,5.0
*BOUNDARY, TYPE=DISPLACEMENT, AMPLITUDE=BCAMP
nodebs,2,2,5.0
**********************************************************************************************
****Define output written to the results file****
*FILE OUTPUT, NUMBER INTERVAL=100
*NODE FILE, NSET=nodeup
U,RF
*NODE FILE, NSET=nodebs
U,RF
*NODE FILE, NSET=gage
U,RF
*ENERGY FILE
ALLIE
ALLWK
ETOTAL
**********************************************************************************************
****Define output requests to the output database****
*OUTPUT, FIELD, NUMBER INTERVALS=100
*NODE OUTPUT
U, RF
*ELEMENT OUTPUT
STATUS, VVF, S, PEEQ
*NODE OUTPUT
U, RF
*OUTPUT, HISTORY, FREQUENCY=100
*NODE OUTPU, NSET=nodeup
```

```
U, RF
*NODE OUTPU, NSET=nodebs
U, RF
*NODE OUTPU, NSET=gage
U, RF
**********************************************************************************************
****End the definition of a step****
*END STEP
**********************************************************************************************
```

APPENDIX II: Code used for the simulation of the Tear specimens in ABAQUS input file for the CAFE technique

```
****Name of the test and reference of external file containing the model data****
*HEADING
Tear test
*INCLUDE, INPUT=3d-tear-19mm-half-mesh.inp
**********************************************************************************************
****Printout for the analysis input file processor****
*PREPRINT, ECHO=NO, HISTORY=NO, CONTACT=NO
*RESTART, WRITE, NUMBER INTERVAL=3
**********************************************************************************************
****Specify element properties of solid elements****
*SOLID SECTION, ELSET=allel1, MATERIAL=steel1
*SOLID SECTION, ELSET=allel2, MATERIAL=steel2
*SOLID SECTION, ELSET=ele-fine, MATERIAL=steelone
**********************************************************************************************
****Description of the material properties for the material steel1****
*MATERIAL, NAME=steel1
*ELASTIC
2.1E5, 0.3
*PLASTIC
*INCLUDE, INPUT=mat.inp
*DENSITY
7.87E-9
**********************************************************************************************
****Description of the material properties for the material steel2****
*MATERIAL, NAME=steel2
*ELASTIC
2.1E5, 0.3
*PLASTIC
*INCLUDE, INPUT=mat.inp
*DENSITY
7.87E-9
**********************************************************************************************
****CAFE MODEL****
*MATERIAL, NAME=steelone
*USER MATERIAL,CONSTANTS=3
20., 0.0065, 50.
*DENSITY
7.87E-9
*DEPVAR, DELETE=1
```

```
6
*INITIAL CONDITIONS, TYPE=SOLUTION
ele-fine, 1., 0., 1., 0., 0., 0.
**********************************************************************************************
****Definition of the surface or region in the model****
*SURFACE, TYPE=ELEMENT, NAME=ONE
pin1-1-3
*SURFACE, TYPE=ELEMENT, NAME=TWO
pin1-1-4
*SURFACE, TYPE=ELEMENT, NAME=THREE
pin1-3-3
*SURFACE, TYPE=ELEMENT, NAME=FOUR
pin1-3-4
*SURFACE, TYPE=ELEMENT, NAME=FIVE
pin2-1-3
*SURFACE, TYPE=ELEMENT, NAME=SIX
pin2-1-4
*SURFACE, TYPE=ELEMENT, NAME=SEVEN
pin2-2-3
*SURFACE, TYPE=ELEMENT, NAME=EIGHT
pin2-2-4
*SURFACE, TYPE=ELEMENT, NAME=NINE
pin2-3-3
*SURFACE, TYPE=ELEMENT, NAME=DIEZ
pin2-3-4
*SURFACE, TYPE=ELEMENT, NAME=TEN
pin3-1-3
*SURFACE, TYPE=ELEMENT, NAME=ELEVEN
pin3-1-4
*SURFACE, TYPE=ELEMENT, NAME=TWELVE
pin3-2-3
*SURFACE, TYPE=ELEMENT, NAME=THIRTEEN
pin3-2-4
*SURFACE, TYPE=ELEMENT, NAME=FOURTEEN
pin3-3-3
*SURFACE, TYPE=ELEMENT, NAME=FIFTEEN
pin3-3-4
*SURFACE, TYPE=ELEMENT, NAME=SIXTEEN
pin4-1-3
*SURFACE, TYPE=ELEMENT, NAME=SEVENTEEN
pin4-1-4
*SURFACE, TYPE=ELEMENT, NAME=EIGHTEEN
pin4-2-3
*SURFACE, TYPE=ELEMENT, NAME=NINETEEN
pin4-2-4
*SURFACE, TYPE=ELEMENT, NAME=TWENTY
pin4-3-3
*SURFACE, TYPE=ELEMENT, NAME=TWENTYONE
pin4-3-4
*SURFACE, TYPE=ELEMENT, NAME= TWENTYTWO
pin5-1-3
*SURFACE, TYPE=ELEMENT, NAME= TWENTYONE
pin5-1-4
*SURFACE, TYPE=ELEMENT, NAME= TWENTYTHREE
```

```
pin5-2-3
*SURFACE, TYPE=ELEMENT, NAME= TWENTYFOUR
pin5-2-4
*SURFACE, TYPE=ELEMENT, NAME= TWENTYFIVE
pin5-3-3
*SURFACE, TYPE=ELEMENT, NAME= TWENTYSIX
pin5-3-4
**********************************************************************************************
****Beginning a step****
*STEP, NLGEOM=YES
*DYNAMIC, EXPLICIT
,0.1
**********************************************************************************************
****Mass scaling is often used in ABAQUS/Explicit for computational efficiency in****
****quasi-static analyses and in some dynamic analyses that contain a few very small****
****elements that control the stable time increment****
*VARIABLE MASS SCALIN, TYPE=BELOW MIN, DT=1E-6, FREQUENCY=10
**********************************************************************************************
****This option allows arbitrary time variations to be given throughout a step****
*AMPLITUDE, NAME=BCAMP, TIME=TOTAL TIME, VALUE=ABSOLUTE, SMOOTH=0.05
0,0,0.25,100.0
**********************************************************************************************
****Define surfaces that contact each other****
*CONTACT PAIR
ONE,TWO
*CONTACT PAIR
THREE,FOUR
*CONTACT PAIR
FIVE,SIX
*CONTACT PAIR
SEVEN, EIGTH
*CONTACT PAIR
NINE,TEN
*CONTACT PAIR
ELEVEN,TWELVE
*CONTACT PAIR
THIRTEEN,FOURTEEN
*CONTACT PAIR
FIFTEEN,SIXTEEN
*CONTACT PAIR
SEVENTEEN,EIGHTEEN
*CONTACT PAIR
NINETEEN,TWENTY
*CONTACT PAIR
TWENTYONE,TWENTYTWO
*CONTACT PAIR
TWENTYTHREE,TWENTYFOUR
*CONTACT PAIR
TWENTYFIVE,TWENTYSIX
*CONTACT PAIR
TWENTYSEVEN,TWENTYEIGHT


**********************************************************************************************
```

```
****Specify boundary conditions****
*BOUNDARY
node-fine,2,
nodeup,1,
nodeup,3,
nodebs,1,
nodebs,3,
all-node-pins,3,
*BOUNDARY, TYPE=DISPLACEMENT, AMPLITUDE=BCAMP
nodeup,2,2,35.0
*BOUNDARY, TYPE=DISPLACEMENT, AMPLITUDE=BCAMP
nodebs,2,2,35.0
**********************************************************************************************
****Define output written to the results file****
*FILE OUTPUT, NUMBER INTERVAL=100
*NODE FILE, NSET=nodeup
U,RF
*NODE FILE, NSET=nodebs
U,RF
*NODE FILE, NSET=gage1
U,RF
*NODE FILE, NSET=gage2
U,RF
*ENERGY FILE
ALLIE
ALLWK
ETOTAL
**********************************************************************************************
****Define output requests to the output database****
*OUTPUT,FIELD,NUMBER INTERVALS=100
*NODE OUTPUT
U,RF
*ELEMENT OUTPUT
STATUS,VVF,S,PEEQ,LE,PE,NE,EP
*NODE OUTPUT
U,RF
*OUTPUT,HISTORY,FREQUENCY=100
*NODE OUTPU,NSET=nodeup
U,RF
*NODE OUTPU,NSET=nodebs
U,RF
*NODE OUTPU,NSET=gage1
U,RF
*NODE OUTPU,NSET=gage2
U,RF
**********************************************************************************************
****End the definition of a step****
*END STEP
```

APPENDIX III: Critical values of the *t*-distribution

This table gives positive critical $t_{\alpha/2,\nu}$ and $t_{\alpha,\nu}$ values for selected t distributions ($\nu = 1, \ldots, 30, 40, 60, 120, \infty$).

	$t_{\alpha/2}$					
	$t_{0.20/2}$	$t_{0.10/2}$	$t_{0.05/2}$	$t_{0.02/2}$	$t_{0.01/2}$	$t_{0.001/2}$
	t_{α}					
ν	$t_{0.10}$	$t_{0.05}$	$t_{0.025}$	$t_{0.01}$	$t_{0.005}$	$t_{0.0005}$
1	3.078	6.314	12.706	31.821	63.657	636.619
2	1.886	2.920	4.303	6.965	9.925	31.598
3	1.638	2.353	3.182	4.541	5.841	12.941
4	1.533	2.132	2.776	3.747	4.604	8.610
5	1.476	2.015	2.571	3.365	4.032	6.859
6	1.440	1.943	2.447	3.143	3.707	5.959
7	1.415	1.895	2.365	2.998	3.499	5.405
8	1.397	1.860	2.306	2.896	3.355	5.041
9	1.383	1.833	2.262	2.821	3.250	4.781
10	1.372	1.812	2.228	2.764	3.169	4.587
11	1.363	1.796	2.201	2.718	3.106	4.437
12	1.356	1.782	2.179	2.681	3.055	4.318
13	1.350	1.771	2.160	2.650	3.012	4.221
14	1.345	1.761	2.145	2.624	2.977	4.140
15	1.341	1.753	2.131	2.602	2.947	4.073
16	1.337	1.746	2.120	2.583	2.921	4.015
17	1.333	1.740	2.110	2.567	2.898	3.965
18	1.330	1.734	2.101	2.552	2.878	3.922
19	1.328	1.729	2.093	2.539	2.861	3.883
20	1.325	1.725	2.086	2.528	2.845	3.850
21	1.323	1.721	2.080	2.518	2.831	3.819
22	1.321	1.717	2.074	2.508	2.819	3.792
23	1.319	1.714	2.069	2.500	2.807	3.767
24	1.318	1.711	2.064	2.492	2.797	3.745
25	1.316	1.708	2.060	2.485	2.787	3.725
26	1.315	1.706	2.056	2.479	2.779	3.707
27	1.314	1.703	2.052	2.473	2.771	3.690
28	1.313	1.701	2.048	2.467	2.763	3.674
29	1.311	1.699	2.045	2.462	2.756	3.659
30	1.310	1.697	2.042	2.457	2.750	3.646
40	1.303	1.684	2.021	2.423	2.704	3.551
60	1.296	1.671	2.000	2.390	2.660	3.460
120	1.289	1.658	1.980	2.358	2.617	3.373
∞	1.282	1.645	1.960	2.326	2.576	3.291

Source: Table III of Ronald A. Fisher and Frank Yates, *Statistical Tables for Biological, Agricultural and Medical Research* (6th ed.), Longman Group Ltd., London, 1974. (Previously published by Oliver & Boyd Ltd., Edinburgh.)